UNIVERSIDADE TÉCNICA DE LISBOA

INSTITUTO SUPERIOR TÉCNICO

TRIBO-MECHANICAL BEHAVIOUR OF THE Ni-Co SYSTEM: FROM MICRO TO NANOSCALE

Sérgio de Almeida Graça

(Licenciado)

Dissertação para obtenção do Grau de Doutor em Engenharia de Materiais

DOCUMENTO PROVISÓRIO

Dezembro de 2008

UNIVERSIDADE TÉCNICA DE LISBOA

INSTITUTO SUPERIOR TÉCNICO

TRIBO-MECHANICAL BEHAVIOUR OF THE Ni-Co SYSTEM: FROM MICRO TO NANOSCALE

Sérgio de Almeida Graça

(Licenciado)

Dissertação para obtenção do Grau de Doutor em Engenharia de Materiais

DOCUMENTO PROVISÓRIO

Dezembro de 2008

ABSTRACT

The tribo-mechanical behaviour of materials is generally characterized by using macro- and microscale tests. In particular, large scale hardness tests are frequently used for a preliminary evaluation of wear resistance. Although several studies showed that hardness can increase significantly with decreasing penetration depth (indentation size effect – ISE), most of them were not conducted in typical rubbing engineering materials and, more importantly, only few revealed interest on the impact of ISE on wear.

In this work, the study of the contact scale dependence of hardness and its consequences to abrasive wear, one of the most frequent forms of wear, was extended to the case of ductile materials with a structural complexity which is common in rubbing engineering metallic components, thereby representing an approach to real sliding contact applications – Ni-Co samples produced by laser cladding. It was found that both the indentation and scratch hardness of these samples increase significantly when the depth decreases to the nanometre range, due essentially to the larger relevance of strain hardening and surface free energy effects at smaller scales. The hardness results, together with nanoabrasive wear tests results, strongly indicate that the tribo-mechanical behaviour of materials that present ISE should be characterised with techniques that reproduce the scale at which surface asperities interact.

Keywords: contact scale, hardness, abrasive wear, ductile materials, Ni-Co system, laser cladding.

RESUMO

O comportamento tribo-mecânico dos materiais é geralmente caracterizado através de ensaios à macro- e microescala. Em particular, ensaios de macro- e microdureza são usados frequentemente para uma avaliação preliminar da resistência ao desgaste. Apesar de diversos estudos terem mostrado que a dureza pode aumentar significativamente com a diminuição da profundidade de penetração (efeito do tamanho da indentação – ETI), a maioria não foi realizada em materiais usados em applicações de engenharia que envolvem contacto deslizante e, mais importante, apenas alguns destes estudos demostraram interesse pela análise do ETI sobre o comportamento ao desgaste.

Neste trabalho, o estudo da dependência da dureza em relação à escala de contacto e as suas consequências para o desgaste abrasivo, um dos tipos mais frequentes de desgaste, foi alargado ao caso de materiais dúcties com uma compexidade estrutural que é comum em componentes metálicos usados em aplicações de engenharia que envolvem contacto deslizante, representando desta forma uma aproximação a applicações reais que envolvem contacto deslizante – amostras Ni-Co produzidas por deposição assistida por laser. Foi observado que, tanto a dureza de indentação como a de riscagem destas amostras, aumentam significativamente quando a produndidade diminuí para a gama dos nanómetros, e que este aumento é causado essencialmente pela maior influência de efeitos relativos ao encruamento e à energia de superfície a escalas menores. Os resultados de dureza, juntamente com os resultados de ensaios de desgaste nanoabrasivo, indicam fortemente que o comportamento tribo-mecânico de materiais que apresentam ETI deve ser caracterizado com técnicas que reproduzam a escala à qual as asperezas da superfície interagem.

Palavras-chave: escala de contacto, dureza, desgaste abrasivo, materiais dúcteis, sistema Ni-Co, deposição assistida por laser.

ACKNOWLEDGEMENTS

First of all, I would like to give my deepest thanks to my supervisor Rogério Anacleto Cordeiro Colaço, Associate Professor of the Department of Materials Engineering of IST, and my co-supervisor Rui Mário Correia da Silva Vilar, Full Professor of the Department of Materials Engineering of IST, who created the conditions that made this work possible and supported me not only over the period of this work but also during my graduation in Materials Engineering.

Next, I would like to thank my colleagues and friends of the Department of Materials Engineering of IST: António Crespo, Anandkumar Ramasamy, Augusto Moita de Deus, Amélia Almeida, Alexandra Jacques, Andrei Outkine, Alexander Lavrov, Ana Gama, Bruno Nunes, Christopher Meacock, Daniela Nunes, Edson Santos, Isabel Nogueira, Luís Fortes, Luís Santos, Patrícia Carvalho, Rodrigo Santos, Sónia Eugénio and Victor Oliveira.

I would also like to thank my colleagues and friends who were former members of the Department of Materials Engineering of IST: Ana Marques, Armando Fernandes, Cristina Gonçalves, Décio Dias, Fernanda Carvalho, Flávio Simões, José Brás, Kevyn Degiampietro, Lino Costa, Ricardo Pires, Sónia Pereira, Sivakumar Manickam and Teresa Adrega.

I could not forget to thank some of my closest friends from the time of my graduation: Ana Cascais, Ana Luísa, Hugo Álvares, Isa Fonseca, João Cruz, Marta Veríssimo, Rolim Carmo, Rui Lopes and Vivian Ramos. Also a special thanks to my friends from Switzerland: Anke Möller, Ana Vujanic, Anca Moina, Anisoara Socoliuc, Akshata Rao, Boriana Neykova, Christian Köhler, Christoph Berssenbrügge, Fahim Chowdhury and his wife, Holger Voß, Kathrin Schweda, Katrin Kalf, Kyumin Lee, Melanie Roth, Matthias Lüthi, Michael de Jesus Pereira, Nadia Stucki, Sabine Maier, Till Heusner and Vanessa Moraes.

I would like to specially acknowledge some people who helped me with some aspects of my work: Anandkumar Ramasamy, for helping me operating the CO_2 laser; Patrícia Carvalho and Isabel Nogueira for teaching me how to operate the transmission electron microscope; Prof. Albano Cavaleiro, Dr. Sofia Ramos and Ana Manaia, of the Department of Mechanical Engineering of the Faculty of Sciences of the University of Coimbra, for teaching me how to operate the ultramicrohardness tester; Dr. Andrzej Kulik of the Institut of Physics of Complex Matter of École Polytechnique Fédérale de Lausanne, and Prof. Stefan Hengsberger of the University of Applied Sciences of Fribourg, for teaching me how to operate the Triboscope nanomechanical test instrument; Prof. Ernst Meyer, Dr. Enrico

Gnecco and Dr. Anisoara Socoliuc, of the Department of Physics and Astronomy of the University of Basel, for helping me on the initiation in AFM-based nanomechanical tests; Dr. Eduardo Pires of CATIM-Lisbon, for the availability to use the microscratch equipment; Prof. Olinda Conde of the Department of Physics of the Faculty of Sciences of the University of Lisbon, for the availability to use the XRD and optical profilometry equipments; Dr. Fátima Montemor of the Department of Chemistry of IST, for the help in performing Auger depth profile chemical analysis.

I would like to thank *Fundação para a Ciência e a Tecnologia* for the financial support of this research (Project Nanonico, POCTI/CTM/59376/2004) and for my PhD grant (SFRH/BD/17758/2004). I would also like to thank the *European Science Foundation* for the financial support of this research (Nanotribology program, Exchange Grant No. 846).

Finally, a particularly special thanks to my family and my fiancée Teresa, for all their support during the long journey of my academic formation.

LIST OF PUBLICATIONS

- S. Graça, R. Colaço, R. Vilar, *Using Atomic Force Microscopy to Retrieve Nanomechanical Surface Properties of Materials*, Materials Science Forum, Vols. 514-516, pp. 1598-1602 (2006).

- S. Graça, R. Colaço, R. Vilar, *Indentation size effect in nickel and cobalt laser clad coatings*, Surface and Coatings Technology, Vol. 202, pp. 538-548 (2007).

- S. Graça, R. Colaço, P. A. Carvalho, R. Vilar, *Determination of dislocation density from hardness measurements in metals*, Materials Letters, Vol. 62, pp. 3812-3814 (2008).

- S. Graça, R. Colaço, A. J. Kulik, R. Vilar, *A displacement sensing nanoindentation study of tribo-mechanical properties of the Ni-Co system*, Applied Surface Science, Vol. 254, pp. 7306-7313 (2008).

- S. Graça, R. Colaço, R. Vilar, *Micro-to-Nano Indentation and Scratch Hardness in the Ni-Co system: Depth Dependence and Implications for Tribological Behavior*, Tribology Letters, Vol. 31, pp. 177-185 (2008).

- S. Graça, R. Colaço, R. Vilar, *Scale dependence of indentation and scratch response of Ni, Co and Ni-Co alloys*, Proceedings of the IV Iberian Congress of Tribology, Escuela Superior de Ingenieros de Bilbao, 21-22 June 2007, pp. 442-447 (2007).

SYMBOLS AND ACRONYMS

a = lattice parameter of the cubic lattice / hexagonal lattice (base)

a_c = contact radius in the purely elastic regime

A = area of the observed region

A' = excess surface area created during the indentation process

A_f = areal fraction

A_{HCS} = area of the average horizontal cross-section of the worn region

A_i = surface contact area of the indentation

A_n = nominal contact area

A_p = projected contact area of the indentation

A_{pores} = total area of pores in an image

A_r = real contact area

A_s = projected contact area in a scratch test

α = angle between the front edge and the axis of the DNISP tip

α_i = apex semi-angle of an ideal conical indenter

b = Burgers vector

B = constant of the load-displacement relation during unloading

β = angle between the back face and the axis of the DNISP tip

β_i = constant for the deviation of the indenter geometry from the circular one

c = lattice parameter of the hexagonal lattice (height)

c_{eff} = effective spring constant of the probe-surface system

c_n = normal spring constant of the cantilever

C = compliance of the system (contact + indentation equipment)

C_c = contact compliance

C_i = coefficients of the area function in the Oliver and Pharr method

C_m = machine compliance

d = separation between the reference plane of the rough surface and the smooth surface in the Greenwood and Williamson model

d_{hkl} = interplanar spacing of the (hkl) planes

δ = constant in the Taylor hardening model

$\Delta H_{dislocations}$ = contribution to hardness arising from the Nix-Gao equation

ΔH_{SFE} = contribution of SFE to hardness

Δx_p = lateral compensating movement of the piezoelectric scanner

Δx_t = lateral movement of the tip during indentation

ΔZ = normal deflection of the cantilever in metric units

Δz_p = vertical displacement of the piezoelectric scanner

ΔZ_V = normal deflection of the cantilever in Volt units

e = spacing between loops of GNDs in the Nix-Gao model

E = Young's modulus of sample material

E_i = Young's modulus of indenter material

E_r = reduced Young's modulus of the contact

E_s = surface free energy

ε = constant for the deviation of the indenter geometry from the flat punch one

ε_r = representative strain

f = correction factor for the size of the plastic zone in the Nix-Gao model

f^* = driving frequency for cantilever oscillation

f_0 = free-surface resonant frequency of the cantilever

f_c = resonant frequency of the cantilever after contact

f_N = normal load applied at an individual asperity in a rough surface

F = structure factor

$F_{\max}$ = maximum load applied in the indentation test

F_N = normal load

F_s = force required to create the excess surface area during the indentation process

F_T = tangential load

$\phi(z)$ = probability density function for the distribution of asperity heights

g = reciprocal lattice vector

G = shear modulus

γ = geometrical constant of the area function of ideal conical and pyramidal indenters

Γ = *X Rotate* parameter

h = indentation depth (also used to represent the indenter displacement)

h^* = characteristic length in the Nix-Gao model

h_{AFM} = contact depth when using an ideal indenter (Antunes *et al*. method)

h_c = contact depth

h_f = final depth

$h_{\max}$ = maximum depth

h_s = surface displacement at the contact perimeter

H = hardness at a certain indentation depth h

H_0 = bulk hardness

H_1 = strain hardening component in the Swadener model for ISE in conical/pyramidal indentation

H_f = hardening component in the model of Elmustafa and Stone

H_i = indentation hardness

H_s = scratch hardness

H_V = Vickers hardness

η = geometrical constant for the calculation of H_s

k_i = coefficients of the area function in the Antunes *et al*. method

K_{ab} = abrasive wear coefficient

K'_{ab} = specific abrasive wear coefficient

K_{ad} = adhesive wear coefficient

κ = geometrical constant in the extended Jäger model

l = length of dislocation lines

l_g = total length of GNDs

l_p = projected length of dislocation lines

L_{worn} = length of the worn region in an AFM-based wear test

λ = wavelength of the radiation

m = exponent of the load-displacement relation during unloading

m_0 = effective mass that loads the cantilever

μ = coefficient of friction

n = order of diffraction

n_a = number of contacting asperities

N_a = number of asperities of a surface

ν = Poisson's ratio of sample material

ν_i = Poisson's ratio of indenter material

Q = wear rate

Q_h = wear rate at a certain indentation depth h

θ = Bragg angle

θ_{is} = angle between the surface of the indenter and the surface plane of the sample (equivalent to the attack angle of the abrasive particle)

r_a = curvature radius of the asperity summits

r_c = contact radius in the fully plastic state

R = curvature radius of the indenter

R^* = characteristic length in the Swadener model for ISE in spherical indentation

R_a = average roughness

R_p = curvature radius of a spherical indentation

R_z = average peak-to-valley height

ρ = dislocation density

ρ_g = density of geometrically necessary dislocations

ρ_s = density of statistically stored dislocations

ρ_T = total dislocation density

s_i = deviation (or excitation error) for the ith Kossel-Möllenstedt fringe in a CBED pattern

S = initial unloading stiffness of the system (contact + indentation equipment)

S_c = initial unloading stiffness of the contact

S_z = cantilever sensitivity

σ = standard deviation of the distribution of asperity heights

σ_0 = uniaxial stress corresponding to the intrinsic lattice resistance

σ_m = mean contact pressure

σ_{max} or p_0 = maximum contact pressure

σ_{mc} = mean pressure at the multiple contacts

σ_r = stress in the radial direction

σ_Y = uniaxial yield stress

σ_z = stress in the direction normal to the sample's surface

σ_θ = angular stress

t = thickness of the observed region

τ = shear yield stress (shear strength)

τ_0 = shear stress corresponding to the intrinsic lattice resistance

τ_1 = principal shear stress (= $\frac{1}{2}|\sigma_z - \sigma_\theta|$)

τ_{max} = maximum shear stress

v = sliding speed

V = volume of the observed region

V_c = hemispherical volume defined by the contact radius r_c

V_f = volume fraction

V_R = volume of material removed during abrasion

V_{worn} = volume of material removed during an AFM-based wear test

w = scratch width

x = sliding distance

ξ_g = extinction distance

ψ = plasticity index

AES = auger electron spectroscopy

AFM = atomic force microscopy

BCC = body centred cubic

BF = bright-field

BRM = blind reconstruction method

BSE = backscattered electrons

CBED = convergent beam electron diffraction

CCD = charge-coupled device

CDF = centred dark-field

CMP = chemical-mechanical polishing

CRT = cathode-ray tube

DF = dark-field

DSI = displacement sensing indentation

DSN = displacement sensing nanoindentation

EDS = energy dispersive spectroscopy

EP = electropolished

FCC = face centred cubic

FD = force-displacement

FSD = fast scan direction

GNDs = geometrically necessary dislocations

HCP = hexagonal closed packed

HPD = helical prismatic dislocations
HRTEM = high resolution transmission electron microscopy
ISE = indentation size effect
LFM = lateral force mode
MD = molecular dynamics
MEMS = microelectromechanical systems
MFM = magnetic force microscopy
MP = mechanically polished
NEMS = nanoelectromechanical systems
OM = optical microscopy
PDL = prismatic dislocation loops
PSD = position-sensitive detector
PZT = piezoelectric transducer
SAD = selected-area diffraction
SE = secondary electrons
SEM = scanning electron microscopy
SFE = surface free energy
SPM = scanning probe microscopy
SSD = slow scan direction
SSDs = statistically stored dislocations
SSS = solid solution strengthening
TEM = transmission electron microscopy
UHV = ultra-high vacuum
XRD = X-ray diffraction

TABLE OF CONTENTS

1. INTRODUCTION

The motivation for the proposed work is given in this chapter. In addition, a brief description of the mechanics of the contact between solid surfaces under single and multiple contact conditions is made. Then, the conventional theory of abrasive wear of ductile materials, which neglects the influence of contact scale, is presented. Finally, the state of the art in the contact scale dependence of abrasive wear and hardness is reviewed.

1.1. Motivation

The relative motion between two contacting solid surfaces can generate wear, which consists on the damage of one or both surfaces, generally involving progressive loss of material. Having control over this phenomenon is fundamental since, among others, it can lead to the failure of mechanical components, which can result in significant economical losses and, more importantly, in damage to human lives. In fact, previous estimations showed that the costs due to wear amount to about 6% of the U.S. Gross National Product [1]. On the other hand, in some cases it is desirable to increase wear, such as in the grinding and polishing of components: e.g. the chemical-mechanical polishing (CMP) process of silicon wafers has nowadays a large economical impact due to the microelectronics industry (see, for instance, [2]).

Depending on the parameters of the tribological system (e.g. body, counterbody, interfacial elements, environment, loading conditions and sliding speed), different types of wear may result (e.g. abrasion, adhesion, surface fatigue and tribochemical reaction) [3]. Abrasive wear is one of the most frequent forms of wear [1]. It consists on the displacement of material caused by the relative motion of hard particles between or embedded in one or both of the matching surfaces, or by the presence of hard asperities on one of the relatively moving surfaces [3]. Damage of the softer surface can occur by plastic deformation and/or fracture [3, 4]. Therefore, the most important properties of the material governing its abrasive wear behaviour are hardness, stiffness and fracture toughness. In the case of ductile materials (e.g. metals and alloys), hardness is usually considered as the property with the largest influence on their abrasive wear resistance, since the damage occurs mainly by plastic deformation of the surface. Therefore, hardness tests (e.g. indentation and scratch) are often used for a preliminary evaluation of the wear resistance [3, 4]. These tests are non-destructive and easy to perform, both in laboratorial and industrial conditions, and usually involve penetration depths in the range of a few micrometers to several tens of micrometers.

A large number of works has recently shown that hardness may increase significantly when the penetration depth is smaller than a few micrometers, especially in the submicrometric range (see, for instance, [5-12]). This effect is commonly known in the literature as *indentation size effect* (ISE). In this way, the contact scale dependence of hardness must considerably affect the abrasive wear behaviour of most rubbing engineering components since the contact between nominally flat surfaces, in dry or boundary lubrication conditions, frequent in rubbing engineering components, occurs between surface asperities

whose contact areas can be of only a few tens of square nanometres or even smaller [13]. Therefore, it can be expected that this effect should be particularly important not only in the case of the tribological behaviour of micro- and nanoelectromechanical systems (MEMS and NEMS, respectively) [14] but also in most cases of rubbing components.

While the macrotribological behaviour of rubbing components has been extensively studied for several decades, the study of the tribological response at the submicrometric contact scale (nanotribology) is a relatively recent and largely unknown research topic. Nanotribology has been largely stimulated by the advent of micro- and nanotechnologies and by the invention of the atomic force microscope [15], which provided the ability of quantitative testing and observation of surfaces down to the atomic scale. Fundamental understanding of the wear process can only be achieved by bridging the gap between nanotribology and macrotribology, a goal that is far from being accomplished [16].

The objective of the present work is to contribute to this goal, by giving further insight into the scale dependence of hardness and its consequences on the abrasive wear response of ductile materials. For this purpose, the Ni-Co system was chosen as case study and a wide range of tribo-mechanical characterisation techniques was used.

The system that results from the combination of Ni and Co is extremely interesting both from the tribological and metallurgical points of view. Properties such as wear, corrosion and heat resistance make Ni and Co the main constituents of two of the most frequently used families of hardfacing alloys for tribological applications, which are the nickel-base/boride type alloys and the cobalt-base/carbide type alloys [17]. Moreover, the equilibrium phase diagram of the Ni-Co system (Figure 1.1) is quite simple, since it only presents a liquid phase and two solid phases ((Ni, α-Co) and ε-Co), and does not present three-phase equilibrium (e.g. eutectic or peritectic) [18]. Solidification takes place in a very short temperature range (e.g. about 0.3 ºC at 50% Co) [19]. The α phase is face-centred cubic (FCC) while the ε phase is hexagonal closed packed (HCP). The lattice parameters of FCC Ni and FCC Co are, respectively, a = 3.5238 Å and a = 3.5520 Å, while in HCP Co a = 2.507 Å and c = 4.069 Å [20]. The phase diagram in Figure 1.1 also shows that Ni and Co present almost complete miscibility in solid state. At room temperature, alloys with Co weight percentage in the range ~ 68–80% consist of a mixture of α and ε [18], though the boundaries of the two-phase region are not well established due to the difficulties in reaching equilibrium at low temperatures [19]. For Co percentages over 68%, a α (FCC) → ε' (HCP) martensitic phase transformation can occur [21]. Another interesting feature of this system is that, for compositions of less than

~ 70% Co, the stacking fault energy presents an approximately linear decrease with increasing proportion of Co (Figure 1.2) [22]. The stacking fault energies of pure Ni and Co are 240 and 27 mJ/m^2, respectively [22, 23].

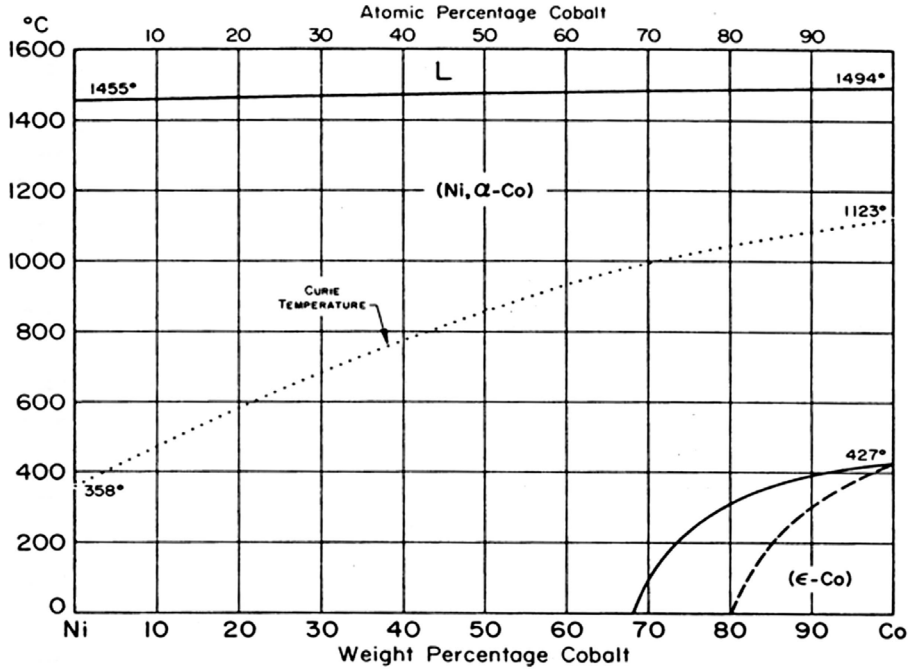

Figure 1.1. Ni-Co equilibrium phase diagram [18].

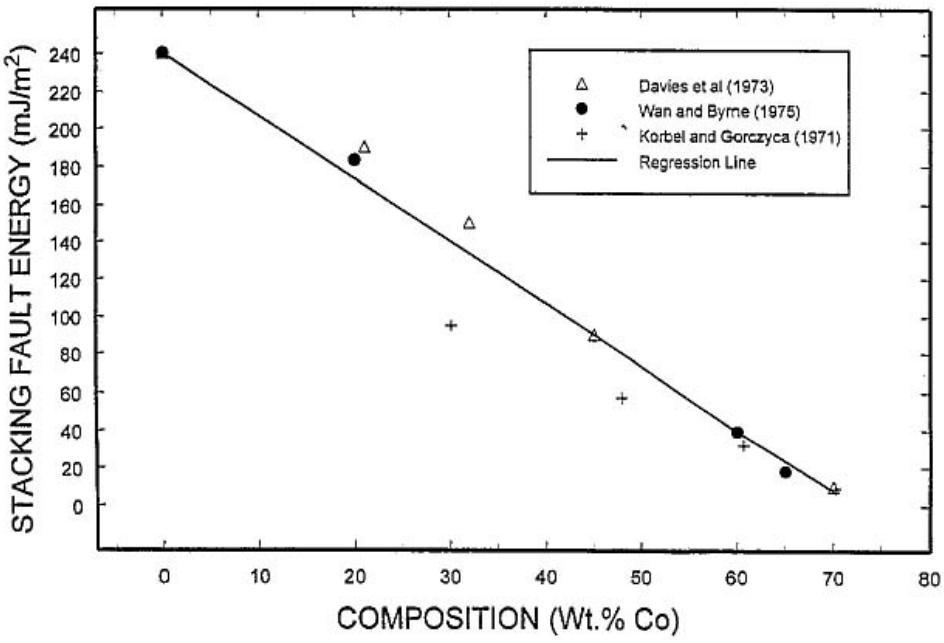

Figure 1.2. Variation of the stacking fault energy in the Ni-Co system, in the range 0 to 70% Co. [22].

The well-defined metallurgical characteristics associated to its simplicity make the Ni-Co system a proper choice for studying the influence of contact scale on the tribo-mechanical response of these materials and allow, to some extent, the possibility of generalization of results to other metallic systems. On the other hand, up to now, most published results concerning ISE were achieved on specially prepared laboratorial samples (high purity, monocrystalline, well-oriented crystallographic surfaces). However, most engineering materials do not present such characteristics and, therefore, by using materials from the Ni-Co system prepared by a technique (laser cladding) which allows them to be polycrystalline, the study of ISE and its impact in terms of abrasive wear can be extended to typical engineering materials of average structural complexity.

Although this work deals exclusively with abrasive wear, ISE is usually intrinsic to the material (as will be shown later in §1.4.2) and, consequently, should also affect the resistance of the material to other forms of wear where hardness plays an important role (e.g. adhesive wear), as long as the contact scale is within the range where ISE occurs.

In the following sections of this chapter, information is given to help the reader on the interpretation of the results of this work. First, a few notions on the mechanics of the contact between two solid surfaces are given. Then, some concepts on the abrasive wear of ductile materials are presented, including the Rabinowicz model and the mechanisms of abrasive wear. Finally, a review of the main achievements in the understanding of the influence of contact scale on abrasive wear and hardness is made, with particular focus on the Nix-Gao and Jäger models for the contribution of geometrically necessary dislocations (GNDs) and surface free energy (SFE), respectively, to the hardness of materials.

1.2. Contact between solid surfaces

The contact between two nominally flat solid surfaces is initially established between the highest surface asperities. As the normal load is increased, more asperities come into contact and the previously created contacts grow. The sum of the areas of all the contact spots is designated as real contact area (A_r), whereas the area of contact which would occur if the surfaces were perfectly smooth is designated as nominal contact area (A_n). These two concepts can be better understood by observing Figure 1.3.

Although real surfaces are composed of numerous asperities, which support the applied load, for simplicity it is customary to start by presenting some notions on the mechanics of single asperity contacts and then move forward to the more complex case of multiple asperity contacts. It is also common to consider the asperities as spherically shaped.

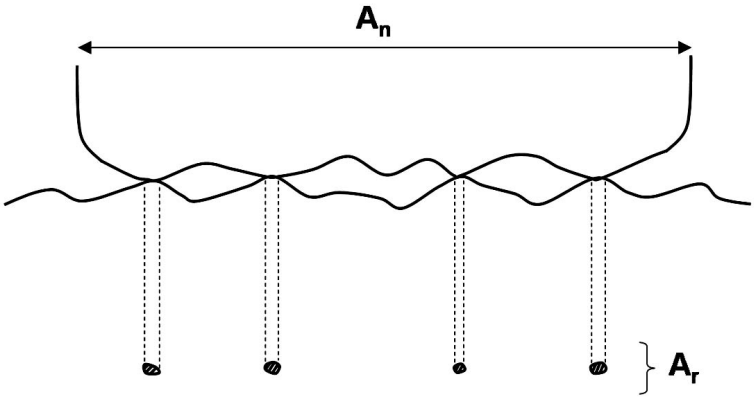

Figure 1.3. Schematic representation of an interface between two contacting solid surfaces, where the nominal and real areas of contact (A_n and A_r, respectively) can be distinguished. The vertical scale is greatly magnified in relation to the horizontal one.

1.2.1. Single asperity contact

The elastic contact between a spherical body and a plane surface body (Figure 1.4) can be analysed by using Hertz theory [24], which is described in several textbooks (e.g. *Contact Mechanics*, by K. L. Johnson [25]).

When the spherical body is pressed against the plane surface body under a normal load F_N, the resulting (projected) contact area, A_p, is a circle of radius a_c, which is given by:

$$a_c = \left(\frac{3F_N R}{4E_r} \right)^{1/3}, \tag{1.1}$$

where R is the curvature radius of the sphere. E_r, the reduced Young's modulus of the contact, accounts for the stiffness of the two bodies, and is given by:

$$E_r = \left(\frac{1-\nu_i^2}{E_i} + \frac{1-\nu^2}{E} \right)^{-1}, \tag{1.2}$$

where E_i and ν_i are the Young's modulus and Poisson's ratio of the spherical body, respectively, and E and ν are the Young's modulus and Poisson's ratio of the plane surface body, respectively.

The contact area can then be determined by:

$$A_p = \pi . a_c^2 = \pi \left(\frac{3F_N R}{4E_r} \right)^{2/3} . \tag{1.3}$$

The elastic displacement of the two bodies is not uniform over the contact area, having a maximum, h, at the centre of the contact area (Figure 1.4). This maximum elastic displacement can be related to F_N by:

$$F_N = \frac{4}{3} E_r R^{1/2} h^{3/2} . \tag{1.4}$$

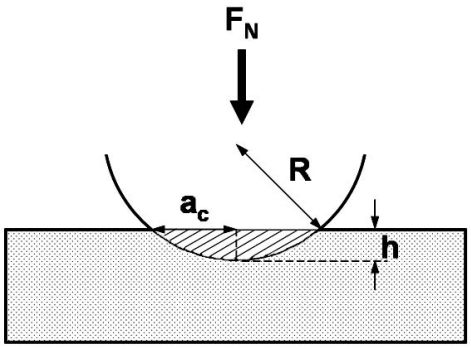

Figure 1.4. Schematic representation of the elastic contact between a spherical body and a plane surface body. The vertical scale is greatly magnified in relation to the horizontal one since in Hertz theory it is assumed that $a_c << R$. The total vertical displacement in the contact corresponds to h.

The mean contact pressure (mean normal stress), σ_m, is given by:

$$\sigma_m = \frac{F_N}{A_p} = \left(\frac{16 F_N E_r^2}{9\pi^3 R^2} \right)^{1/3} . \tag{1.5}$$

The normal stress over the contact area is not uniform: it has a maximum value $\sigma_{max} = 3/2 \sigma_m$ at the centre of the contact circle and is zero at the circumference which defines the perimeter of the contact (Figure 1.5.a). Inside the contact area the normal stress is compressive, whereas outside it is tensile. The maximum shear stress, τ_{max}, occurs at a depth $0.47 a_c$ below the centre of the contact area and is about $0.47 \sigma_m$ (or $0.31 \sigma_{max}$, as depicted in Figures 1.5.b and c):

$$\tau_{max} = 0.47 \left(\frac{16 F_N E_r^2}{9\pi^3 R^2} \right)^{1/3} . \tag{1.6}$$

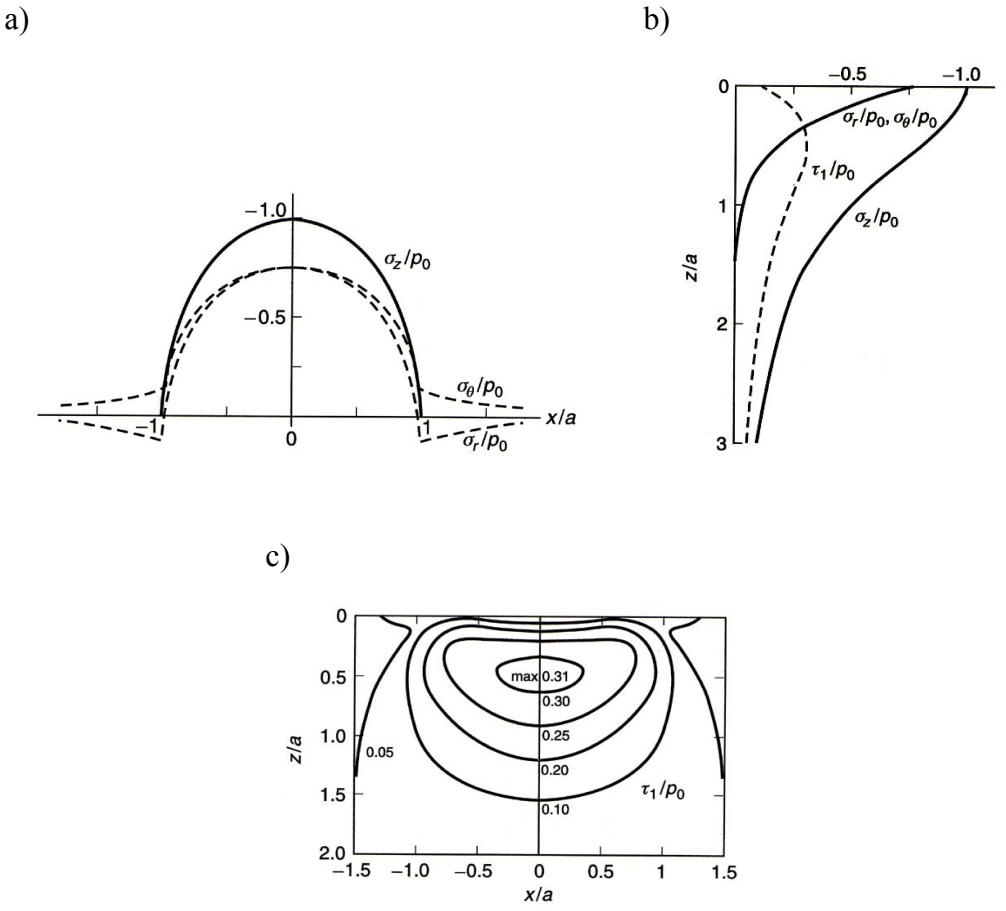

Figure 1.5. Stress distributions at the surface of a plane body loaded by a spherical body and along the *Z* axis of symmetry (a and b, respectively). σ_r, σ_θ and σ_z are the components of the normal stress field• and are related to the principal shear stress τ_1 by $\tau_1 = ½|\sigma_z - \sigma_\theta|$. Contours of the principal shear stress τ_1 in the subsurface (c). All the stresses are normalized to the maximum normal stress, which is designated in the plots as p_0 [26].

As the normal load is increased, plastic deformation will start at the point of τ_{max} in the body with the smallest hardness, once the mean contact pressure reaches a critical value (Figure 1.6.a). According to Tresca's maximum shear stress criterion, yielding will occur when $\tau_{max} = \sigma_Y/2$, where σ_Y is the uniaxial yield stress of the material. Therefore, the critical mean pressure for the onset of plasticity is:

$$\sigma_m \approx 1.1\sigma_Y . \tag{1.7}$$

The plastic zone created below the surface is enclosed by elastically strained material and expands in a roughly radial way as the load is increased. Eventually, the plastic zone reaches the free surface and completely embraces the region around the spherical body

• σ_r is the stress in the radial direction; σ_θ is the angular stress; σ_z is the stress in the direction normal to the sample's surface.

(Figure 1.6.b). The contact is now said to be fully plastic and the mean contact pressure is [27]:

$$\sigma_m \approx 3\sigma_Y . \tag{1.8}$$

If it is assumed that the material is perfectly plastic, i.e. no strain hardening occurs once the contact becomes fully plasticized, σ_m remains constant for subsequent increases in load and its value corresponds to the indentation hardness of the material (H_i). Consequently, from Eq. 1.8 results the well-known relation:

$$H_i \approx 3\sigma_Y , \tag{1.9}$$

usually designated as the Tabor relation [27].

Therefore, the plastic deformation of single asperity contacts is characterized by $A_p \propto F_N$ (regarding that σ_m remains constant once the contact becomes fully plasticized), whereas in elastic deformation $A_p \propto F_N^{2/3}$ (Eq. 1.3).

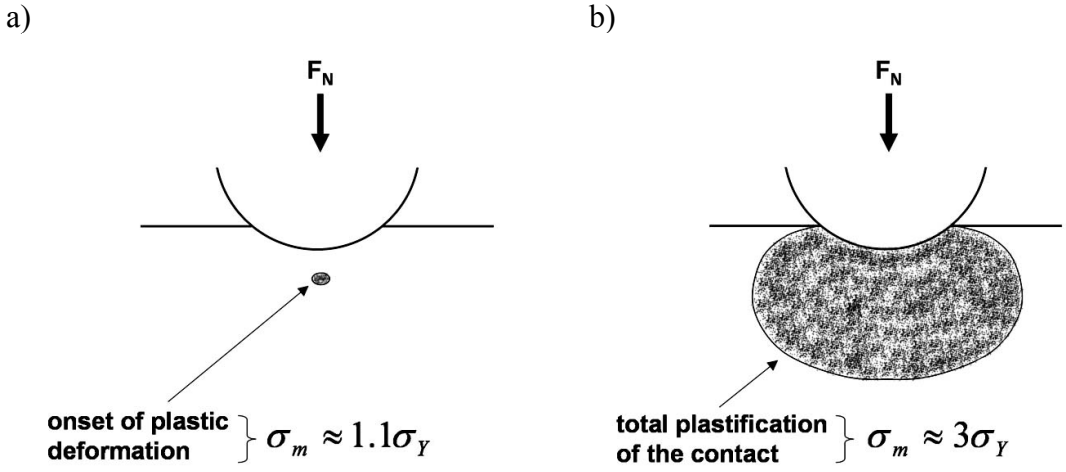

Figure 1.6. Contact between a spherical body and a plane surface body: a) beginning of plastic deformation at the point of maximum shear stress; b) full plasticity of the contact. The plastic region corresponds to the shaded area.

1.2.2. Multiple asperity contact

The contact between real surfaces is established simultaneously between several asperities (Figure 1.3) and, consequently, the resulting elastic and plastic behaviour is more complex than in the case of single asperity contacts.

One of the most accepted models for the contact of rough surfaces is the statistical model of Greenwood and Williamson [28]. For simplicity, these authors considered the contact between a smooth and a rough surface formed by N_a statistically distributed asperities with spherical summits of the same curvature radius r_a (Figure 1.7)•.

The applied load F_N will be supported only by asperities whose height above the reference plane of the rough surface, z, is larger than the separation between the reference plane and the smooth surface, d. Considering that the heights of the asperities are described by a probability density function $\phi(z)$, the expected number of contacts, n_a, is given by:

$$n_a = N_a \int_d^\infty \phi(z) dz \,. \tag{1.10}$$

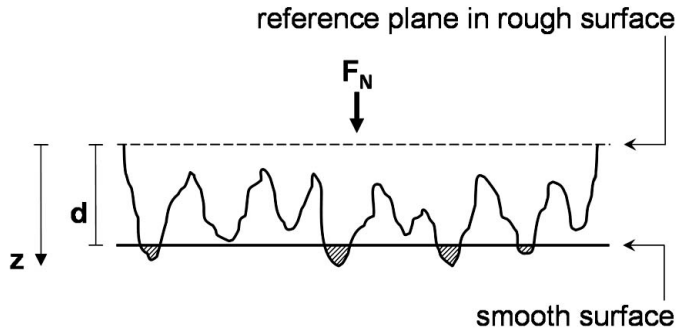

Figure 1.7. Contact between a rough and a smooth surface. The applied load is supported by the shaded asperities.

At a separation d, each contacting asperity of height z will deform elastically according to Eq. 1.4 (where $h = z - d$):

$$f_N(z) = \frac{4}{3} E_r r_a^{1/2} (z-d)^{3/2} \,. \tag{1.11}$$

$f_N(z)$ is the load supported by an asperity of height z when the separation distance is d.

Accordingly, the total applied load, F_N, is carried by all contacting asperities, and the equilibrium condition of the contacting surfaces is given by:

$$F_N = N_a \int_d^\infty \phi(z) f(z) dz = \frac{4}{3} N_a E_r r_a^{1/2} \int_d^\infty (z-d)^{3/2} \phi(z) dz \,. \tag{1.12}$$

• Nevertheless, later works on the contact between two rough surfaces supported the broad conclusions of the Greenwood and Williamson model [26].

Greenwood and Williamson applied their model to exponential and Gaussian distributions of asperity heights [28], and found that the real contact area (A_r in Figure 1.3) is linearly proportional to the load in the first case and almost linearly proportional in the second case. This observation is different from what occurs in the elastic contact between a single spherical asperity and a smooth surface, where the contact area is proportional to $F_N^{2/3}$ (Eq. 1.3).

Linear proportionality between A_r and F_N is also obtained if the asperities deform to the fully plastic state and no strain hardening occurs, as in single asperity contacts. For simplicity, it can be assumed that one surface is harder than the other and that the asperities with spherical summits in the harder surface indent the plane surface of the softer material. In this case, each individual contact can be considered as a small indentation in the fully plastic state and the mean pressure at the multiple contacts, σ_{mc}, is equal to the indentation hardness of the softer material (in agreement with Eqs. 1.8 and 1.9) [27]:

$$\sigma_{mc} = \frac{F_N}{A_r} = H_i \,. \tag{1.13}$$

A prediction on whether the contacting asperities will undergo preferentially elastic or plastic deformation can be made by using a parameter that results from the theory of Greenwood and Williamson [28]. This parameter is known as plasticity index, ψ, and is given by:

$$\psi = \frac{E_r}{H_i}\sqrt{\frac{\sigma}{r_a}}, \tag{1.14}$$

where σ is the standard deviation of the distribution of asperity heights $\phi(z)$. For $\psi < 0.6$ the deformation is essentially elastic, whereas for $\psi > 1$ most asperities will deform plastically under even the lightest of loads.

Therefore, in materials with high E_r/H_i, such as metals, the contacts will tend to be plastic, whereas in ceramics and polymers the contacts are more likely to be elastic due to the low E_r/H_i of these materials. On the other hand, if during the running-in period of rubbing components the highest asperities are worn, the distribution of asperity heights will be narrower (σ decreases) and the asperities more blunt (r_a increases). Consequently, the contact may change from predominantly plastic to predominantly elastic due to the decrease of ψ.

1.3. Abrasive wear of ductile materials

Abrasive wear occurs when particles or surface asperities of a hard material slide against a softer surface, leading to the formation of scratches. The material originally in the scratches may either be removed from the surface or displaced sideways and ahead of the abrasive bodies and, in the case of brittle materials (e.g. ceramics), material in the neighbourhood of the scratches may also be removed by fracture [3].

Abrasive wear may be of the two-body kind or of the three-body kind. In the first case the abrasive bodies are fixed on a surface and scratch the soft counter-surface (e.g. grinding with abrasive paper), whereas in the second case the abrasive bodies are free to roll and slide between the two surfaces (e.g. polishing). While in two-body abrasive wear the surface is scratched, in three-body abrasive wear the surface may also be indented, as a result of the rolling movement of the abrasive particles. Consequently, two-body abrasive wear generally leads to larger wear rates [4].

Although abrasive wear may involve both plastic deformation and brittle fracture, only the first mechanism will be considered in this work due to the ductile character of the studied materials. A simple model for two-body abrasive wear by plastic deformation has been proposed by Rabinowicz [29], where it is considered the sliding of conical abrasive particles against a softer material with flat surface and indentation hardness H_i (Figure 1.8).

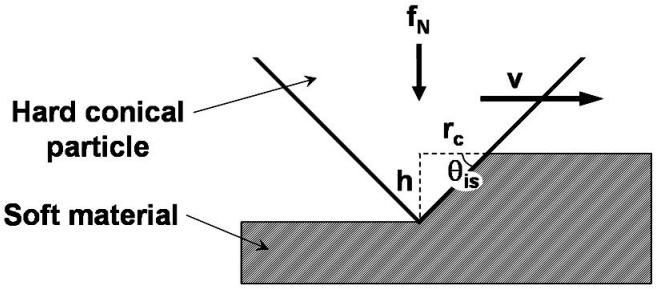

Figure 1.8. Schematic representation of a conical abrasive particle sliding against a soft material with flat surface. The sliding speed is represented by the letter v.

The wear rate produced by a single abrasive particle (dQ), which corresponds to the volume of material removed (dV_R) per unit sliding distance (dx), is given by:

$$dQ = \frac{dV_R}{dx} = r_c h = r_c^2 \tan\theta_{is}, \tag{1.15}$$

where r_c is the contact radius, h the penetration depth and θ_{is} the attack angle of the abrasive particle.

The load carried by the abrasive particle is a fraction f_N of the total applied load F_N and, according to Eq. 1.13•, can be determined by:

$$f_N = H_i \frac{\pi . r_c^2}{2}, \tag{1.16}$$

regarding that only half the surface of the particle, below the surface plane, contacts the soft material during sliding.

From the combination of Eqs. 1.15 and 1.16 results:

$$dQ = \frac{2 \tan \theta_{is}}{\pi} \frac{f_N}{H_i}. \tag{1.17}$$

If the contribution from all the abrasive particles is considered, the total abrasive wear rate (Q) is given by:

$$Q = \frac{2\overline{\tan \theta_{is}}}{\pi} \frac{F_N}{H_i}, \tag{1.18}$$

where $\overline{\tan \theta_{is}}$ is a weighted average of the $\tan \theta_{is}$ values of all the individual particles••. This equation can be written in the form•••:

$$Q = K_{ab} \frac{F_N}{H_i} \tag{1.19}$$

with the constant K_{ab}, which is known as abrasive wear coefficient, given by:

• Considering only a single contact.

•• Note that $\overline{\tan \theta_{is}} = \frac{\sum \tan \theta_{is} . f_N}{F_N}$.

••• It is interesting to note that Eq. 1.19 has the same form as the Archard equation for adhesive wear [30]: $Q = K_{ad} \frac{F_N}{H_i}$, where K_{ad} is the adhesive wear coefficient. Nevertheless, the physical meaning of K_{ad} is different from that of K_{ab}.

$$K_{ab} = \frac{2\overline{\tan\theta_{is}}}{\pi}. \tag{1.20}$$

In the Rabinowicz model it is assumed that pure microcutting (Figure 1.9.a) occurs, i.e. all material displaced by the abrasive particles is removed as wear debris in a single pass, and, consequently, K_{ab} depends only on the geometry of the particles. However, this situation can be considered as an upper limit of wear loss for ductile materials, since part or even all the displaced material may be just plastically deformed, the last situation corresponding to pure microploughing (Figure 1.9.b). In addition, the repeated ploughing of material by the abrasive particles may lead to microfatigue (Figure 1.9.c), which consists on the detachment of material from the surface by low cycle fatigue. Therefore, the value of K_{ab} in ductile materials is, in general, smaller than the value obtained from Eq. 1.20.

The transition between pure microploughing and pure microcutting is controlled by the attack angle of the abrasive particles and by the shear strength of the interface between the particles and the soft surface, which can be expressed as the ratio between the shear stress at the interface and the shear yield stress of the softer material [4]. Therefore, K_{ab} depends also on the mechanical properties of the softer material.

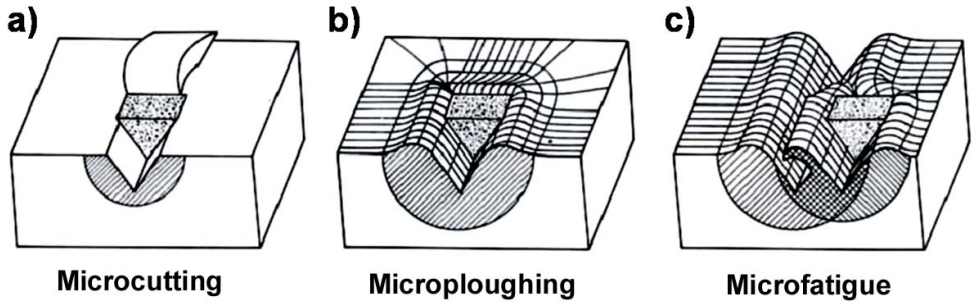

Figure 1.9. Possible abrasive wear mechanisms in ductile materials: a) microcutting; b) microploughing; c) microfatigue (adapted from [3]).

Since both K_{ab} and H_i in Eq. 1.19 are related to the wear response of the softer material, it is common practice to group these parameters into a single coefficient, which results in a simplification of Eq. 1.19 to [4]:

$$Q = K'_{ab} F_N. \tag{1.21}$$

The factor K'_{ab}, usually known as specific wear coefficient, is not dimensionless, contrary to K_{ab}, and represents the volume of material removed per unit sliding distance, per unit applied load.

The advantage of using Eq. 1.21 and hence K'_{ab} is the fact that it is not required the previous knowledge of H_i. However, by using K'_{ab} as a criterion for the selection of materials in terms of abrasive wear resistance, variations of hardness due to differences between the contact scales [31] in laboratorial test conditions and real operation conditions will not be accounted for, which can lead to incorrect conclusions. Therefore, the contact scale dependence of hardness must be taken into account when evaluating the wear behaviour of materials. A revision is made in the next section to bring the reader up to date with the main findings on the influence of contact scale both on the abrasive wear and hardness of materials.

1.4. Influence of contact scale

According to what was mentioned in §1.1, great interest exists among the tribological community on answering the following question [13]: is the contact scale a characteristic of the tribological system that influences its response (such as load, speed and environment) or, on the contrary, is the phenomenology kept if the tribological system is (homothetically) scaled down?

This topic will be addressed in the following two sections, first by reporting the large gap that presently exists between macroscale wear studies and atomic scale wear studies, with particular emphasis on abrasive wear, and then by presenting hardness as a possible solution to eliminate (or to minimize) this gap.

1.4.1. Abrasive wear

A great number of experimental studies of abrasive wear involving macroscopic nominal contact areas has been conducted since the mid-1960s, initially driven by the well-known *Jost Report* [32] on the economical impact of friction and wear.

On the other hand, with the advent of the atomic force microscope in the mid-1980s [15], it became possible to perform experimental studies of abrasive wear phenomena from the atomic to the microscale. In these studies, atomic force microscopy (AFM) tips are used to simulate a sharp abrasive asperity sliding over a surface, enabling to produce scratches or worn areas in that surface (see, for instance, [33-36]).

In general, the abrasive wear by plastic deformation of the contacting asperities, which can result in the formation of debris particles, involves the creation and movement of dislocations. However, if the abrasive bodies interact with the soft material in only a few atomic layers, dislocations cannot be responsible for the occurrence of wear.

Many fewer single asperity experimental and simulation studies have been dedicated to wear and its atomic origins, in comparison to those concerning the wearless regime of friction [16]. Still, several AFM wear experiments in different materials and environments (ambient air, gas, liquid and UHV[•]) have shown that observable tip-induced wear of the sample can occur when the tip slides against the sample above some threshold load [37]. AFM tip-induced wear experiments have been performed in ceramics (e.g. muscovite mica [33, 38], NaCl [39], KBr [40] and SiO_2 [41]), semiconductors (e.g. Si [41-43] and InSb [44]), metallic materials (e.g. Au [42, 43, 45], Cu [43] and stainless steel [36]), and polymers (e.g. UHMWPE[••] [46], polystyrene [35, 47] and polycarbonate [48]).

Particular emphasis should be given to a few experimental studies of atomic scale wear, which suggest that the precursor mechanism for atomic scale wear is the formation of point defects that, in turn, lead to the formation of small clusters (nanodebris) [13].

By monitoring the friction force generated during the scanning of an AFM Si_3N_4 tip repeatedly back and forth over the same line on a cleaved mica surface while the applied load increased linearly, Hu *et al*. [33] observed that, once a certain threshold load was reached, the dependence of friction on load stopped being linear. Subsequent observation of the tested regions showed that this irregular behaviour was caused by the removal of a single atomic layer of mica, marking the transition threshold for detectable wear. Another interesting observation was that the atomic layer could be removed by single scans at high loads, or multiple scans at low loads, which shows that both the load and the number of scans can contribute to wear. Hu *et al*. [33] suggested that, in the low-load regime, point defects can be produced (by rupturing of Si−O bonds at the surface) and accumulated during each scan until the concentration of defects is high enough to cause the formation of a nanodebris, as a result of the removal of one atomic layer. However, these authors also observed that below a certain load value (~ 40 nN) no wear of the mica surface occurred, even after a large number of scans, which led them to conclude that an effective load threshold for observable wear exists, independent of the number of scans. Recently, Helt and Batteas [49] were able to observe the nucleation of defects in mica under aqueous environment, prior to the formation of visible wear scars, supporting the mechanism proposed by Hu *et al*.

Reciprocal scratching experiments with an AFM Si tip on KBr (001), under UHV conditions, have been carried out by Gnecco *et al*. [40]. These authors showed that the atomic scale wear mechanism in KBr consists on the removal of ionic pairs or small clusters of ionic

[•] Ultra-high vacuum
[••] Ultra-high molecular weight polyethylene

pairs by the tip, and that the produced wear debris is reorganized in regular terraces with the same periodicity and orientation as the unscratched surface. Similar experiments in KBr by Socoliuc *et al*. [50] also confirmed the cumulative nature of wear at atomic scales, with the occurrence of wear at loads as low as 1.7 nN after prolonged scratching. After the onset of wear, a ripple-like structure is generally formed both inside and at the edges of the grooves, with a wavelength on the order of the tip radius.

Recently, Ribeiro *et al*. [51] have performed *in situ* observation of nanoabrasive wear by using a nanoindentation device in a transmission electron microscope, a technique which was developed about a decade ago by Wall and Dahmen [52]. By sliding a gold-coated diamond indenter against Si (100), these authors observed that wear occurred due to the formation of cracks under the indenter. They proposed that wear could be initiated by the formation and propagation of voids (atomic vacancies), fracture, or the nucleation and movement of dislocations. After an analysis of the elastic strain energy required for these three mechanisms, they suggested that the most energetically favourable mechanism and, accordingly, the one responsible for the onset of wear, is the formation of voids along the elastic stress contour under the indenter. These voids can coalesce into cracks as well as act as sites for the nucleation of dislocations, thus providing ways by which material can be removed.

Atomistic simulations based on the molecular dynamics (MD) technique[•] can provide theoretical support for experimental results of atomic scale wear, due to their capability to track the motion of individual atoms [16]. Furthermore, some of the drawbacks of the experimental field, such as sample preparation and tip characterisation issues, can be avoided in simulations and, if the necessary computer resources are available, any tribological system can be virtually created. However, some difficulties are also found in the field of atomistic simulations, such as the need of using interatomic potential models that accurately describe the interaction between all the atoms in the system, and the impossibility of formation and breaking of chemical bounds in some models, which is a fundamental requirement for the study of wear [16].

Nevertheless, some interesting predictions on atomic scale wear have been obtained by using atomistic simulations. Simulations of sliding contact between two bodies where only a few atomic layers are involved in the contact have shown that wear is essentially controlled by the dragging of atoms from their initial positions, and not by dislocation or crack

[•] During these simulations, the response of a material subjected to an external force is evaluated by following the response of every atom in the material.

nucleation and propagation processes [53, 54]. Moreover, D'Acunto [55] has recently proposed a model for atomic scale wear that considers the contribution of both adhesion and abrasion to the wear of an atomically flat surface sliding against an AFM tip. In this model it is assumed that atoms of the softer surface adhere to the tip if the vertical (van der Waals) forces are predominant relatively to the shear forces, whereas in the opposite case, the atoms are dragged from their original positions to other positions, without material transfer to the tip. In both cases, atomic vacancies may be left in the scanned surface and the wear debris (single atoms or clusters) may be rearranged on the surface, as in the mechanism proposed by Gnecco *et al*. for KBr [40]. The model not only enables quantifying wear at the atomic scale but also demonstrates that, at very low applied loads (F_N = 0.65 nN), abrasion is predominant over adhesion.

At the moment, two issues prevent the direct comparison between simulation results and AFM experimental results, which are the length and time scales of the simulations, both dependent on the hardware skills (e.g. number and speed of processors). In comparison to AFM experiments, the number of atoms used in the simulations is generally small and the shear velocity is extremely high (imposed by short simulation time scales) [16], allowing only comparisons to be made from the qualitative point of view. Although effort has been recently made to approach the real dimensions of probe and sample in atomistic simulations [56], the linear dependence of simulation velocity on processor speed does not allow, presently, to overcome the time scale issue [16].

In spite of the differences between the experimental and theoretical studies of atomic scale wear performed up to now, both seem to indicate that, in general, the generation of point defects in sliding contacts is the precursor mechanism for atomic scale wear, i.e. before the onset of plastic deformation or crack nucleation.

Although some effort has been made in the last two decades to find out more about wear and its relation to contact scale, a large number of studies [13, 16, 57] has recently pointed out that it is crucial to further understand the atomic origins of wear as well as to establish relations between macro-, micro- and nanowear phenomena, so that the large gap between length scales can be bridged and better ways to control wear can be developed. Particular interest exists on the length-scale range from a few atomic layers to submicrometric lengths, in which, although the usual plastic deformation mechanisms (nucleation and movement of dislocations) are already active, the mechanical response of the material can be different from its "bulk" mechanical response [13]. This length-scale range marks the transition from "atomic wear" mechanisms to "bulk wear" mechanisms [13], and is poorly

characterised because it is too large to be studied by atomistic simulations and too small for continuum mechanics theories to be still valid [58].

Regarding the abrasive wear of ductile materials, a good approach for evaluating the wear response in this transition range is by studying the penetration depth dependence of hardness, since this mechanical property is intimately related to the wear response of the material (Eq. 1.19). Although several studies exist on the influence of contact scale on hardness (see, for instance, [5-12]), most of them are not performed in typical rubbing engineering materials (e.g. polycrystalline metallic alloys) and, more importantly, only few reveal interest on the impact of this phenomenon on wear [59-61].

Backer *et al*. [62] were one of the first to associate the contact scale dependence of abrasive wear to the dependence of the material's resistance to plastic deformation on the length scale of the deformation. These authors observed that the specific energy[•] in grinding of annealed SAE 1112 steel increased as the size of the removed chip decreased, and related this effect to the increasing resistance of the material to plastic deformation with decreasing size of the deformed region. Moreover, they estimated that the shear stress necessary to remove a chip of maximum thickness smaller than a critical value (about 700 nm for the used experimental conditions) is on the order of the theoretical shear stress of steel, which indicates that such small deformed regions might be dislocation free.

Later on, Misra and Finnie [63] performed a detailed analysis of the influence of abrasive particle size on the wear rate of metals subjected to two- and three-body abrasion and erosion[••]. Figures 1.10.a and b show the variation of the wear rate with abrasive particle size, respectively, in annealed Al and annealed Cu subjected to two-body abrasive wear tests with SiC particles and using two sliding speeds which differ by three orders of magnitude. As can be observed from the figures, a decrease of the wear rate occurs when the size of the abrasive particles decreases below a critical size of about 100 μm, independently of the sliding speed. This effect is commonly known in the literature as *particle size effect* [64-66]. Misra and Finnie [63] also pointed out that, in the particular case of two-body abrasive wear, the depth of cut is typically about 12% of the abrasive particle size, which results in a critical penetration depth of 12 μm when the critical particle size is 100 μm.

[•] Energy required to remove a unit volume of material.
[••] Type of wear caused by the impact of hard particles, carried by a fluid medium, on a surface [1].

a)

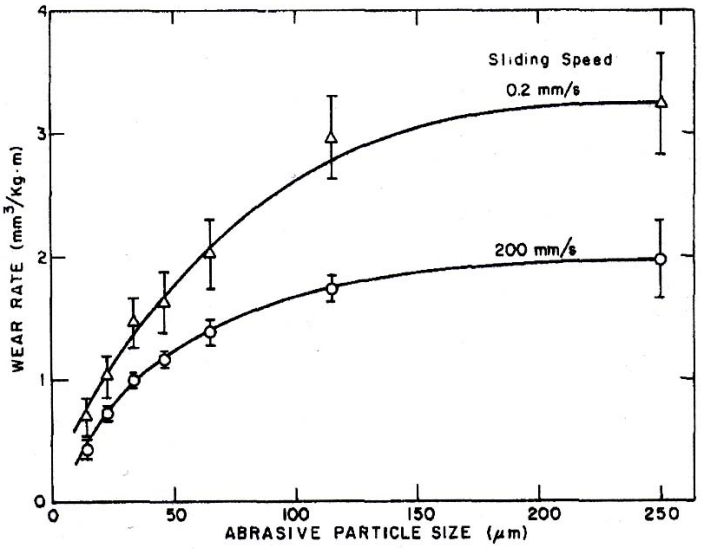

b)

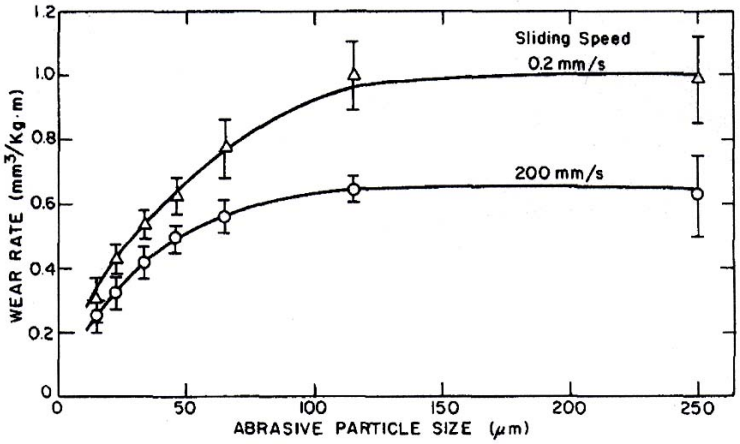

Figure 1.10. Experimental results of Misra and Finnie for the variation of two-body abrasive wear rate with SiC particle size in annealed Al (a) and annealed Cu (b), at two different sliding speeds [63]. The wear rate values are normalized to the applied load.

The particle size effect has been previously attributed to a number of different causes, such as the larger influence of particle tip bluntness in the case of smaller particles•, which results from wear or fracture of the particles and decreases both the attack angle and the ratio of ploughing cross-section area to load bearing area [64, 67], and the clogging of finer grade abrasive papers by wear debris, which prevent the particles from contacting the softer surface [68].

• Smaller particles pack more closely and, consequently, each particle carries a smaller fraction of the applied load (thus penetrating less into the softer material) than in the case of larger particles.

Nevertheless, an extensive review by Misra and Finnie [63] showed that none of the explanations proposed previously is applicable over the wide range of conditions (two- and three-body abrasion and erosion) for which the particle size effect is observed, except for a true physical size effect in which a shallow layer (~ 10 μm thick) near the abraded or eroded surface exhibits a higher yield stress than that of the bulk material. The hardness gradient present near the surface will only affect the wear rate in the case of small particles, where the indentation depths are totally or mostly confined to this layer, whereas for particle sizes above the critical value, the influence of the hard layer on the wear rate will be small as compared to that of the softer bulk material.

The works of Backer *et al*. and Misra and Finnie clearly show that the influence of contact scale on hardness cannot be neglected when evaluating the wear resistance of materials. In this way, a review of the state of the art in the scale dependence of hardness is made in the next section, which is a critical topic for the understanding of the present work.

1.4.2. Hardness

The pioneering work of Gane and Bowden [69] showed that, undoubtedly, the resistance of a material to indentation when measured on a very small scale can be significantly different from that measured by conventional large scale techniques. By performing indentation tests with very low loads in a scanning electron microscope, these authors were able to directly observe the deformation caused by a sharp indenter on electropolished Au, Cu and Al. They observed that no indentation was formed until a critical load was reached, after which the indenter suddenly penetrated the surface to produce an indentation. Although the critical load varied considerably from region to region, the estimated shear stress at this load was usually similar to the theoretical shear stress of perfect crystals.

After Gane and Bowden, many other authors also found experimental evidence of the occurrence of such high shear stress values, under indentation conditions, in other metallic materials (e.g. Ni [70-72], W [72-74], Fe-3Si [75], Mo-3Nb [76] and Mo-10Al-4Ni [76]), semiconductors (e.g. GaAs [72, 77, 78], InP [72] and ZnSe [72]) and ceramics (e.g. sapphire [79], SiC [79], MgO [80, 81], LiF [81] and CaF_2 [72]). As in the experiments of Gane and Bowden, these high shear stress values were generally associated to the homogeneous nucleation of dislocations. Below the critical load for dislocation nucleation the material deforms only elastically, whereas above this load the deformation is elastoplastic. In load-

controlled[•] indentation tests, the transition between these two regimes corresponds to a sudden jump in indenter displacement [82], which is commonly know as *pop-in*.

Independently of the presence or absence of pop-in behaviour, a continuous increase of the hardness with decreasing penetration depth (indentation size effect), especially in the submicrometric depth range, has been observed in a wide range of materials: Ag [7], Cu [8, 9, 83], Mo and W [6], Al and brass [10], Si [12], sapphire [12], MgO [12, 84], TiO_2 and SnO_2 [5], LiF and NaCl [11], among others.

Several explanations have been proposed for the observed ISE, including artifacts caused by sample preparation and test methods [12]. The presence of strain hardened surface layers (e.g. caused by surface preparation) [9, 12] and chemical contamination surface layers (e.g hydrocarbon and native oxide layers) [12, 70] can lead to hardness variations when the measurements are made near the surface. In addition, measurement errors due to the inadequate capability of some instruments (e.g. optical microscopes) of measuring small areas of indentations and to the presence of pile-up or sink-in behaviour[••] [8], bluntness of the indenter [12], creep deformation during the indentation cycle [85] and friction between indenter and sample [86] can also affect hardness measurements.

Nevertheless, even when sample preparation and test method artifacts are avoided by adopting certain operation procedures (e.g. electropolishing to eliminate strain hardened surface layers; hold periods at maximum load to minimize the influence of creep), it is still possible to observe ISE [12]. Therefore, the results obtained up to now strongly indicate that ISE is an intrinsic material characteristic.

Conventional plasticity theories, which are based on continuous mechanics, cannot explain ISE because they do not incorporate material length scales. Up to now, the theory that seems to provide the best explanation for ISE is the theory of geometrically necessary dislocations associated to plastic strain gradients [58, 87], which will be reviewed next.

The plastic deformation of a crystalline material involves the creation, movement and storage of dislocations. Dislocations that are randomly distributed and stored, forming a network of defects in the crystal lattice, are designated as statistically stored dislocations

[•] During these tests the load is varied at a fixed rate (μN/s). Conversely, in displacement-controlled tests the indenter displacement is varied at a fixed rate (nm/s) and, consequently, a sudden drop in load is observed at the pop-in event [82].

[••] Pile-up behaviour consists on the rising of the material in the periphery of the indenter above the surface level, flowing against the faces of the indenter, whereas in sink-in behaviour the material in the periphery of the indenter is depressed below the surface level.

(SSDs) [88]. If the deformation is non-uniform and, accordingly, plastic strain gradients are present, dislocations also need to be stored for the compatible deformation of various parts of the material. Therefore, these dislocations accommodate the plastic strain gradients and are designated as geometrically necessary dislocations [88, 89]. As explained by Ashby [88], stored dislocations are responsible for the strain hardening of the material because they obstruct the motion of other moving dislocations. Consequently, the yield stress of the material depends both on the density of SSDs (ρ_s) and the density of GNDs (ρ_g).

In the particular case of indentation tests, GNDs are created to accommodate the plastic strain gradient surrounding the indentation. In general, the magnitude of plastic strain gradients is inversely proportional to the length scale over which the deformation occurs, which in the case of indentation tests corresponds to the indentation size [58]. Therefore, as the size of the indentation decreases, ρ_g must increase in order to compensate for the increase of the magnitude of the strain gradient. On the contrary, since ρ_s is independent of strain gradients, it does not present length scale dependency. For macroscopic deformations, $\rho_s >> \rho_g$ and, consequently, the yield stress is independent of strain gradients. However, by decreasing the size of the deformed region ρ_g increases and, for $\rho_g >> \rho_s$, strain gradients will significantly affect the yield stress of the material [88].

Following the concepts proposed by Ashby on the contribution of GNDs to the yield stress of the material [88], some authors have developed dislocation-based models to describe the hardness dependence on indentation size [6, 7, 83, 87]. Nevertheless, the only model that provides a geometrical description of the arrangement of GNDs under the indenter is the one developed by Nix and Gao [87], which is the most accepted up to now.

In the Nix-Gao model the indentation of a monocrystalline material by a rigid conical indenter is considered (Figure 1.11). The angle between the surface of the indenter and the surface plane of the indented material is θ_{is}, the contact radius is r_c and the indentation depth is h. For simplicity, it is assumed that the shape of the indentation is accommodated by circular loops of GNDs with Burgers vector b normal to the surface of the material, and that the loops are equally spaced along the surface of the indentation by a distance e. Thus, as the indenter penetrates into the material, slip steps spaced by e are formed on the indented surface (see inset on the right side of Figure 1.11).

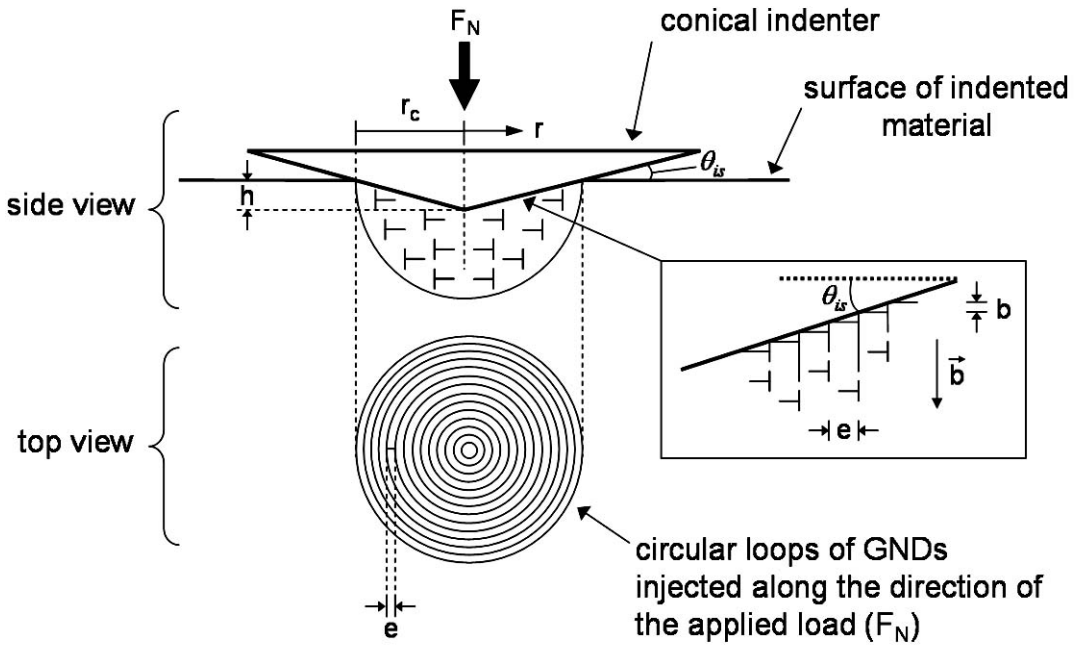

Figure 1.11. Distribution of geometrically necessary dislocations (GNDs) in a material indented by a rigid conical indenter, as considered by Nix and Gao [87]. The spacing between individual loops of GNDs corresponds to the spacing between individual slip steps on the indented surface, as can be observed in the inset on the right. The indenter has been omitted in the top view schematic.

From simple trigonometry, the following relation can be obtained:

$$\tan\theta_{is} = \frac{h}{r_c} = \frac{b}{e} \tag{1.22}$$

and hence the spacing between dislocation loops can be expressed as function of the indentation dimensions and the Burgers vector of the dislocations:

$$e = \frac{br_c}{h}. \tag{1.23}$$

The length of the dislocation loops injected between r and $r + dr$ is given by:

$$dl_g = 2\pi.r\frac{dr}{e} = \frac{2\pi.h}{br_c}rdr. \tag{1.24}$$

By integrating Eq. 1.24 between 0 and r_c, the total length of GNDs, l_g, can be obtained:

$$l_g = \frac{\pi.hr_c}{b}. \tag{1.25}$$

In the Nix-Gao model it is also assumed that the loops of GNDs remain within the hemispherical volume, V_c, defined by the contact radius:

$$V_c = \frac{2}{3}\pi.r_c^3. \tag{1.26}$$

By dividing the total length of GNDs by the volume which contains them, the density of GNDs can be determined:

$$\rho_g = \frac{l_g}{V_c} = \frac{3}{2}\frac{h}{br_c^2} = \frac{3}{2}\frac{\tan^2\theta_{is}}{bh}. \tag{1.27}$$

Equation 1.27 shows that ρ_g is inversely proportional to the length scale of the deformation (h in this case) and depends both on the geometry of the indenter and on the Burgers vector of the dislocations[•].

Two hardness values are considered in the Nix-Gao model. The first is the hardness in the limit of infinite depth (bulk hardness), H_0, which does not depend on plastic strain gradients and, therefore, is only related to ρ_s. The second is the hardness for a certain indentation depth, H, which takes into account the existence of strain gradients and thus depends both on ρ_s and ρ_g. The bulk hardness can be determined by combining the von Mises yield criterion ($\sigma_Y = \sqrt{3}\tau$, where τ is the shear yield stress[••]), the Tabor relation ($H_i = 3\sigma_Y$) and the Taylor hardening model [90] ($\tau = \delta Gb\sqrt{\rho_T}$, where G is the shear modulus, ρ_T the total dislocation density in the indentation and δ is a constant which is about 0.3 [88]):

$$H_o = 3\sqrt{3}\delta Gb\sqrt{\rho_s}, \tag{1.28}$$

where $\rho_T = \rho_s$ in the absence of strain gradients. If strain gradients are considered, $\rho_T = \rho_s + \rho_g$ and H can be determined in the same way as H_0 and is given by:

[•] Note that $\rho_g \rightarrow 0$ when $h \rightarrow \infty$, i.e. for large penetration depths only statistically stored dislocations are relevant.
[••] Also commonly known as shear strength.

$$H = 3\sqrt{3}\delta G b\sqrt{\rho_s + \rho_g} \ . \tag{1.29}$$

By combining Eqs. 1.27, 1.28 and 1.29, it can be obtained:

$$\frac{H}{H_0} = \sqrt{1 + \frac{3\tan^2\theta_{is}}{2b\rho_s h}} \ . \tag{1.30}$$

By defining a characteristic length h^* as:

$$h^* = \frac{3}{2}\frac{\tan^2\theta_{is}}{b\rho_s} , \tag{1.31}$$

Eq. 1.30 can be written in the form:

$$\frac{H}{H_0} = \sqrt{1 + \frac{h^*}{h}} \ . \tag{1.32}$$

Eq. 1.32 is usually designated as the Nix-Gao equation. According to the Nix-Gao equation, for an indentation depth on the order of the characteristic length h^*, or smaller, the measured hardness is larger than the bulk hardness. Moreover, from Eq. 1.31 results that high dislocation density materials (e.g. cold-worked materials) have smaller h^* values and, consequently, should be less sensitive to ISE.

Although the Nix-Gao model was strictly developed for a conical indenter, it can be equally applied to a pyramidal indenter. An equivalent cone angle θ_{is} can be found for the pyramidal indenter by relating the area functions of the pyramidal and conical indenters. For instance, the area function of a Vickers indenter is $A_p = 24.5h^2$, whereas for a cone $A_p = \pi.r_c^2$. Therefore, by equating these two area functions the following relation is obtained:

$$\frac{h}{r_c} = 0.358 \, . \tag{1.33}$$

By combining Eq.1.33 with Eq. 1.22, a value of $\theta_{is} \approx 20^\circ$ is obtained for the Vickers indenter. Nix and Gao observed that Eq. 1.32 describes well the ISE in Cu and Ag, reported by McElhaney *et al*. [8] and Ma *et al*. [7], respectively.

The Nix-Gao model has been the base for other models of ISE. Qiu *et al*. [91] have extended the Nix-Gao model to take into account the intrinsic lattice resistance (τ_0)[•], which corresponds to shear stress needed to move a dislocation in the absence of other dislocations (negligibly small in FCC metals but not in body centred cubic (BCC) metals [93]). The expression obtained by these authors is:

$$\frac{H}{H_0} = \frac{3\sigma_0}{H_0} + \sqrt{\left(1 - \frac{3\sigma_0}{H_0}\right)^2 + \frac{h^*}{h}}, \tag{1.34}$$

where $\sigma_0 = \sqrt{3}\tau_0$, assuming that the von Mises yield criterion can be applied. Qiu *et al*. [91] found that Eq. 1.34 describes reasonably well the ISE reported by Stelmashenko *et al*. in monocrystalline W [6], which has a BCC structure.

Swadener *et al*. [11] modified Eq. 1.32 to:

$$\frac{H}{H_0} = \sqrt{1 + \frac{h^*}{h}} + \frac{H_1}{H_0}, \tag{1.35}$$

where H_1 is a depth-independent strain hardening component representing the increase in hardness from the onset of plastic deformation to a representative strain $\varepsilon_r \approx 0.2 \tan \theta_{is}$. Eq. 1.35 was used by Swadener *et al*. to study the ISE in NaCl and LiF monocrystals. An expression similar to Eq. 1.35 was proposed by Elmustafa and Stone [10, 94], where a depth-independent constant, H_f, which represents the contribution of hardening mechanisms other than dislocations, replaces H_1 in Eq. 1.35.

Indentation experiments with spherical indenters in Cu [95] and Ir [96] showed that ISE is related to the indenter radius rather than indentation depth in the case of spherical indentation. Swadener *et al*. [96] extended the Nix-Gao model to the case of spherical indenters and obtained an expression similar to Eq.1.32:

$$\frac{H}{H_0} = \sqrt{1 + \frac{R^*}{R_p}}, \tag{1.36}$$

[•] A more complete expression for the Taylor dislocation model is $\tau = \tau_0 + \delta G b \sqrt{\rho_T}$, which includes the intrinsic lattice resistance τ_0 [92].

where R_p is the curvature radius of the spherical indentation and R^* the characteristic length for spherical indentation. Equation 1.36 shows that, for a spherical indenter, the hardness depends not on the indentation depth but on the curvature radius of the indentation, which is generally found experimentally to be 10–25% larger than the indenter radius due to partial elastic recovery during unloading [96]. While in conical and pyramidal indentation the density of GNDs is inversely proportional to indentation depth (Eq. 1.27), in spherical indentation ρ_g is independent of h and inversely proportional to R_p [96]:

$$\rho_g = \frac{1}{bR_p}, \tag{1.37}$$

which explains the difference between ISE in conical/pyramidal indentation and in spherical indentation. Furthermore, Swadener *et al*. [96] also studied the correlation of the ISE determined with spherical and pyramidal indenters (Vickers and Berkovich) and found that, for $R^* = 5.2h^*$, the same total length of GNDs is required to accommodate the shape of the indentation.

Swadener *et al*. [96] also observed that the hardness retrieved from indentation tests in iridium with a Berkovich indenter is overestimated by the Nix-Gao model when the indentation depth is smaller than 1 μm. Similar observations were reported by Feng and Nix [84] in MgO indented with a Berkovich indenter, for indentation depths smaller than 200 nm. Swadener *et al*. [96] suggested that, for very small indentation depths, the strong repulsive forces between GNDs would cause them to spread beyond the hemispherical volume considered in the model (Figure 1.11). As consequence, the model would overestimate the density of GNDs and hence the hardness. To account for this effect, Feng and Nix [84] and Durst *et al*. [97] proposed an extension to the Nix-Gao model, which consists on assuming an effective radius of the plastic zone $f.r_c$ larger than r_c. As a result, the density of GNDs and the characteristic length become:

$$\rho_g = \frac{3}{2}\frac{1}{f^3}\frac{\tan^2\theta_{is}}{bh} \tag{1.38}$$

and

$$h^* = \frac{3}{2}\frac{1}{f^3}\frac{\tan^2\theta_{is}}{b\rho_s}, \tag{1.39}$$

respectively, and Eq. 1.32 can still be applied to analyse ISE. Values of f in the range 1 to 1.7 were obtained by Feng and Nix [84] from hardness data of MgO and Ir, whereas Durst *et al*. [97] used finite element simulations to analyse the size of the plastic zone in Cu indented with a Berkovich indenter and found that f = 1.9 yields h^* values closer to those determined experimentally than f = 1 (original Nix-Gao model). In more recent works of Durst *et al*. [98-100], values of f in the range 1.6 to 2.4 were obtained for other metals and metallic alloys indented with various types of indenters.

A different approach (to minimize the strong assumption in the Nix-Gao model that all GNDs are contained in the plastic zone defined by the contact radius) has been recently proposed by Huang *et al*. [101], and consists on defining a maximum allowable density of GNDs, which is determined experimentally to be on the order of 10^{12} cm^{-2}. Similarly to the approach of Feng and Nix [84] and Durst *et al*. [97], the approach of Huang *et al*. also reduces the density of GNDs underneath the indenter. This same approach was again used in a more recent work by Huang *et al*. [102] for the case of spherical indenters.

Besides geometrically necessary dislocations, the other factor that is intrinsic to the material and, therefore, cannot be eliminated by any experimental procedure, is the surface free energy of the material. Although not so much attention has been dedicated to this factor in comparison to GNDs, a few works [103-106] have shown that SFE can affect the hardness measurements when the deformed regions are small, due to the large surface-to-volume ratio of such regions.

Gerberich *et al*. [103] proposed a model that relates ISE to the ratio between the energy of the newly created surface (surface work) and the plastic strain energy dissipation (plastic volume work). Their model predicts hardness to decrease as $(hR)^{-1/3}$ and fits experimental hardness data obtained from indentation tests in (100) monocrystals of Au, Al, Fe-3Si and W with spherical indenters of radius in the range 70 nm to 20 μm. The results of Gerberich *et al*. differ from the predictions by Swadener *et al*. [96], which are exclusively based on GNDs and indicate no depth dependence of hardness in spherical indentation, thereby showing that surface effects may play an important role in addition to GNDs.

Zhang *et al*. [104, 105] considered that the work done by the load applied during an indentation test can be divided into bulk work, which causes the deformation of the bulk material, and surface work, which causes the deformation of the rough surface layer. The surface work is composed of the energy dissipated per projected contact area in the plastic deformation of the rough surface layer and the energy necessary to create the new surface, which depends on the SFE of the material. Moreover, these authors also proposed that the

surface work predominates for indentation depths smaller than a critical depth, which increases with increasing surface roughness, whereas the bulk work predominates in the opposite case. By applying their model to the hardness data of Liu and Ngan [9] for Cu, Zhang *et al*. [104] found that the critical depth is around 100 nm, which indicates that surface effects should be considered in the nanometric depth range.

A simple geometric model which enables the direct evaluation of the contribution of SFE to the measured hardness has been recently proposed by Jäger [106]. In this model it is assumed that the indenter has an ideal self-similar geometry, which can be conical or pyramidal, the material is perfectly plastic, pile-up and sink-in effects can be neglected, the elastic recovery can be neglected (due to the low H_i/E of metals) and the SFE is isotropic. Figure 1.12 shows the indentation process with the simplifications considered in the Jäger model, where A_p and A_i represent the projected and surface contact areas of the indentation, respectively, and α_i is the apex semi-angle of the indenter.

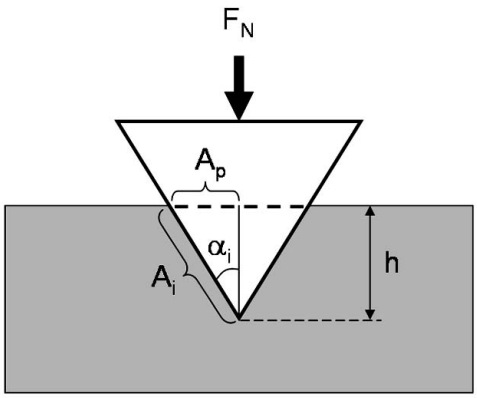

Figure 1.12. Schematic representation of an ideal indentation as considered by Jäger [106].

From simple trigonometry, the projected and surface areas of the indentation can be related by:

$$A_i = \frac{A_p}{\sin \alpha_i}. \tag{1.40}$$

On the other hand, it can be easily demonstrated that the area function of an ideal conical or pyramidal indenter is given by:

$$A_p = \gamma . h^2 \tan^2 \alpha_i, \tag{1.41}$$

where γ is a geometrical constant equal to π and 4 for a cone and a four-sided pyramid, respectively.

The excess surface area created by the indentation process, *A'*, is simply given by the difference between the created area (A_p) and the destroyed area (A_i):

$$A' = A_i - A_p \,. \tag{1.42}$$

By combining Eqs. 1.40, 1.41 and 1.42, *A'* can be expressed by:

$$A' = A_p\left(\frac{1}{\sin\alpha_i} - 1\right) = \gamma.h^2 \tan^2\alpha_i\left(\frac{1}{\sin\alpha_i} - 1\right) \tag{1.43}$$

and the force required to create the excess surface area, F_s, can be determined by:

$$F_s = \frac{d}{dh}(A' \cdot E_s) = \frac{2}{h} A_p\left(\frac{1}{\sin\alpha_i} - 1\right)E_s \,, \tag{1.44}$$

where E_s is the SFE of the material.

Finally, the contribution of SFE to hardness, ΔH_{SFE}, is given by:

$$\Delta H_{SFE} = \frac{F_s}{A_p} = 2\left(\frac{1}{\sin\alpha_i} - 1\right)\frac{E_s}{h} \,. \tag{1.45}$$

By applying the model just described to Cu, Ni-Al, PMMA[•] and quartz, indented by Berkovich and cube-corner indenters (α_i = 70.3º and 35º, respectively), Jäger [106] concluded that SFE may have an important contribution to the hardness measured from nanoindentation tests provided that the three following conditions are simultaneously met: 1) ductile metallic samples with high SFE; 2) sharp indenters, i.e. with small α_i angle and small tip radius; 3) shallow indentations.

Although it was not previously mentioned in this work, an effect opposite to ISE has also been sporadically observed in some ceramics and semiconductors [12, 107, 108] and in a

[•] Polymethylmethacrylate

few metals [12, 95]. This effect is known in the literature as reverse ISE and consists on a hardness increase with increasing indentation depth until a maximum value is reached, and is generally followed by a normal ISE behaviour as the depth is further increased. Reverse ISE is far less common and understood than the normal ISE. Up to now, the most accepted explanation for this effect has been given by Sangwal [108], which suggested that an initial strain hardening of the material at low loads may be responsible for the initial hardness increase with increasing depth.

The revision made in this section shows that, in general, the hardness of crystalline materials depends on contact scale. Nevertheless, the explanations given for most of the scale dependent hardness data presented in the literature are usually concerned with a single factor, and are based on theoretical models but lack other type of confirmation, such as experimental studies of the dislocation structures produced during indentation (e.g. configuration and density). Moreover, most of the tested materials are simple and do not display the characteristics of typical rubbing engineering materials, which is understandable due to the intrinsic complexity of scale related phenomena.

In this way, the main motivation of the present work was to extend the study of the scale dependence of hardness and its relations with wear response to materials of higher structural complexity, namely those of the Ni-Co system, which is an important metallic system for tribological applications as was previously explained in §1.1.

2. EXPERIMENTAL METHODS

This chapter begins with a description of the methods used to prepare the Ni-Co samples, followed by a description of the methods used to characterise the topography, chemical composition, microstructure, and the tribo-mechanical behaviour of the samples. Measurement protocols and calibration procedures are also presented and discussed here.

2.1. Material preparation methods

The samples used in this work were prepared in the form of thick coatings by powder injection laser cladding. After laser processing, the surface of the coatings was mechanically ground and polished. The majority of the samples was polished using suspensions of diamond particles while the remaining ones were electropolished. Samples for transmission electron microscopy (TEM) were also prepared from the laser clad coatings. A detailed description of the sample preparation procedures is given in the sections bellow.

2.1.1. Laser Cladding processing

Laser cladding was chosen to produce Ni-Co samples, with compositions ranging from 100% Ni to 100% Co, because it enables producing with promptness and reliability small amounts of materials, in the form of high quality thick coatings, that can be used for detailed characterisation [109]. In this process, powder of the clad material is delivered by means of a carrier gas to the melt pool generated by a high power laser beam, which is scanned in a continuous motion in relation to the substrate. A schematic drawing with the most important components involved in the laser cladding process can be seen in Figure 2.1, while in Figure 2.2 an image of the components is shown. The laser beam melts the incoming powder and a thin layer of the substrate, forming an adherent clad track (Figure 2.3.a). By partially overlapping successive tracks a surface coating is produced (Figures 2.3.b and c).

The cladding experiments were performed using an Eurolas 3000 Messer Griesheim 3 kW CO_2 fast axial flow laser with a TEM $_{01}$* mode (Figure 2.2.a). Laser cladding of Ni-Co alloys on Ni substrates was initially tried, but the metallurgical bonding between the coatings and the substrate was insufficient. In this way, AISI 304 stainless steel (in the form of plates) was chosen for the substrate since the adherence of the Ni-Co coatings to this material was observed to be quite good. The steel plates were sandblasted in order to further reduce the reflectivity of the substrates.

Commercially pure Ni and Co (> 99.5 wt. %) with average particle sizes of 90 and 150 μm, respectively, were used in the experiments. Prior to laser processing, the powders were pre-heated at 100 ºC during 1 h to remove the adsorbed humidity. A laser power density of 400 W/mm^2, scanning speeds in the range 5 to 10 mm/s and powder feed rates in the range 0.11 to 0.27 g/s were used in the cladding experiments. These laser cladding parameters enabled producing good quality thick coatings (~ 1 mm thick) and keeping the dilution low (contamination of the coating material by the substrate material was smaller than 4.5% -

please see Table 3.2 on page 98). Argon was used as carrying gas for particle transport and as protection gas to avoid oxidation of the melt pool.

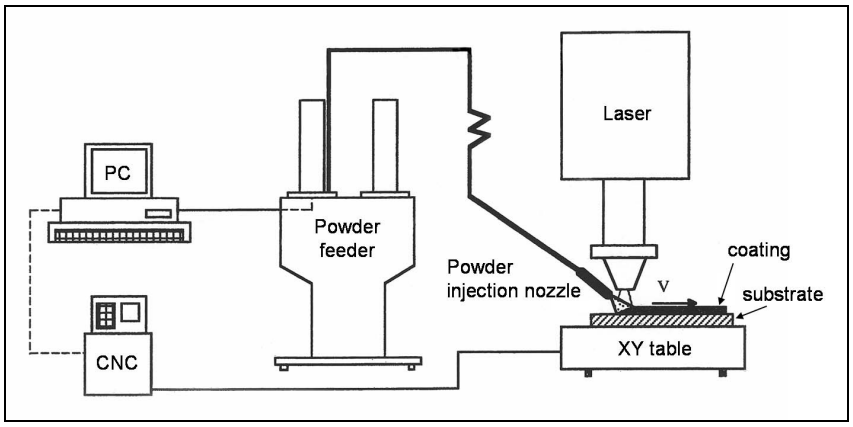

Figure 2.1. Schematic drawing of the main components used in the laser cladding process.

a) b)

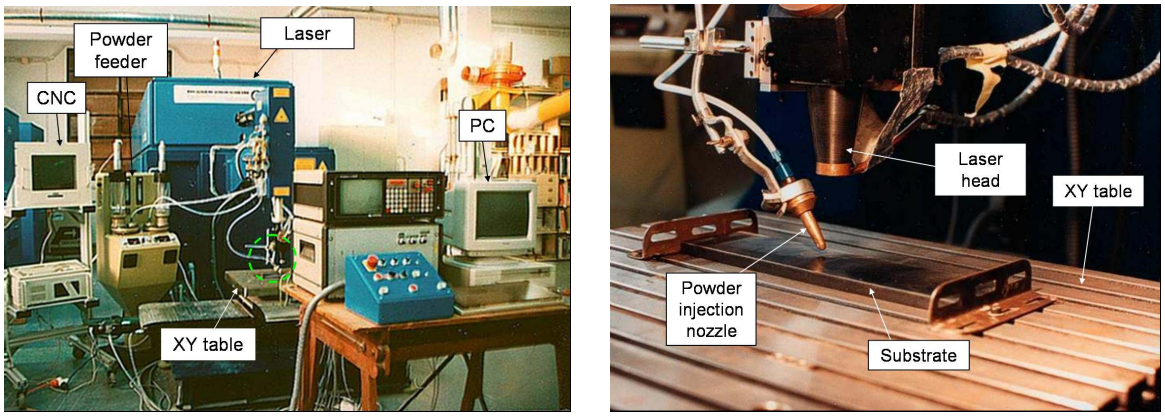

Figure 2.2. a) Components used in the laser cladding process. The area inside the green dashed circle (centre of the picture) contains the laser head, the powder injection nozzle and the substrate material. b) Zoom-in of the area inside the green dashed circle in a).

a) b) c)

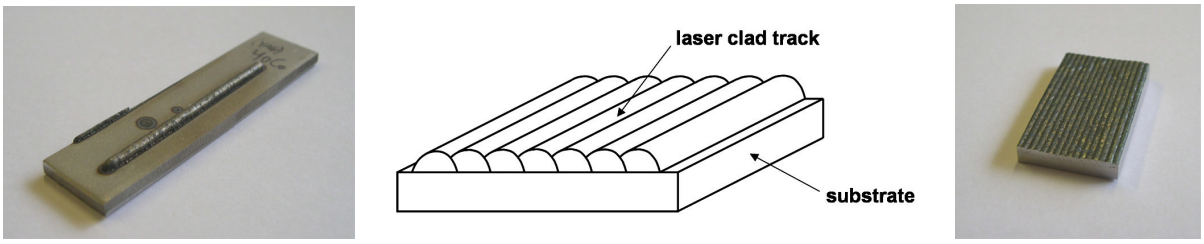

Figure 2.3. Track (a) and coating (b and c) produced by powder injection laser cladding. The coating is formed by several partially overlapped laser clad tracks, which are deposited on a substrate.

2.1.2. Surface preparation

After laser processing the surface of most Ni-Co coatings was mechanically ground and polished. Grinding was carried out with successively smaller granulometry SiC abrasive papers, ending with a 4000 mesh paper. Afterwards, the samples were polished with a sequence of diamond particles suspensions, ending with a 0.1 μm average diameter diamond particles suspension. After mechanical polishing, the coatings were ~ 500 μm thick and presented a mirror-like finished surface (Figure 2.4).

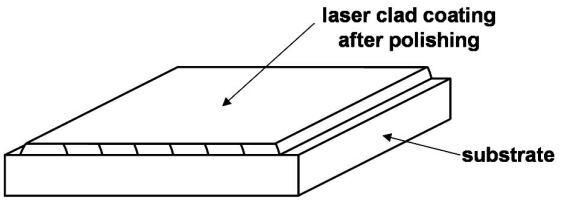

Figure 2.4. Drawing of laser clad coating (deposited on a substrate) after mechanical polishing of the surface.

For some of the experiments performed in this work it was necessary to prepare the surface of pure Ni and pure Co samples by electropolishing. After laser processing, these samples were first ground with SiC abrasive papers until 1000 mesh paper and then electropolished. Electropolishing was carried out with a home made apparatus for beaker electropolishing [110], specially built for this work. The apparatus (Figure 2.5) is composed of an electrolytic cell, an Isotech IPS303D DC power supply and a Variomag Monotherm magnetic stirrer. The electrolytic cell is formed by a 250 ml beaker with a PVC cover on the top, four alligator clamps (surrounding the cover) fixing the cover to the beaker, and two alligator clamps fixed in the middle of the cover. These last clamps were used to grab the anode (sample) and the cathode (stainless steel plate), which were then immersed in the electrolyte. The ground surface of the coating (part of the anode) was facing the larger rectangular area of the cathode and the distance between them was about 2 cm. The anode and cathode were connected, respectively, to the positive and negative terminals of the power supply. The generic anodic and cathodic reactions are described, respectively, by:

$$M \rightarrow M^{+2} + 2e^{-} \qquad (2.1.a)$$

and

$$2H_2O + 2e^- \rightarrow H_2 + 2OH^- \qquad (2.1.b)$$

where *M* is the metal being polished (anode) and hydrogen evolution at the cathode occurs.

a) b)

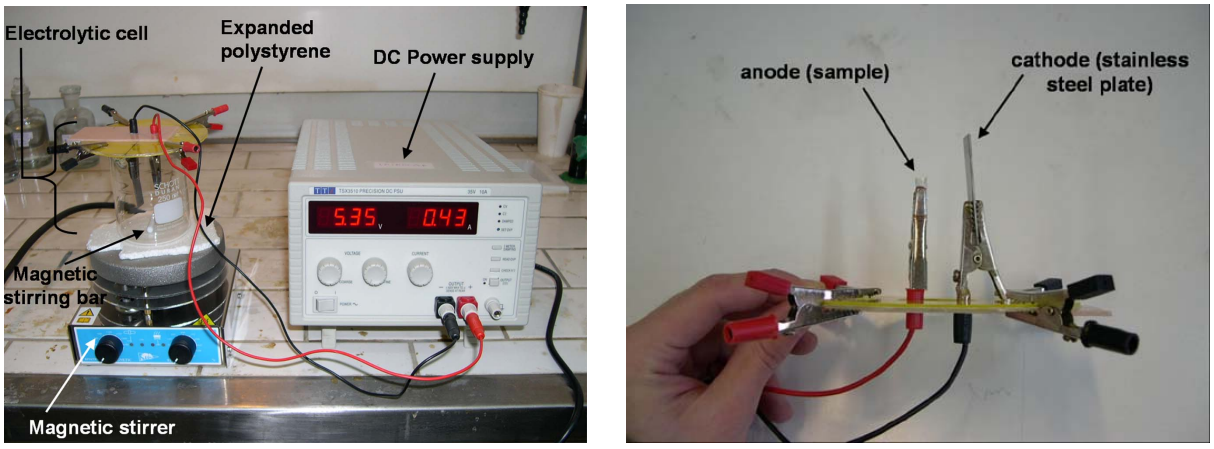

Figure 2.5. a) Components used in beaker electropolishing; b) Anode and cathode fixed by two alligator clamps at the centre of the PVC cover.

Ni was electropolished for 220 s using a 40%H_3PO_4–35%H_2SO_4–25%H_2O solution [111], with an applied voltage of 12 V. The electrolyte was magnetically stirred. During the process the temperature increased from – 9 to 1 ºC, leading to an increase in the current from 1.63 to 2.99 A. Co was electropolished for 60 s using an 80%CH_3OH–20%$HCLO_4$ solution[•] [111], with an applied voltage of 11.5 V and no stirring of the electrolyte. The temperature increased from -34 to -27 ºC, leading to a slight increase in the current from 0.75 to 0.78 A. A thin stainless steel plate was used as cathode in both cases. Both electrolytes were cooled by adding liquid nitrogen directly into the solution prior to electropolishing. An expanded polystyrene plate was placed under the beaker to reduce the amount of heat transferred from the magnetic stirring motor to the electrolyte.

[•] Extra care should be taken when working with perchloric acid ($HCLO_4$), since this substance is a strong oxidizing agent that in the presence of materials containing carbon (e.g. acetic anhydride, paper, wood, rubber, grease and oils) can lead to fire or even explosions [110, 111]. The electrolyte used to electropolish pure Co is an alcohol solution of $HClO_4$. These solutions are unstable above room temperature (the acid should be cooled to 0 ºC or lower before mixing with alcohol) and should not contain more than 30% stock acid concentrations due to the possibility of spontaneous combustion or explosion at higher concentrations (e.g. exposition to the air for long periods leads the alcohol to evaporate from the solution, which consequently increases the $HClO_4$ concentration). Additional information on this substance can be found in the literature [112].

2.1.3. Transmission electron microscopy samples

Samples for TEM observations were prepared by cutting the coatings from the substrates with a thin low speed abrasive saw, and then grinding both faces (top and bottom) of the coatings with successively smaller granulometry SiC papers (ending with a 2000 mesh paper) down to a foil thickness of 50 to 60 μm.

Part of the TEM observations consisted on the study of the density and arrangement of dislocations in some of the samples produced by laser cladding and so, in order to avoid modifying the initial dislocation structure of the material, especial preparation procedures were carried out. Firstly, instead of using the traditional punching method [113] that may introduce a considerable amount of plastic deformation in the sample, the 3 mm discs necessary for TEM observations were cut with a 70 W Q-switched Nd/YAG laser. Secondly, dimpling of the thin foil discs was also avoided and the discs were immediately ion milled to perforation with a Gatan DuoMill 600DIF ion milling machine, using a 4 kV Ar^+ beam (gun current in the range 1 to 1.5 mA) and a 12º incidence angle. After ion milling, electron transparent regions were present in the periphery of the hole created at the centre of the discs (Figure 2.6)[•].

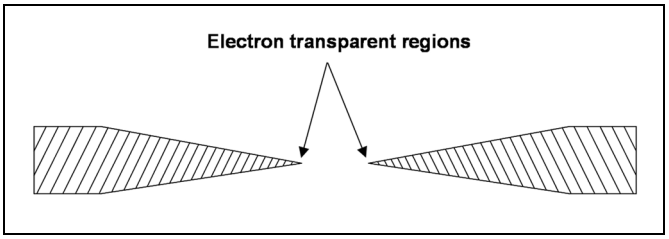

Figure 2.6. Schematic drawing of cross-section of the 3 mm diameter TEM disk perforated by ion milling. The electron transparent regions that are observed by TEM are located in the periphery of the hole.

2.2. Topographical and structural characterisation methods

The topographical and structural characterisation of the samples consisted on the determination of their surface roughness, microporosity, surface and bulk chemical composition, microstructure and substructure. The techniques used for the characterisation are described in the following sections.

[•] Of course, the best way to avoid introducing dislocations in the sample would be to perforate the TEM discs by electropolishing [111]. This method was also tried, by using a single vertical jet electropolisher (model 550D from South Bay Technology). However, the parameters of the process necessary to obtain good TEM samples could not be found, even though some recipes from the literature were tried insistently [110].

2.2.1. Atomic force microscopy

Atomic force microscopy was used for surface characterisation of the samples. This technique belongs to a family of techniques designated as scanning probe microscopy (SPM), which make use of the interactions forces (e.g. van der Waals forces, magnetic forces, electrostatic forces) between the surface of a sample and the surface of a sharp tip.

In this work all AFM observations were carried out in air using four atomic force microscope models from Veeco: Multimode, CP, CP-II and D3100. Images of the three AFM systems used in the present work are shown in Figure 2.7.

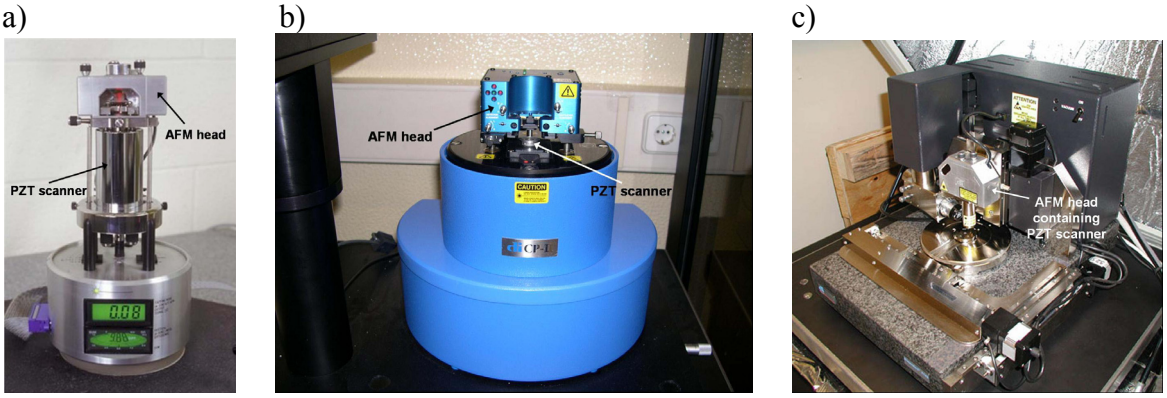

Figure 2.7. Multimode (a), CP-II (b) and D3100 (c) atomic force microscopes from Veeco. In models Multimode and CP-II the PZT scanner is located under the sample holder, while in model D3100 the scanner is located above the tip holder. Model CP from Vecco is very similar to model CP-II.

The atomic force microscope is composed of three major components: a piezoelectric transducer (PZT) scanner that moves the sample in relation to the tip (or vice-versa, depending on the atomic force microscope model) in the plane of the surface (X–Y plane) and in the direction normal to this plane (Z direction), a tip that interacts with the material's surface and is attached to the end of a flexible cantilever beam, and a cantilever position detection system. The scanning movement of the PZT scanner in the X–Y plane is commonly made in a raster pattern (Figure 2.8), where a fast and a slow (step-by-step) scan direction exist (FSD and SSD, respectively). During this movement the X and Y positions of the scanner are periodically stored by a computer (dark points in Figure 2.8) as, respectively, X and Y coordinates of data points, along with other information which constitutes the Z coordinate. The information contained in the Z coordinate can have different meanings depending on the signal collected by the control unit (e.g. scanner vertical position, amplitude error, phase lag between cantilever excitation signal and cantilever response signal). The AFM image is formed by the stored data points, and the information that it contains increases with increasing number of data points (which consequently increases the time for image acquisition).

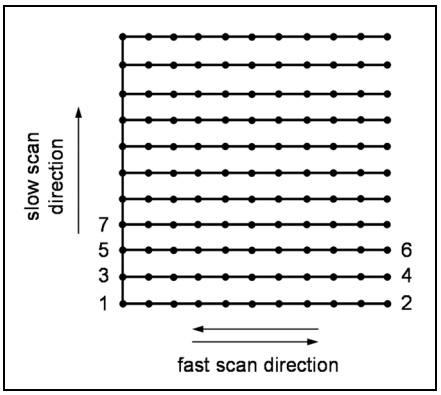

Figure 2.8. Raster pattern scanning movement of the PZT scanners used in the present work, in the plane of the material's surface (*X*-*Y* plane). The movement occurs as follows: 1→2→1→3→4→3→5→6→5→7→… → ending point. The dark points all over the scanned area mark the positions where data is acquired by the control unit of the atomic force microscope.

There are two main types of AFM probes (in this work the designation "probe" refers to the tip-cantilever assembly), the ones made of silicon and the ones made of silicon nitride. In Si probes, the tip has an approximately conical geometry and is attached to a rectangular Si cantilever, while in Si_3N_4 probes a square pyramidal tip is attached to a triangular (also know as V-shaped) or a rectangular (less common) Si_3N_4 cantilever (Figure 2.9). Table 2.1 shows the characteristics of two models of AFM probes manufactured by Veeco which were used in this work.

Variations of the cantilever position (bending or torsion) are usually detected by the movement of a HeNe laser beam, which strikes the rear side of the cantilever (side opposite to that where the tip is attached) in the region where the tip is located and is reflected onto a two- or four-quadrant position-sensitive detector (PSD), along the surface of the detector (Figure 2.10). Normal bending of the cantilever, which is caused by normal forces acting between the surfaces of tip and sample, leads to movements of the laser spot along the vertical direction of the photo-detector. On the other hand, under certain scanning conditions, frictional forces acting between these surfaces produce cantilever torsion, which results in horizontal movements of the laser spot on the photo-detector. There are other cantilever position detection methods (e.g. electron tunneling, optical interferometry, capacitance, piezoresistance and piezoelectricity) but laser beam deflection is the most common one [114] and was present in all the atomic force microscopes used in this work.

Besides the PZT scanner which moves the sample (or the tip) in the *X*, *Y* and *Z* directions, another piezoelectric material can exist in the microscope. This piezo is located in the tip holder and is responsible for the vibration of the AFM cantilever which is used in some of the operational modes (dynamic modes).

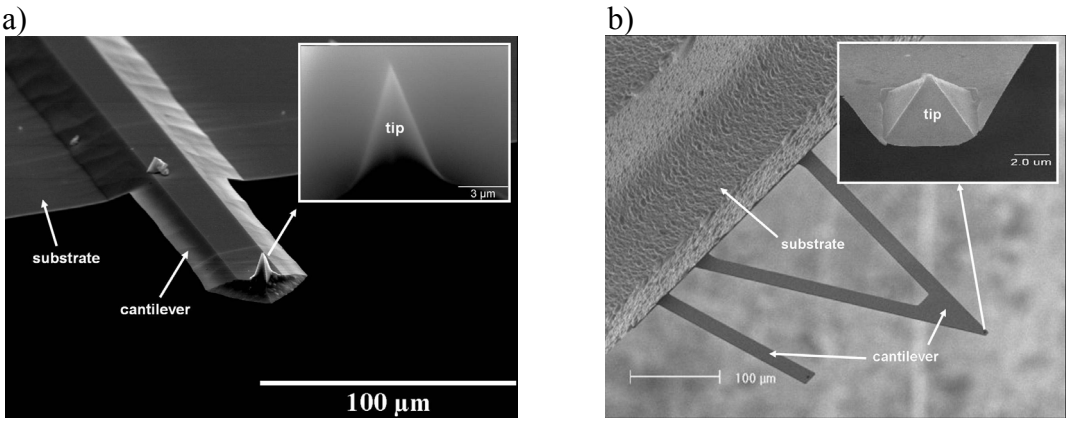

Figure 2.9. a) AFM Si tapping mode probe with rectangular cantilever. b) AFM Si_3N_4 contact mode probes with rectangular (left) and triangular (right) cantilevers. The insets show high magnification images of the tips.

Table 2.1. Characteristics of two models of AFM probes manufactured by Veeco and used in the present work: MPP-11100 (non-contact mode and tapping mode) and MPP-31100 (contact mode) [115].

Model	MPP-11100		MPP-31100	
Part	cantilever	tip	cantilever	tip
Material	phosphorus doped silicon	phosphorus doped silicon	phosphorus doped silicon	phosphorus doped silicon
Geometry	rectangular	irregular, sharp	rectangular	irregular, sharp
Dimensions	l = 115-125 µm w = 30-40 µm t = 3.5-4.5 µm	h = 15-20 µm R < 12.5 nm	l = 440-450 µm w = 30-40 µm t = 3.5-4.5 µm	h = 15-20 µm R < 12.5 nm
Normal stiffness	c_n = 20-80 N/m	—	c_n = 0.45-1.8 N/m	—
Resonant frequency	f_0 = 200-400 kHz		f_0 = 13-27 kHz	

l – length; w – width; t – thickness; h – height; R – tip curvature radius; c_n – normal spring constant.

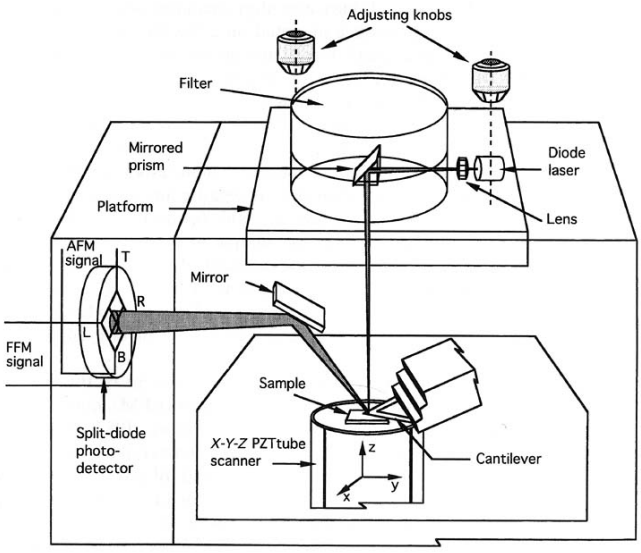

Figure 2.10. Schematic drawing of a commercial atomic force microscope (model Multimode from Veeco) where the cantilever position is detected by means of a laser and a position-sensitive detector. In this case, a four-quadrant photo-detector is used and the PZT scanner responsible for movement in the X, Y and Z directions is located under the sample [26].

AFM can be performed in ambient air, gas, liquid environment or in ultra-high vacuum (UHV) conditions. For observations in liquids, both the sample and the probe are immersed in the liquid contained in a liquid cell and there is no influence of capillary forces [116]. Such forces are also absent in UHV-AFM, where the microscope is located inside a UHV chamber and sample observations are carried out under pressures of ~ 10^{-11} mbar [117].

Depending on the distance of separation between tip and sample and, consequently, the resulting magnitude of the interatomic force (van der Walls force) established between the surfaces, three different operational modes can be used in AFM: contact, intermittent-contact or tapping and non-contact (Figure 2.11). The first mode is static, which means that the cantilever does not oscillate during scanning, while the other two modes are dynamic. In contact mode the tip and sample surfaces are brought so close that the repulsive forces between the electron clouds of the atoms of tip and sample (Coulomb repulsion) dominate over the attractive forces between the nuclei of the atoms of one surface and the valence electrons of the atoms of the other surface (Coulomb attraction). The other extreme case is the non-contact mode, where tip and sample are separated at a distance where attractive forces between the surfaces dominate over repulsive ones. In between these two modes there is a mode (tapping) where the interaction force continuously changes from predominantly repulsive to predominantly attractive and vice-versa during the oscillatory movement of the cantilever.

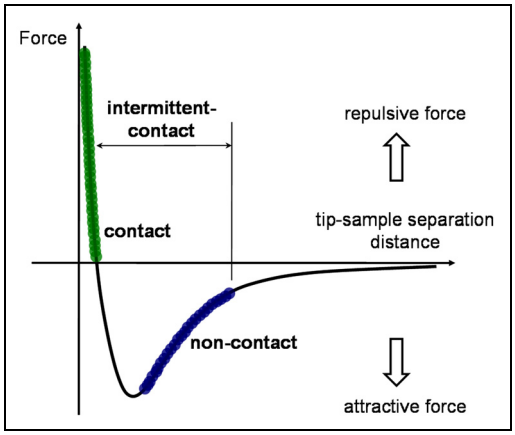

Figure 2.11. Variation of the interatomic force (van der Waals force) with the separation distance between tip and sample. The green region of the curve is used for contact mode, the blue for non-contact mode, and in intermittent-contact the interactions change periodically between repulsive and attractive.

The cantilevers used in dynamic AFM modes are stiffer than those used in contact mode (see Table 2.1), in order to prevent the tip from being pulled by the surface attractive forces into permanent contact. In contact mode, the interaction force causes the cantilever to bend

(or deflect) and the normal force applied by the cantilever (F_N) can be determined from Hooke's law [118]:

$$F_N = c_n \Delta Z \,, \tag{2.2}$$

where c_n and ΔZ are, respectively, the normal spring constant and normal deflection of the cantilever. Forces in the nN to μN range can be applied by the tip in contact mode. There are different variants of contact mode [118] but the most common is *constant force imaging*, which was used in this work. In this mode the force is maintained constant during scanning by keeping the cantilever deflection constant through a feedback mechanism. Any variation of the cantilever deflection from the initial value (deflection setpoint defined by the operator), results in a deviation of the laser spot position from the centre and along the vertical direction of the detector. This deviation is registered by the control unit, which immediately forces the PZT scanner to move vertically (by varying the voltage applied to the piezo) until the setpoint deflection is restored. This process occurs in all (X, Y) data collection positions in the scanned area (Figure 2.8), and the vertical distances moved by the scanner are stored by the computer to generate the Z coordinate of the points that form the topographic image of the sample's surface. In *constant force imaging*, when the fast scan direction is perpendicular to the long axis of the cantilever, a particular SPM technique designated as lateral force microscopy (LFM) [119, 120] can be obtained. Here, the friction force between tip and sample, which produces torsion of the cantilever, can be determined from the voltage signal generated when the laser beam moves along the horizontal direction of the photo-detector.

In non-contact mode the cantilever is oscillated at a frequency (driving frequency f^* in Figure 2.12) which is slightly above its resonant frequency and with an amplitude of less than 10 nm [118]. The tip does not contact the surface during scanning, but oscillates above the adsorbed water layer (when present), keeping a distance from the sample in the range 10 to 100 nm. The load applied by the tip is on the order of pN. When the tip is far away from the sample the resonant frequency of the cantilever (free-surface resonant frequency, f_0) is given by [15]:

$$f_0 = \frac{1}{2\pi}\sqrt{\frac{c_n}{m_0}} \,, \tag{2.3}$$

where m_0 is the effective mass that loads the spring (cantilever + tip). When the tip approaches the sample's surface the resonant frequency decreases due to the influence of the

attractive forces between the atoms of opposite surfaces. The resonant frequency (f_c) is now given by [118, 121]:

$$f_c = \frac{1}{2\pi}\sqrt{\frac{c_{eff}}{m_0}}, \tag{2.4}$$

where c_{eff} is the effective spring constant of the probe-surface system. This constant depends not only on the cantilever's spring constant (c_n) but also on the attractive force gradient (dF_N / dz):

$$c_{eff} = c_n - \frac{dF_N}{dz}. \tag{2.5}$$

By decreasing the tip-sample separation distance in the attractive regime the force gradient increases (Figure 2.11), thus leading to a decrease of c_{eff} and, consequently, of f_c (Figure 2.12). This shift of the resonant frequency peak will lead to a decrease of the vibration amplitude at the driving frequency chosen by the operator (Figure 2.12.a). During scanning, the vibration amplitude or the resonant frequency of the cantilever is kept constant (setpoint amplitude or frequency, respectively) by means of a feedback mechanism similar to that in *constant force imaging*. Here, any changes in the vibration amplitude or in the resonant frequency (caused by changes of the average tip-sample separation distance) are detected at the photo-detector and registered by the control unit, which forces the PZT scanner to move vertically until the setpoint amplitude/frequency is obtained. The vertical displacements of the scanner at each (X, Y) point are stored by the computer to form the topographic image of the sample's surface as in *constant force imaging*.

The third operational mode in AFM is intermittent-contact or tapping mode, and was also used in this work. This mode is similar to non-contact mode, since the cantilever is also oscillated during scanning. However, in this case the oscillation usually occurs at a driving frequency which is slightly lower than the cantilever's free-space resonant frequency. Consequently, the shift of the resonant frequency peak due to the decrease of the tip-sample separation distance, will lead to an increase of the vibration amplitude at the driving frequency chosen by the operator (Figure 2.12.b). In this mode, amplitudes of vibration ranging from 20 to 100 nm are used [122]. The larger vibration amplitude of the cantilever, in comparison to that used in non-contact mode, leads the tip to lightly "tap" the sample's surface during scanning, at the bottom of its swing. In this way, forces between tip and

sample are predominantly repulsive and attractive, respectively, at the bottom and top position of the cantilever oscillatory movement. In this mode the vibration amplitude is maintained constant by a feedback mechanism similar to that used in non-contact mode and the topographic image is built in the same way as in non-contact mode.

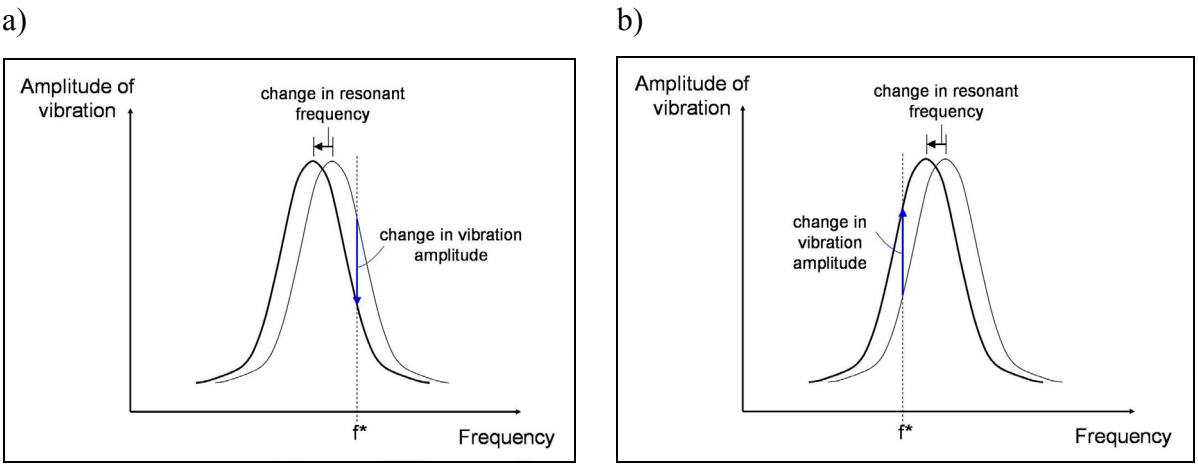

Figure 2.12. Cantilever vibration amplitude-frequency curve. Attractive forces originate a shift of the resonant frequency peak to the left side of the plot (thin to thick curve), leading to a shift of the vibration amplitude at a certain driving frequency *f**: a) non-contact mode conditions; b) tapping mode conditions.

Tapping is the most common mode for simple topographical visualization because it presents some of the advantages of both contact and non-contact modes. The forces exerted by the tip on the sample are lower than in contact mode, enabling imaging soft samples and increasing the tip lifetime. Also, because the tip only contacts the surface for a very short period of time during scanning, the lateral forces between tip and sample are practically inexistent and, consequently, there is less tip contamination and wear. On the other hand, the introduction of image artifacts due to the presence of an adsorbed water layer is minimized because the tip periodically taps the sample's surface during scanning and, in this way, follows the real sample topography. On the contrary, in non-contact mode, differences in thickness of the adsorbed water layer along the scanned region may lead to an incorrect determination of the sample topography. Finally, because there is no problem of contacting the adsorbed water layer (contrary to non-contact mode, where the trapping of the tip by this layer causes instabilities in the feedback mechanism), higher scanning speeds can be used, thereby reducing the time for image acquisition.

2.2.2. Scanning electron microscopy

Scanning electron microscopy (SEM) with a Hitachi S2400 microscope was used to determine the microstructure of the samples. A schematic representation of a scanning

electron microscope is shown in Figure 2.13.a. Electrons are emitted from a thermionic or field-emission cathode (negative electrode) and accelerated by a voltage in the range 1 to 50 kV towards an anode (positive electrode), where both the cathode and anode are part of the electron gun. A hole in the anode allows a fraction of the produced electrons to proceed down the column towards the magnetic lenses. The electron column is kept under vacuum to avoid the scattering of electrons by air molecules. The electron beam is then focused and directed towards the sample by the magnetic lenses, which are usually composed of one to three condenser lenses plus the objective lens. The diameter of the electron probe at the sample's surface is usually less than 10 nm. A deflection coil system in front of the final lens (objective) scans the electron probe in a rectangular raster across the sample's surface and in synchronism with the electron beam of a separate cathode-ray tube (CRT). The rectangular scanned area is formed by successive scan lines which are composed by discrete point locations. One or more detectors are used to collect the electrons and radiation emitted from the sample, which generate electrical signals. The signals collected from the electron beam-sample interaction are then converted by the signal processing electronics into an image on the CRT.

Figure 2.13.b shows the main signals that result from the interaction between the primary electron beam and the sample, where the most used in SEM imaging are secondary electrons (SE) and backscattered electrons (BSE). SE are loosely bound outer shell electrons from the sample atoms which receive sufficient kinetic energy during inelastic scattering of the beam electrons to be ejected from the atoms and set into motion. They are emitted from a thin surface layer (thickness < 10 nm), with an energy less than 50 eV, and contain information on the surface topography. BE are produced by single large-angle as well as multiple small-angle elastic scattering events of the primary electrons, such that their trajectory is deviated from the incident beam path and they return to the sample's surface to escape. They are more energetic than SE, with energies ranging from 50 eV to the primary electron energy, and are generated at much larger depths and widths than SE. Because the number of backscattered electrons increases with increasing atomic number of the material, variations of the chemical composition of the sample usually originate contrast in the BSE image. Besides SE and BE, other signals can be collected using the appropriate detectors. In this work, characteristic X-rays and Auger electrons were used to further characterize the samples. A description of the corresponding techniques is made in §2.2.4 and §2.2.5, respectively.

In this work an accelerating voltage of 25 kV was used to visualize the samples. The electrons were emitted from a tungsten thermionic cathode.

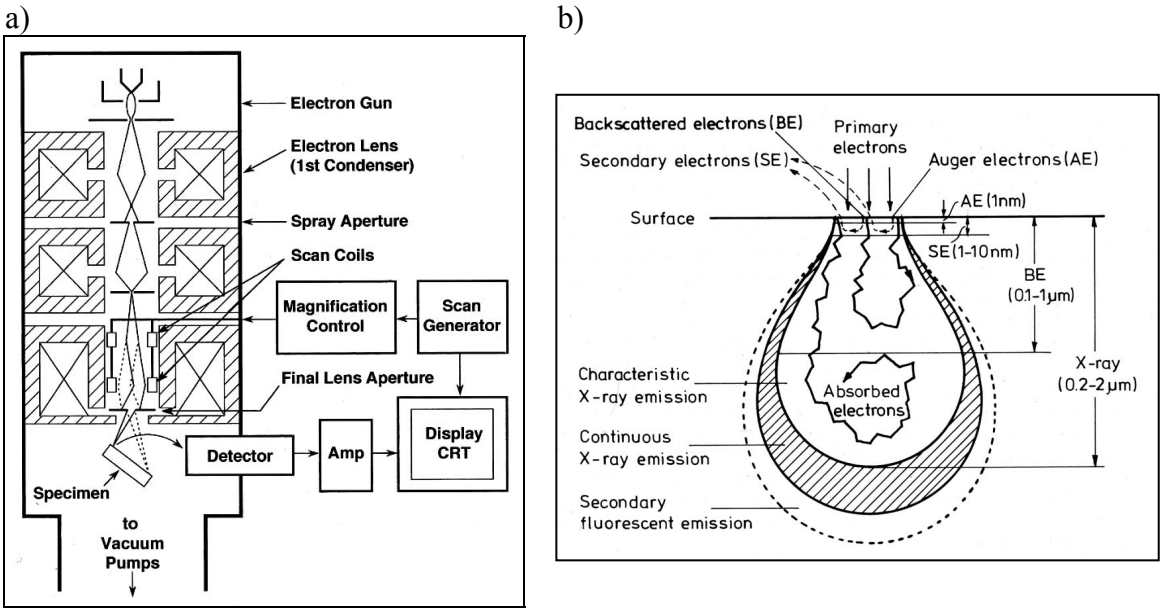

Figure 2.13. a) Schematic representation of a scanning electron microscope [123]; b) Schematic representation of the different types of electron-beam excited electrons and radiation and the correspondent depths of information, generated in a scanning electron microscope. The fluorescence emission can come from as deep as 100 μm [124].

2.2.3. Transmission electron microscopy

Conventional transmission electron microscopy with a Hitachi H8100 microscope was used to determine both the microstructure and the substructure of the samples. A schematic representation of a transmission electron microscope is shown in Figure 2.14.a. Similarly to SEM, all the components are located inside a vacuum column to reduce the interaction of electrons with air molecules. Electrons are emitted in the electron gun by a thermionic or field-emission cathode and accelerated towards an anode, which has a small hole at its centre so that the electrons can move down the column. The electron beam then goes through an illumination system, which is composed of two or three magnetic condenser lenses and controls the sample illumination, producing either a broad or focused beam. The electron beam crosses a very thin sample (thickness usually less than 100 nm) and goes to the imaging system, which is generally composed of three magnetic lenses: the objective lens, the intermediate lens and the projector lens. The objective lens takes the electrons emerging from the exit surface of the sample and uses them to form the image and the diffraction pattern. The image or the diffraction pattern (depending on the operation mode chosen by the operator) is then magnified and projected onto a fluorescent screen by the intermediate and projector

lenses. The images and patterns can also be recorded by direct exposure of photographic emulsions or, as was done in this work, with a charge-coupled device (CCD) detector.

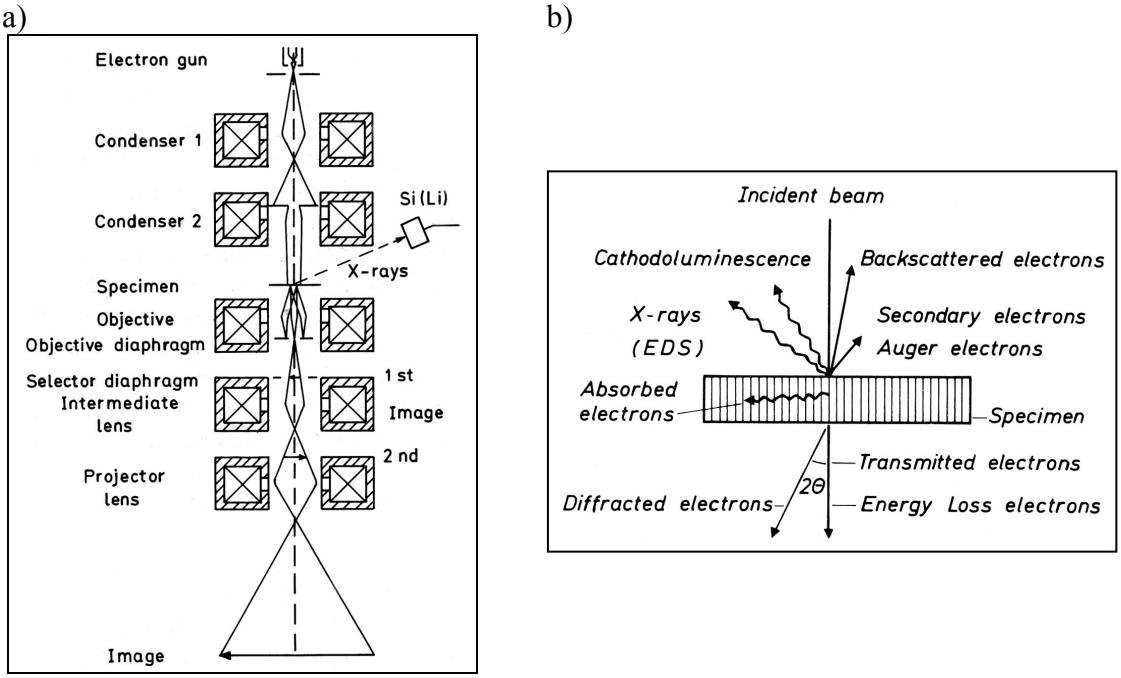

Figure 2.14. a) Schematic representation of a transmission electron microscope equipped for additional X-ray spectroscopy [125]. Although it is not represented in this drawing, all the components are contained in a vacuum column. b) Schematic representation of the different types of interactions between the incident electron beam and a TEM sample [124].

As in the case of SEM, different kinds of interactions can occur between the electron beam and the sample in TEM (Figure 2.14.b). The major source of contrast in TEM images and the origin of the intensity distributions in diffraction patterns are the elastically scattered electrons. On the other hand, inelastic scattering of electrons is equally important since it generates a range of signals (e.g. X-rays and secondary electrons) that contain additional sample information.

The diffraction patterns of this work were obtained using the standard Selected-Area Diffraction (SAD) technique, in which the beam incident on the sample is parallel and relatively large, with a diameter usually between 1 and 10 μm. An aperture is inserted in the image plane of the objective lens to select only the electrons diffracted from a specific area of the sample and, consequently, electrons diffracted from other sample areas do not contribute to the diffraction pattern that is projected onto the fluorescent screen. Although in this work the only imaging mode used was Bright-Field (BF), there are also two other modes that are commonly used in TEM observations, which are designated as Dark-Field (DF) and Centred

Dark-Field (CDF). In BF, only electrons from the direct beam are used to form the image (Figure 2.15.a), whereas in DF, electrons diffracted by a particular set of crystallographic planes are used to form the image (Figure 2.15.b). A particular case of DF imaging is the CDF mode, where the diffracted beam used to form the image is tilted so that the electrons travel down the optic axis (Figure 2.15.c). CDF is preferable to DF because the images obtained by DF are more difficult to focus and the electrons that travel off the optic axis suffer aberrations and astigmatism, resulting in poorer image quality. In a few observations in this work, a two-beam condition set-up was used to improve image contrast, which consists on tilting the crystal around until only one diffracted beam is strongly excited. A less commonly used technique designated as Convergent-Beam Electron Diffraction (CBED) was also applied to determine the thickness of TEM samples (see §3.5). Contrary to SAD, in CBED the electron beam is highly focused on a small sample region, with a spot diameter usually in the range 10 to 100 nm.

All the TEM observations of this work were carried out using an accelerating voltage of 200 kV and a double-tilt sample holder (Figure 2.16). This sample holder enables rotating the sample along two axis perpendicular to the normal direction of the sample's surface. Tungsten and LaB_6 cathodes were used to produce the primary electron beam.

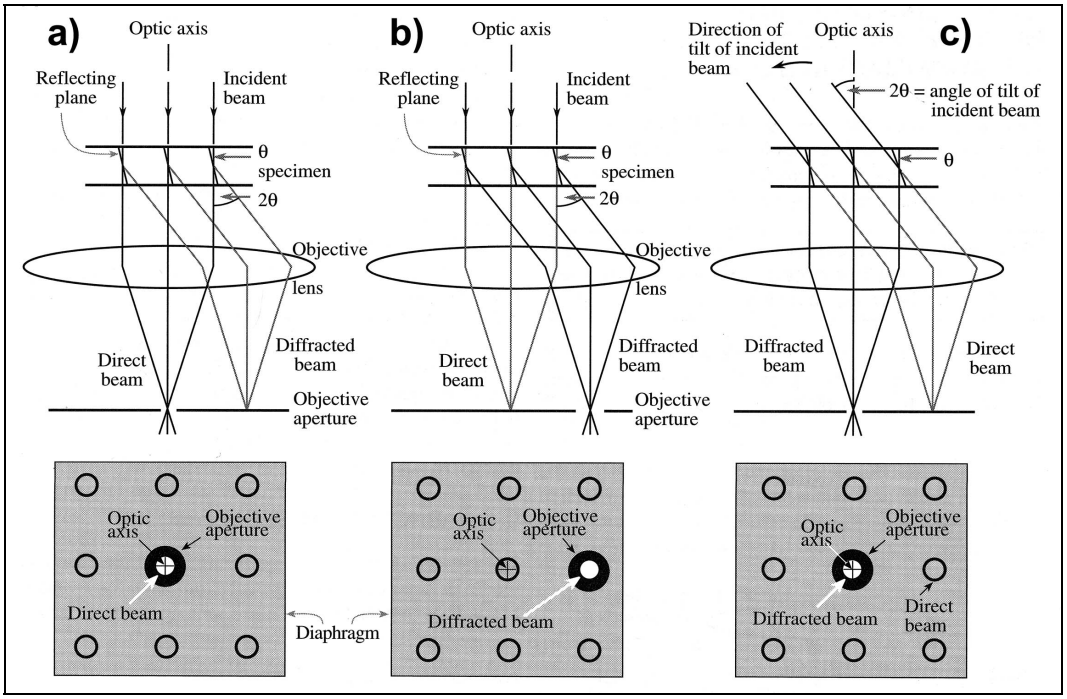

Figure 2.15. Ray diagrams showing how the objective lens/aperture are used in combination to produce a BF image (a), a DF image (b) and a CDF image (c). The area selected by the objective aperture, as seen on the fluorescent TEM screen, is shown below each ray diagram [126].

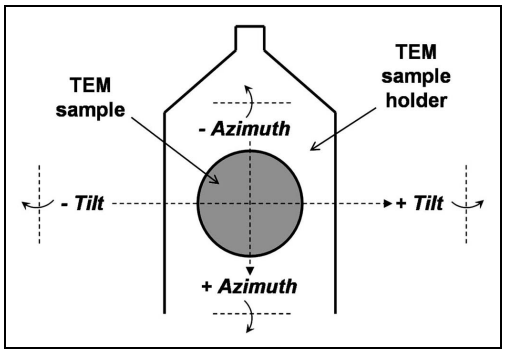

Figure 2.16. Schematic representation of the extremity region of the double-tilt TEM sample holder used in this work, with a sample disc mounted. The sample can be rotated to a maximum of ± 45º along the vertical axis (*tilt* rotation angle) and ± 30º along the horizontal axis (*azimuth* rotation angle) of the holder.

2.2.4. Energy dispersive spectroscopy

Energy dispersive spectroscopy (EDS) was used to determine the chemical composition and homogeneity of the samples. Chemical composition was determined from EDS spectra whereas chemical homogeneity was determined from X-ray maps. Both the scanning and the transmission electron microscopes used in this work have a Rontec EDS detector attached, which enables measuring the energy and intensity distribution of the X-ray signal generated by the interaction between the electron beam and the sample (Figure 2.17). Rectangular areas of 260 × 195 and 104 × 78 μm^2 were analysed qualitatively and quantitatively by EDS in the case of SEM samples, whereas in TEM samples, approximately circular areas with diameters between 100 and 200 nm were analysed qualitatively.

EDS spectra are formed by a continuous background (*Bremsstrahlung* radiation) and peaks characteristic of the elements present in the sample. In this work, standardless quantification was carried out to determine the composition of the samples, i.e. without the use of standards of known composition. After spectrum acquisition, a chemical analysis commercial software was used to identify the peaks, subtract the background, deconvolute the peaks and finally to integrate the peak intensities and perform the corrections for the atomic number, X-ray absorption and X-ray fluorescence effects (the so-called ZAF correction). The resulting analytical total is normalized to unity (100%).

In X-ray mapping, the counts from characteristic peaks of the EDS spectrum are selected in a multichannel analyser by setting energy windows at these peaks, in order to produce distribution maps of the corresponding elements. During sample scanning in the scanning electron microscope, all the positions in the sample which generate X-ray photons with energies within the selected energy range will be represented by bright dots in the X-ray map. Therefore, the concentration of elements is proportional to the number of bright dots per

unit area. The presence of background radiation generates a random distribution of bright dots, which makes this method not very useful to locate poorly concentrated elements.

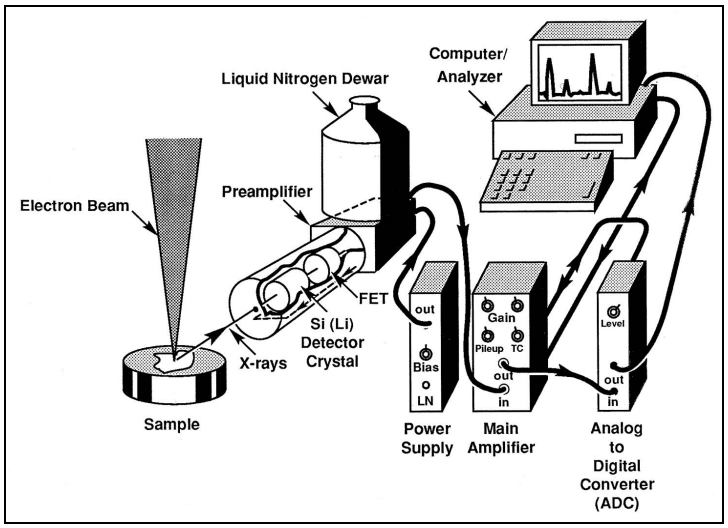

Figure 2.17. Schematic representation of an energy dispersive spectrometer and associated electronics [123].

2.2.5. Auger electron spectroscopy

Auger electron spectroscopy (AES) combined with ion sputtering was performed with a VG Scientific Microlab 310 F scanning Auger microprobe equipped with a field emission type electron gun, a concentric hemispherical analyser and a differentially pumped Ar^+ ion gun, to obtain chemical composition depth profiles of the samples.

A schematic representation of the Auger process is shown in Figure 2.18. When an atom is struck by a high energy electron, an electron from one of its inner shells may be removed, thus leading to the formation of an electronic vacancy. This vacancy can be filled by another electron from an outer shell, resulting in the relaxation of the excited atom. The photon that results from the relaxation process can be emitted from the atom in the form of radiation (e.g. X-ray photon in EDS) or absorbed by another electron, causing its ejection from the atom. This ejected electron is known as Auger electron and its kinetic energy is characteristic of the analysed chemical element. The energy of an Auger electron is typically in the range 10 to 1000 eV, while its mean free path (average distance travelled by the electrons without energy losses) in a solid is in the range 0.4 to 4 nm [127]. Since the AES technique requires that the Auger electrons do not suffer energy losses during their movement towards the surface, the information retrieved from this technique is referent only to the first few surface layers (see Figure 2.13.b). An Auger spectrum consists of a plot of intensity against the kinetic energy of the Auger electrons, and is formed by a continuous background

and peaks corresponding to characteristic Auger transitions. Because different chemical elements emit Auger electrons with different kinetic energies, the Auger transition peaks enable identifying the elements present at the sample's surface. Moreover, a quantitative analysis is also possible because the peak areas are proportional to the atomic concentrations of the elements.

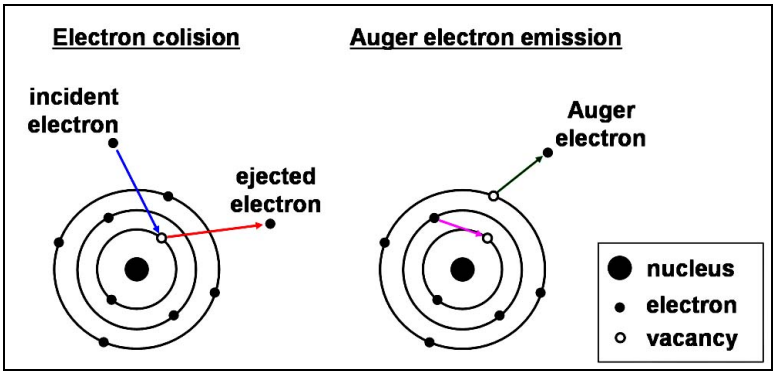

Figure 2.18. Schematic representation of Auger electron emission due to the interaction of a high energy electron with an atom. The photon that causes the ejection of the Auger electron is omitted in the schematics.

In order to determine the chemical composition of a material as function of depth, it is necessary to combine AES with a technique to remove material from the surface, such as ion sputtering (Figure 2.19). In this technique an ion gun produces a beam of ions (through the ionization of an inert gas by electrons) which is accelerated towards the sample's surface. When the fast-moving ions hit the surface, chemical bonds are broken and some surface atoms are removed from the sample. Each sputtering cycle removes a layer of material typically a few angstroms thick. By performing alternate sputtering and AES cycles a chemical composition depth profile can be obtained, down to depths of about 1 μm into the bulk.

In this work, the Auger spectra were obtained using an electron beam accelerated at 10 keV and a target current of 50 nA. Removal of material from the sample's surface was achieved with an Ar^+ ion beam accelerated at 3 keV, at an angle of incidence of 30º. The ion beam current density varied from 0.4 to 0.7 $\mu A.mm^{-2}$. The sputtered region was a crater with a diameter of 700 μm, whereas the electron beam had a spatial resolution of ~ 100 nm and was aligned with the centre of this region. Because the sputtering rates of both Ni and Co oxides for the used experimental conditions could not be found in the literature, the sputtering rate of FeO, 0.33 $nm.s^{-1}$, was used as first approximation to obtain the chemical composition depth profiles [128].

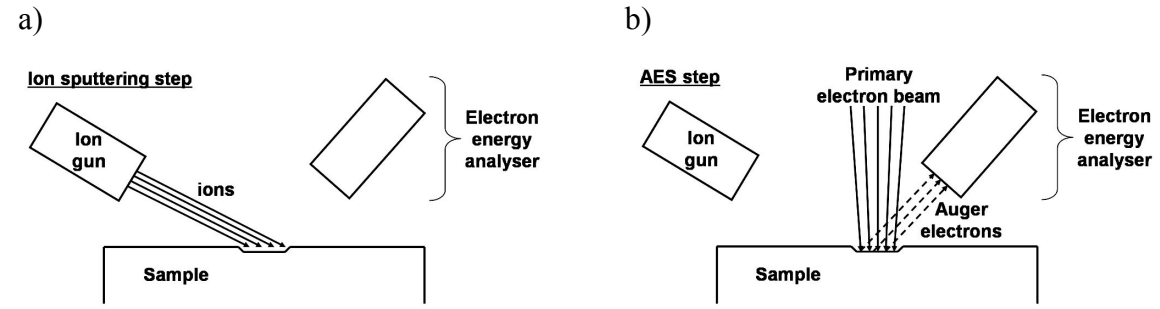

Figure 2.19. Steps used to perform Auger depth profiling: a) ion sputtering; b) Auger electron spectroscopy.

2.2.6. X-Ray diffraction

X-Ray diffraction (XRD) with a Siemens D5000 Bragg-Brentano diffractometer and CuK_α radiation ($\lambda_{average}$ = 1.5418 Å) was used to determine the microstructural phases present in the samples.

A schematic representation of the Bragg-Brentano geometry is shown in Figure 2.20. The X-ray source contains a cathode (generally a tungsten filament) and an anode target metal (e.g. Mo, Cu, Co, Fe, Cr), which are kept under vacuum. Electrons are produced at the cathode by thermionic emission and accelerated by a high voltage towards the anode. When the electrons strike the anode, most of their kinetic energy (about 98 %) is converted into heat and the remaining part is used to eject core electrons from the atoms of the target metal. Refilling of the left vacancies by electrons from higher energy shells is accompanied by X-ray emission. These well defined electronic transitions generate the characteristic peaks (also known as lines) of the atoms present in the target metal, which are superimposed on a continuous background in the target spectrum. The designation of the characteristic lines is related to the transitions, as represented in Figure 2.21. The X-radiation used in this work was K_α, which results from the filling of vacancies in the K-shell of Cu by electrons in the L-shell. The K_α radiation is formed by two components, $K_{\alpha1}$ and $K_{\alpha2}$, which correspond to transitions from the LIII- and LII- shells to the K-shell, respectively. Because these components have very close wavelengths (1.54056 Å for $K_{\alpha1}$ and 1.54439 Å for $K_{\alpha2}$), they are not always resolved as separate lines, and in this case the radiation is designated simply as the K_α line. If the two peaks can be distinguished in the diffractogram, they are called the K_α doublet. Because $K_{\alpha1}$ is about twice as strong as $K_{\alpha2}$, the wavelength of an unresolved K_α doublet may be taken as the weighted average of the wavelengths of its components ($\lambda_{average}$ = 1.5418 Å in the case of CuK_α) [129]. The weaker K_β and background radiations, which are also produced

during electron bombardment of the Cu target, are strongly absorbed by the Ni filter present in the diffractometer, enabling to obtain an essentially monochromatic radiation.

When a monochromatic beam of X-rays strikes a set of parallel crystal planes (*hkl*), diffraction will only occur if the re-emitted waves are in phase, which is known as constructive interference. A condition necessary for constructive interference is given by Bragg's law:

$$n\lambda = 2d_{hkl}\sin\theta, \tag{2.6}$$

where n is an integer known as order of diffraction, λ is the wavelength of the radiation (in this case, X-rays), d_{hkl} is the interplanar spacing of the (*hkl*) planes and θ is the angle between the incident beam and the (*hkl*) planes, which is known as Bragg angle. However, this condition by itself is not sufficient for diffraction to occur. Another parameter that needs to be considered is the structure factor F[•], which expresses both the amplitude and phase of the resultant wave scattered by all the atoms of the unit cell. Since the intensity of the diffracted beam is proportional to $|F|^2$, diffraction will not occur if the structure factor for the *hkl* reflection is zero (e.g. $F = 0$ for reflections in FCC crystals where h, k and l are not all even or all odd) [129].

The produced K_α radiation diverges from the X-ray source and is diffracted by the sample to form a convergent beam which comes to a focus at the receiving slit and then enters the detector (Figure 2.20). During the test, the source is fixed and the sample and detector rotate in the same sense, where the angular velocity of the detector is twice as that of the sample. In this way, a rotation of the sample through x degrees is automatically accompanied by rotation of the detector trough $2x$ degrees. For any position of the detector, the receiving slit and the X-ray source are always located on the goniometer circle, which means that the sample's surface, because of its mechanical coupling with the detector, is always tangent to the focusing circle. The radius of the focusing circle decreases as the angle between the incident and diffracted beams (diffraction angle), 2θ, increases. A diffractogram is obtained by plotting the intensity of the diffracted beam against 2θ.

In this work, an accelerating voltage between anode and cathode of 40 kV and a current of 30 mA were used to produce the X-rays. The angular increment during the tests was 0.04º and the scan speed was 6º/min. The 2θ angle was varied between 40º and 100º.

[•] A detailed description of this parameter can be found in textbooks on diffraction, such as the book *Elements of X-Ray Diffraction*, by Cullity [129].

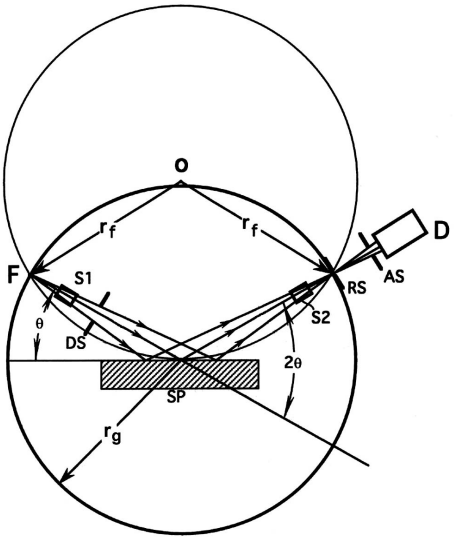

Figure 2.20. Schematic representation of the Bragg-Brentano geometry: F – X-ray source; S1 and S2 – Soller slits; DS – divergence slit; SP – sample; RS – receiving slit; AS – antiscatter slit; D – detector; O – centre of the focusing circle; r_f – radius of the focusing circle; r_g – radius of the goniometer; θ – Bragg angle; 2θ – diffraction angle [130].

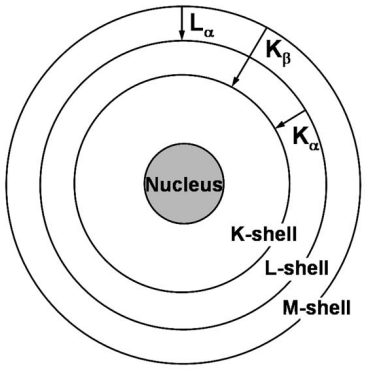

Figure 2.21. Schematic representation of electronic transitions in an atom, common in XRD. The arrows indicate the emission processes from which result the characteristic lines of the anode target metal.

2.3. Tribo-mechanical characterisation methods

The tribo-mechanical characterisation was performed by using indentation, scratch and abrasive wear tests. The terms *micro*, *ultramicro* and *nano*, used in this work as prefixes for the names of the tribo-mechanical characterisation techniques, are only related to the typical scale of contact between the bodies involved in the tests and, therefore, should not be taken to be strictly related to a particular range of applied loads or dimensions of the test features (e.g. indentations, scratches or wear scars). These techniques are described in the following sections.

2.3.1. Indentation

Static indentation tests were used to determine both the indentation hardness (H_i) and the Young's modulus (E) of the samples. In the remaining text, static indentation will be simply referred to as indentation.

In an indentation test, an indenter, usually made of diamond, tungsten carbide or hardened steel and with a given geometry (e.g. pyramidal, conical, spherical), is pressed against the surface of the material to be tested. In general, an indentation cycle is composed of three stages. The first stage corresponds to loading, where the indenter is continuously pressed against the sample's surface until the maximum value of the load is reached. In the second stage, the sample is kept under the influence of this maximum load for a short period of time (usually from 10 to 30 s), in order to avoid the influence of creep of the material on the measurements [74]. Finally, in the third stage, the sample is continuously unloaded by removing the indenter from the surface until the applied load is zero. In some cases (e.g. ultramicroindentation tests of this work) it is common to have a fourth stage, where the sample is not completely unloaded during the third stage, but is kept under the influence of a residual value of the load for a short period of time. This stage can be used to evaluate and correct the influence of thermal drift of the equipment (variation of the dimensions of the components due to temperature changes during the tests) on the experimental results [74, 131].

Aiming to compare the hardness values measured under different conditions (loads, equipments and indenter geometries), in the present work the hardness of the samples was expressed by its Meyer hardness [132] or indentation hardness, given by [133]:

$$H_i = \frac{F_{\max}}{A_P}, \tag{2.7}$$

where F_{max} is the maximum load and A_p is the projected contact area of the indentation at that load (which remains approximately constant during elastic recovery of the sample [27, 134]).

In the present work, the influence of contact scale on the mechanical properties of the samples under static-contact conditions was analysed by using three types of indentation tests: conventional microindentation, displacement sensing indentation (ultramicro- and nanoindentation) and AFM cantilever-based nanoindentation. These techniques, as well as the theoretical support for the calculations, are described in detail in the next three sections.

2.3.1.1. Microindentation

Conventional microindentation tests were carried out with a Shimadzu HMV2000 apparatus and a Vickers indenter, whose geometry is shown in Figure 2.22. The applied load was in the range 0.5 to 2 N and the holding time at maximum load was 20 s.

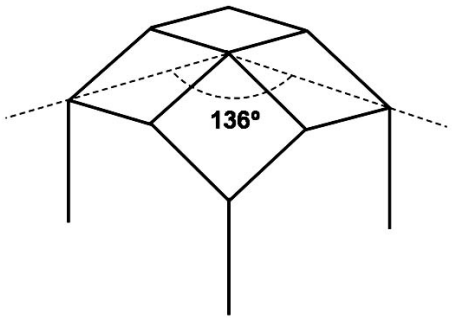

Figure 2.22. Schematic representation of the Vickers indenter (upside down), which consists on a four-sided diamond pyramid with square base. The opposite faces of the pyramid make an angle of 136º [27].

Microhardness was calculated from measurements of the length of the diagonals of the indentation, which were carried out using the optical microscope attached to the apparatus•. Since Vickers hardness (H_V) is defined as the quotient of the maximum load, in kg, and surface contact area of the indentation, in mm^2, the indentation hardness (H_i, defined in Eq. 2.7) can be related to H_V by [27]••:

$$H_i = \frac{H_V}{0.927}. \tag{2.8}$$

2.3.1.2. Displacement sensing indentation

In displacement sensing indentation (DSI) the vertical position of the indenter is continuously monitored along with the applied normal load. From the tests result load-displacement (F_N-h) curves which are used to extract the mechanical properties of the samples. Schematic representation of the indentation process and of the correspondent F_N-h curve can be seen in Figures 2.23.a and b, respectively. This technique is applied when the dimensions of the indentations are too small to be measured by optical microscopy. Moreover, from the

• Due to the small magnification of the optical microscope attached to the microindenter, it was found that the hardness values obtained by measuring the length of the diagonals using optical microscopy ($H_{V\,(OM)}$) was about 10% higher than those obtained by determining the real length by SEM observation. In this way, all $H_{V\,(OM)}$ values retrieved from the microindenter were corrected by $H_V = 0.9H_{V\,(OM)}$.

•• After conversion of kgf to N.

unloading stage of the test the Young's modulus of the sample can be determined, which is not possible with conventional microindentation.

a)

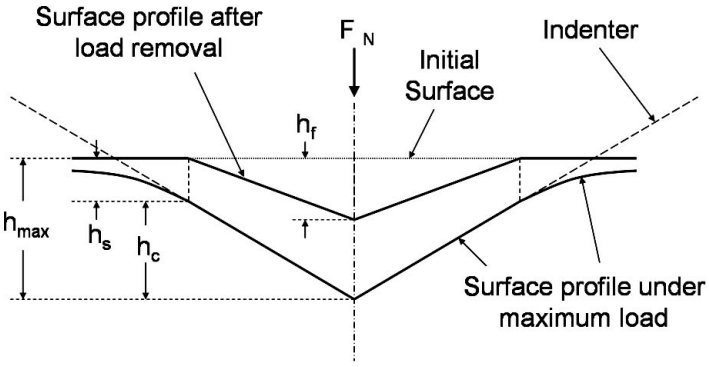

b)

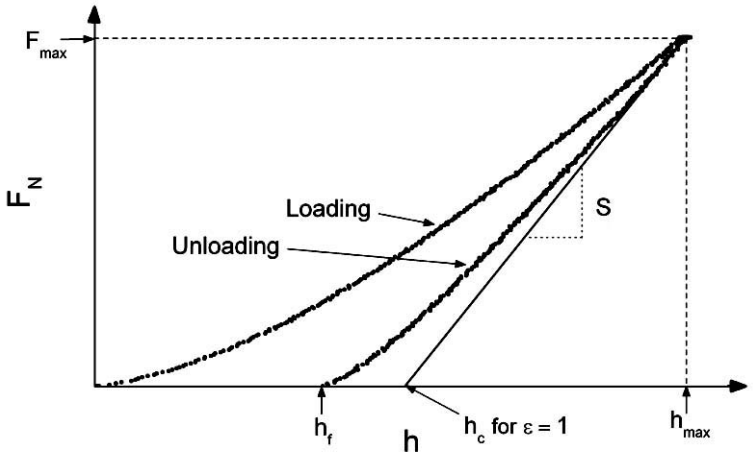

Figure 2.23. (a) Two-dimensional schematic representation of an indentation test using a conical indenter, with the sample's surface profile at maximum load and after unloading. (b) Load-displacement curve resulting from an indentation test. (F_N – normal load; h_{max} – maximum depth; h_c – contact depth; h_s – surface displacement at the contact perimeter ; h_f – final depth, after elastic recovery of the sample; S – initial unloading stiffness)

In this work two different DSI apparatus were used, one to do ultramicroindentation tests and the other to do nanoindentation tests.

Ultramicroindentation tests were performed with a Fischerscope H100 apparatus and a Vickers indenter. The applied load was in the range 10 to 200 mN and the holding time at maximum load was 30 s. The room temperature varied between 18 and 23 ºC.

Nanoindentation tests were performed with a Hysitron Triboscope nanomechanical test instrument mounted on a Park Scientific Instruments CP AFM, where the Hysitron transducer

was replacing the usual AFM head (Figure 2.24). In this way, the mechanical stability and precision of the displacement sensing nanoindenter can be combined with the *in situ* imaging capability of the AFM, allowing visualising the surface before and after the indentation test with the same tip that is used to perform the test. Visualization of the samples was performed in AFM-like contact mode (*constant force imaging*) using a load of 2 μN, where the transducer replaces the laser beam deflection method of the standard AFM contact mode. Observation of successively larger scan areas showed that no apparent modification of the surface occurs during scanning with this load. A conospherical indenter with an included cone angle of 90º and nominal tip radius of 1 μm (Figure 2.25) was used in the nanoindentation tests. The applied load was in the range 0.05 to 10 mN and the holding time at maximum load was 10 s[•]. The room temperature varied between 22 and 24 ºC, while the relative air humidity varied between 15 and 27%.

Before analysing the F_N-h curves which resulted from the ultramicro- and nanoindentation tests, the displacement data was corrected in respect to the thermal drift of the equipment. In the ultramicroindentation tests, the procedure for thermal drift correction was applied by the software Hardness 5.00[••] and is described in the literature [131]. This software was also used to analyse the data resulting from the ultramicroindentation tests. Correction of the thermal drift of the nanoindentation equipment was automatically performed by the software Triboscope 3.6 FL (trademark of Hysitron) [135], which was used to analyse the data resulting from the nanoindentation tests and is responsible for controlling the Hysitron transducer (Figure 2.24).

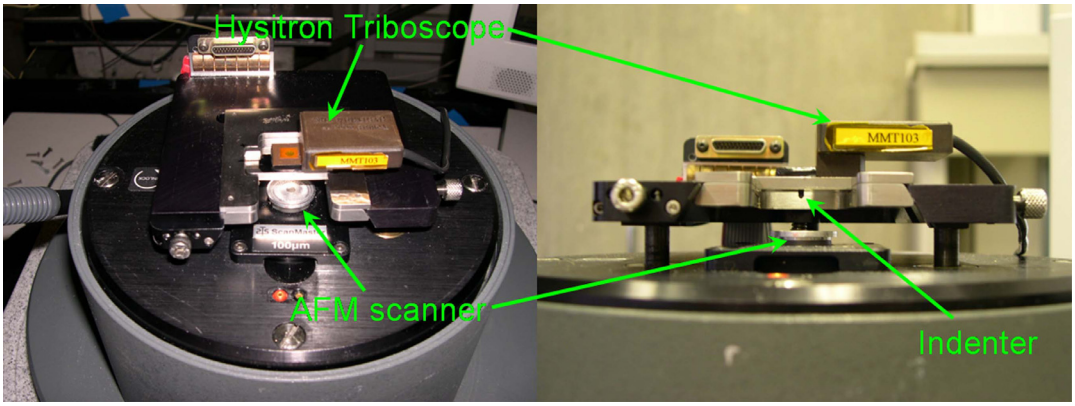

Figure 2.24. Hysitron Triboscope nanomechanical test instrument mounted on a Park Scientific Instruments CP AFM. A conospherical indenter is mounted on the Hysitron transducer.

[•] A few preliminary tests were made using larger holding times, but no apparent differences on the mechanical property values were observed.

[••] Developed by J. C. Oliveira, of the Department of Mechanical Engineering of the University of Coimbra.

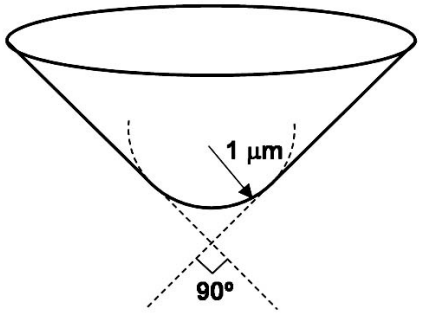

Figure 2.25. Schematic representation of the conospherical indenter, which consists on a cone with 90º aperture angle and a 1 μm radius spherical end (as specified by Hysitron).

While the hardness of the samples is determined by using Eq. 2.7, the determination of the Young's modulus from DSI tests is usually based on an equation that relates the reduced Young's modulus of the contact (E_r) with the initial unloading stiffness of the contact (S_c) and the projected contact area of the indentation (A_p, as in Eq. 2.7) [136, 137]:

$$E_r = \frac{\sqrt{\pi}}{2}\frac{S_c}{\sqrt{A_p}}. \tag{2.9}$$

This equation is valid for all indenters that can be described as bodies of revolution. In the case of non-axisymmetric indenters (e.g. triangular and square pyramids), King [138] has introduced a correction factor (β_i) in Eq. 2.9, which results from numerical analysis of the indentation of an isotropic elastic half-space with flat-ended triangular and square punches:

$$E_r = \frac{\sqrt{\pi}}{2\beta_i}\frac{S_c}{\sqrt{A_p}}, \tag{2.10}$$

where β_i is equal to 1, 1.034 and 1.012, respectively, for circular, triangular and square geometries. The deviation of the values of β_i for the triangular and square geometries from the circular one is quite small (3.4% and 1.2%, respectively), meaning that Eq. 2.9 can be used without great error even in the case of indenters that cannot be described as bodies of revolution [137].

Once E_r is determined, and knowing the values of the Young's modulus of the indenter (E_i) and the Poisson's ratio of both indenter and sample (ν_i and ν, respectively), the Young's modulus of the sample (E) can be determined by solving Eq. 1.2 in relation to E. In this work

all indenters were made of diamond, whose elastic properties can be found in the literature [74]: E_i = 1141 GPa and ν_i = 0.07. The Poisson's ratio of pure Ni and pure Co is, respectively, 0.31 and 0.32 [139].

In order to determine H_i and E_r, S_c and A_p have to be previously determined. The methods of determination of S_c and A_p in the software that analyses the data files from the ultramicroindentation tests (Hardness 5.00) are different from those used in the software that analyses the data files from the nanoindentation tests (Triboscope 3.6 FL). A description of the methods is made below.

The unloading part of the F_N-h curve is used to determine the elastic properties of the sample because, in general and contrary to the loading part, it has no contribution from the plastic deformation of the sample (it is related to the elastic recovery of the material after load removal). However, the stiffness of the contact cannot be determined immediately from the initial portion of the unloading curve, since during the test there is also elastic deformation of the equipment. In this way, the parameter extracted from the unloading curve is the total stiffness of the system, S, which accounts for the stiffness of both the contact and the equipment (see Figure 2.23.b).

Two different methods are often used to determine S, and it is assumed in both that non-elastic effects (e.g. time-dependent plasticity) do not occur during unloading. The method used by the software Hardness 5.0 was proposed by Doerner and Nix [140] and consists on fitting a line tangent to the initial portion of the unloading curve (Figure 2.23.b), where S is given by the slope of this line. In this method it is assumed that, during initial unloading, the area of contact between indenter and sample remains constant as the indenter is withdrawn. Though this behaviour is typical of a flat cylindrical punch, Doerner and Nix justified the application of the method to other more common geometries based on the experimental observation that the initial portion of the unloading curve of some materials (mostly metals), indented with a Berkovich• indenter, is linear. The method used by the software Triboscope 3.6 FL was proposed by Oliver and Pharr [74] and consists on fitting the unloading data with the power law relation:

$$F_N = B\left(h - h_f\right)^m, \tag{2.11}$$

• The Berkovich indenter is a three-sided pyramid. The edges make angles of ~ 142º with the corresponding opposite faces of the pyramid, whereas the axis of the pyramid makes angles of ~ 65º with the faces of the pyramid [141].

where F_N is the applied load, h the indenter displacement, B and m are constants and h_f is the final depth of the indentation after load removal (Figure 2.23.a). B, m and h_f can be determined from the fitting (e.g. least squares fitting procedure). S can then be determined by differentiating Eq. 2.11 in relation to h and calculating the derivative at maximum load and displacement:

$$S = \left(\frac{dF_N}{dh} \right)_{F\max, h\max} = Bm\left(h_{\max} - h_f\right)^{m-1} \tag{2.12}$$

Oliver and Pharr justified the application of this method based on the observation that the unloading data of a wide range of materials (aluminium, tungsten, sapphire, quartz, soda lime glass and fused silica) are well described by a power law relation such as Eq. 2.11.

In order to determine S_c from the value of S retrieved from the unloading curve, it is necessary to determine the machine compliance (C_m, also know in the literature as load-frame compliance), i.e. the elastic displacement of the equipment per unit load applied. This procedure becomes crucial when large applied loads and relatively rigid samples are used, where the displacement of the equipment can represent a significant portion of the total displacement. The total compliance of the system (C) is equal to the sum of the compliance of the contact (C_c) and the compliance of the equipment:

$$C = C_m + C_c . \tag{2.13}$$

Since the compliance is the inverse of the stiffness, S_c can be determined by rewriting Eq. 2.13 in the form:

$$S_c = \left(\frac{1}{S} - C_m \right)^{-1} . \tag{2.14}$$

The value of C_m of the ultramicroindentation equipment has been determined by Trindade *et al*. [142] and is 0.04 nm/mN, whereas the value of C_m of the nanoindentation equipment was determined in this work by using a procedure recommended by Hysitron [135]. This procedure results from the combination of Eqs. 2.9 and 2.13, where C and C_c are given by the inverse of S and S_c, respectively:

$$\frac{1}{S} = C_m + \frac{\sqrt{\pi}}{2E_r\sqrt{A_p}}. \tag{2.15}$$

For large indentation depths, where the hardness and the reduced Young's modulus can be assumed to be constant (independent of indentation depth), Eq. 2.7 can be combined with Eq. 2.15 to give:

$$\frac{1}{S} = C_m + \frac{\sqrt{\pi}\sqrt{H_i}}{2E_r}\frac{1}{\sqrt{F_{\max}}}. \tag{2.16}$$

Hysitron recommends the operators to perform this procedure on an elastically isotropic material such as fused silica, using loads larger than 5 mN. Several indentation tests should be performed in this sample and the values of S extracted from the resulting unloading curves using one of the methods described previously. Afterwards, the values of $(1/S)$ are plotted against the values of $(1/F_{max}^{1/2})$ and a straight line is fitted to the data points. The equipment compliance is given by the interception of this line with the $(1/S)$ axis. This procedure was strictly followed in this work by performing several indentation tests with loads in the range 5 to 14.5• mN in a finely polished fused silica standard, and the measured machine compliance was 1.504 nm/mN (Figure 2.26).

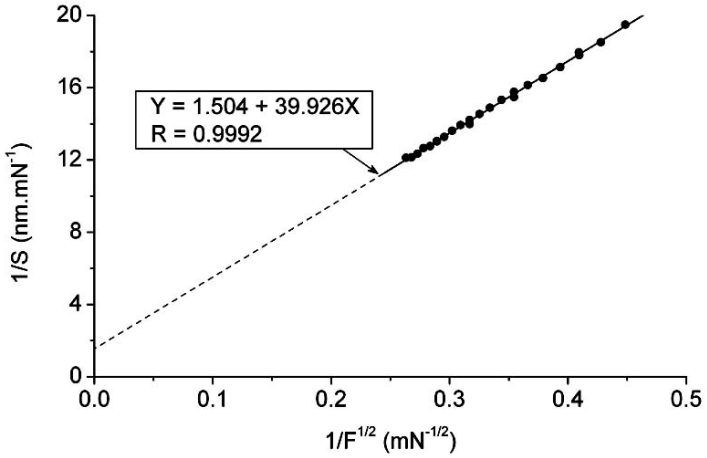

Figure 2.26. Measurement of machine compliance of the Hysitron Triboscope with a conospherical indenter mounted.

• Maximum load attainable by the Hysitron transducer.

The determination of the projected contact area of the indentation in DSI tests is usually achieved by determining the contact depth (h_c in Figure 2.23.a) and introducing this value in the area function $A_p(h_c)$ of the indenter. If it is assumed that the indenter has an ideal geometry, i.e. does not contain geometrical imperfections, $A_p(h_c)$ can be directly obtained from geometrical calculations. However, real indenters always present some imperfections arising from manufacturing, such as small deviations of the characteristic angles of the indenter (e.g. between opposite faces in the Vickers indenter), tip bluntness, and other imperfections characteristic of each geometry[•]. All geometrical imperfections of the indenter modify its area function to some extent and, therefore, it is necessary to determine the real area function of the indenter before determining the mechanical properties of the material. This is especially critical in small size indentations, due to the larger contribution of tip imperfections to the indentation test. On the other hand, in large indentations, most of the indentation shape will be produced by the ideal geometry part of the indenter and, consequently, the influence of tip imperfections can be neglected.

The method used by the software Triboscope 3.6 FL [143] to determine A_p is based on the Oliver and Pharr method [74], which is the most widely used in DSI and does not require observation of indentations or indenter. The first step is to make several indentations with a large range of loads in a material with known Young's modulus and Poisson's ratio, and preferentially isotropic.

The second step is to determine the values of the contact depth h_c from each of the F_N-h curves resulting from the indentation tests. By observing Figure 2.23.a, one can see that, at $F_{\max}$, h_c is given by:

$$h_c = h_{\max} - h_s \,, \tag{2.17}$$

where $h_{\max}$ and h_s are the displacement of the indenter at $F_{\max}$ (or the maximum displacement during the indentation test) and the displacement of the surface at the contact perimeter, respectively. The maximum displacement can be directly extracted from the F_N-h curve (Figure 2.23.b). The displacement of the surface at the contact perimeter depends on the indenter geometry and is given by [74]:

[•] For instance, the production of a Vickers indenter with a point-ended tip is difficult and usually a edge-ended tip is obtained [131], as a result of the intersection of the four faces of the square pyramid along a line instead of a point.

$$h_s = \varepsilon \frac{F_{\max}}{S_c}, \tag{2.18}$$

where ε is a geometric constant equal to 1 for a flat punch, 0.75 for a paraboloid of revolution and 0.72 for a conical indenter. The contact stiffness is calculated by using Eq. 2.14, where S is retrieved from the unloading curve by using one of the two methods described previously and C_m is the machine compliance value determined previously. The contact depth can then be determined by combining Eqs. 2.17 and 2.18:

$$h_c = h_{\max} - \varepsilon \frac{F_{\max}}{S_c}, \tag{2.19}$$

and, for the case of the flat punch geometry, it is given by the interception of the line tangent to the initial portion of the unloading curve with the horizontal axis of the F_N-h curve (Figure 2.23.b). For reasons of geometry similarity between the conospherical and paraboloid geometries, a value of ε = 0.75 was used in the analysis of the displacement sensing nanoindentation (DSN) results.

The third step of this method is to determine the projected area of all the indentations performed in the material with known Young's modulus and Poisson's ratio, which can be done by solving Eq. 2.9 in relation to A_p:

$$A_p = \frac{\pi}{4}\left(\frac{S_c}{E_r}\right)^2, \tag{2.20}$$

where E_r can be determined from Eq. 1.2 since the elastic properties of the indenter and sample are known.

Finally, a plot of the projected areas against the correspondent contact depths is made and the points are fitted with a polynomial function of the type [74]:

$$A_p = C_0 h_c^2 + C_1 h_c + C_2 h_c^{1/2} + C_3 h_c^{1/4} + C_4 h_c^{1/8} + C_5 h_c^{1/16}, \tag{2.21}$$

where C_i (i = 0, ...,5) are geometrical coefficients. In the case of an ideal Vickers indenter C_0 = 24.5 and the remaining C_i coefficients are zero, while for an ideal spherical indenter of radius

R, $C_0 = -\pi$, $C_1 = 2\pi R$ and the remaining coefficients are zero. In real indenters the null coefficients are different from zero and reflect the geometrical imperfections of the indenter.

The method just described was applied using a finely polished fused silica standard. Several indentations were performed in this sample with the conospherical indenter and loads in the range 0.05 to 14.5 mN. By introducing both the elastic properties of the diamond indenter and of the sample (E = 72 GPa; ν = 0.17 [74]) in Eq. 1.2, a value of E_r = 69.6 GPa is obtained. After determining the values of h_c and A_p for all the indentations, the (h_c, A_p) points were fitted with Eq. 2.21 and the following area function for the conospherical indenter was obtained:

$$A_p = -3.14h_c^2 + 23314h_c - 969440h_c^{1/2} + 7859000h_c^{1/4} - 17365000h_c^{1/8} + 10441000h_c^{1/16}. \quad (2.22)$$

Figure 2.27.a shows the experimental (h_c, A_p) points retrieved from the indentation tests in fused silica, the area function determined for the conospherical indenter and the area function of an ideal spherical indenter with R = 1 μm ($A_p = 2\pi R h_c - \pi h_c^2$). It can be observed that the experimentally determined area function deviates significantly from that of the ideal spherical indenter. This deviation can be attributed to small variations of the curvature radius, scratches at the tip surface of the indenter and deviations from axisymmetry [144], as can be observed from the AFM image of a nanoindentation in Figure 2.27.b. Figure 2.27.c shows the values of H_i and E of fused silica, calculated after determining the area function. The drop in H_i and E for contact depths smaller than 50 nm can be due to a poor description of the area function at these shallow depths, where the influence of tip imperfections is larger. Therefore, DSN data resulting from tests where the contact depth is smaller than 50 nm was not considered in this work. For contact depths larger than 50 nm, average values of 9.8 ± 0.2 GPa and 72.0 ± 0.6 GPa were obtained, respectively, for H_i and E of fused silica. The good agreement between the experimental values of H_i and E and those given by Hysitron [135] (horizontal lines in Figure 2.27.c) shows that the deviation of the indenter shape from axisymmetry is not significant to the determination of H_i and E and supports the approximation of the constant β_i in Eq. 2.10 to unity.

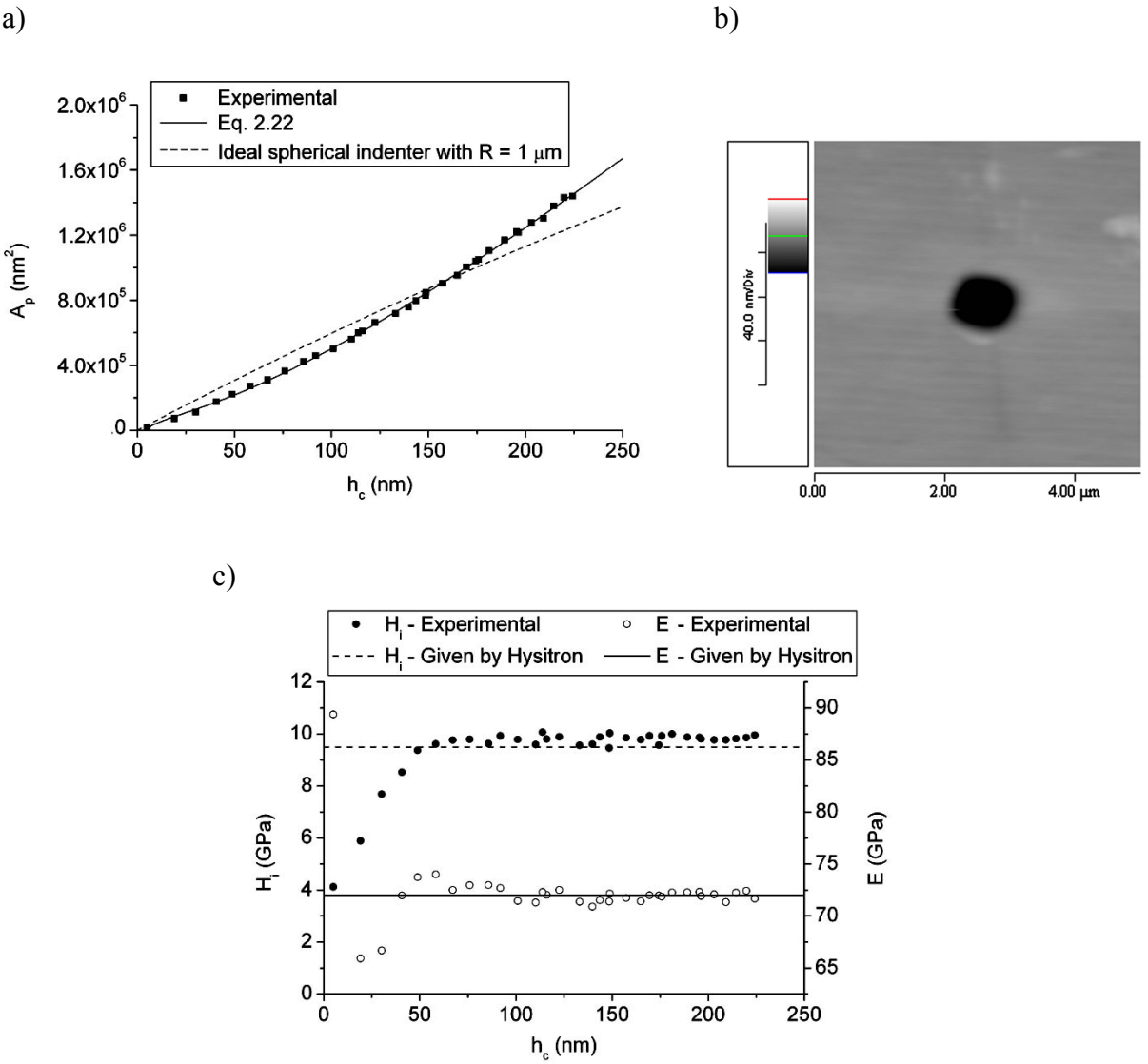

Figure 2.27. a) Fitting of A_p versus h_c experimental data retrieved from DSN tests in a fused silica standard with Eq. 2.21. The area function of an ideal spherical indenter with R = 1 μm is also shown for comparison. b) AFM image of a nanoindentation performed in fused silica with the conospherical indenter, using a load of 14.5 mN. The shape of the nanoindentation clearly shows that the conospherical indenter is not totally axisymmetric. c) Values of H_i and E of fused silica obtained after determining the indenter area function. The values of H_i and E given by Hysitron are also shown for comparison.

In ultramicroindentation tests, the method used by the software Hardness 5.0 to determine A_p was proposed by Antunes *et al*. [131] and is based on the direct observation of the indenter shape by AFM and on the area function of an ideal Vickers indenter:

$$A_p = 24.5h_c^2 \ . \tag{2.23}$$

The AFM topographic image of the indenter enables determining the cross-section area of the indenter (which corresponds to A_p if it is assumed that the indenter is rigid) as function

of the distance from the tip of the indenter (which corresponds to h_c if it is assumed that the indenter is rigid). The idea is to calibrate the depth measured with an ideal indenter (h_{AFM}) in relation to the depth measured with the real indenter (h_c), which can be done by using:

$$h_{AFM} = \sqrt{\frac{A_p}{24.5}}, \tag{2.24}$$

where several A_p values are retrieved from the AFM image of the indenter for the corresponding h_c values (see Figure 2.28.a). By plotting the h_{AFM} values (obtained from the A_p values by using Eq. 2.24) against the corresponding h_c values, and fitting the points with a function of the type:

$$h_{AFM} = -k_1\left[\exp\left(-h_c\frac{k_2}{k_1}\right)-1\right]+k_3h_c, \tag{2.25}$$

the geometric constants k_1, k_2 and k_3 can be determined (Figure 2.28.b). By using this procedure, Antunes *et al*. [131] found the following values of the constants for the Vickers indenter used in the ultramicroindentation tests: k_1 = 0.050 μm, k_2 = 2.034 and k_3 = 1.023. By replacing h_c in Eq. 2.23 by h_{AFM} (Eq. 2.25), the area function for the real Vickers indenter is obtained:

$$A_p = 24.5\left[-0.05\left[\exp\left(-h_c\frac{2.034}{0.05}\right)-1\right]+1.023h_c\right]^2. \tag{2.26}$$

When a DSI test is performed with this indenter, h_c is first determined by using Eq. 2.19 and then introduced in Eq. 2.26 to obtain A_p. The indentation experiments with a Berkovich indenter performed in several materials by Oliver and Pharr [74] showed that the unloading behaviour of the material, when using this indenter geometry, is best described by the paraboloid geometry and, consequently, a value of ε = 0.75 should be used in Eq. 2.19 to determine h_c. Because the Vickers indenter is also pyramidal and has the same area function as a Berkovich indenter ($A_p = 24.5h_c^2$), a value of ε = 0.75 was used for the determination of h_c in the ultramicroindentation tests.

a)

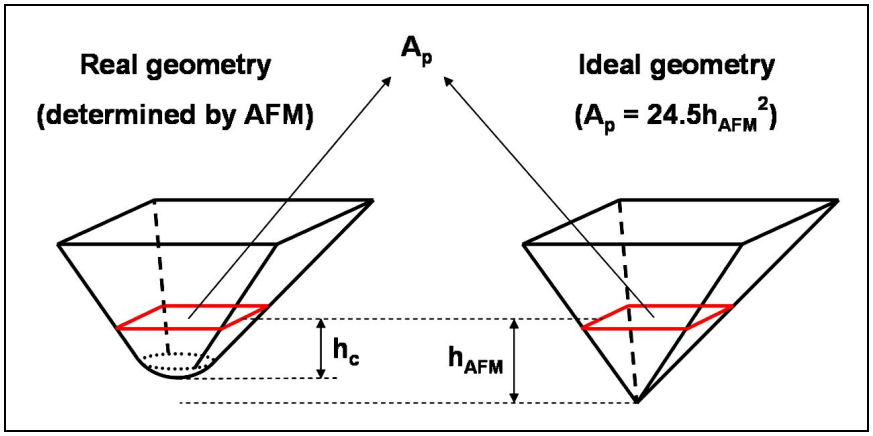

b)

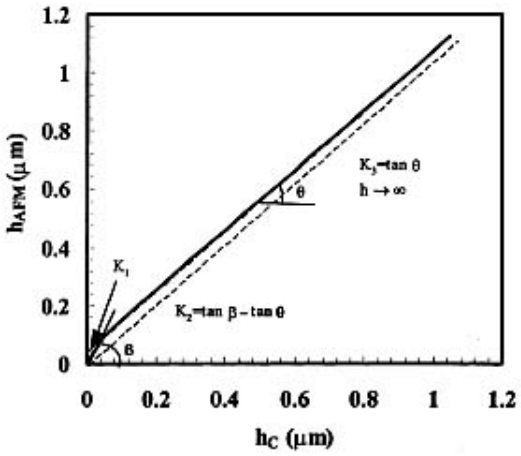

Figure 2.28. a) Schematic representation of the real and ideal Vickers geometries. The area A_p measured from the AFM image of the real indenter for a depth h_c is only obtained in the ideal indenter at a depth h_{AFM}. b) Results of Antunes *et al*. [131] for the correction of the contact depth based on AFM visualization of the indenter. The solid line represents Eq.2.25, whereas the dashed line corresponds to the situation where the real and ideal geometries are equal.

To summarise, in both nano- and ultramicroindentation displacement sensing tests, once the machine compliance and the indenter area function are determined, the hardness and the reduced Young's modulus (and hence the Young's modulus, if the Poisson's ratio of the sample is known) of the tested sample can be calculated by using Eqs. 2.7 and 2.9, respectively. The only parameters that must be retrieved from the F_N-h curves are S and h_{max} (Figure 2.23.b), which are used to determine S_c and h_c by using Eqs. 2.14 and 2.19, respectively. A_p is determined by introducing the value of h_c in Eqs. 2.22 and 2.26, respectively, in the case of nano- and ultramicroindentation tests.

2.3.1.3. AFM cantilever-based indentation

From all the used indentation techniques, indentation with an AFM probe is the one that enables applying the lowest loads. The AFM cantilever-based nanoindentation tests that were used to extract the indentation hardness of the samples were carried out with a maximum load of 57 μN. The principle of this technique is the same as that for the acquisition of AFM force-displacement (FD) curves (Figure 2.29) [145]. In this process the tip is approached to and retracted from the sample's surface, perpendicularly to the surface, without any surface scanning. In the beginning the tip is moved towards the sample and the cantilever is not deflected since there are no interaction forces between tip and sample (1). When the tip is extremely close to the surface the interatomic attractive forces between the atoms of the tip and the atoms of the sample pull the tip towards the sample, causing the cantilever to bend towards the sample (2). By further approaching the tip to the sample the repulsive forces between the atoms of both surfaces increase and the cantilever is bent in the opposite direction (3) until reaching a certain value of deflection chosen by the operator (4). Afterwards, the tip is withdrawn from the sample and the repulsion decreases and, consequently, the cantilever deflection too (5). However, at position (2), the tip does not immediately jump off contact from the sample due to the influence of the tip-sample adhesive forces (e.g. chemical bonds, wrap of sample material around the tip, capillary forces), and the cantilever is bent towards the sample by further pulling the tip from the sample (6). When the force applied to remove the tip from the sample (pull-off force) is larger than the adhesive forces that keep tip and sample together, the tip jumps off contact (7) and the cantilever re-acquires its rest position (8).

However, in AFM nanoindentation the applied loads must be much larger than those used for imaging. In this way, stiffer cantilevers and harder tips are required. In this work two DNISP nanoindentation probes (manufactured by Veeco) mounted in a DI Multimode Extended atomic force microscope were used for the nanoindentation tests. These probes consist on three-sided diamond pyramids (plus a residual bottom) mounted on stainless steel cantilevers and their characteristics are presented in Table 2.2. A schematic drawing of these probes can be seen in Figure 2.30.a, while in Figures 2.30.b and c SEM images of one of the probes used in this work are shown. The two main features of these probes are the large stiffness of the cantilever and the large hardness of the tip, which make them more adequate to perform nanomechanical tests (e.g. nanoindentation, nanoscratching and nanowear) than Si or Si_3N_4 probes. It should be mentioned that DNISP probes also enable imaging the sample in tapping and contact mode, before and after the tests.

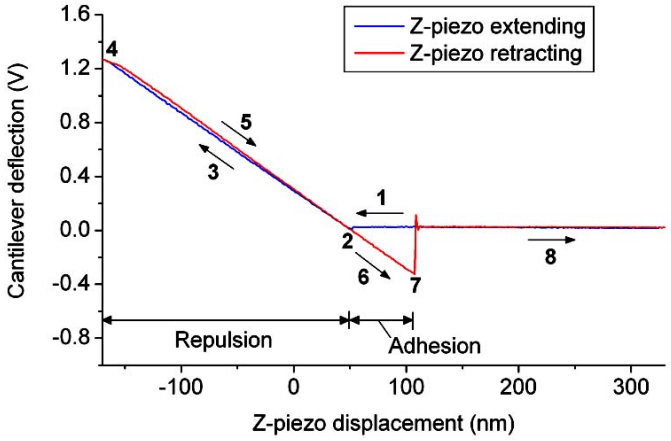

Figure 2.29. Force-displacement curve obtained in AFM contact mode. The vertical axis represents the normal deflection of the cantilever (in V units), which is proportional to the vertical displacement of the laser beam on the photo-detector, while the horizontal axis represents the displacement of the piezoelectric scanner in the *Z* direction (direction normal to the sample's surface).

Table 2.2. Characteristics of the DNISP nanoindentation probes manufactured by Veeco [115]. The tip angle is the angle between a face and the opposite edge of the pyramid. The values of tip radius, cantilever spring constant and resonant frequency are given by Veeco, while all other values were measured from SEM images of the probes.

Model	DNISP (probe 1)		DNISP (probe 2)	
Part	cantilever	tip	cantilever	tip
Material	stainless steel	diamond	stainless steel	diamond
Geometry	rectangular	triangular pyramid	rectangular	triangular pyramid
Dimensions	$l \sim 386$ µm $w \sim 111$ µm $t \sim 13.3$ µm	$h \sim 41$ µm tip angle ~ 95º $R < 50$ nm	$l \sim 398$ µm $w \sim 112$ µm $t \sim 13.4$ µm	$h \sim 41$ µm tip angle ~ 93º $R < 50$ nm
Normal stiffness	$c_n = 215.8$ N/m	—	$c_n = 256$ N/m	—
Resonant frequency	$f_0 = 70$ kHz		$f_0 = 70$ kHz	

l – length; w – width; t – thickness; h – height; R – tip curvature radius; c_n – normal spring constant.

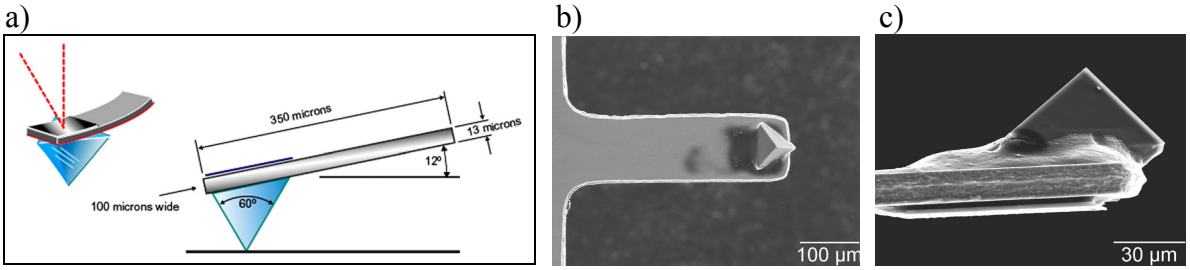

Figure 2.30. a) Schematic drawing of Veeco DNISP nanoindentation probe [146]. Although it is mentioned on the nanoindentation manual from Veeco that the apex angle of these tips is of 60º, SEM observations of both tips showed that the angle is of ~ 90º. b) SEM image of Veeco DNISP probe 1, showing the triangular pyramid tip viewed from top. c) SEM image of the same probe, showing the triangular pyramid tip viewed from side, where the apex angle of ~ 95º can be seen.

The software that controls the atomic force microscope – Nanoscope III (trademark of Veeco) – enables to compensate the lateral motion of the tip that occurs during AFM cantilever-based nanoindentation tests [147], which is a major source of error in these tests and will be explained some paragraphs below. However, the control software does not allow maintaining the sample under the influence of maximum load for a period of time, i.e. the sample is immediately unloaded after the maximum load is reached.

When performing nanomechanical tests with AFM probes some procedures must be followed in order to minimize instrumentation and measurement errors [147]. Similarly to what happens when visualizing a sample by AFM contact mode, in an AFM indentation test the load applied by the tip on the sample must be chosen by the operator. As previously mentioned in §2.2.1, the deflection of the cantilever produces a movement of the laser beam which is reflected from the backside of the cantilever, along the vertical direction of the photo-detector leading to a certain voltage value measured by the detector. In order to determine the applied load it is necessary to determine the cantilever sensitivity (S_z), i.e. the distance that the scanner has to move in the Z direction in order to produce a cantilever deflection of 1 V [146]. This parameter is given in nm/V units and corresponds to the inverse of the slope of the repulsion portion of a FD curve (see Figure 2.29)•. In order to correctly determine S_z, a hard and rigid sample such as sapphire must be used so that sample deformation effects are minimized. Every time the probe is moved on the probe support or the laser beam is repositioned on the cantilever the sensitivity changes and needs to be re-determined. Once S_z is known, the load can be calculated by:

$$F_N = c_n S_z \Delta Z_V , \tag{2.27}$$

where ΔZ_V is the cantilever deflection measured in volts by the photodetector. The spring constant value of each individual DNISP nanoindentation probe is measured by the manufacturer with an accuracy of ± 10% [146].

Typical piezoelectric scanners used in atomic force microscopes exhibit nonlinear behaviours. In particular, hysteresis and creep can affect the indentation test measurements if not properly controlled [147]. When the voltage applied to the piezoelectric scanner is increased to a certain value and then decrease back to zero, the extension and retraction of the

• Some authors [147] consider the sensitivity to be given by the slope of the repulsion portion of the FD curve and, consequently, to have V/nm units.

piezo may not follow the same path, i.e. the variation of the piezo displacement with the applied voltage is not linear and there is some hysteresis between the two ways (extension and retraction). Creep consists on a slow time-dependent displacement of the piezo after an initial fast displacement when a voltage is applied. A detailed analysis of these nonlinearities made by VanLandingham [147] showed that: for the typical range of voltages applied to the piezoelectric scanner in nanoindentation tests (< ± 10 V), hysteresis of piezoelectric scanners leads to errors in the displacement of less than ± 1nm; creep of the scanner in the *Z* direction is the most significant nonlinearity in quantitative nanoindentation measurements.

In the present work, the influence of creep of the piezoelectric scanner of the Multimode atomic force microscope on indentation measurements was evaluated by performing several indentation tests with different force curve scan rates (speed, in Hz, at which the cantilever/sample is loaded and unloaded during indentation) in a Ni-31%Co alloy (ductile) and sapphire (rigid, brittle) and observing the shape of the resulting FD curves. Scan rates of 8, 6, 4, 2, 1, 0.1, 0.05, 0.02 and 0.01 Hz were used in the tests.

It was observed that, for this microscope, the minimum value that should be used in order to avoid the influence of creep of the scanner on the nanoindentation tests is 2 Hz. Lower values of the scan rate generate anomalies on the FD curves. Figures 2.31.a and b show FD curves resulting from indentation tests performed in the Ni-31%Co alloy with scan rates of 2 and 0.01 Hz (minimum value allowable by the apparatus), respectively. The applied load was 54 μN in both cases. When a scan rate of 2 Hz was used, the FD plot presented a normal shape with a small hysteresis between the extended and retracted curves due to the plastic deformation of the sample (Figure 2.31.a). However, when smaller scan rates were used the hysteresis between the two curves decreased and, for values smaller than 0.1 Hz, the relative position of the two curves changed (Figure 2.31.b). This effect was previously observed by Hues *et al*. [148] and is an instrumentation artifact caused by hysteresis and creep of the piezoelectric scanner during load application. These authors named this effect of *reverse-path effect*. In the nanoindentation tests conducted in sapphire a load of only 2 μN was used in order to avoid tip wear. No hysteresis between the extended and retracted curves of the FD plots was observed, which means that the sample was only deformed elastically. When the tests were carried out using a scan rate value of 2 Hz (Figure 2.31.c) or higher, the FD curves showed a normal shape except for the small undulations which are probably caused by a stick-slip phenomenon of the tip on the sample. However, for smaller scan rate values this stick-slip of the tip is largely increased (Figure 2.31.d), which will affect the tests. Higher

scan rate values correspond to larger indenter displacement speeds and, consequently, to smaller time periods for accommodation of plastic deformation in the material.

In this way, all AFM nanoindentation tests performed in the samples from the Ni-Co system were carried out using a scan rate of 2 Hz.

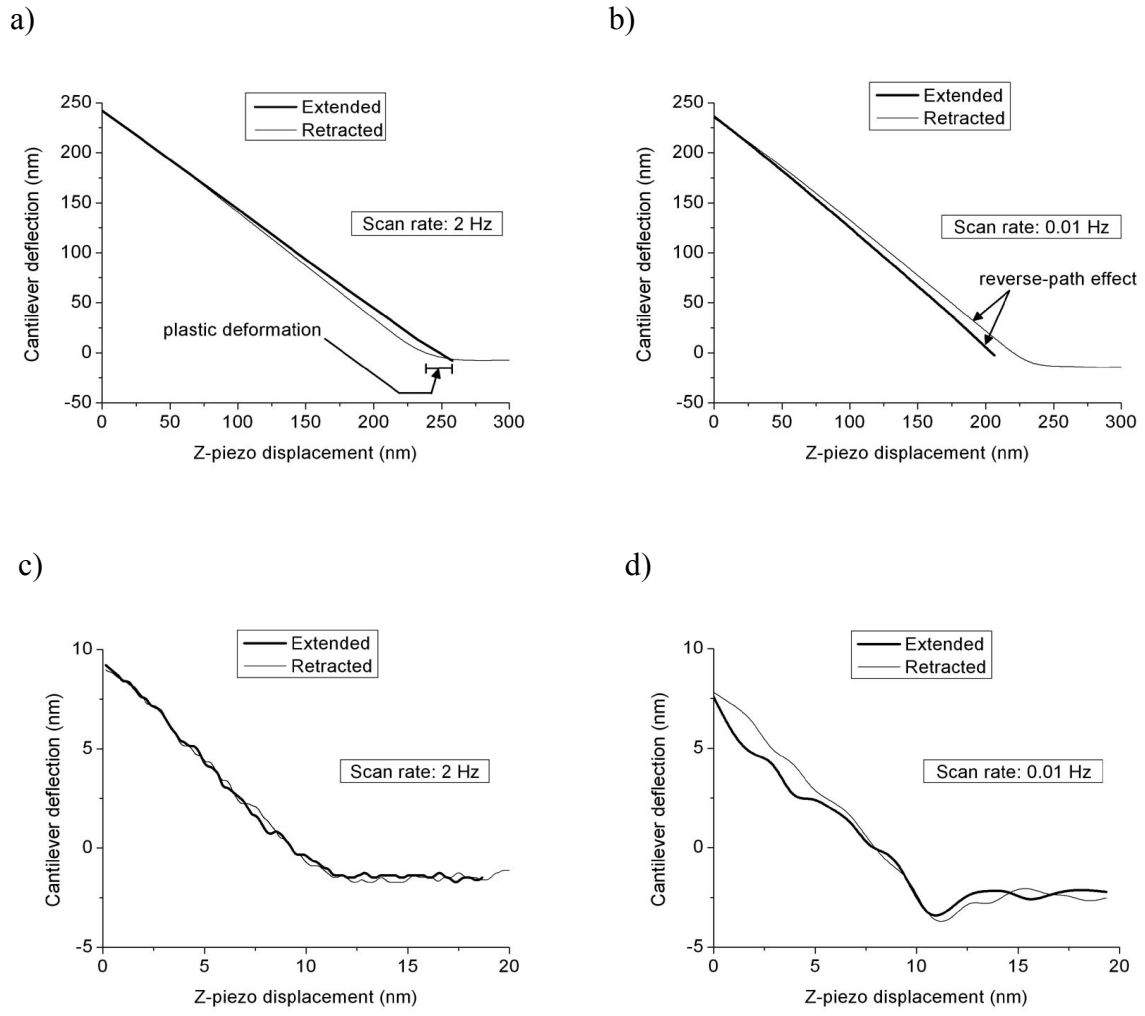

Figure 2.31. Force-displacement curves resulting from AFM indentation tests performed on: Ni-31%Co (a and b) and sapphire (c and d). The extended curves of the plots in a) and b) are cut near the region where contact occurs. The plots on the left and right sides result from tests where scan rates of 2 and 0.01 Hz, respectively, were used.

The lateral motion of the tip during the AFM cantilever-based nanoindentation test can be a non-negligible error source [147] (Figure 2.32.a). If a point load is applied at the tip, not only the cantilever will bend but the tip will also move laterally, in the positive direction of the axis of the cantilever (direction towards the tip). However, when the tip contacts the sample and is pushed against the sample, friction between tip and sample, local deformation

of the sample and/or the presence of surface roughness will restrict the lateral movement of the tip, generating a lateral reaction force at the sample's surface that pushes the tip in the opposite direction and, consequently, forces the cantilever to bend in the direction opposite to the usual bending direction in an indentation test. As consequence, the axis of the pyramid will no longer be perpendicular to the sample's surface, invalidating the indentation test. This feature of cantilever-based indentation can be corrected by slightly moving the cantilever in the negative direction of the axis of the cantilever (direction away from the tip) or the sample in the opposite direction, in order to keep the axis of the pyramid perpendicular to the sample's surface during the test. This movement is performed at the cantilever or at the sample depending on the location of the scanner in the microscope (in the probe support or under the sample, respectively), as discussed in §2.2.1.

The software Nanoscope III contains a parameter called *X Rotate* (Γ) that enables moving the scanner during the test in order to compensate the lateral motion of the tip. This parameter corresponds to the angle of rotation of the tip during the indentation process [147]:

$$\Gamma = \tan^{-1}\left(\frac{\Delta x_p}{\Delta z_p}\right), \tag{2.28}$$

where Δx_p and Δz_p are, respectively, the lateral compensating movement (in the ideal case, equal to the lateral movement of the tip Δx_t) and the vertical displacement of the piezoelectric scanner (Figure 2.32.b).

The amount of tip lateral motion compensation will essentially depend on the geometry of the probe being used. In order to optimize this parameter for the application of the DNISP probe, several indentation tests with a load of 54 μN, a scan rate of 2 Hz and different values of Γ (0º, 5º, 10º, 15º, 20º, 25º, 30º, 35º, 40º) were performed in a Ni-31%Co alloy and can be seen in Figure 2.32.c. From this figure it is possible to conclude that Γ values in the range 15º to 35º minimize pile-up effect around the indentations, which means that the load is effectively applied perpendicularly to the sample's surface.

A Γ of 22º, which is within this range and is the value recommended by the probe's manufacturer [146], was used in all AFM nanoindentation tests performed in the samples from the Ni-Co system.

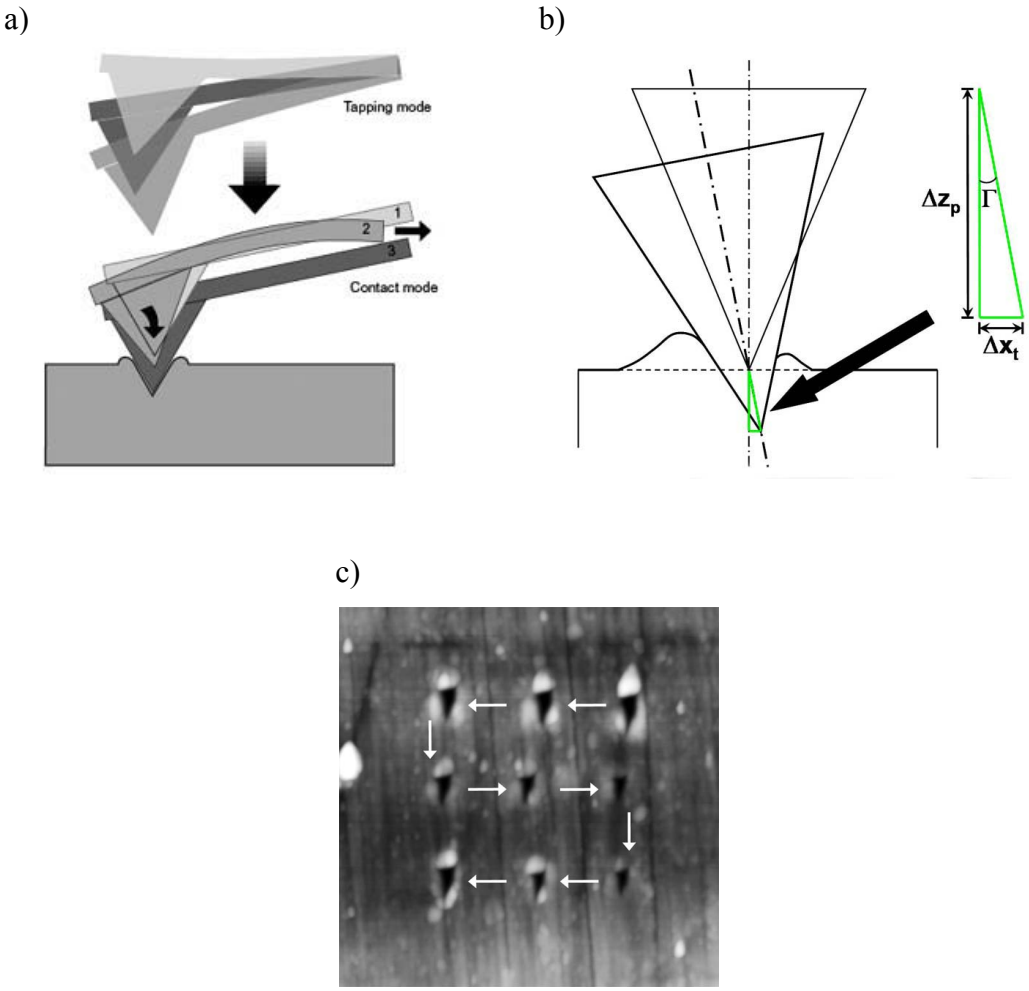

Figure 2.32. a) Schematic drawing showing the lateral motion of the tip during an indentation test [146]. The tip approaches the surface in tapping mode and immediately stops vibrating once contact occurs. At first contact with the sample's surface the tip is oriented normally to the surface (1); however, as the tip is pressed against the surface, it tends to pitch forward (2); by slightly pulling the cantilever in the negative direction of the axis of the cantilever (black arrow pointing right) or the sample in the opposite direction, the tip is brought to its non-rotated position (3). b) Sketch of tip before and after indentation, where the scanner moves vertically a distance Δz_p and the tip moves laterally, under the influence of a lateral reaction force at the sample's surface, a distance Δx_t. The angle Γ corresponds to the tip lateral motion compensation parameter that exists in the Nanoscope III software. c) AFM topographic image (2.5 × 2.5 μm^2; *Z* range = 50 nm) of nanoindentations performed in a Ni-31%Co alloy. A load of 54 μN and a scan rate of 2 Hz were used and the *X Rotate* parameter was increased in the direction of the white arrows: 0º, 5º, 10º, 15º, 20º, 25º, 30º, 35º, 40º.

Errors arising from the visualization of test features with the AFM tips may also affect nanoindentation results. An AFM topographic image results from the convolution (also known as dilation) of the surface topography by the tip shape, where peaks and bumps are broadened while holes and valleys are shrunk (Figure 2.33). Convolution becomes significant whenever the scanned surface contains features with aspect ratios comparable to that of the tip. Most of the nanoindentations performed in this work were visualized with the same tip that was used to perform them, i.e. the DNISP tip. Consequently, convolution may affect the AFM

topographic images of the indentations to some extent, leading to underestimates of their projected areas, especially at the vertices of the triangle. One good way of minimizing this effect is to use a sharp Si tip to visualize the indentations. However, this process is unacceptably time consuming, because it is necessary to locate the nanoindentations with the new tip. A more efficient way is to use an image deconvolution software that uses the tip geometry to deconvolute the AFM image. A software well known among the SPM community is the scanning probe image processor (SPIP – trademark of Image Metrology), which uses the *blind reconstruction method* (BRM) [149-152] to estimate the tip shape from an AFM topographic image of an unknown tip characterizer sample, enabling afterwards to deconvolute AFM images obtained with that tip.

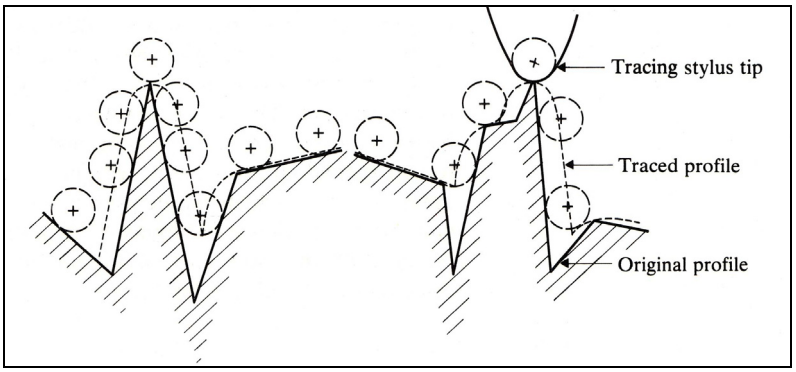

Figure 2.33. Image convolution due to the finite dimensions of the scanning tip [153]. The AFM topographic profile of the surface corresponds to the dashed profile, which results from a morphological dilation of the surface topography by the tip shape.

AFM images of nanoindentations performed in the Ni-Co samples were deconvoluted by using the software SPIP 3.3, after determining the tip shape with the BRM. Figures 2.34.a and b show an AFM image of nanoindentations performed in Ni, respectively, before and after deconvolution. Surprisingly, it can be observed that the deconvolution process slightly bends the edges of the triangular areas of the indentations (Figure 2.34.b). The observation of these nanoindentations with a sharper Si tip (Figure 2.34.c) clearly shows that the real shape of the indentations is much closer to that seen in the convoluted image than in the deconvoluted one, which means that the curved edges produced by the deconvolution process are artifacts. In this way, only convoluted images were used to obtain AFM nanoindentation results in this work. Nevertheless, the influence of image convolution on the results was analysed by comparing nanoindentation hardness values retrieved from a few images of nanoindentations obtained with a DNISP tip and with Si tips (see §4.1.1).

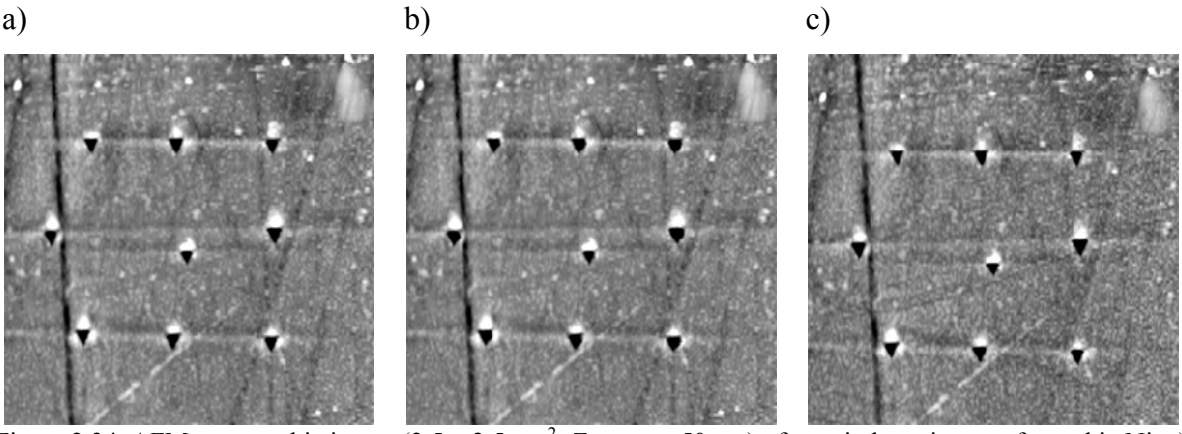

Figure 2.34. AFM topographic image (2.5 × 2.5 μm^2; *Z* range = 50 nm) of nanoindentations performed in Ni: a) obtained with the DNISP tip; b) same as (a) but after deconvolution with the software SPIP 3.3; c) obtained with a Si tip.

The projected area of the nanoindentations was determined by using the commercial image analysis software Mocha (trademark of former Jandel Scientific), which enables performing flood fill measurements of objects in an image. An example of this process applied to an AFM image of nanoindentations can be seen in Figure 2.35. In order to measure the area of an object, a 2-point spatial calibration of the image must be previously performed, which consists on defining the spatial dimensions of the pixels. This can be done by dividing the scan size of the AFM image by the horizontal (or vertical, since AFM images are squared) length of the image given in number of pixels units. When the object is defined with the flood fill process, the areas of all pixels that form the object are summed to obtain the total area of the object. Finally, once the project area of a nanoindentation is determined, the indentation hardness can be calculated by using Eq. 2.7.

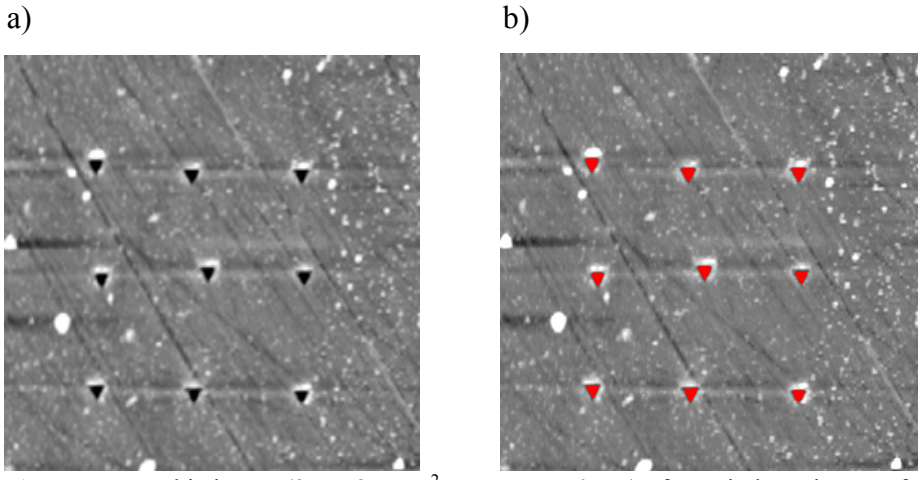

Figure 2.35. AFM topographic image (2.5 × 2.5 μm^2; *Z* range = 50 nm) of nanoindentations performed in Ni-42%Co, before (a) and after (b) the flood fill measurement with the software Mocha. The red areas in (b) correspond to the projected areas of the nanoindentations in (a).

2.3.2. Scratching

Low-speed scratch tests were used to determine the scratch hardness of the samples. In these tests an indenter is pressed against the surface of the tested material with a constant load and moved laterally at constant speed. This lateral movement may be single pass, reciprocating or multiple pass, as shown in Figure 2.36 [154].

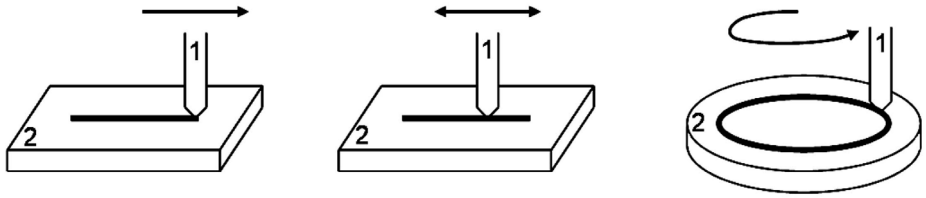

Figure 2.36. Schematic drawings of the possible movements of the indenter (1) in a low-speed scratch test: single pass (left), reciprocating (middle) and multiple pass (right). The thick dark lines represent the scratch made in the sample (2), while the arrows indicate the direction of motion of the indenter.

The scratch hardness, H_s, is expressed in terms of the scratch width, w, as:

$$H_s = \eta \frac{F_N}{w^2}, \tag{2.29}$$

where F_N is the applied normal load and η is a constant that depends on the indenter geometry. For an indenter of circular cross-section area (cone, sphere, paraboloid) $\eta = 8/\pi$ [154], for square-base pyramids of leading edge or leading face orientation $\eta = 4$ [154], and for the DNISP tip used in the nanoscratch tests it can be demonstrated that $\eta = 4.786$ (see §2.3.2.2). Due to the uncertainty on the exact location of the perimeter of the contact between the sliding indenter and the material, it was assumed in this work that, during the scratch test, the perimeter is located at the surface mean line. In this way, w is measured at the surface mean line (Figure 2.37) and, consequently, the influence of pile-up or sink-in on the contact area is neglected. In order to avoid start and stop effects from the scratch tests, only the centre portion of the scratches was used for the determination of w.

In the present work two types of scratch tests were performed: microscratching with a CSEM Revtest apparatus and AFM cantilever-based nanoscratching. Single pass scratches (Figure 2.36, left) were made in the direction of the laser clad tracks and height profiles were retrieved from the scratches. Details concerning each type of scratch test are given in the following two sections.

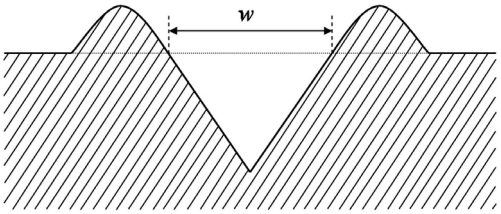

Figure 2.37. Drawing of the cross-section of a scratch showing the width of the scratch (*w*) as considered in this work.

2.3.2.1. CSEM Revtest

Microscratch tests with a nominal normal load of 20 N, a scratching speed of 10 mm/min and a scratch length of 10 mm, were performed with a CSEM Revtest apparatus and a Rockwell C indenter (diamond cone with included angle of 120º) with nominal tip radius of 100 μm. Due to some sample inclination resulting from grinding/polishing of the surface, a variation in the applied normal load that can go up to ± 10 N occurred during the tests. This problem cannot be avoided during the microscratch tests due to the lack of a feedback mechanism that keeps the applied load constant.

A Rodenstock RM600 optical profilometer was used to retrieve several cross-section profiles of the produced scratches, from which the widths of the scratches were determined. The microscratch hardness of the material was calculated by using Eq. 2.29, with $\eta = 8/\pi$.

2.3.2.2. AFM cantilever-based scratching

Nanoscratch tests with a nominal normal load of 69 μN, a scratching speed of 3 μm/s and a scratch length of 3 μm, were performed with a DI Multimode Extended atomic force microscope and a DNISP probe (probe 2 in Table 2.2). The scratches were performed in the direction of the long axis of the cantilever, with the tip moved in the direction of the front edge of the pyramid, as shown in Figure 2.38.a. In this way, contact between indenter and material only occurs at the two front faces of the pyramid (dark areas at the bottom part of Figure 2.38.a).

The nanoscratches were visualized in tapping mode with this probe. Similarly to the case of nanoindentations, the AFM topographic images of nanoscratches were also affected by convolution from the tip shape. The influence of image convolution on the results was analysed by comparing nanoscratch hardness values retrieved from a few images of nanoscratches obtained with the DNISP tip and with Si tips (see §6.1.1). Similarly to what occurs in microscratch tests, sample inclination can lead to a variation up to ± 12 μN in the

applied normal load because the feedback mechanism, which keeps the applied load constant during AFM scanning, is disabled during the nanoscratch tests.

The nanoscratch hardness of the material was given by Eq. 2.29, with the corresponding η for the DNISP tip geometry. The apex semi-angles of the DNISP tip are represented in Figure 2.38.b, where the angle between the back face and the axis of the pyramid (β) is ~ 47.5º, and the angle between the front edge and the axis of the pyramid (α) is ~ 45.5º. For the calculation of η, it is assumed that the tip is a perfect pyramid with an equilateral triangular base.

a) b)

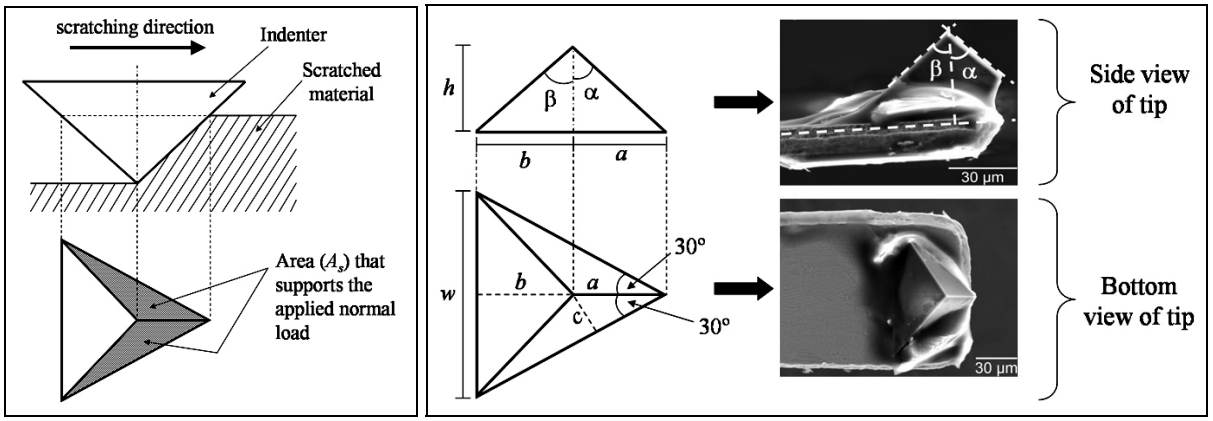

Figure 2.38. a) Schematic drawing of scratching process using the Veeco DNISP tip. The lateral view of the process and the bottom view of the tip are shown, respectively, in the top and bottom parts of the figure. b) Schematic drawing of tip with letters representing its dimensions, and respective SEM images of the DNISP probe 2, where the tip apex angle $\alpha + \beta \approx 93º$ can be seen.

By using simple trigonometric relations, the following equations can be obtained:

$$a = h \tan \alpha , \tag{2.30}$$

$$b = h \tan \beta , \tag{2.31}$$

$$w = \frac{a+b}{\cos 30} . \tag{2.32}$$

By introducing the values of a and b given by Eqs. 2.30 and 2.31, respectively, in Eq. 2.32 and solving this equation in relation to h, the following relation is obtained:

$$h = \frac{\sqrt{3} w}{2(\tan \alpha + \tan \beta)} . \tag{2.33}$$

From Figure 2.38.b results:

$$c = a\sin 30 = \frac{h\tan\alpha}{2}. \tag{2.34}$$

Combining Eqs. 2.33 and 2.34, c can be written as function of w:

$$c = \frac{\sqrt{3}w}{4\left(1+\frac{\tan\beta}{\tan\alpha}\right)}. \tag{2.35}$$

The projected area of contact between indenter and material during the scratch test, A_s, is then given by:

$$A_s = 2\left(\frac{wc}{2}\right) = \frac{\sqrt{3}w^2}{4\left(1+\frac{\tan\beta}{\tan\alpha}\right)}, \tag{2.36}$$

and, finally, the scratch hardness (H_s) can determined:

$$H_s = \frac{F_N}{A_s} = \eta\frac{F_N}{w^2}, \tag{2.37}$$

with

$$\eta = \frac{4}{\sqrt{3}}\left(1+\frac{\tan\beta}{\tan\alpha}\right). \tag{2.38}$$

Replacing the apex semi-angles α and β in Eq. 2.38 by the values retrieved from the SEM image of Figure 2.38.b leads to $\eta = 4.786$ for the DNISP tip.

2.3.3. AFM cantilever-based wear tests

The abrasive wear behaviour of the samples was characterised at the submicrometric contact scale by performing AFM-based abrasive wear tests. The tests were carried out with the DNISP probe 2 (Table 2.2) mounted on the Veeco CP-II atomic force microscope. As in the indentation and scratch tests of this work, the counterbody material was diamond and no lubricant was used in the wear tests.

In AFM-based nanoabrasive wear tests the sample is scanned in contact mode using loads larger than those employed in simple contact mode visualization, in order to generate material removal [36]. A schematic drawing of these tests can be seen in Figure 2.39.

Areas of 2 μm × 2 μm were scanned at a rate of 1 Hz, which corresponds to a scanning speed of 4 μm/s. The resolution of 256 scan lines per image, used in the tests, corresponds to a step size of ~ 7.84 nm (= 2 μm / 255 steps). Only one scan was performed in each test.

Trial tests with the DNISP probe 1 (Table 2.2) and F_N = 10 μN were performed on pure Ni to determine which tip/scanning path orientation generates the largest worn volumes. Figures 2.40.a, b and c show AFM images of worn regions in Ni resulting from the trial tests with different orientations of the tip in relation to the scanning path. The corresponding average horizontal cross-section profiles of the worn regions plus the debris and a small part of unworn material are shown in Figures 2.40.d, e and f, respectively. It can be observed that the largest area of the average horizontal cross-section of the worn region (A_{HCS}, defined in Figures 2.40.d, e and f) is obtained when using the tip/scanning path orientation shown in the schematic drawing of Figure 2.39.b, which corresponds to the case of Figure 2.40.a. The smaller wear efficiency when using the other tip/scanning path orientations can be due to the smaller resistance of the cantilever to normal deflection when the slow scan direction corresponds to the direction pointing from the front edge to the back face of the pyramid (Figure 2.40.b), or due to some cantilever buckling when the fast scan direction is parallel to the long axis of the cantilever (Figure 2.40.c). Therefore, all the wear tests were carried out with the fast scan direction perpendicular to the long axis of the cantilever and the slow scan direction pointing from the back face to the front edge of the pyramid, as illustrated in Figure 2.39.b. Two different normal loads were used in the tests: 2.5 and 15 μN. Sharp Si tips (R < 10 nm) were used to visualize the worn regions in contact-lateral force mode, so that friction differences between worn and unworn regions could be detected.

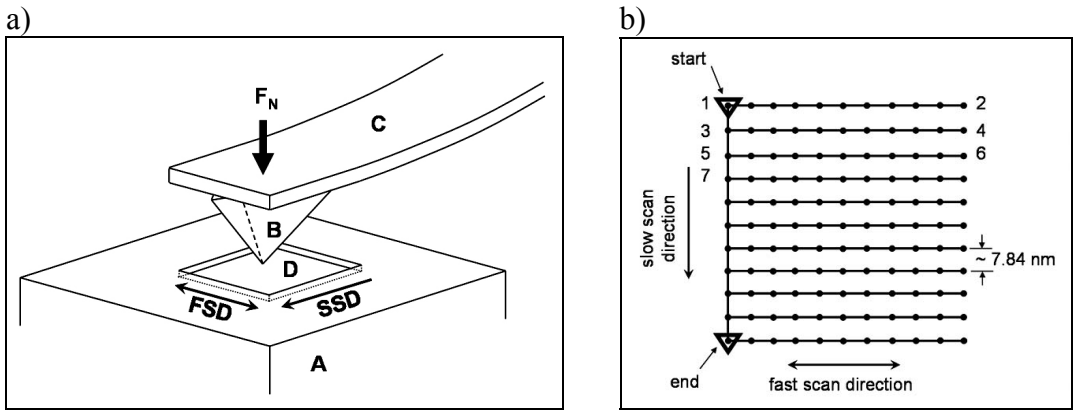

Figure 2.39 a) Schematic drawing of an AFM-based nanoabrasive wear test: A- sample; B – diamond tip; C – cantilever; D – worn region; FSD – fast scan direction; SSD – slow scan direction; F_N – normal load. b) Schematic representation of the raster pattern scanning movement of the AFM scanner, applied in the wear tests. The orientation of the triangular pyramid tip in relation to the scanning path is given by the black triangles at the starting and ending points of the path.

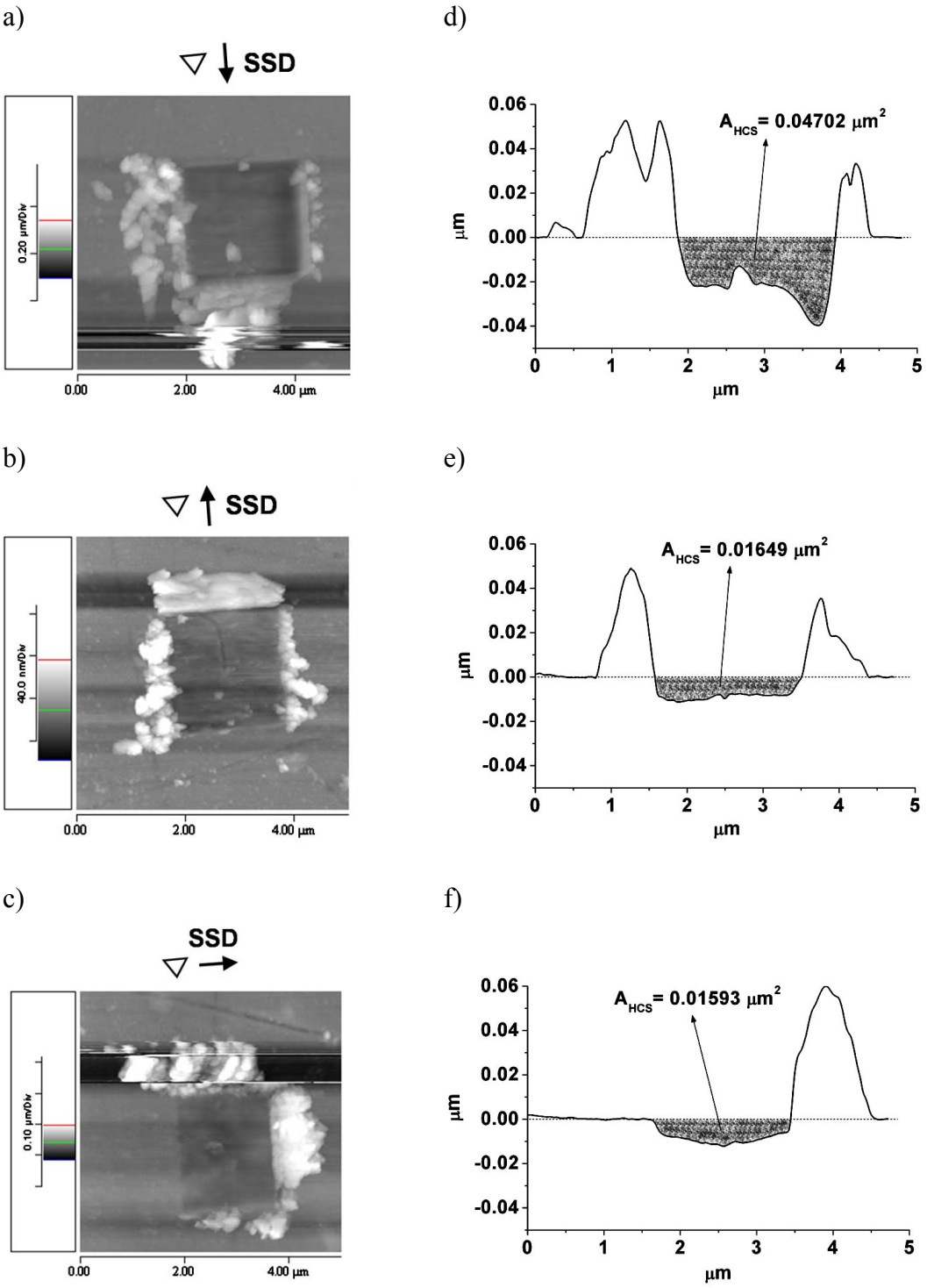

Figure 2.40. AFM topographic images of worn regions in Ni resulting from single scan wear tests with the DNISP probe 1 (a, b and c) and F_N = 10 μN. The slow scan direction (SSD) was different in the three cases and is given by the drawings over the AFM images. Average horizontal cross-section profiles of the worn regions plus the debris and part of the unworn material are shown on the right side of each image (d, e and f). The areas of the average horizontal cross-section of the worn regions (A_{HCS}) correspond to the shaded areas in the profiles.

In order to obtain comparable results of wear tests performed in different samples, it is fundamental to keep the geometry of the abrasive body constant in all tests, regarding that wear of AFM diamond tips used in scratch/wear tests may occur and is more severe when

testing harder samples [155]. In this way, a procedure to minimize the influence of the tip running-in period on the wear tests was adopted in this work, which consisted on performing 100 wear tests with F_N = 20 μN on the Ni-85%Co alloy, which is one of the hardest samples of the Ni-Co system (see §4.1.1 and §6.1.1). The tip radius was estimated every 25 tests by using the blind reconstruction method, applied by the software SPIP, to determine the tip shape from AFM images (see §2.3.1.3).

The variation of the tip radius with the number of wear tests is presented in the plot of Figure 2.41 and shows that R seems to have stabilized after 75 tests. After 100 tests the value of R was in the range 366 to 490 nm and it was assumed that the tip running-in period was over. By comparing this range of R values with the one estimated after performing the wear tests with F_N = 2.5 and 15 μN on Ni, Ni-85%Co and Co (Figure 2.41), it can be concluded that no significant variation of R occurred during the tests on the three samples. SEM images of the tip after the running-in tests on Ni-85%Co can be seen in Figure 2.42. The magnified image of the top of the pyramid (Figure 2.42.b) shows that the tip radius is around 500 nm, which is in good agreement with the values obtained by the blind reconstruction method.

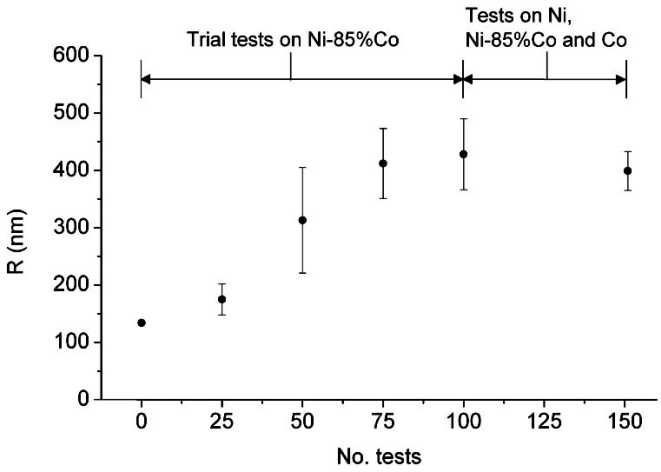

Figure 2.41. Variation of tip radius (R) with number of wear tests. Error bars result from four estimations of R using the software SPIP. The point corresponding to zero tests results from a single estimation of R.

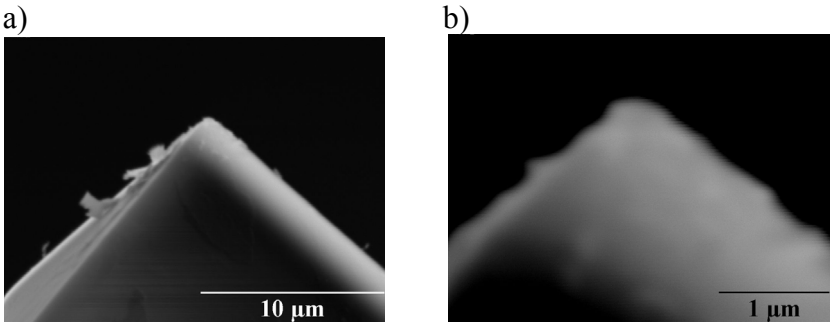

Figure 2.42. SEM images of Veeco DNISP tip after the running-in tests on Ni-85%Co: a) diamond pyramid; b) top of diamond pyramid.

The volume of material removed (V_{worn}) during an AFM-based wear test was calculated by:

$$V_{worn} = A_{HCS} \cdot L_{worn}, \tag{2.39}$$

where the length of the worn region, L_{worn}, was assumed to be equal to the scan size used in the tests, i.e. 2 μm. The area of the average horizontal cross-section of the worn region, A_{HCS}, was determined by numerical integration over the profile of the worn region (see Figures 2.40.d, e and f).

3. TOPOGRAPHY AND STRUCTURE

Experimental results concerning the topographical and structural characterisation of the Ni-Co samples are presented in this chapter. Characterisation of the surface topography and composition is presented first, followed by the determination of the bulk chemical composition of the samples. Then, results concerning the microstructure and substructure of the samples are presented, including a section with dislocation density estimations.

3.1. Topography

The topography of the samples was characterised by AFM using tapping mode. Figures 3.1.a and b show AFM images of mechanically polished (MP) and electropolished (EP) surfaces, respectively. The surfaces contain some nanometric dirtiness (bright particles in the images), which is not removed during sample cleaning with organic solvents, and some microporosity (dark spots). In the case of MP samples, some nanometric scratches also remain after polishing. Although these surface irregularities are few and nanometric, and thus certainly with negligible influence on the results, only relatively clean and flat areas such as that in Figure 3.2 were selected to perform the nanoscale tests.

Five equally spaced horizontal and five equally spaced vertical profiles were retrieved from 10 μm × 10 μm areas to determine the average roughness (R_a)• of the samples. Table 3.1 shows the R_a values of Ni-Co samples prepared with the different surface finishing methods and of a mechanically polished Ni (100) monocrystal••.

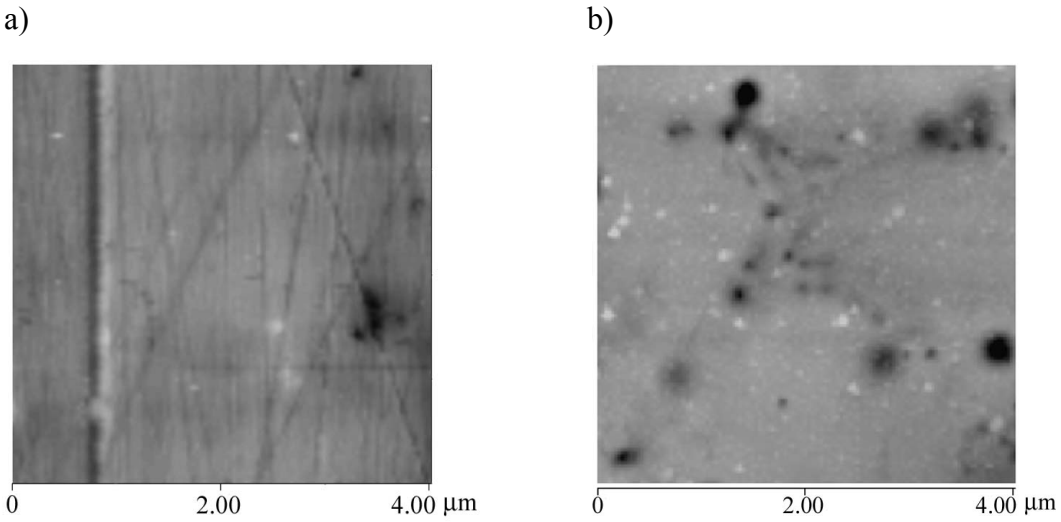

Figure 3.1. AFM topographic images of mechanically polished (a) and electropolished (b) Ni. The *Z* scale in both images is 100 nm. The bright particles in the images correspond to residual dirtiness, whereas the dark spots correspond to micropores. Scratches are only found in the mechanically polished samples and result from the polishing process.

• $R_a = \frac{1}{L}\int_0^L |z(x)|dx$, with $z(x)$ the surface envelope function and L the profile length, can be defined as the average deviation of the surface asperities from the surface mean line [153].

•• Used in the experiments of §4.2.

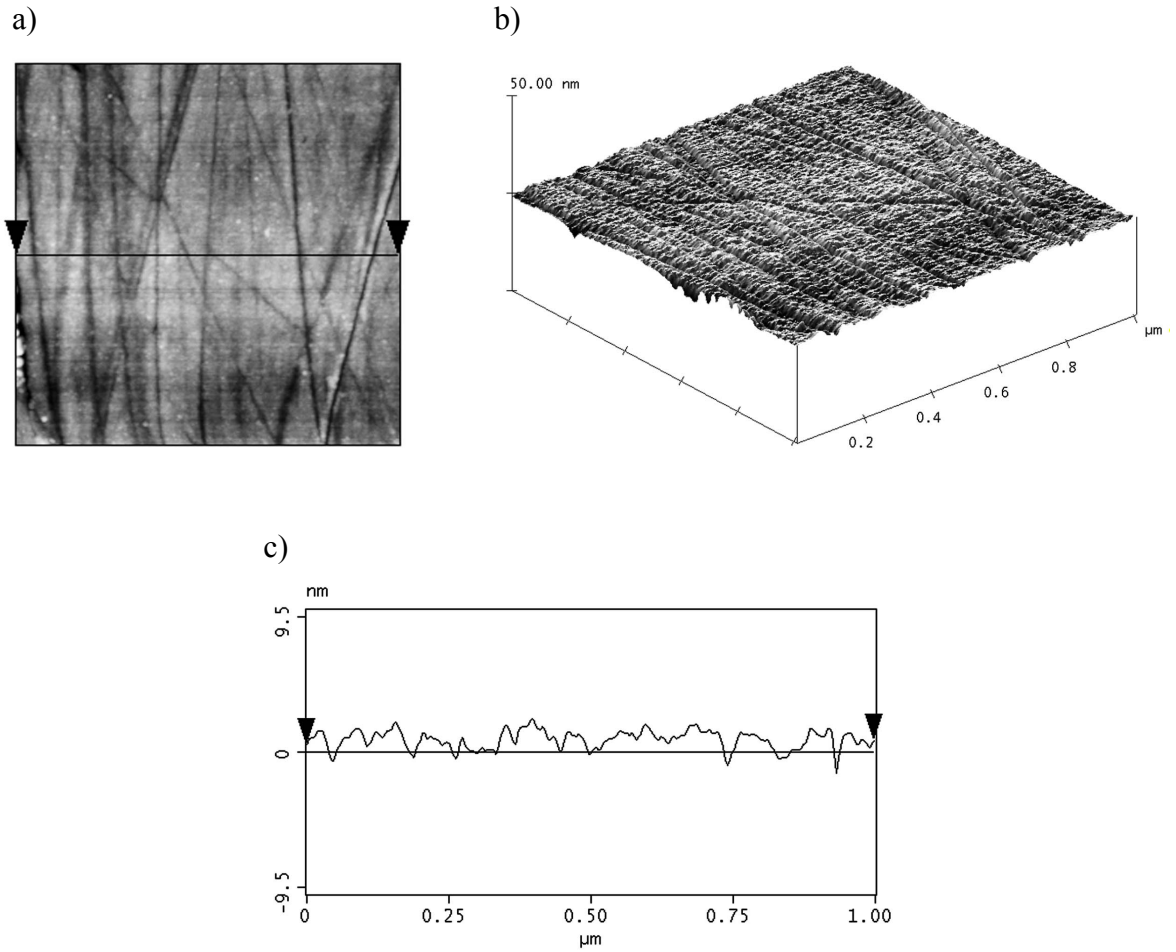

Figure 3.2. AFM topographic image of a clean and considerably flat region in Ni: 2D (a) and 3D (b). The scanned area is 1 × 1 μm^2. c) Topographic profile corresponding to the region defined by the horizontal line in a).

Table 3.1. Average roughness of Ni-Co samples prepared with different surface finishing methods. The roughness of a Ni (100) monocrystal is also presented. MP and EP stand for mechanically polished and electropolished, respectively•.

Sample	**Surface finishing method**		R_a **(nm)**
	Final step	**Notes on the final step**	
Ni, Ni-Co alloys, Co	MP	0.1 μm diamond particles suspension	< 3
Ni	EP	40%H_3PO_4–35%H_2SO_4–25%H_2O solution (-9 to 1 ºC; 12 V; 1.63-2.99 A; magnetically stirred; 220 s)	10 ± 4
Co	EP	80%CH_3OH–20%$HCLO_4$ solution (-34 to -27 º C; 11.5 V; 0.75-0.78 A; no stirring; 60 s)	39 ± 6
Ni (100)	MP	0.05 μm colloidal silica particles suspension	< 1

• Note that R_a < 0.1 μm in an ultra-high quality minor-like surface finishing.

3.2. Surface composition

The chemical composition of the samples' surfaces was determined from Auger spectra for Ni, Ni-21%Co, Ni-55%Co, Ni-85%Co, and Co (Figure 3.3). In particular, the thickness of the surface oxide layer was estimated from Auger chemical composition depth profiles. The only elements considered in the quantification were O, Co and Ni, whose selected peaks were, respectively, O KL1 at 512 eV, Co LM7 at 648 eV and Ni LM2 at 845 eV (pointed with thick arrows in the plots of Figure 3.3). Besides the typical peaks of O, Co and Ni, three other peaks are present in the spectra. One is due to carbon, which is present during the first sputtering cycles and results from the presence of organic contaminants at the surface. Another is due to the residual nitrogen which exists inside the UHV chamber and is adsorbed at the sputtered surface during Auger analysis. Finally, a residual amount of chlorine was detected before sputtering the surface of Ni-85%Co, which can be due to the retention of the dichloromethane (CH_2Cl_2) used to clean the samples, in micropores at the surface.

Figure 3.4 shows Auger chemical composition depth profiles of the five analysed samples, where the depth was estimated from the sputtering time using the sputtering rate of FeO, 0.33 nm/s [128]. The sample with the thinnest oxide layer is nickel, with a maximum thickness of 10 nm, if it is assumed that the metal-oxide interface is found when the atomic percentage of oxygen is approximately 10%. The thickest oxide layer is found in Ni-21%Co, with a maximum thickness of 52 nm. For larger Co proportions the oxide layer thickness decreases and its maximum value is 40, 35 and 28 nm for Ni-55%Co, Ni-85%Co and Co, respectively.

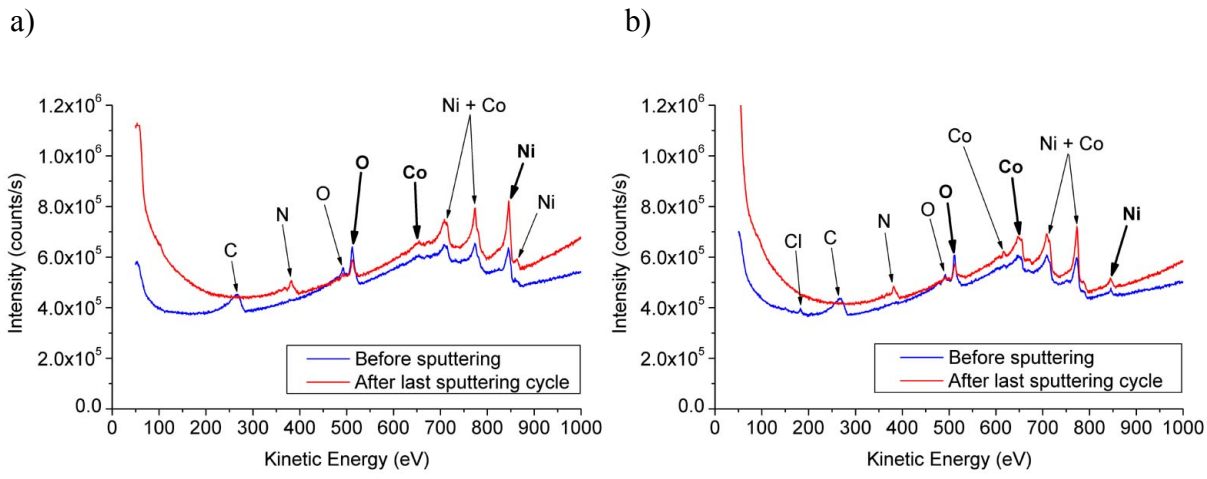

Figure 3.3. Auger spectra of Ni-21%Co (a) and Ni-85%Co (b), before sputtering and after the last sputtering cycle. The peaks used to determine the concentration of O, Ni and Co are pointed with thick arrows.

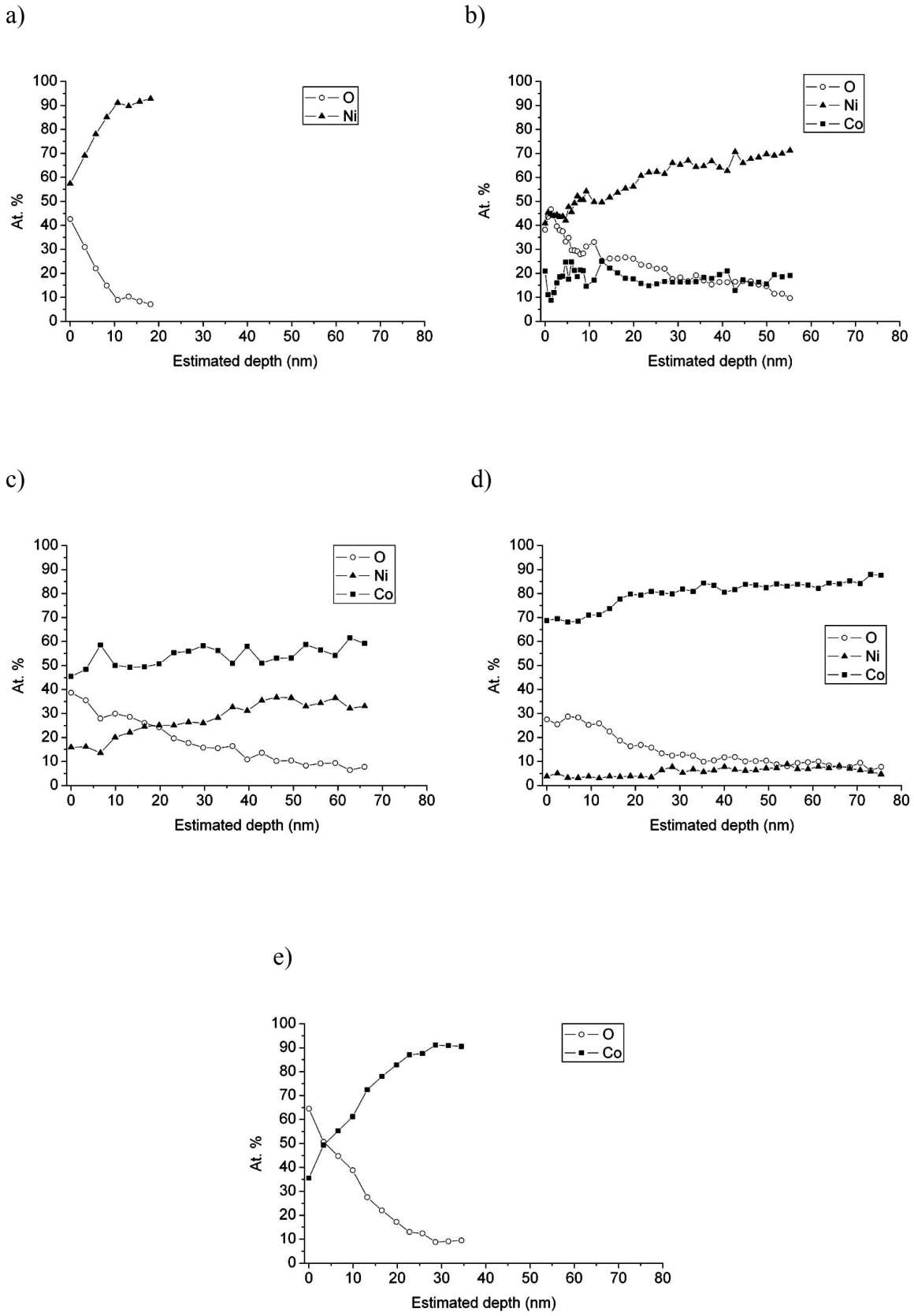

Figure 3.4. Auger chemical composition depth profiles: Ni (a); Ni-21%Co (b); Ni-55%Co (c); Ni-85%Co (d); Co (e).

3.3. Bulk composition

The bulk chemical composition and homogeneity of the samples was determined with an energy dispersive spectroscopy microprobe attached to the scanning electron microscope used in the present work. Figure 3.5 shows examples of EDS spectra used to determine the chemical composition of the samples. The peak at 0 keV that appears in all spectra is just a calibration peak, which is used to define the origin of the energy axis. The most intense peaks of Ni and Co are located at 7.46 and 6.92 keV, respectively. In a few samples, small isolated peaks of Fe and Cr are also found at 6.40 and 5.42 keV, respectively. These four peaks correspond to K_α transitions.

The chemical composition of the samples determined from standardless quantitative analysis of the EDS spectra is shown in Table 3.2•. The standard deviation values result from measurements in three different regions in each sample. The nominal compositions of the samples (without taking into account Fe and Cr impurities) are also shown in the table.

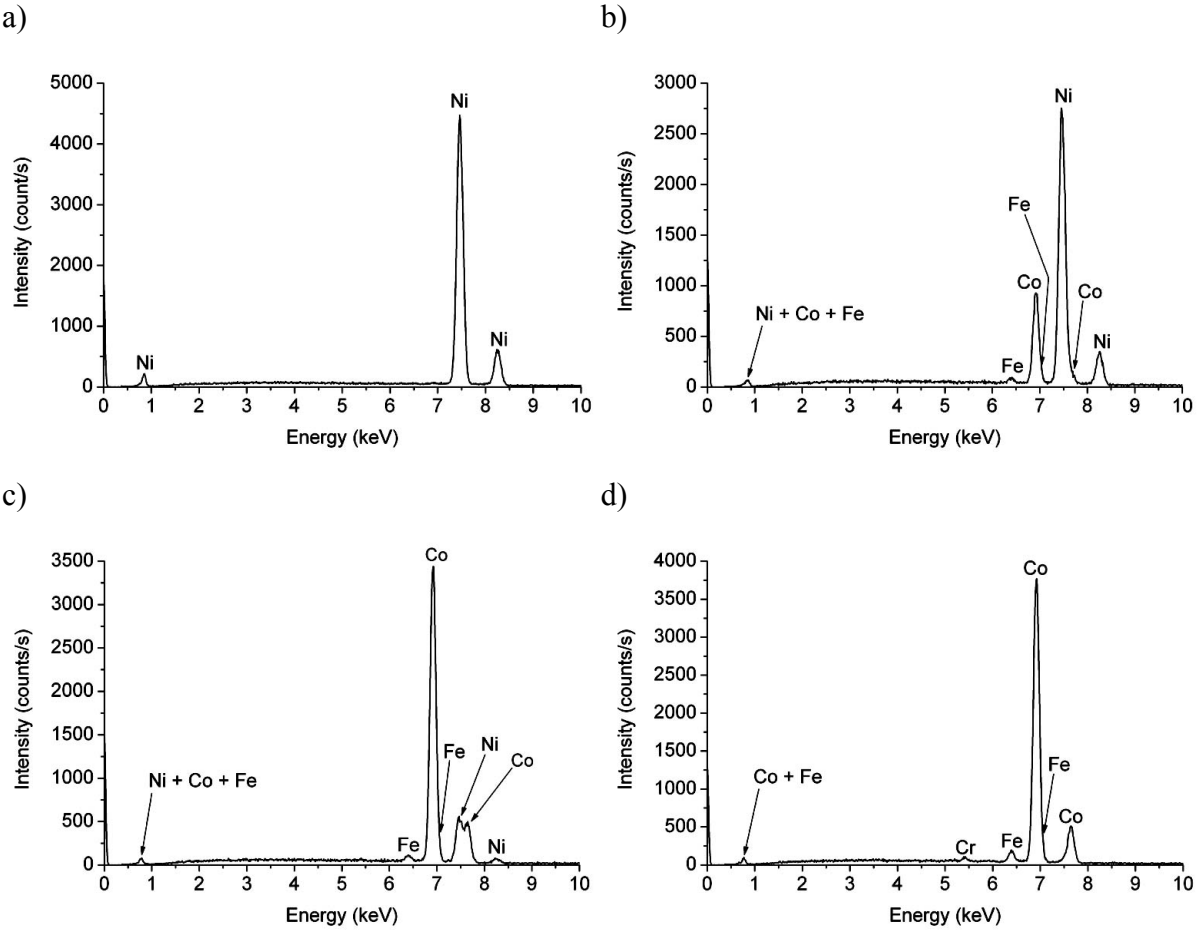

Figure 3.5. EDS spectra of Ni (a), Ni-21%Co (b), Ni-85%Co (c) and Co (d).

• The nomenclature used in this work to designate the Ni-Co samples does not include impurities, i.e. the designations correspond to nominal compositions.

Table 3.2. Chemical composition of the laser clad Ni-Co samples, obtained from standardless quantitative analysis of the EDS spectra. The two columns on the right show the nominal percentages of Ni and Co, i.e. without the contribution of the Fe and Cr impurities.

Sample	Ni (wt.%)	Co (wt.%)	Fe (wt.%)	Cr (wt.%)	$Ni_{nominal}$ (wt.%)	$Co_{nominal}$ (wt.%)
Ni	100.0	–	–	–	100.0	–
Ni-9%Co	91.0 ± 0.7	9.0 ± 0.7	–	–	91.0 ± 0.7	9.0 ± 0.7
Ni-21%Co	77.7 ± 0.9	21.2 ± 0.9	1.1 ± 0.1	–	78.6 ± 0.9	21.4 ± 0.9
Ni-26%Co	74.4 ± 0.9	25.6 ± 0.9	–	–	74.4 ± 0.9	25.6 ± 0.9
Ni-31%Co	68.9 ± 1.9	31.1 ± 1.9	–	–	68.9 ± 1.9	31.1 ± 1.9
Ni-42%Co	57.4 ± 3.3	41.9 ± 3.4	0.7 ± 0.1	–	57.8 ± 3.4	42.2 ± 3.4
Ni-55%Co	45.3 ± 0.5	54.4 ± 1.0	0.3 ± 0.5	–	45.4 ± 0.7	54.6 ± 0.7
Ni-60%Co	38.8 ± 0.2	58.3 ± 0.5	2.5 ± 0.1	0.4 ± 0.4	40.0 ± 0.3	60.0 ± 0.3
Ni-73%Co	26.2 ± 1.0	69.7 ± 1.5	3.3 ± 1.3	0.8 ± 0.5	27.3 ± 0.8	72.7 ± 0.8
Ni-82%Co	17.7 ± 0.8	81.9 ± 0.4	0.4 ± 0.6	–	17.8 ± 0.7	82.2 ± 0.7
Ni-85%Co	14.9 ± 1.2	83.3 ± 0.8	1.8 ± 0.4	–	15.2 ± 1.2	84.8 ± 1.2
Ni-92%Co	7.9 ± 0.2	87.8 ± 1.2	3.5 ± 1.1	0.8 ± 0.3	8.3 ± 0.1	91.7 ± 0.1
Co	97.0 ± 1.4	–	2.5 ± 1.0	0.5 ± 0.4	–	100.0

The homogeneity of the samples was analysed from XRD maps obtained with the same EDS detector used to determine the chemical compositions. As an example, SE images and XRD maps of Ni-42%Co and Ni-73%Co are shown in Figures 3.6 and 3.7, respectively. The maps show that the samples are chemically homogeneous, though some concentration of Cr contaminations in small regions can be observed in some of the samples. (bottom right of Figure 3.7).

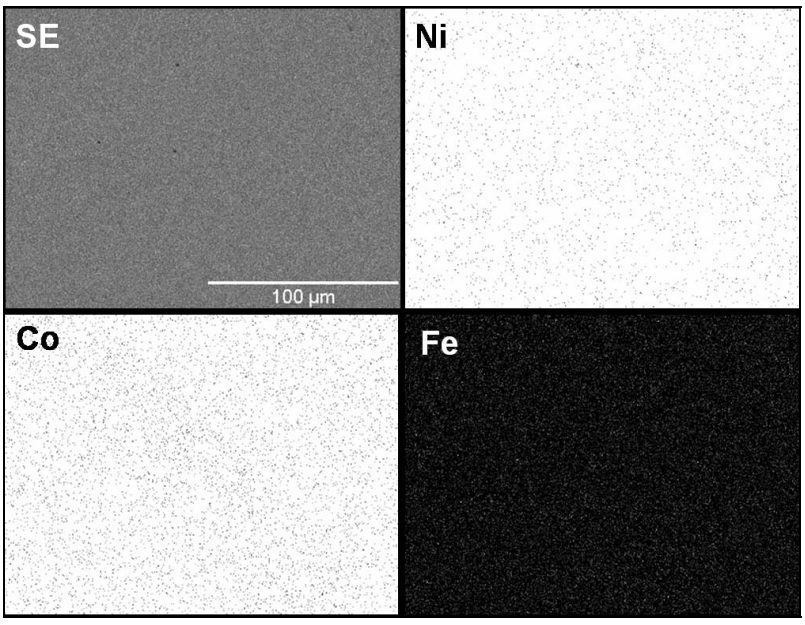

Figure 3.6. SE image and XRD maps of Ni-42%Co. The map of Cr for this sample is totally black and hence is not shown in the figure.

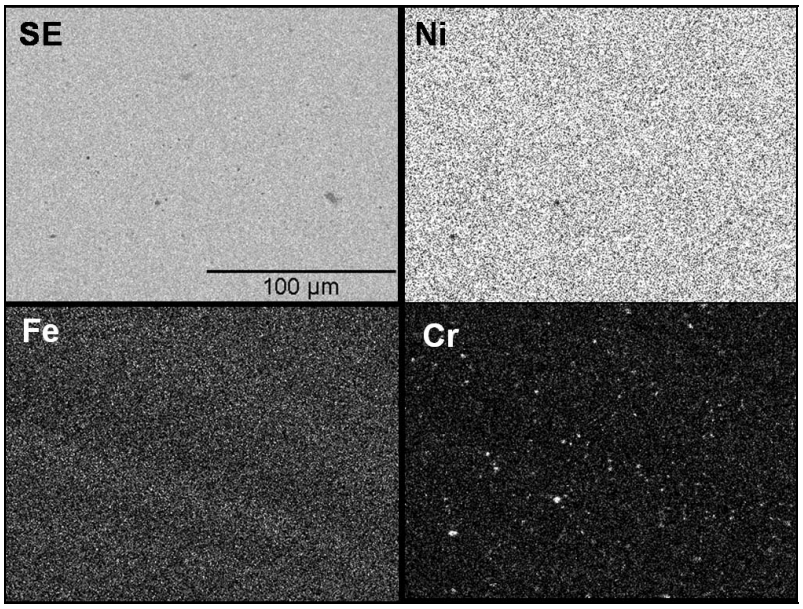

Figure 3.7. SE image and XRD maps of Ni-73%Co. The map of Co for this sample is almost totally white and hence is not shown in the figure.

3.4. Microstructure and substructure

One of the main difficulties of this work was to reveal the microstructure of the samples, especially Co-richer ones, for scanning electron microscopy. This was caused by the high corrosion resistance of both Ni and Co, which decreased the effectiveness of some of the most active etchants recommended in the literature (e.g. Marble's reagent and diluted Aqua Regia [156]). Nevertheless, a further effort was made in relation to pure Ni and Co, which were electrolitically etched (by using the method described in §2.1.2), thus enabling to characterise the microstructure by OM and SEM. Samples of pure Ni and Co were also observed by TEM in order to analyse the substructure of these materials.

Figure 3.8 shows SEM images of electrolitically etched Ni and Co[•]. The grain structure of Ni consists of grains with dimensions in the range 40 to 80 μm (Figure 3.8.a), which are formed by dendrites with a primary arm spacing of a few micrometers (Figure 3.8.b). Submicrometric spherical pores are present in the interdendritic regions, as was also observed by AFM (see Figure 3.1). The microstructure of Co was not as clearly revealed by the electrolytical etching as in the case of Ni (Figure 3.8.c). However, by using backscattered electrons (where the contaminants appear as dark particles), it can be observed that the grains of Co are even larger than those of Ni, some of them reaching dimensions over 100 μm, and

[•] Some contaminants from the electrolyte adhered to the samples' surfaces, especially in the case of Co, and were not removed during sample cleaning in ultrasonic bath.

are formed by martensite plates (Figure 3.8.d) which result from the α (FCC) → ε' (HCP) martensitic phase transformation on cooling [21].

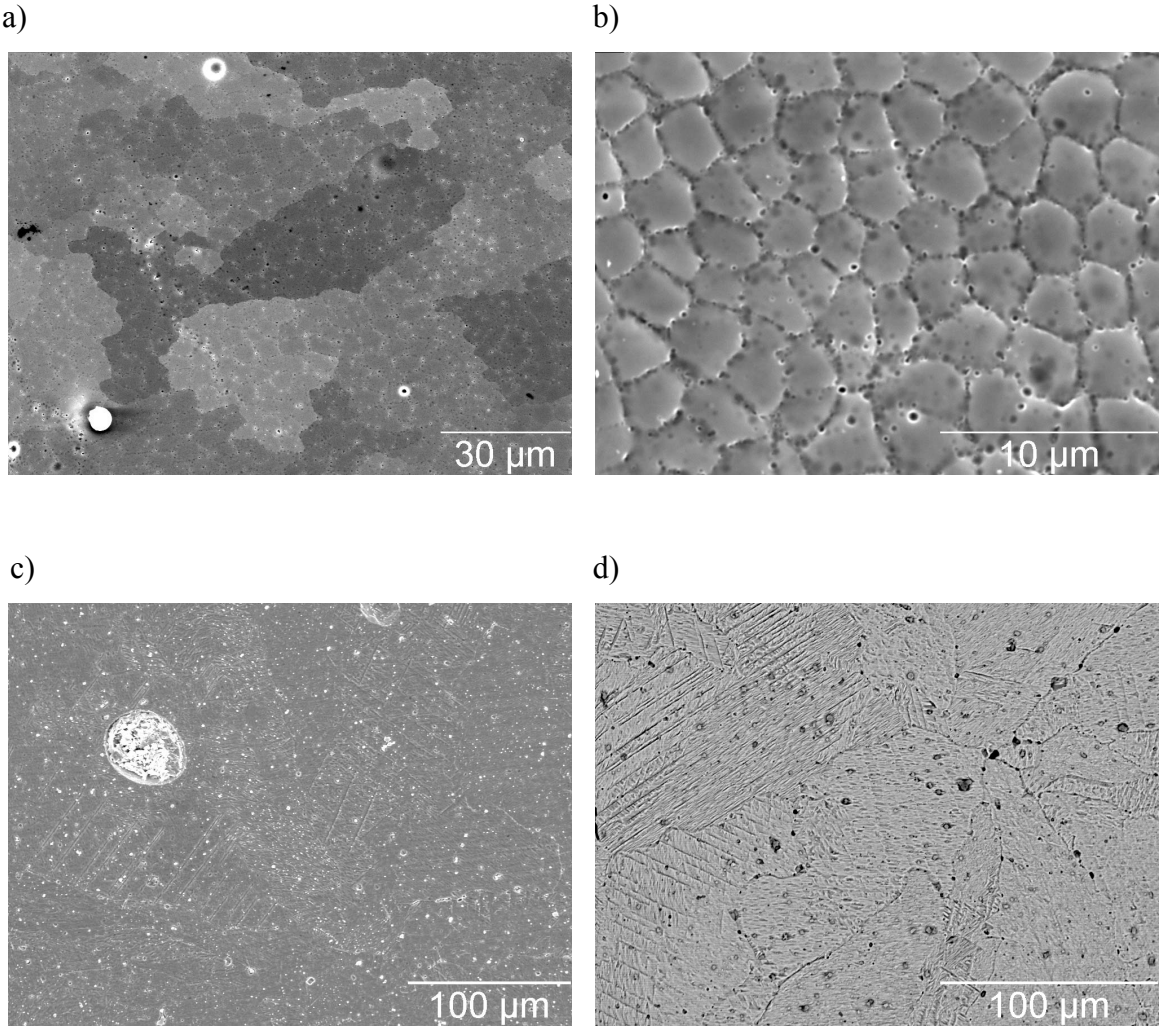

Figure 3.8. SE SEM images of Ni (a and b) and SE and BSE SEM images of Co (c and d, respectively). The white particles in c) and dark particles in d) are contaminants which adhered to the samples' surfaces during electrolytical etching.

As can be observed from Figure 3.8, the samples presented some residual microporosity. The volume fraction (V_f) of a phase randomly distributed in a material can be estimated from the average areal fraction (A_f) of that phase determined on several parallel sections through the considered volume [157]. The areal fraction of pores can be determined from several SEM images, which form a group of parallel sections through a volume of the sample, by:

$$A_f = \frac{A_{pores}}{A}, \tag{3.1}$$

where A_{pores} is the total area of pores in an image and A is the area of the observed region. A_{pores} can be measured by applying the method used in the determination of projected areas of nanoindentations from AFM images (see §2.3.1.3). The volume fraction of micropores in the samples, determined using the method described in the former paragraph, was found to be smaller than 2%. AFM observation of the pores shows that their average diameter is usually submicrometric (see Figure 3.1).

XRD patterns of the samples are shown in Figure 3.9. Samples with Co proportions smaller than approximately 68% present only the FCC α phase (Figures 3.9.a to e), while in those with more than 80% Co only the HCP ε' martensitic phase seems to be present (Figures 3.9.g to i). In the pattern of Ni-73%Co (Figure 3.9.f), not only the peaks of ε' are present but also the (200) peak of α, which is the only peak of α that is not overlapped by a peak of ε' in the case of biphasic Ni-Co alloys. Moreover, conversely to what is observed in the patterns of Ni-82%Co, Ni-85%Co and Co, in the pattern of Ni-73%Co the (002) peak of ε' is more intense than the remaining peaks, which is most probably a result of the contribution from the strong (111) reflection of the α phase. Consequently, the Ni-73%Co alloy contains a mixture of these two phases (α and ε').

The microstructure of Ni observed by TEM is shown in Figure 3.10.a. The grains observed in this image correspond to dendrites of FCC α, since the size and shape of these features are comparable to those of the dendrites shown in Figure 3.8.b. Figure 3.10.b shows a dendrite with the [011] direction parallel to the electron beam, as can be observed from the diffraction pattern in Figure 3.10.c, which was taken at this dendrite. The distribution of dislocations in Ni is relatively heterogeneous, as can be observed in Figure 3.10.d, which shows a particular arrangement of dislocations inside a dendrite, with regions containing dislocations and others where they are absent.

A small number of spherical and irregular shaped precipitates with sizes in the range 50 to 200 nm was found in a few regions, both inside grains and at grain boundaries (Figures 3.11.a and b). As can be observed in Figure 3.11.a, these small precipitates can pin the dislocations, forming a barrier to their movement. EDS analysis of the precipitates revealed that their composition is very similar to that of the matrix, except for the presence of Fe (Figure 3.12)•.

• The carbon and oxygen peaks that appear both in the EDS spectra of the precipitates and matrix are caused by contamination of the samples during preparation and TEM observation.

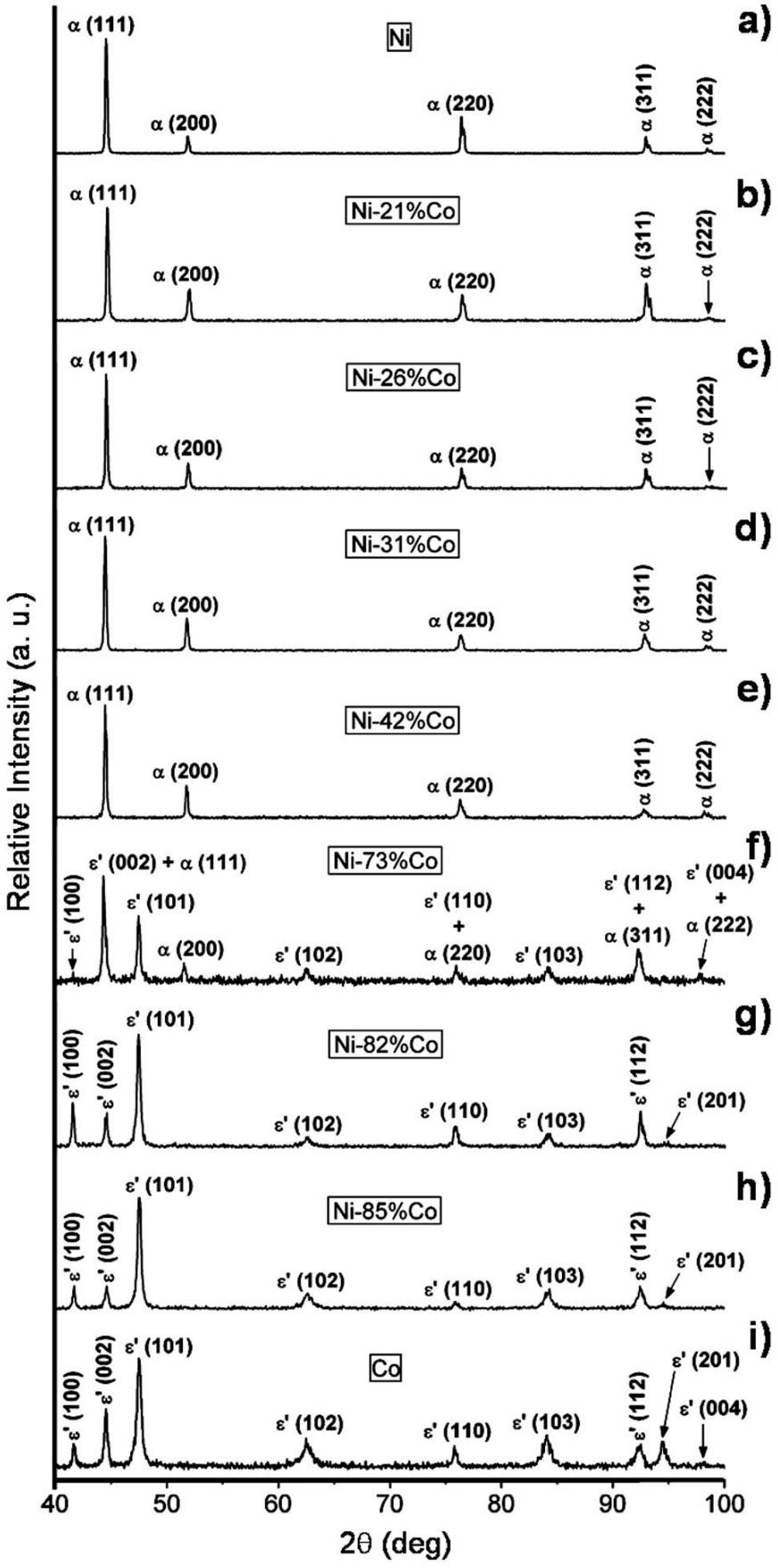

Figure 3.9. XRD patterns of Ni-Co samples (a to i). The radiation used is CuK_{α}.

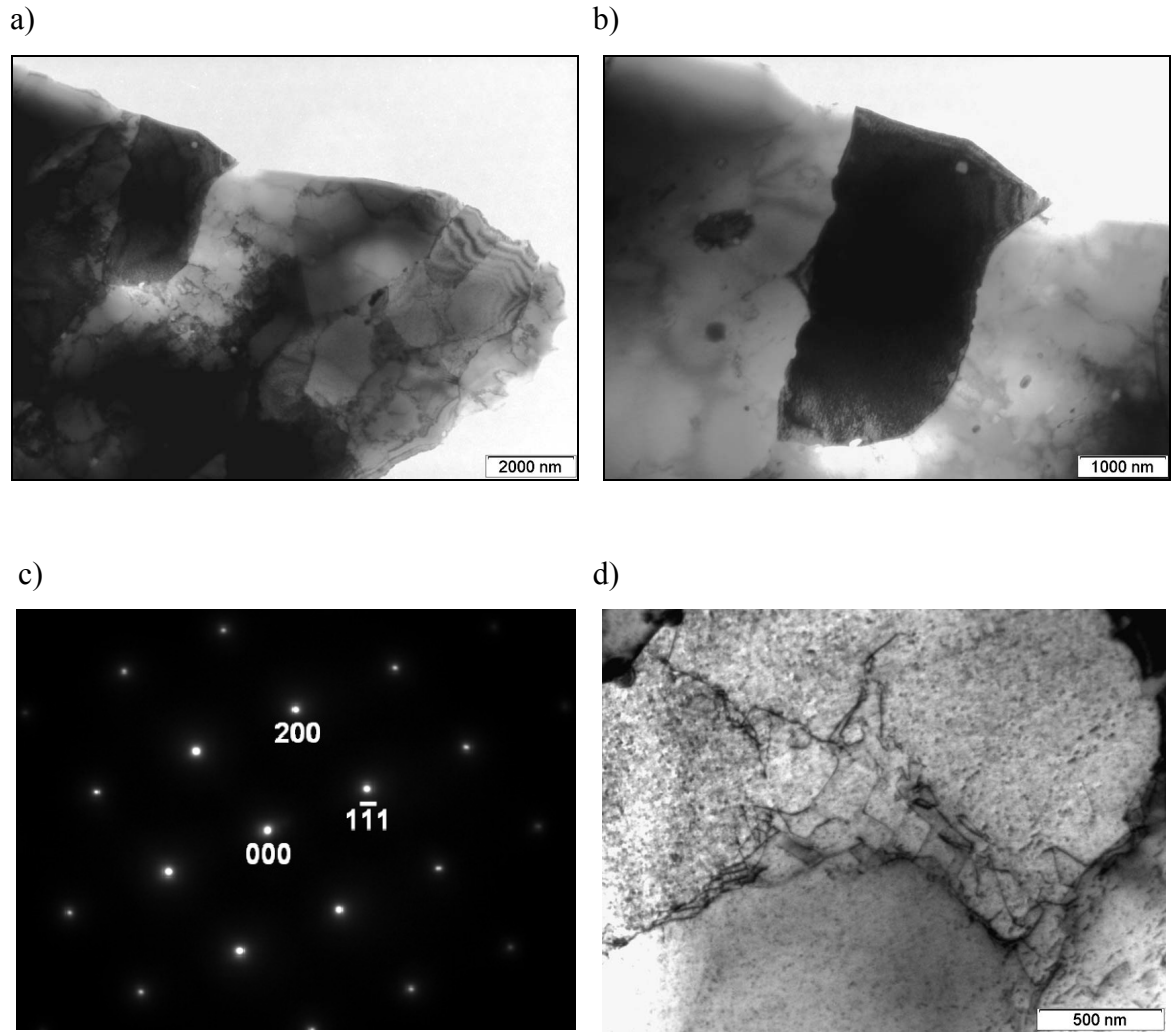

Figure 3.10. BF TEM images of Ni: several dendrites (a); dendrite with the [011] direction parallel to the electron beam (b); region containing dislocations heterogeneously distributed (d). SAD [011] zone-axis diffraction pattern of dark dendrite in b) (c).

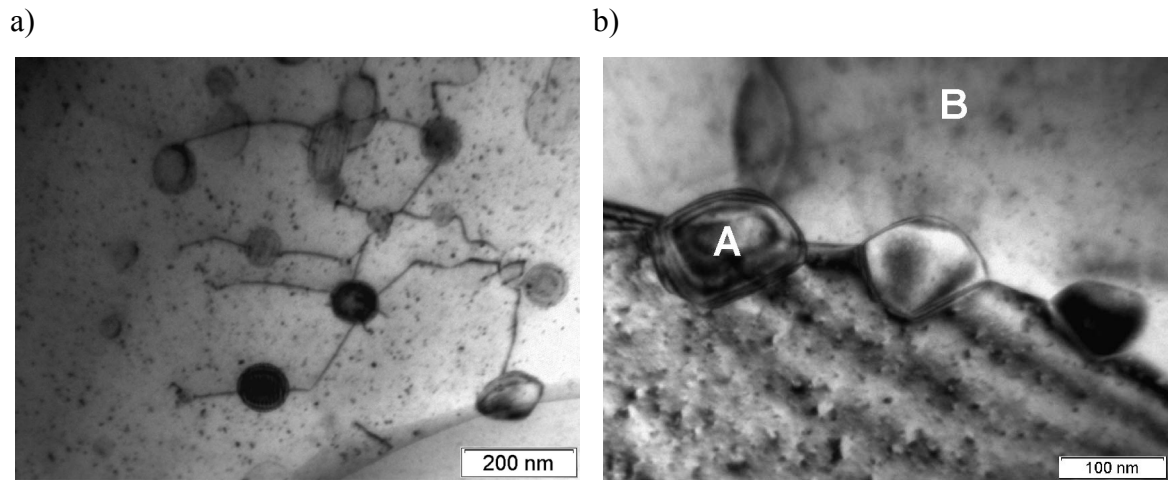

Figure 3.11. BF TEM images of Ni: precipitates anchoring dislocations (a); precipitates at a grain boundary (b).

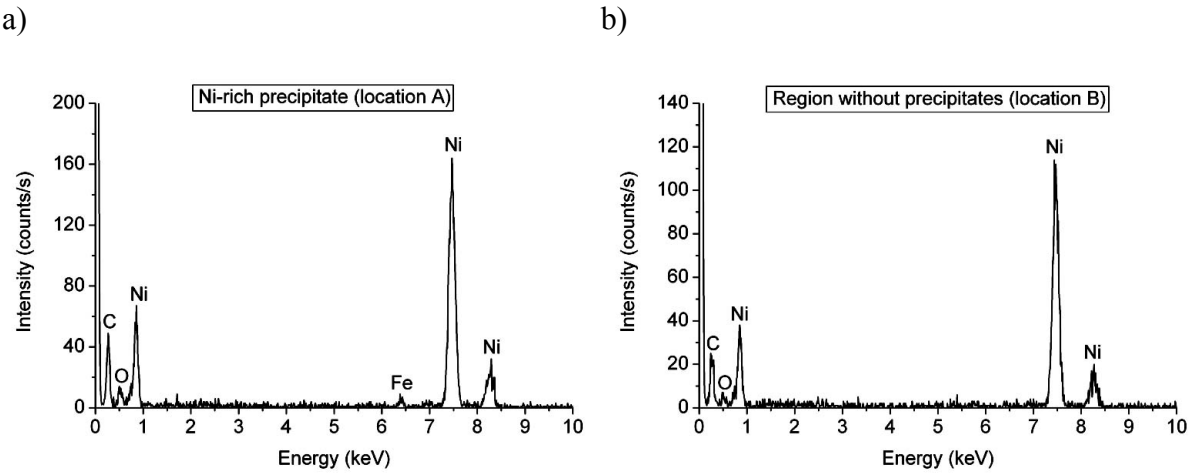

Figure 3.12. EDS spectra of the left precipitate in Figure 3.11.b, at location A (a), and of a region without precipitates, at location B (b). The peak at 0 keV in the spectra is a calibration peak used to define the origin of the energy axis.

The TEM observation of Co confirms the presence of ε' martensite plates, as well as of a few precipitates (Figure 3.13.a). Figure 3.13.b shows part of a martensite plate, with the $[0\,\bar{1}\,10]$ direction parallel to the electron beam (see diffraction pattern in Figure 3.13.c). The stripes inside the martensite plate correspond to stacking faults produced during the α (FCC) → ε' (HCP) martensitic phase transformation, where the orientation between the α phase and the ε' phase is given by the Shoji-Nishiyama relation [21]: $(111)_\alpha//(0001)_{\varepsilon'}$ and $[11\,\bar{2}]_\alpha//[1\,\bar{1}\,00]_{\varepsilon'}$ or $[1\,\bar{1}\,0]_\alpha//[11\,\bar{2}\,0]_{\varepsilon'}$. The habit plane of the martensite is the (111) plane, as can be confirmed by observing that the stacking faults in Figure 3.13.b are perpendicular to g_{0002} • in Figure 3.13.c. The formation of stacking faults generates a high density of dislocations, as can be observed in Figure 3.13.d.

Martensite was found in most of the observed regions in Co. However, in a few localized regions it was found high temperature α phase without stacking faults (Figures 3.13.e and f).

A few precipitates were also found in Co, some with spherical shape (Figure 3.14.a) and containing Co and small amounts of Fe and Cr (Figure 3.15.a), and others with approximately polyhedral shape (Figure 3.14.b) and containing Cr, Co and a small amount of Fe (Figure 3.15.b). These precipitates are larger than those found in Ni, with dimensions in the range 200 to 1000 nm, and are located inside the martensite plates. The amount of impurities in the matrix is much smaller than in the precipitates (Figure 3.15.c).

• Reciprocal lattice vector for the (0002) reflection.

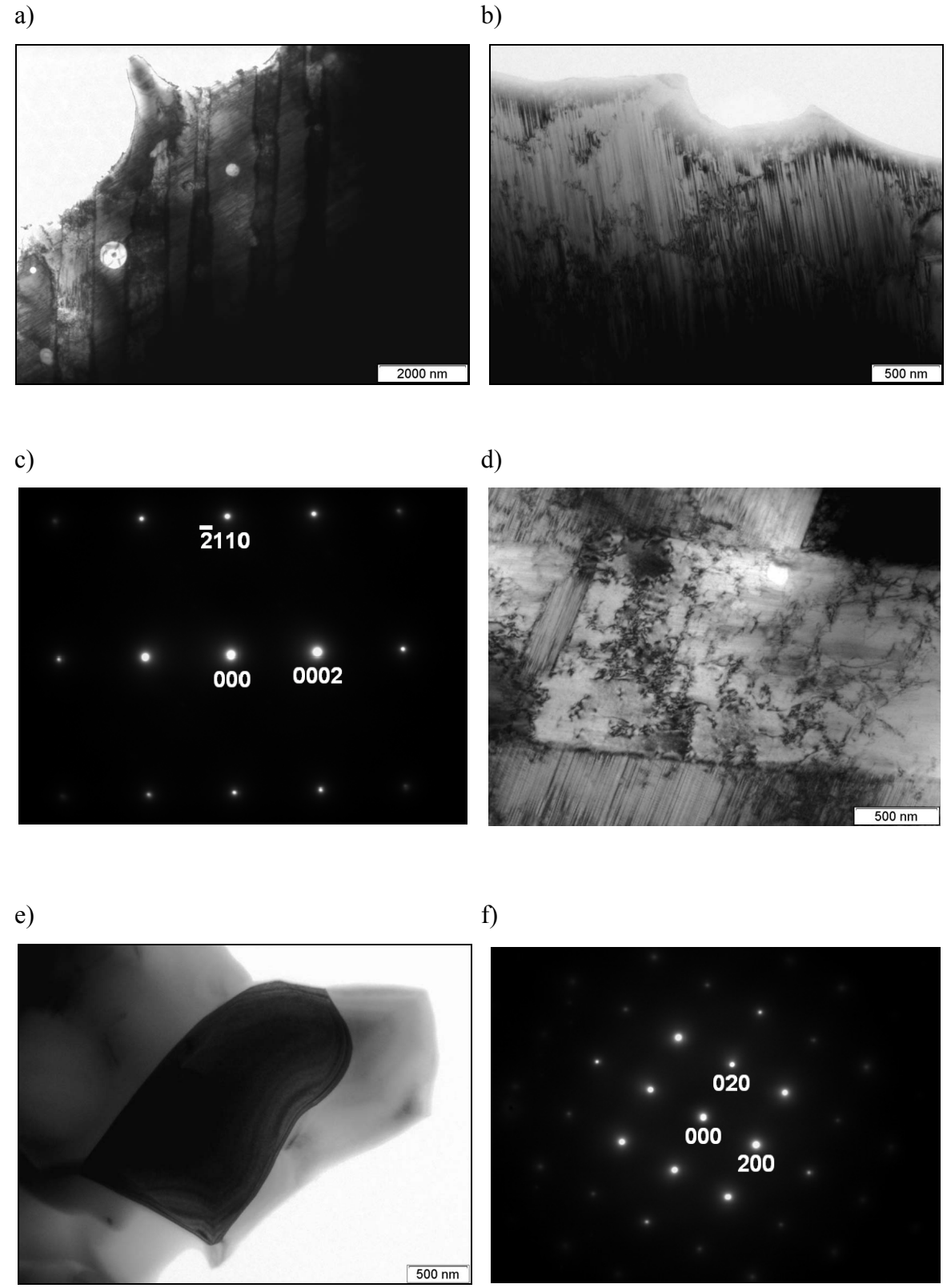

Figure 3.13. BF TEM images of Co: several martensite plates and a few precipitates (a); part of a large martensite plate with the [0 $\bar{1}$ 10] direction parallel to the electron beam and filled with stacking faults (b); two almost perpendicular martensite plates, one with an orientation that enables visualizing the stacking faults (top and bottom) and the other oriented in a way such that the dislocations become visible (middle) (d); region containing a grain of FCC α with the [001] direction parallel to the electron beam (e). SAD [0 $\bar{1}$ 10] zone-axis diffraction pattern of the region shown in b) (c). SAD [001] zone-axis diffraction pattern of dark grain shown in e) (f).

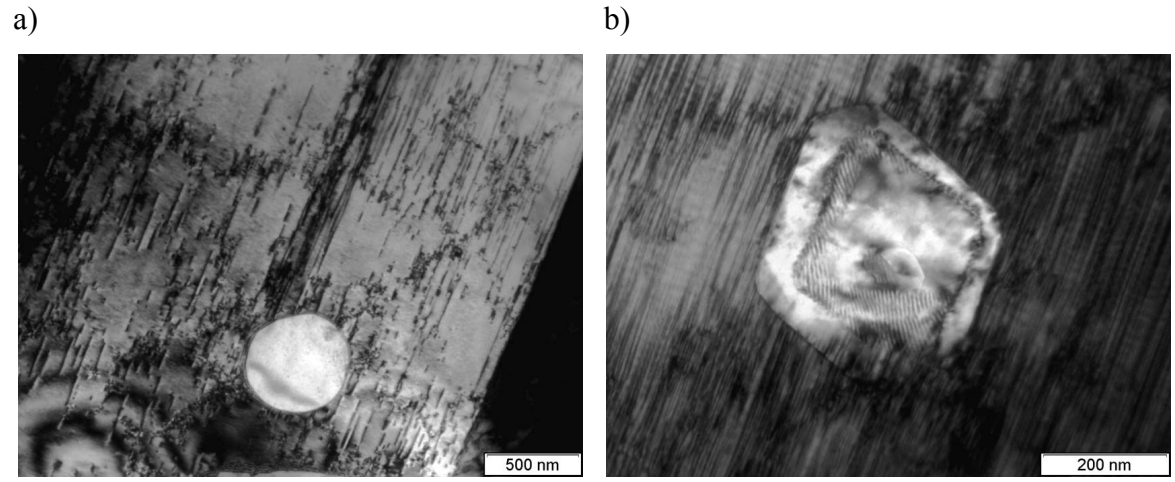

Figure 3.14. BF TEM images of Co: Co-rich precipitate (a); Cr- and Co-rich precipitate (b).

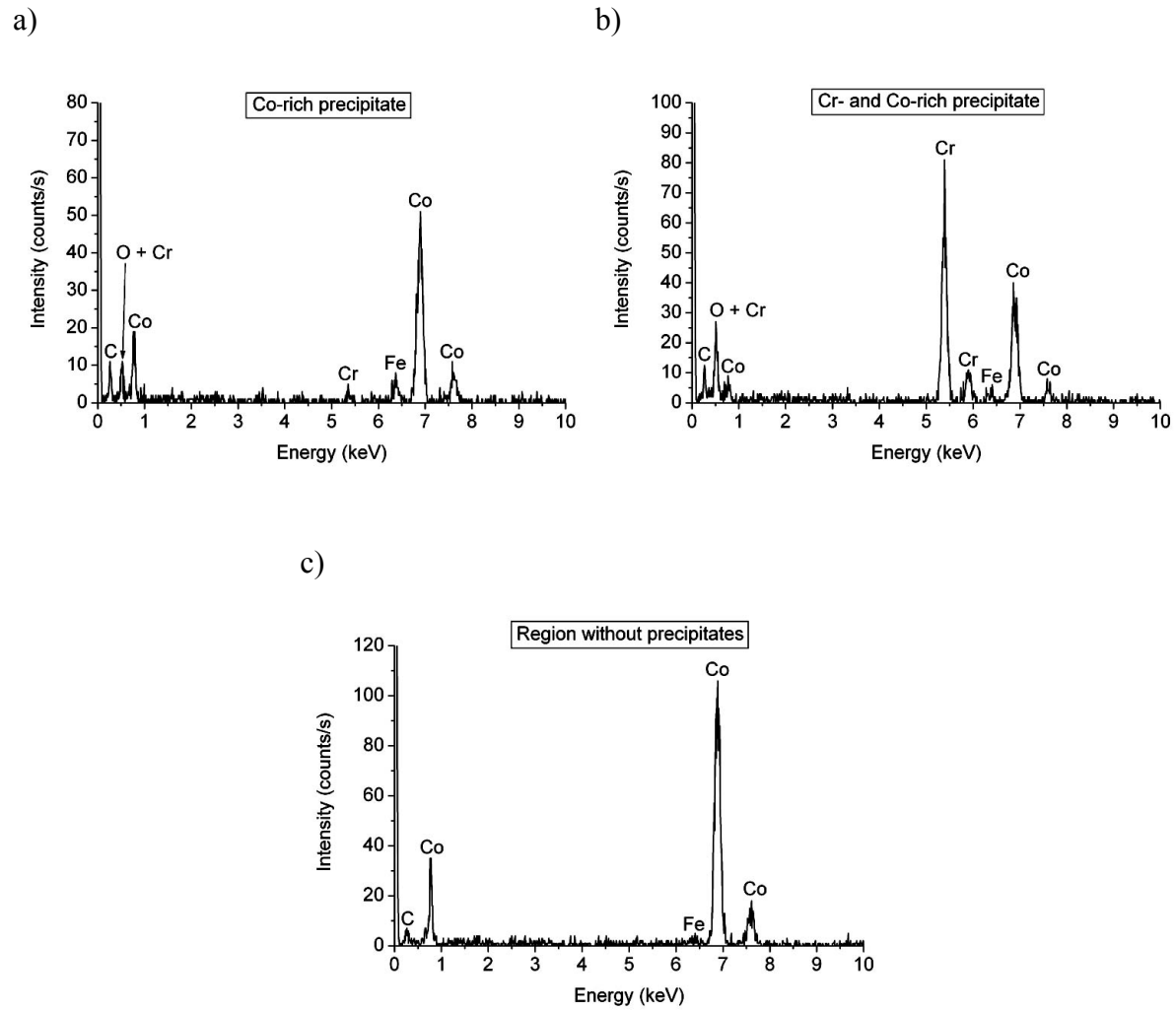

Figure 3.15. EDS spectra of the precipitates in Figures 3.14.a and b (a and b, respectively), and of a region without precipitates (c). The peak at 0 keV in the spectra is a calibration peak used to define the origin of the energy axis.

3.5. Dislocation density

The dislocation density (ρ) is a key parameter in the plastic behaviour of metallic crystalline materials. The most accurate method for the determination of dislocation density is by TEM, since it allows the direct observation of the dislocation structure. Although this method (or variations of the method) has been previously applied in several works (see for instance [158, 159]), a detailed explanation of the method is usually absent.

The Ni sample was chosen for the estimation by TEM of the average dislocation density in the materials used in the present work. A general description of the method used for the estimation of ρ is presented next, followed by its application to the case of Ni.

The dislocation density is defined as the total length (l) of dislocation lines per unit volume (V) of material:

$$\rho = \frac{l}{V}. \tag{3.2}$$

The dislocation line lengths measured in a TEM image are projected lengths and not true lengths. Assuming that the dislocations are randomly oriented in the material, the projected length (l_p) can be related to the length of dislocation lines by [160]:

$$l = \frac{4}{\pi} l_p. \tag{3.3}$$

The volume of the observed regions is calculated by:

$$V = At, \tag{3.4}$$

where A is the area of the observed region and t is the sample thickness. The sample thickness can be estimated by applying the graphical method first described by Kelly *et al*. [161] and later developed in detail by Allen [162] to convergent beam electron diffraction data. The first step is to choose a grain of the polycrystalline sample and obtain a SAD pattern at that grain. Then, a two-beam condition has to be established by tilting the crystal around until only one *hkl* reflection is strongly excited, i.e. all the spots in the pattern become very weak or may even disappear, except that of the direct beam and that of the strongly diffracted beam. A CBED pattern is then obtained by changing the parallel and relatively large beam used in

SAD to a highly focused beam. While spots in a SAD pattern consist of intensity peaks only (Figure 3.16.a), CBED disks (since they are larger than SAD spots) present Kossel-Möllenstedt intensity fringes if the observed region is more than one extinction distance (ξ_g) thick (Figure 3.16.b), i.e. if its thickness is larger than the critical distance in the perfect crystal at which the transmitted intensity falls to zero before increasing again. ξ_g is characteristic for the strongly excited *hkl* reflection. The Kossel-Möllenstedt fringes are asymmetric in the 000 disk (direct beam) and symmetric in the *hkl* disk (diffracted beam) and contain sample thickness information.

a) b)

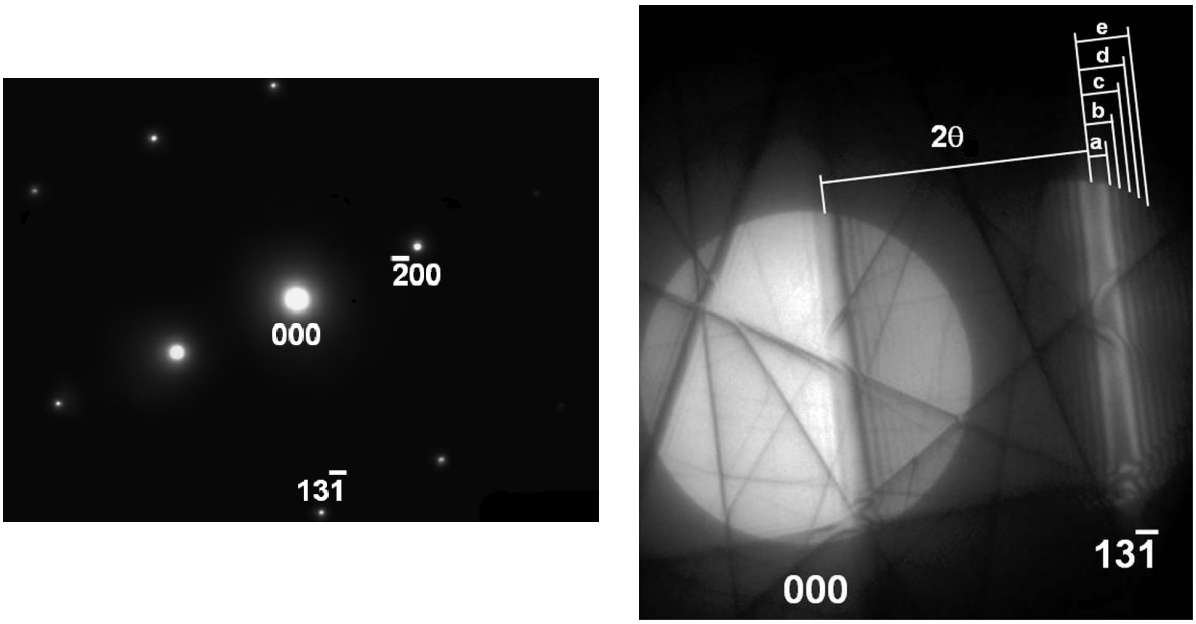

Figure 3.16. (a) SAD [013] zone-axis diffraction pattern of a dendrite in Ni. (b) CBED pattern of the same dendrite taken under a (000)/(13 $\bar{1}$) two-beam condition. The CBED pattern is rotated 90º anti-clockwise in relation to the SAD pattern. Several parallel Kossel-Möllenstedt intensity fringes can be observed in both disks of the CBED pattern, as well as Kikuchi lines intersecting the disks. Letters "a", "b", "c", "d" and "e" correspond, respectively, to the angles $\Delta\theta_1$, $\Delta\theta_2$, $\Delta\theta_3$, $\Delta\theta_4$ and $\Delta\theta_5$.

From the CBED pattern one can extract the distances between the central fringe of the *hkl* disk and each of the dark fringes of the same disk, which correspond to angles $\Delta\theta_i$, as well as the distance between the central fringes of the two disks, which corresponds to the angle 2θ, being θ the Bragg angle for the (*hkl*) planes (see Figure 3.16.b). Using these values, the deviation (or excitation error) s_i for the *i*th fringe can be calculated by [163]:

$$s_i = \lambda \frac{\Delta\theta_i}{2\theta\, d_{hkl}^{\,2}}, \tag{3.5}$$

where λ is the wavelength of the electrons and d_{hkl} is the interplanar spacing of the (*hkl*) planes. As can be observed from Eq. 3.5, there is no need of measuring the distances $\Delta\theta_i$ and 2θ in reciprocal length units since these two parameters appear as a ratio. In this way, the distances can be measured directly in pixel units by using an image analysis software. The value of λ must be corrected for the relativistic effects that occur when performing observations with high accelerating voltage values (≥ 100 kV). Tables with relativistic corrected λ values can be found in the literature [164]. The spacing d_{hkl} can be calculated using equations found in the literature [164], once the SAD pattern is indexed and the *hkl* spot (chosen for the two-beam condition) identified.

After calculating the deviations s_i for all the fringes visible in the *hkl* disk, the sample thickness, *t*, can be estimated according to [163]:

$$\frac{s_i^{\,2}}{n_k^{\,2}} = \frac{1}{t^2} - \frac{1}{\xi_g^{\,2}}\frac{1}{n_k^{\,2}}, \tag{3.6}$$

where n_k is an integer. The graphical method consists on plotting $(s_i / n_k)^2$ against $1 / n_k^2$ and fitting the data points with a straight line. The intersection of this line with the vertical axis is equal to $1/t^2$, enabling to estimate the sample thickness, while its slope is equal to $-1/\xi_g^{\,2}$, enabling to estimate the extinction distance. The procedure starts by attributing the value 1 to n_1 (first fringe), $n_1 + 1$ to n_2 (second fringe), $n_1 + 2$ to n_3 (third fringe) and so on until the *i*th fringe ($n_i = n_1 + i - 1$) visible on the *hkl* disk of the CBED pattern. If the straight line has negative slope and correlates well with the data points, then, in principle, the attribution of the value 1 to n_1 was correct. However, this criterion alone is insufficient since more than one integer value for n_1 can lead to a negative slope straight line with good correlation to the data points. Therefore, it is also necessary to check if the value obtained for the extinction distance is in agreement with the theoretical value for the same λ and *hkl* reflection (values for many materials can be found in the literature [164]). If not, then a new plot must be made with $n_1 = n_{1(\text{previous iteration})} + 1$, $n_2 = n_1 + 1$, $n_3 = n_1 + 2$....$n_i = n_1 + i - 1$. This iterative procedure should be repeated until obtaining a straight line with negative slope, which correlates well with the data points and enables to determine the correct ξ_g value.

For the determination of the sample thickness by the early described procedure, the Ni sample was tilted until the electron beam was parallel to the [013] zone-axis of the dendrite marked with the letter "X" in Figure 3.17. After obtaining and indexing the SAD pattern taken at this dendrite (Figure 3.16.a), and then obtaining the CBED pattern taken under a

(000)/(13 $\bar{1}$) two-beam condition (Figure 3.16.b) and measuring the distances 2θ and $\Delta\theta_i$ in pixel units using the software Mocha, the deviations s_i were calculated by using Eq. 3.5. The relativistic corrected λ value for a 200 kV electron beam, as was used in the TEM observations of this work, is 0.0251 Å [164]. The interplanar spacing for the (13 $\bar{1}$) planes was determined by using the corresponding equation for cubic structures [164]:

$$d_{hkl} = \frac{a}{\sqrt{h^2 + k^2 + l^2}}, \tag{3.7}$$

where the lattice parameter a of Ni is 3.5238 Å. In this way, $d_{13\bar{1}}$ = 1.06247 Å.

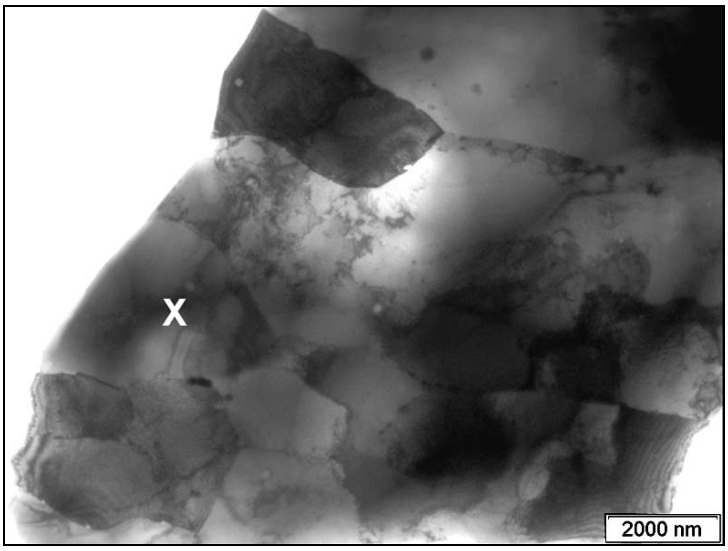

Figure 3.17. BF TEM image of a region in Ni where several estimations of the dislocation density were made. The letter "X" marks the location where the sample thickness was measured.

After calculating s_i for all the visible fringes (i = 5) in the (13 $\bar{1}$) disk of the CBED pattern, the graphical method of Allen was applied (Figure 3.18). Table 3.3 shows the ξ_g and t values extracted from the plots in Figure 3.18, for n_1 varying from 1 to 4. The theoretical ξ_g of Ni for the {311} reflections and a 200 kV electron beam is 63.3 nm [164]. The best estimates of the thickness occur when n_1 is 3 or 4 (Figures 3.18.c and d and Table 3.3). In both cases (n_1 = 3 or 4), negative slope straight lines which correlate well with the experimental data are obtained, as well as good estimates of the extinction distance of Ni for the {311} reflections and a 200 kV electron beam. For n_1 = 3, ξ_g = 73.1 nm and t = 149.2 nm, whereas for n_1 = 4, ξ_g = 51.3 nm and t = 164.6 nm. Therefore, it can be admitted that the sample thickness of the regions where the dislocation density was estimated is 150 ± 50 nm, due to the local thickness fluctuation caused by the sample preparation method.

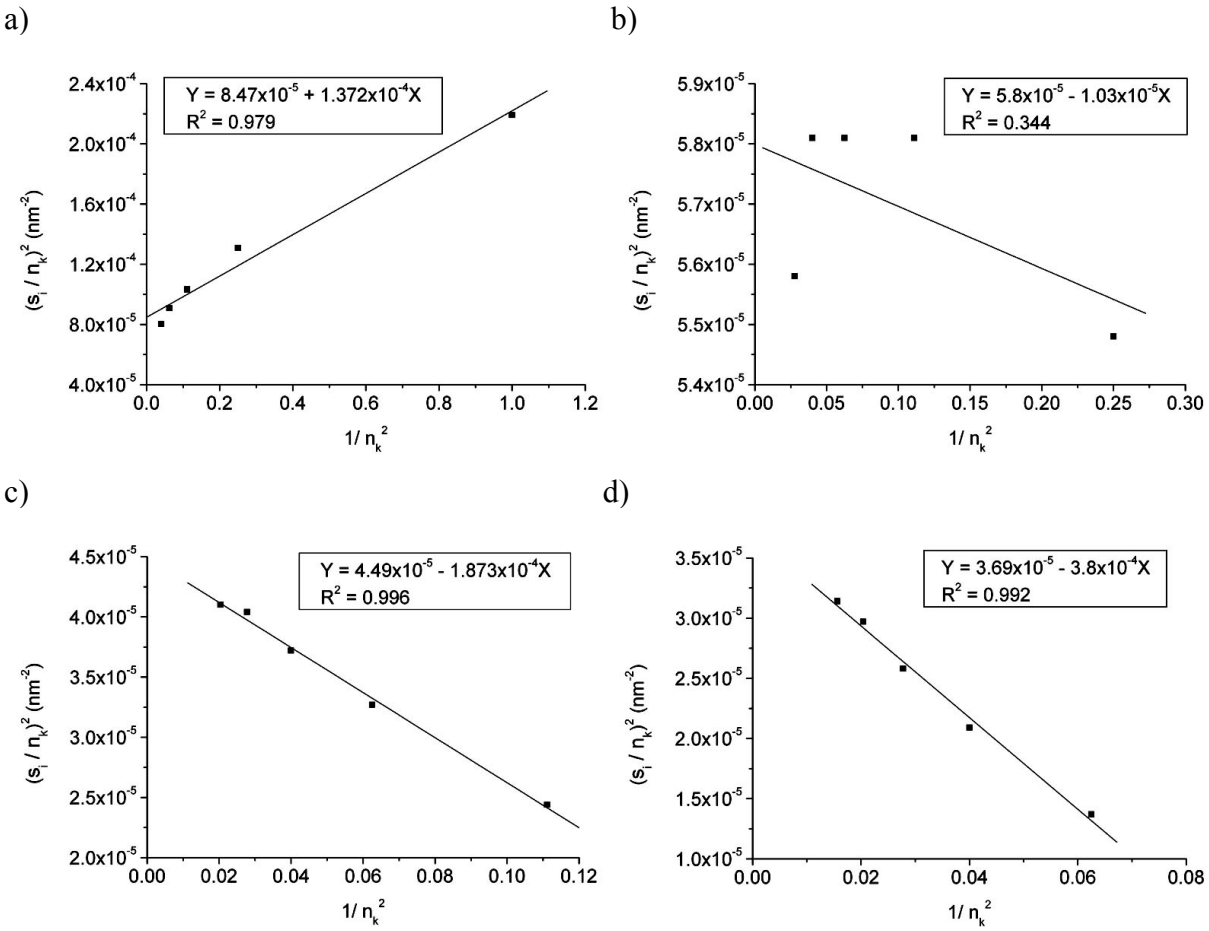

Figure 3.18. Estimation of the sample thickness at location "X" of the region shown in Figure 3.17, using the graphical method of Allen: (a) $n_1 = 1$; (b) $n_1 = 2$; (c) $n_1 = 3$; (d) $n_1 = 4$.

Table 3.3. Extinction distance (ξ_g) and sample thickness (t) estimated with the graphical method of Allen, for different values of n_1. The theoretical value of ξ_g of Ni, for the {311} reflections and a 200 kV electron beam, is 63.3 nm.

n_1	ξ_g (nm)	t (nm)
1	–	108.7
2	311.6	131.3
3	73.1	149.2
4	51.3	164.6

Once the thickness of the observed region is calculated, the projected length of dislocations present in that region must be measured. Special care should be taken in this step regarding the magnification to be used in the TEM observations: too low magnifications may not enable distinguishing clearly individual dislocation lines, whereas too high magnifications may lead to over- or underestimations of l_p. On the other hand, tilting of the sample must also be performed in order to put into evidence the largest possible number of dislocations present. In this way, the systematic errors in the determination of dislocation length values are minimized.

Figure 3.17 shows a BF TEM image of a region in Ni where several estimations of the dislocation density were made. It was found that a 30000× magnification enables a clear visualization of the dislocation lines in this sample, which corresponds to sample areas of 630200 nm^2. Figures 3.19.a and b show, as example, two of the eighteen regions observed by TEM. Figures 3.19.c and d show these images after analysis with the commercial image analysis software Mocha, where the white lines define the path considered for the determination of the projected length of dislocation lines. No dislocations were found in four of the observed regions.

Similar observations were made in Co but, as can be observed from the TEM images of Figure 3.20, it is difficult to distinguish the dislocation lines from the background of stacking faults. Even with the sample oriented in a way that makes the stacking faults becoming almost invisible (Figure 3.20.b) it is impossible to clearly visualize the dislocation lines in order to measure l_p. Therefore, it is not possible to estimate the dislocation density in Co.

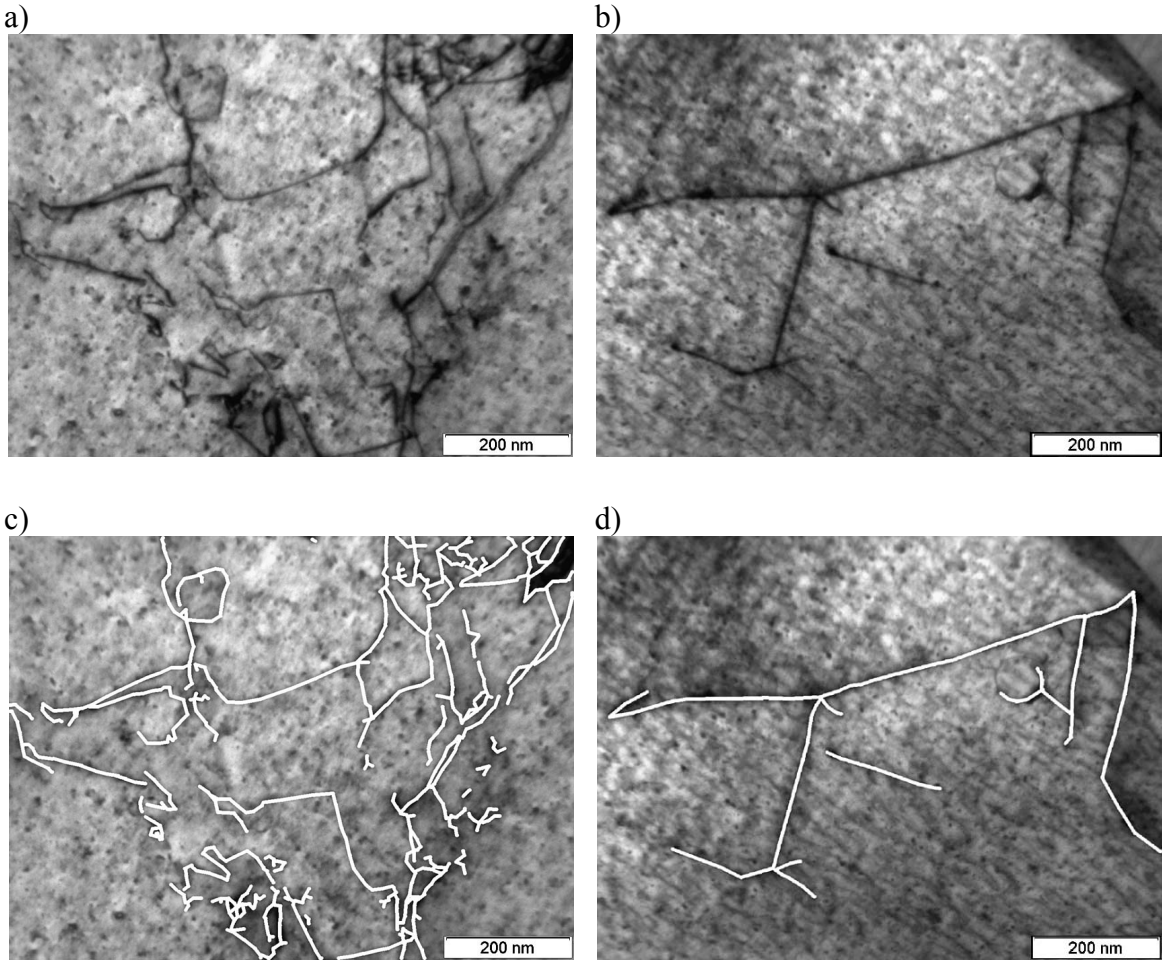

Figure 3.19. (a and b) BF TEM images of two of the eighteen regions where the dislocation density was estimated. The magnification used is 30000×. (c and d) Same images as in a) and b), but after measuring the projected length of dislocation lines using the software Mocha. The white lines follow the dislocation lines in a) and b) and their length corresponds to l_p.

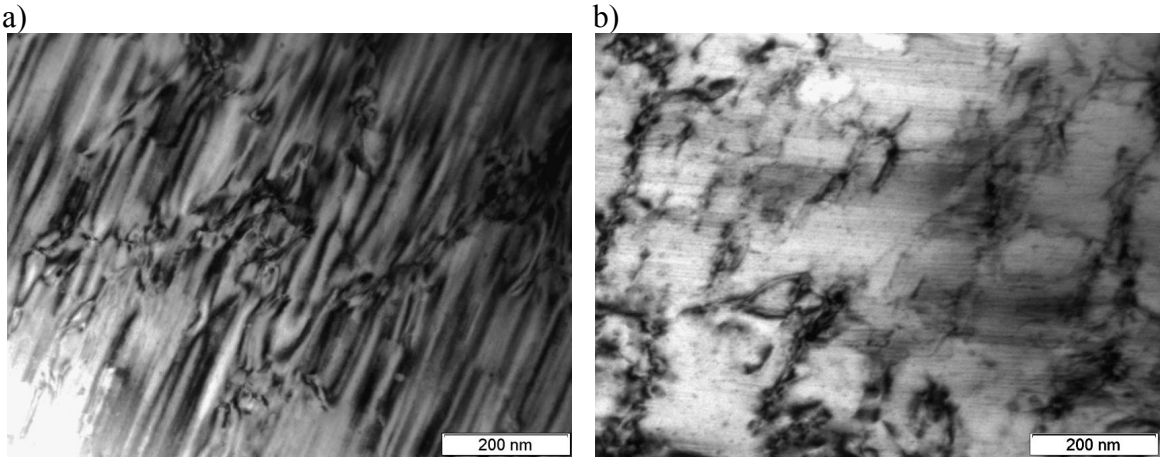

Figure 3.20. (a and b) BF TEM images of two regions in Co containing dislocations and a background of stacking faults. The region in b) is oriented in a way that makes the stacking faults becoming almost invisible.

The dislocation densities estimated from the eighteen regions observed by TEM in the Ni sample, assuming the two limits of the thickness range (100 and 200 nm), are presented in Table 3.4. The average dislocation density of laser clad Ni obtained from these values is (4.1 ± 3.2)×10^9 cm^{-2} and (8.3 ± 6.4)×10^9 cm^{-2} when the estimate in made considering the upper and lower limits of the thickness range, respectively.

Table 3.4. Dislocation densities (ρ) estimated for the eighteen regions observed by TEM and assuming that the thickness of all regions is 200 nm (middle column) or 100 nm (right column).

Region	ρ (t = 200 nm) **(cm^{-2})**	ρ (t = 100 nm) **(cm^{-2})**
1	6.16×10^{9}	1.23×10^{10}
2	0	0
3	2.68×10^{9}	5.36×10^{9}
4	1.86×10^{9}	3.72×10^{9}
5	2.21×10^{9}	4.41×10^{9}
6	0	0
7	1.45×10^{9}	2.91×10^{9}
8	6.51×10^{9}	1.30×10^{10}
9	5.11×10^{9}	1.02×10^{10}
10	5.98×10^{9}	1.20×10^{10}
11	8.45×10^{9}	1.69×10^{10}
12	3.46×10^{9}	6.91×10^{9}
13	0	0
14	9.25×10^{9}	1.85×10^{10}
15	8.46×10^{9}	1.69×10^{10}
16	0	0
17	6.66×10^{9}	1.33×10^{10}
18	6.14×10^{9}	1.23×10^{10}

3.6. Discussion

Both the mechanical and electrolytical polishing methods adopted in this work enabled obtaining extremely smooth surfaces. Nevertheless, the average roughness of the electropolished samples is slightly larger than that of the mechanically polished ones. Therefore, the electropolished samples were not used in the AFM cantilever-based tests, which were the only tests of this work where the depth of the test features (e.g. indentations, scratches and worn areas) is typically of the same order of magnitude as their R_a values.

The estimated values for the thickness of the oxide layer present at the surface of the samples are slightly larger than those found in the literature for metals at environmental conditions, which are usually on the order of a few nanometres [148, 165, 166]. This discrepancy can be attributed to two causes: the uncertainty on the position of the oxide-metal interface and on the sputtering rates of the nickel and cobalt native oxides (NiO, CoO and Co_3O_4 [165, 167]) for the used sputtering conditions. If it is assumed that the interface is found when the percentage of oxygen is half of its initial value, then the oxide layer thickness of Ni, Ni-21%Co, Ni-55%Co, Ni-85%Co and Co is reduced to 6, 28, 25, 25 and 12 nm, respectively, which are still slightly larger than the values presented in the literature. Therefore, apparently the main reason for the larger estimated thickness values is the fact that the sputtering rate used (that of FeO) is overestimated. The calibration of the sputtering rate in order to obtain exact values of the native oxide film thickness can be made with calibration samples, which is clearly out of the scope of this work. Even so, the Auger profiles (Figure 3.4) enable comparing the thickness of the oxide layer of the different Ni-Co samples, which is larger in the Ni-Co alloys than in pure Ni and Co, possibly due to the presence of complex Ni-Co oxides in the alloys.

The analysis of the bulk chemical composition of the samples revealed the presence of Fe and Cr impurities, which result from contamination of the coatings by the substrate during laser cladding processing. Nevertheless, the contamination by Fe and Cr is smaller than 4.5% (Table 3.2) in all the samples. Moreover, the distribution of Ni and Co in the samples is homogeneous which, in addition to the low dilution of the coatings by the substrates, shows that laser cladding is a reliable process for quickly obtaining high quality thick coatings.

All the samples contain micropores that may have been formed from chemical reactions or gas entrapment in the melt pool during laser cladding processing [168]. Nevertheless, the volume fraction of pores is smaller than 2% and the average size of the pores is submicrometric.

Although the grain structure was only analysed in pure Ni and Co, it can be expected that the other materials used in this work also present grains with dimensions of several tens of micrometers, since both the chemical nature and the processing conditions of these materials are similar to those of Ni and Co.

According to the Ni-Co equilibrium phase diagram (Figure 1.1), at room temperature, samples with Co weight percentages smaller than 68% are formed by the FCC α phase, while those with more than 80% Co are formed by the stable HCP ε phase. In the compositional range 68 to 80% Co, the alloys are a mixture of these two phases.

Nevertheless, previous works have shown that in alloys with Co percentages over ~ 68%, a microstructure formed of a mixture of α and ε' can be obtained, even for low cooling rates, in which ε' results from the α → ε' martensitic transformation on cooling [21]. The presence of the two phases in pure Co, for higher cooling rates (in the range 1×10^2 to 5×10^5 K/s, which comprises the typical cooling rates found in laser cladding [109]) has also been observed [169].

The XRD results show that the samples with Co content smaller than 68% Co are formed only by α, those with more than 80% Co contain ε'[•], and the Ni-73%Co alloy contains a mixture of the two phases.

Some authors [170-176] have suggested that ordering may occur in Ni-25%Co (ordered phase Ni_3Co), while others have not found evidence of its existence [177-181]. The presence of a superlattice, eventually in the Ni-26%Co alloy[••], is not detectable with XRD (see Figure 3.9.c) due to the great similarity in the X-ray scattering factors of Ni and Co atoms [129], i.e. these elements scatter X-rays with similar efficiency. An extensive review of previously published data concerning the possible existence of order in Ni-25%Co was carried out by Thompson [175, 182], where it has been concluded that long-range order is absent in this alloy and, if existent, only a small amount of short-range order would be present. The values reported in the literature for the critical temperature for order are in the range 700 to 750 ºC [174]. More recently, Garlipp *et al*. [176] found evidence of short-range order in Ni-25%Co by using measurements of electrical resistivity associated to isochronal annealing treatments in this alloy. Nevertheless, they concluded that the decomposition of short-range order tends to stabilize above 700 ºC and that quenching from a higher temperature (780 ºC in their

[•] The absence of the (200) peak of the α phase in the samples with Co content over 80% (Figure 3.9.g to i), which is the only peak of α that is not overlapped by a peak of ε', shows that, if existent, the amount of α in these samples is residual, as was confirmed by the TEM observations.

[••] The true composition of this sample is 25.6 ± 0.9 wt.% Co and, consequently, some sample regions may contain Co percentages of 25%.

experiments) is adequate to completely disorder the alloy. Since in powder injection laser cladding the material is submitted to high cooling rates, the disorder-order transformation on cooling in Ni-26%Co, if existent, is most probably suppressed.

The formation of a few precipitates in Ni and Co is due to the presence of small amounts of Fe and Cr impurities, which come from the substrate, and it can be expected that a few precipitates will also be present in the remaining Ni-Co samples.

The determination of ρ by TEM may involve several errors. In order to minimize modifications to the original dislocation configuration, in this work the TEM discs were cut from finely ground 50 to 60 μm foils using a low power Q-switched laser instead of the traditional punch cutting method [113] and dimpling of the discs was avoided. The errors resulting from the dislocation line length and sample thickness measurements were minimized by strictly following an optimized measurement protocol: tilting of the samples in order to maximize the number of visible dislocations present in the observed regions, as well as the measurement of lengths using the image analysis software Mocha. The largest measurement error introduced in the dislocation density calculations is usually associated to the sample thickness determination [164]. Although CBED is the most accurate method of determining sample thickness in crystalline materials [163], it is not easily achievable. Besides the need of having a well focused convergent beam and a sample oriented for a two-beam condition, the observed areas should be relatively flat and undistorted in order to avoid the influence of bending effects, and sufficiently thick in order to enable obtaining CBED discs with a relatively large number of intensity fringes, in this way improving the efficiency of the graphical method of Allen [162]. Finally, the choice of the magnification for the TEM observations may also affect the estimated ρ values. Nevertheless, one has to consider that the observed area cannot be too large due to the difficulty of identifying individual dislocation lines, or too small due to the large over- and underestimations of the dislocation density. Consequently, though TEM is the best method to determine the dislocation density of materials because it enables visualizing the dislocation lines, it may be disadvantageous from the statistical point of view in the case of heterogeneous distributions of dislocations.

The density of statistically stored dislocations (see definition in page 23) estimated by TEM for laser clad Ni was in the range $1-14\times10^{9}$ cm^{-2}. Dislocation densities in the range 10^{6} to 10^{8} cm^{-2} are found in annealed metals, whereas in plastically deformed metals values in the range 10^{11} to 10^{12} cm^{-2} can be reached [183]. Metals produced by laser cladding usually possess higher ρ values than in the annealed state [184], although these values should not be

as high as those found in plastically deformed metals. Therefore, the order of magnitude of 10^9 cm^{-2} obtained for the average dislocation density of laser clad Ni by TEM is physically consistent.

3.7. Conclusions

The topographical and structural characteristics of the Ni-Co samples produced by laser cladding of elemental powder are adequate for the tribo-mechanical study proposed in this work:

- The surface of these materials is extremely smooth and covered by an oxide layer, which is thicker in the Ni-Co alloys than in pure Ni and Co. The proportion of Fe and Cr contaminations coming from the substrate is low (less than 4.5%) and the chemical homogeneity of the coatings is good.
- The microstructure of the samples is simple, with a maximum number of two phases (in agreement with the Ni-Co phase diagram) and grains with dimensions of several tens of micrometers.
- A residual amount of pores and precipitates, both submicrometric, can be found in the samples, but neither their proportion (< 2%) nor their size (submicrometric) is likely to affect significantly the results.

Values on the order of 10^9 cm^{-2} have been measured for the density of SSDs in pure Ni by TEM observation of thin foils. This is a reasonable value for a metal processed by laser cladding.

4. CONTACT SCALE DEPENDENCE OF INDENTATION HARDNESS

The indentation response of the Ni-Co samples at different contact scales is analysed in this chapter. The samples were submitted to indentation tests with diamond indenters and loads from the μN to the N range. The factors responsible for the observed scale dependence of hardness are analysed.

4.1. Influence of load and alloy composition

The influence of contact scale on the indentation hardness of the Ni-Co samples was analysed by performing microindentation and ultramicroindentation tests using a Vickers indenter, and AFM cantilever-based nanoindentation tests using a DNISP tip.

4.1.1. Results

Figure 4.1.a shows the variation of hardness with chemical composition in the Ni-Co system, for three sets of tests with loads of 18 and 40 mN (ultramicroindentation) and 1 N (microindentation). Two aspects can be immediately retrieved from this figure: a) the hardness trend with composition is kept in all the range of loads used, but: b) H_i increases with decreasing load in all the Ni-Co system.

We will start by analysing the first aspect. The hardness of the samples tends to increase when the Co proportion increases up to 35% and then decreases with increasing Co content from 35 to 55%. The exception in this compositional range is the composition Ni-26%Co, which presents lower hardness than the alloys in its vicinity (clearly visible in the ultramicroindentation results). For Co percentages larger than 68%, the hardness of the alloys increases again, with the maximum hardness value obtained at approximately 80% Co.

Figure 4.1.b shows the nanohardness of the Ni-Co system (measured with the AFM cantilever-based system), in which a load of 57 μN was applied. The nanohardness values, besides being substantially larger than those retrieved from ultramicro- and microindentation tests, present a more undefined tendency with composition and, moreover, their scatter is higher. The influence of image convolution on the nanoindentation results was analysed by comparing the H_i values retrieved from nanoindentations in Ni and Co visualized with the DNISP tip (cross markers in Figure 4.1.b) and with a sharper Si tip (square markers in Figure 4.1.b). It was concluded that, even when convolution is greatly reduced by visualizing the nanoindentations with a Si tip, the hardness values in nanoindentation tests are still much larger and more scattered than in ultramicro- and microindentation ones.

a)

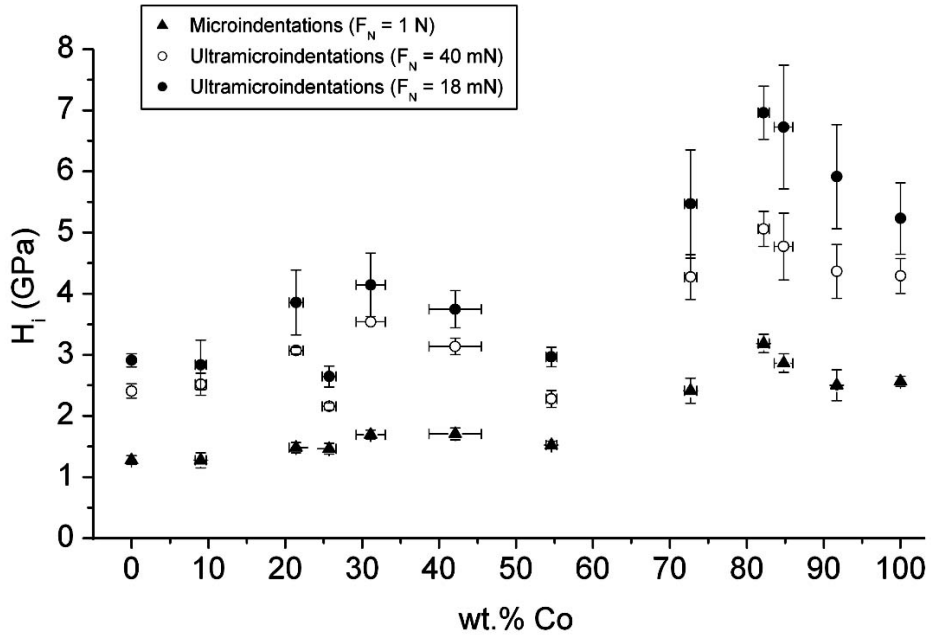

b)

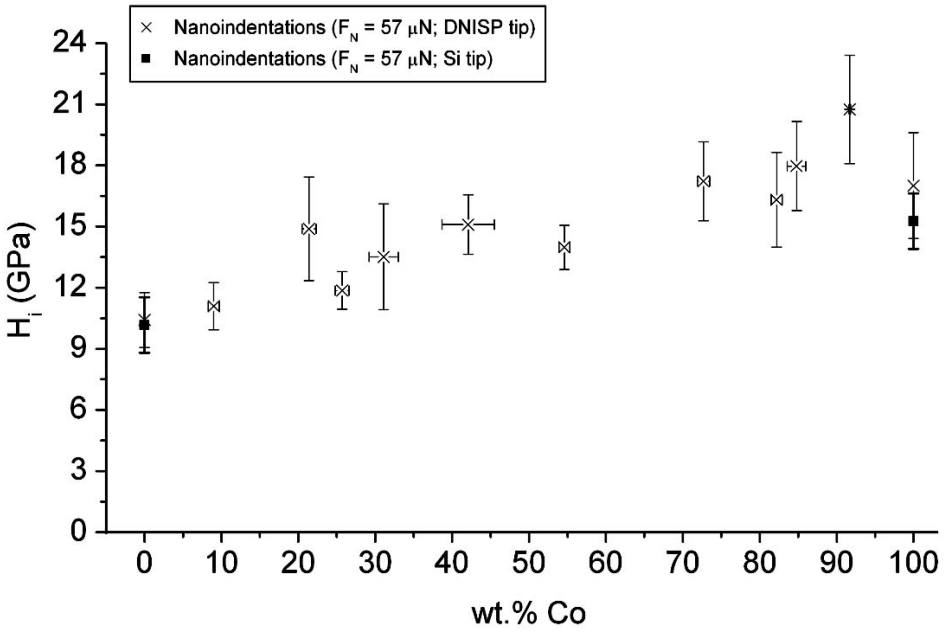

Figure 4.1. Variation of micro- and ultramicroindentation hardness (a) and nanoindentation hardness (b) with chemical composition in the Ni-Co system. A Vickers indenter was used in micro- and ultramicroindentation tests, whereas the nanoindentation tests were performed with a Veeco DNISP nanoindentation probe. Visualization of the nanoindentations was carried out with the DNISP tip in all samples and also with a Si tip in Ni and Co.

SEM images of hardness test features resulting from micro- and ultramicroindentation tests in Ni and Co can be seen in Figure 4.2. Small spherical pores in both samples can also be observed in the images. In most microindentation tests in Co and Ni-Co alloys belonging to the ε domain of the Ni-Co phase diagram (Figure 1.1), mechanical twins were formed during indenter penetration, as can be observed in Figure 4.2.b (see arrows in the figure)•.

AFM images of nanoindentations performed in Ni and Co (acquired with a Si tip) can be observed in Figure 4.3. These images, together with those of Figure 4.2, show that the width of the indentations is of a few tens of micrometers for microindentations, a few micrometers for ultramicroindentations and around 100 nm for nanoindentations, which corresponds to an indentation depth of some micrometers for microindentations, hundreds of nanometres for ultramicroindentations and some tens of nanometres for nanoindentations. Therefore, the nanoindentations are about one order of magnitude smaller than the ultramicroindentations and two orders of magnitude smaller than the microindentations.

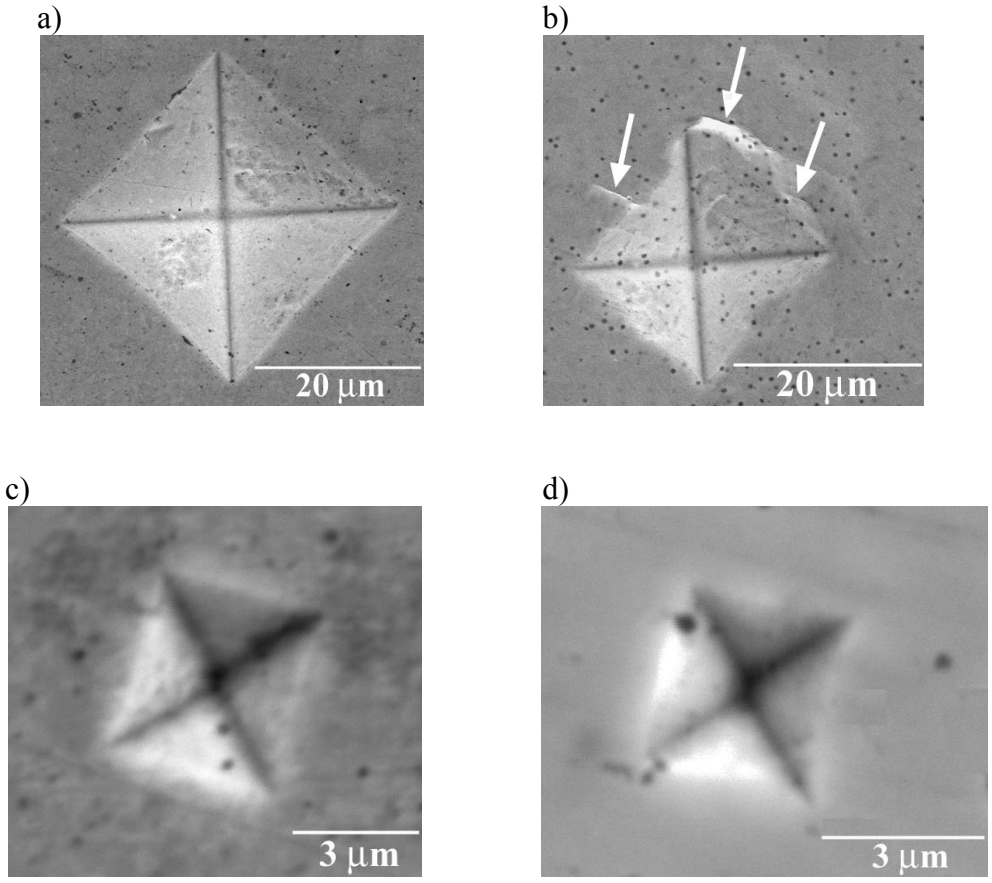

Figure 4.2. SE SEM images of Vickers microindentations (load = 1 N) and ultramicroindentations (load = 40 mN) in Ni (a and c, respectively) and Co (b and d, respectively). The samples contain small spherical pores which result from the laser cladding process. The white arrows in b) point to mechanical twins which were formed during indenter penetration.

• A discussion on this topic along with similar observations in microscratch tests will be made in §6.1.1.

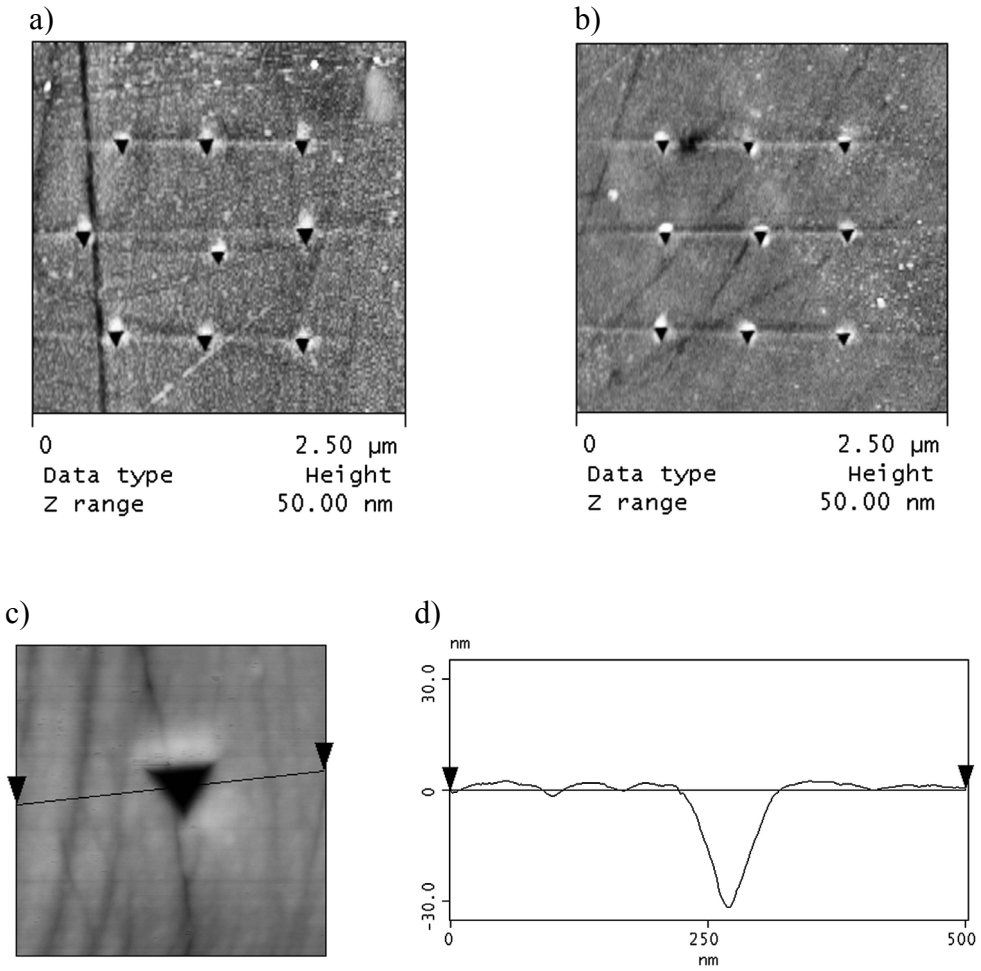

Figure 4.3. AFM topographic images of a group of nanoindentations in Ni (a) and Co (b) performed with a DNISP probe and a load of 57 µN. Topographic image (c) and profile (d) of a single nanoindentation in Ni, where the profile corresponds to the region defined by the straight line in the AFM image.

As can be observed from Figures 4.1.a and b, the influence of the applied load on H_i is similar for all the samples of the Ni-Co system, i.e. H_i increases with decreasing load. The Ni and Co samples were chosen for a detailed investigation of this effect (Figures 4.4.a and b, respectively). It was observed that, for indentation depths larger than 2 µm, the hardness of Ni and Co tends asymptotically to 1.3 and 2.2 GPa, respectively, as the load increases. Depending on the material metallurgical conditions (e.g. annealed or cold worked), hardness values in the range 0.6 to 2 GPa for Ni (> 99.0 wt.%), and 1.7 to 3.2 GPa for Co (99.9 wt.%), are found in the literature [139, 185]. This means that the asymptotic values, obtained for loads larger than 1 N (corresponding to penetration depths larger than 2 µm), are within the expected values for the bulk hardness $(H_0)^{\bullet}$ of these materials. Therefore, 1.3 and 2.2 GPa can be taken as the H_0 values of laser clad Ni and Co, respectively.

$^{\bullet}$ H_0 is defined by Eq. 1.28.

For indentation depths smaller than 2 μm, the hardness of both Ni and Co increases with decreasing depth, reaching values up to 11 and 16 GPa in Ni and Co, respectively.

Both the increase of hardness with decreasing load (or indentation size) and the less defined hardness trend with chemical composition in the case of nanoindentation results are caused by factors which become increasingly relevant as the contact scale decreases. In the following section some of the factors that can contribute to the contact scale dependence of indentation hardness observed in the Ni-Co system will be analyzed.

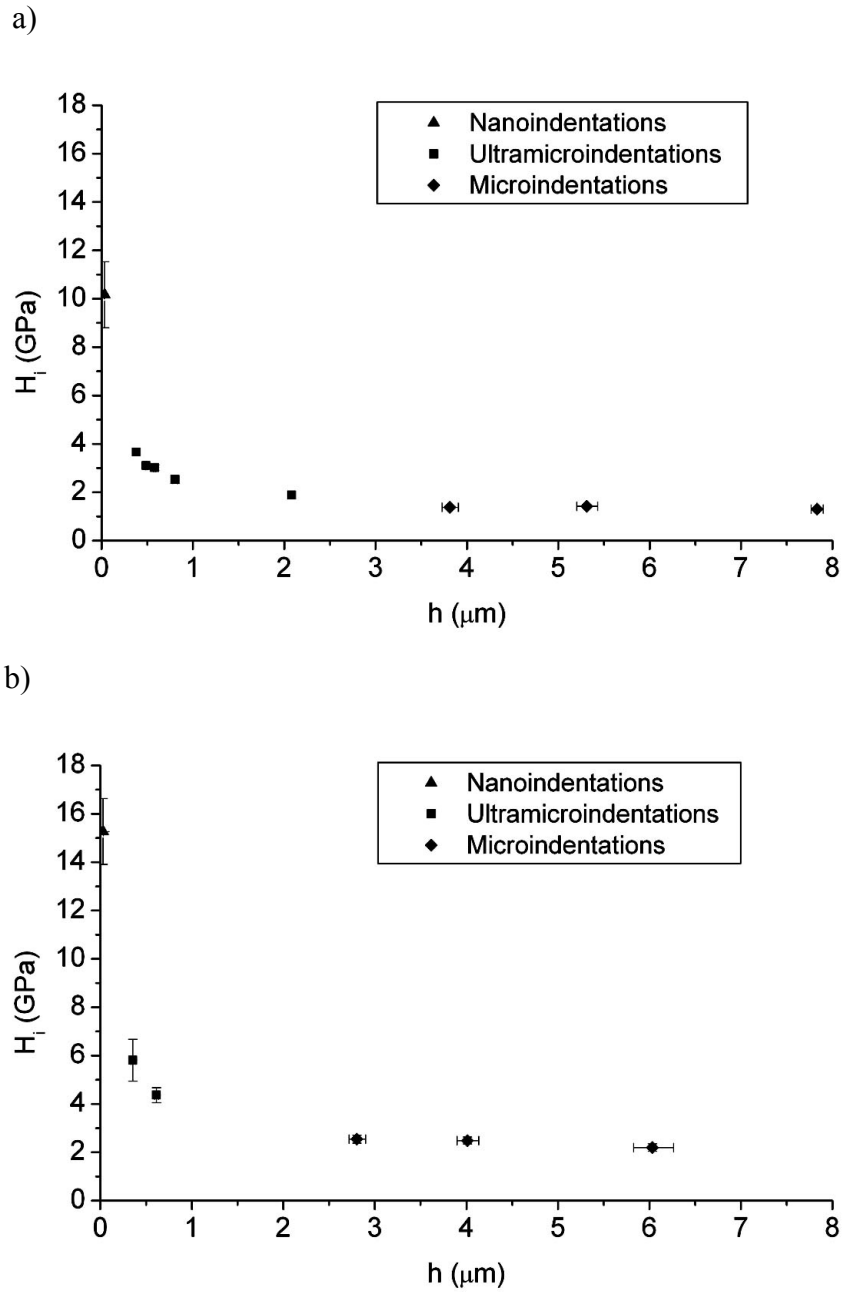

Figure 4.4. Variation of indentation hardness with indentation depth in Ni (a) and Co (b). The nanoindentation hardness values presented in the plots are the ones given by the square markers in the plot of Figure 4.1.b, i.e. those without the influence of image convolution.

4.1.2. Discussion

4.1.2.1. Compositional dependence of hardness

The variation of the hardness of the Ni-Co samples in the compositional range 9 to 55% Co can be attributed, most plausibly, to solid solution strengthening (SSS), since the alloys are formed only by the α phase, as was seen in the XRD results of Figures 3.9.b to e. The largest influence of the SSS effect occurs for a Co content of about 35%, which corresponds approximately to the middle of the compositional range (up to 68% Co) where the alloys are formed only by the α phase, resulting in a local maximum of H_i at this composition. Nevertheless, the contribution of SSS to hardness is not too strong because Ni and Co have similar atomic radius (~ 1.25 Å in both cases [186]), valence (2 valence electrons on the 4s shell) and shear modulus (76 and 82.6 GPa, respectively [139]). Therefore, the addition of Co atoms produces only minimum spherical distortions in the Ni lattice and slightly increases the frictional resistance to dislocation motion [92].

The alloy Ni-26%Co presents a minimum of hardness as compared to the other alloys in its compositional vicinity. It was discussed in §3.6 that there is a possibility of formation of short-range order for a Co proportion of 25% (ordered phase Ni_3Co), although the high cooling rates associated to the laser cladding process are propitious for maintaining the alloy in a disordered state after cooling. Furthermore, because the movement of dislocations through regions of short-range order reduces the degree of local order, thus increasing the energy of the material, extra work must be provided in order to move the dislocations across such regions. Consequently, the presence of short-range order tends to strengthen the material, which is contrary to what is observed for the Ni-26%Co alloy. Therefore, it is unlikely that the decrease in hardness in the short compositional range around 25% Co is solely related to a simple ordering effect. Still, this local minimum in the hardness trend for the alloys within the single α-phase region was detected in all the load ranges of indentation tests, showing that this is an intrinsic characteristic of the Ni-Co system in this compositional range.

The hardness increase for Co percentages over 68% is caused by the presence of ε' martensite in these samples, as could be observed from the XRD results of Figures 3.9.f to i. On one side, the hexagonal structure of this phase results in a smaller number of slip systems when compared to the cubic α-phase and, on the other side, the formation of stacking faults, which fill the martensite plates, involves the generation of a large number of $\frac{a}{6} < 11\bar{2} >$ partial dislocations on the octahedral planes of the parent FCC phase (or equivalently, on the basal

plane of the martensitic phase) [187]. Therefore, not only the plastic deformation of the HCP phase is statistically unfavourable in relation to that of the FCC phase, since it is less probable that the slip system is well oriented in relation to the stress axis in the HCP phase, but also the density of statistically stored dislocations is higher in this phase. Both these factors tend to increase the bulk hardness of the samples.

4.1.2.2. Indentation size effect

The main factors which may be responsible for the indentation size effect, i.e. the trend of hardness increase with decreasing load, observed for all the Ni-Co system (Figures 4.1 and 4.4), are analysed in the following sections.

Stacking fault energy

As previously mentioned in §1.1, the staking fault energy of the Ni-Co system presents an approximately linear decrease with increasing proportion of Co up to ~ 70% Co (see Figure 1.2). However, the load dependence of hardness does not seem to be affected by this variation of the stacking fault energy (see Figure 4.1). This observation is in good agreement with those of Elmustafa and Stone [188] and Rester *et al*. [189], who performed indentation tests with different loads in several FCC materials of different stacking fault energy, and found no relation between the ISE observed in these materials and the stacking fault energy.

Hall-Petch effect

The pile-up[•] of dislocations at grain boundaries (Hall-Petch effect) can affect the hardness values of polycrystalline materials [190]. For indentations smaller than grains, this pile-up is more probable to occur in larger indentations than in smaller ones, since plastic deformation is initiated at the region in the neighbourhood of the indenter. Therefore, the Hall-Petch effect would have larger influence in the case of microindentations than in ultramicro- and nanoindentations, which are much smaller than the grain size of the Ni-Co samples. However, the Hall-Petch effect is contrary to the hardness increase observed when the indentation size decreases and hence cannot explain the observed ISE. Moreover, the largest indentations performed in the Ni-Co samples are less than 8 μm deep, which is much smaller than the grain size of the samples and, consequently, the influence of grain boundaries in the

[•] In this work, as well as in the literature, the term "pile-up" is used to describe both the accumulation of dislocations against an obstacle and the accumulation of material against the faces of an indenter.

movement of dislocations is even smaller when considering the tri-dimensional shape of the grains and indentations. Therefore, it can be concluded that grain size is not responsible for the load dependence of the hardness in the Ni-Co samples.

Microporosity

Another factor that can contribute to the load dependence of hardness is the microporosity found in the samples (§3.4). Nevertheless, not only the volume fraction of micropores is smaller than 2%, but also the majority of the pores have submicrometric dimensions. Chen *et al*. [191] recently used a finite element algorithm based on the Gurson model [192] for the plastic deformation of porous materials to evaluate the influence of porosity on indentation hardness. These authors found that the hardness of a sample with a volume fraction of pores of 5% should be only 4% lower than that of a dense sample of the same material. This means that the microporosity present in the Ni-Co samples cannot explain the observed hardness variation with applied load, which goes up to nine times from micro to nanoindentation tests.

Native oxide layer

The native oxide layer present at the surface of the Ni-Co samples may have a contribution to the measured hardness when the indentation depth is comparable to the oxide thickness. Therefore, since the nanoindentations performed in the samples are only a few tens of nanometres deep, the oxide layer may have a contribution to the higher nanoindentation hardness values in comparison to ultramicro- and microindentation ones.

A value of about 6 GPa for the hardness of NiO was measured by Qi *et al*. [193] using Vickers indentation tests in thick NiO layers (thickness in the range 122 to 218 μm) thermally grown from pure Ni substrates. For one side, this value is only 2.3 GPa larger than that obtained from the ultramicroindentation tests in Ni using the smallest load (13 mN), where the influence of the oxide layer can be neglected due to the large depth of the indentations (~ 380 nm), and, for the other side, it is much smaller than the 10 GPa measured from the nanoindentation tests in Ni. Therefore, although the oxide layer may contribute to the higher nanoindentation hardness values which were measured, it cannot be the main factor responsible for the observed ISE[•].

[•] Nevertheless, the effect of native oxide layers on hardness will be further discussed in §6.1.2.

Strain hardened layer

The strain hardened layer of material in the near surface region [194] may have an important contribution to the observed ISE.

As previously described (§2.1.2), polishing of the Ni-Co samples was carefully carried out using a 0.1 μm diamond particles suspension, leading to a mirror-like surface with a maximum scratch depth of only a few nanometres (Figure 3.2). According to Samuels [195], the thickness of the deformed layer in mechanically polished metals is smaller than 15 times the depth of surface scratches, i.e. in the present case this value should not exceed 100 nm. If the deformed layers created by previous polishing steps are not fully removed by subsequent ones, the strain hardened layer may extend up to a few tens of micrometers [196]. However, these extreme values do not occur in the Ni-Co samples prepared in this work, since their hardness becomes constant for indentation depths larger than about 2 μm (Figure 4.4).

Therefore, strain hardening of the material due to mechanical polishing may affect to some extent the nano- and ultramicroindentation results. The influence of mechanical polishing on the hardness of the samples will be further analysed in the next section (§4.2) by comparing the results from nanoindentation tests in mechanically polished and electropolished samples.

Surface free energy

When the indentation depths are very small, the surface free energy of the material may have a non-negligible influence on hardness, due to the large surface-to-volume ratio of the indentations. Jäger [106] proposed a model for the contribution of SFE to the hardness (see description of the model in §1.4.2). According to the observations of Jäger, it can be concluded that the three conditions necessary for the influence of SFE on hardness to be considered are present in the nanoindentation tests of this work: 1) the Ni-Co samples are relatively ductile and have a large SFE, as most metals do; 2) the DNISP tip is sharp; 3) the indentations are shallow. Therefore, Eq. 1.45 can be extended to the DNISP tip geometry, resulting in a contribution of SFE to hardness given by:

$$\Delta H_{SFE} = \kappa \frac{E_s}{h}, \tag{4.1}$$

with the geometrical constant $\kappa = 1.532$ (see Appendix for details). If the Vickers geometry is considered instead of the DNISP one, $\kappa = 0.157$.

Figure 4.5 shows the variation of ΔH_{SFE} with indentation depth, obtained from the application of Eq. 4.1 to the DNISP and Vickers geometries and considering E_s = 2.2 J/m^2 [106] for the Ni-Co system•. As could be expected, the influence of SFE on hardness is larger when using the DNISP geometry instead of the Vickers one, since the former is sharper. However, the contribution of SFE to the hardness of the Ni-Co samples is only significant when the indentation depth is on the order of a few tens of nanometres or smaller, which is the case of the nanoindentations performed with the DNISP tip. For extremely sharp geometries, such as those of regular AFM tips, κ can reach very high values (see end of Appendix for an analysis of the influence of tip apex angle on the value of κ), thus resulting in larger ΔH_{SFE} values. Nevertheless, the ΔH_{SFE} values estimated for shallow depths are small in comparison to the hardness values measured from the nanoindentation tests. Therefore, SFE cannot be the only responsible for the observed hardness increase.

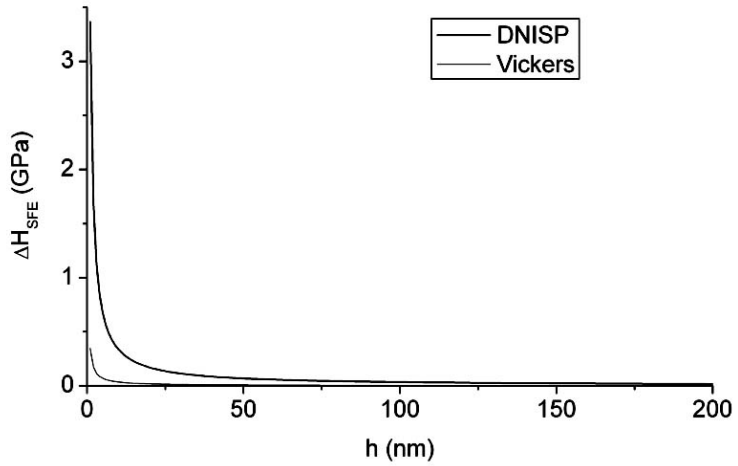

Figure 4.5. Contribution of surface free energy to the hardness of the Ni-Co samples as function of indentation depth, according to the application of the Jäger model both to the DNISP and Vickers geometries.

Plastic strain gradients

The indentation of a crystalline material by a pyramidal indenter generates a plastic strain gradient in the material, whose magnitude increases with decreasing indentation depth [58, 87]. Because the strain gradient is accommodated through the creation of geometrically necessary dislocations, the increase of the magnitude of the strain gradient with decreasing size of the deformed region results directly in an increase of the density of GNDs. The increase of the density of GNDs strain hardens the material and, consequently, its hardness

• Because the E_s values of Ni and Co at zero temperature are, respectively, 2.45 and 2.55 mJ/m^2 [197], and the SFE of metals slowly decreases with increasing temperature, a value of 2.2 J/m^2 for the SFE of the Ni-Co system is an acceptable estimate.

increases with decreasing deformation scale. This effect can be described by the Nix-Gao model (see description of the model in §1.4.2). The equation that results from this model (Eq. 1.32) can be written in the form of a linear equation:

$$\left(\frac{H}{H_0}\right)^2 = 1 + h^* . \left(\frac{1}{h}\right). \tag{4.2}$$

Equation 4.2 can be fitted to the micro- and ultramicrohardness results obtained in this work, as shown in Figures 4.6.a and b[•]. As can be observed, the Nix-Gao equation fits extremely well to the experimental data, with a correlation factor R > 0.98. The value of the characteristic length h^* (the slope of the fitting line) is 2.451 and 2.023 μm for Ni and Co, respectively. This parameter can be related to the density of the dislocations statistically stored in the crystal lattice (Eq. 1.39), which are independent of strain gradients. Therefore, the density of SSDs in Ni and Co can be estimated by introducing in Eq. 1.39 the h^* values determined from the fitting, along with $\theta_{is} \approx 20^o$ for the Vickers indenter, $f = 1.9$ and $b \approx 0.25$ nm[••] both for Ni and Co. The estimated ρ_s is 4.7×10^9 and 5.7×10^9 cm^{-2} for Ni and Co, respectively.

The ρ_s value obtained for Ni is in remarkably good agreement with that estimated by TEM (on the order of 10^9 cm^{-2}, as presented in §3.5), which shows that the Nix-Gao model is physically sustainable and, consequently, GNDs have a significant contribution to the ISE observed experimentally.

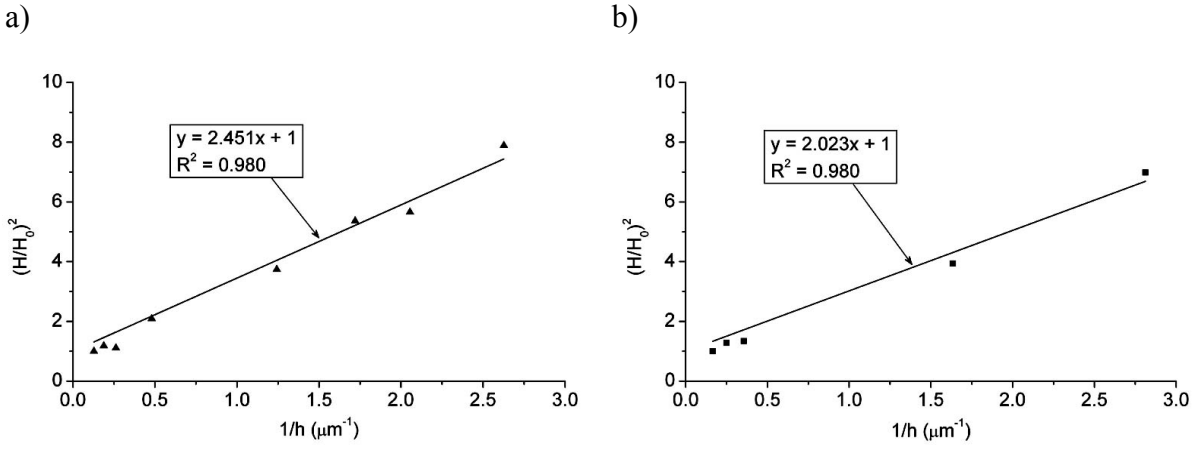

Figure 4.6.Fitting of Nix-Gao equation to the micro- and ultramicroindentation hardness data of Ni (a) and Co (b) shown in Figures 4.4.a and b, respectively.

[•] The nanohardness was excluded from the fitting due to the possible influence of SFE and oxide layers that, as previously mentioned, may have an important contribution at very small deformation scales.

[••] The magnitude of the Burgers vector of perfect dislocations in FCC and most HCP metals (including Co) is equal to $a/\sqrt{2}$ and a, respectively, where a is the lattice parameter [93].

Summary

The analysis presented in the previous points suggests that the most probable causes for the observed indentation size effect in the Ni-Co samples are the strain hardening effects caused by the increase of dislocation density, which become relevant when the indentation depth is smaller than 2 μm, and the influence of surface free energy, which becomes noticeable for nanometric indentation depths. The increase of dislocation density may have two origins: the deformed surface layer, originated by the sample surface preparation (mechanical polishing in the present case), and the increase of the density of GNDs as the deformation scale decreases.

According to the Taylor hardening model [90], an increase of the total dislocation density (ρ_T), which includes both the SSDs and GNDs, results in an increase in the shear yield stress (τ), given by:

$$\tau \propto Gb\sqrt{\rho_T}\ , \tag{4.3}$$

Assuming that both the von Mises criterion for plastic flow ($\sigma_Y = \sqrt{3}\tau$) and the Tabor relation ($H_i = 3\sigma_Y$) are applicable to the Ni-Co samples, this increase of τ results in an increase of the hardness of the material.

Although the Nix-Gao model has been developed to take into account only the influence of GNDs (see §1.4.2), the adjustment of Eq. 4.2 to the micro and ultramicrohardness values of Ni and Co is remarkably good (Figure 4.6). Eq. 4.2 works well even for mechanically polished samples because the characteristic length h^* depends on the initial dislocation density of the material and, consequently, the effect of mechanical polishing is included in h^*. Therefore, the observed ISE can be accurately described by the Nix-Gao equation, at least for indentation depths larger than 100 nm, where surface free energy effects can be neglected.

For nanometric indentation depths, the influence of surface free energy on hardness should be considered, especially when using sharp indenter geometries.

The results presented in this work suggest that Eqs 4.1 and 4.2 can be combined and used as an analytical model to predict hardness variations with depth, by assuming that surface free energy and dislocation density effects are independent. This assumption leads to:

$$H_{TOT} = H_0 + \Delta H_{dislocations} + \Delta H_{SFE} = H_0\sqrt{1+\frac{h^*}{h}} + \kappa\frac{E_s}{h}, \tag{4.4}$$

where H_{TOT} is the measured hardness at each indentation depth, $\Delta H_{dislocations}$ is the contribution to hardness arising from the Nix-Gao equation, and ΔH_{SFE} is the contribution arising from surface free energy.

The hardness data of Ni and Co is plotted in Figures 4.7.a and b, respectively, along with the hardness values calculated with Eq. 4.4, using the value of κ for the DNISP indenter•. The representative strain (ε_r) generated in the samples by the Vickers indenter is different from that produced by the DNISP indenter. Considering $\varepsilon_r \approx 0.2 \tan \theta_{is}$ [25] and θ_{is} of about 20º for the Vickers indenter and 42º for the DNISP indenter, ε_r is about 0.07 and 0.22 for indentations performed with the Vickers and DNISP indenters, respectively. Figure 4.7 shows that, within the limits of experimental error, the experimental values agree remarkably well with the theoretical curve.

Equation 4.4 has been recently validated by Ma *et al*. [198] in nanoindentation hardness data of electrodeposited Ni films (thickness of 3 μm) subjected to 0% and 10% tensile strains, tested with a Berkovich indenter. These authors concluded that the ISE observed in the Ni films can be attributed both to the increase of the dislocation density in the material and to its surface free energy, as proposed in the present thesis.

• This value of κ is used because, as mentioned earlier, SFE effects are only noticeable for nanometric indentation depths.

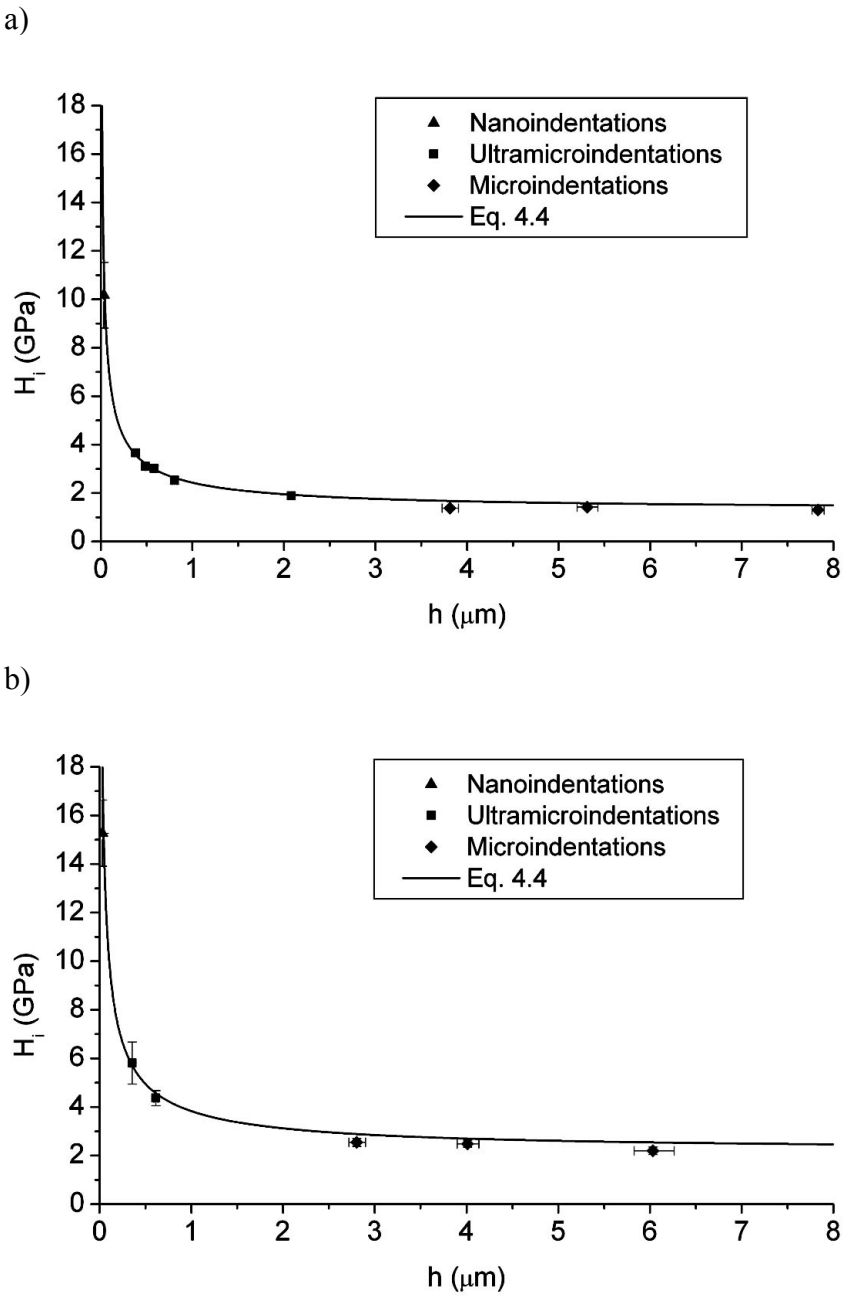

Figure 4.7. Comparison of the experimental hardness data (including nanoindentation data) for Ni (a) and Co (b) with the hardness values obtained from Eq. 4.4.

4.2. Influence of surface finishing and crystallographic anisotropy

As mentioned in the previous section, the component of ISE due to the increase of dislocation density can be divided in two parts: one is due to the increase of the density of statistically stored dislocations caused by mechanical polishing of the surface, and the other is due to the increase of the density of geometrically necessary dislocations caused by the increasing magnitude of plastic strain gradients with decreasing contact scale. In this section, these two contributions are separated by analysing hardness data resulting from displacement sensing

nanoindentation tests with a conospherical indenter[•] in a few mechanically polished and electropolished samples of the Ni-Co system.

To analyse the influence of crystallographic anisotropy on the results, a series of DSN tests were also performed on a Ni (100) monocrystal and the results are compared with those obtained for the polycrystalline samples. DSN was also used to analyse the influence of chemical composition on H_i, E and the combined parametric ratio H_i/E, which is related to the plasticity index ψ (Eq. 1.14) and, consequently, to the tribological response of the material.

4.2.1. Results

Figure 4.8 shows AFM topographic images and the corresponding profiles of nanoindentations performed in mechanically polished Ni, Co and in a Ni (100) monocrystal using a load of 6 mN. The width of all indentations produced in the DSN tests is smaller than 2 μm, which is much smaller than the grain size of the samples.

In the nanoindentations performed in polycrystalline Ni and Co shown in Figures 4.8.a and c, respectively, the pile-up of material against the sides of the indenter presents a two-fold symmetric distribution, while in the nanoindentation performed on the Ni (100) monocrystal the pile-up is four-fold symmetric (Figure 4.8.e). The four-fold symmetry pile-up in Ni (100) results from slip along the four {111} planes in the FCC structure, which make an angle of ~ 54.74º with the (100) plane, while the two-fold symmetry pile-up in polycrystalline Ni and Co is related to the particular grain orientation in the region where the indentation was performed. Although an explanation for this last case is not possible due to the lack of knowledge of the grain orientations, comparison of Figures 4.8.a and e shows that crystallographic anisotropy plays an important role on the deformation behaviour of polycrystalline samples when the indentation size to grain size ratio is small. The topographic profiles of the nanoindentations performed in Ni (Figure 4.8.b) and Co (Figure 4.8.d) show that the height of the pile-ups is small when compared to the residual indentation depth (note that the Z axis in the topographic images is magnified as compared to the X and Y ones). Moreover, because the nanoindentations were visualized with the conospherical tip, which is extremely blunt when compared to regular AFM tips, image convolution by the tip shape occurs and hence the width of the pile-ups should be even smaller than that retrieved from the AFM images. In this way, the contribution of pile-up to the contact area was assumed to be negligible in the analysis of the nanoindentation results.

[•] This indenter geometry was chosen to minimize the influence of the indenter-to-grain orientation on the hardness results, since the size of the indentations is much smaller than the grain size.

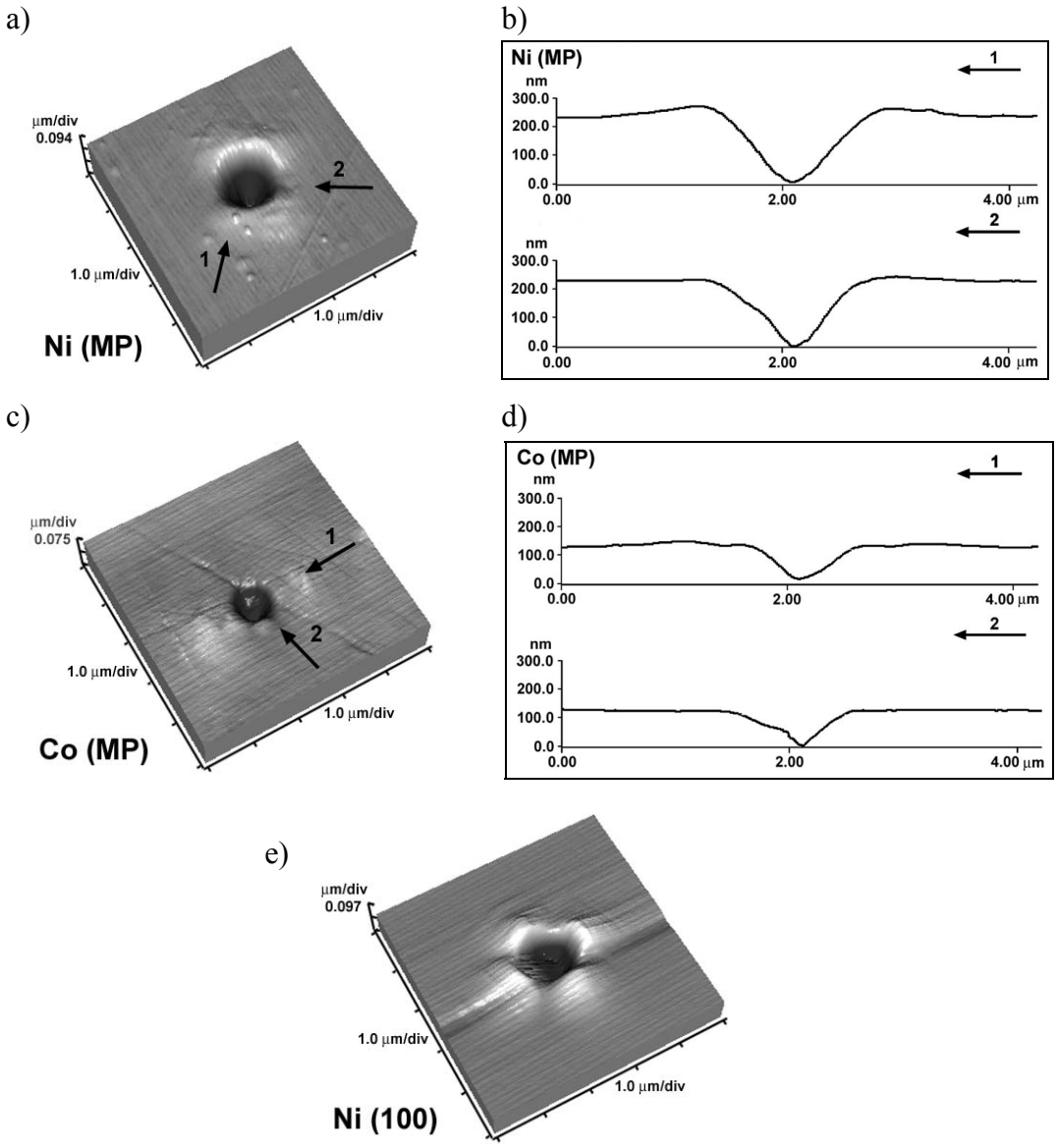

Figure 4.8. AFM topographic images of nanoindentations performed in mechanically polished Ni (a), Co (c) and Ni (100) (e), using a conospherical indenter and a load of 6 mN. Topographic profiles of the nanoindentations in Ni (b) and Co (d). The direction of the profiles is given by the black arrows in the topographic images of the nanoindentations.

Figures 4.9.a and b show the variation of hardness with indentation depth and surface finishing method (mechanical or electrolytical polishing) in Ni and Co, respectively. Mechanical polishing induces an increase of the hardness of the material, which can be higher than 1 GPa, both in Ni and Co. Nevertheless, independently of the surface finishing method, the hardness increases with decreasing depth both in Ni and Co, though the size effect is less pronounced in electropolished samples. Moreover, indentation size effect is easier to observe in Ni than in Co due to the smaller scattering of the hardness values in the former material. As can be observed from Figures 4.9.a and b, the difference in the scattering of the hardness values of Ni and Co is also independent of the surface finishing method.

Figure 4.9.c shows the depth dependence of the hardness of Ni and the Ni (100) monocrystal, both mechanically polished. The hardness of the poly- and monocrystalline samples is very similar and only at indentation depths larger than 250 nm the hardness of the polycrystal is slightly smaller than that of the monocrystal.

Figures 4.10.a and b show the variation of Young's modulus (E) with indentation depth in Ni and Co, respectively. In the range of used loads, the values of E are not too sensitive to indentation depth. The E value of Ni and Co found in the literature, obtained under compressive conditions, is 207 and 183 GPa for Ni and Co, respectively [139] and, within the experimental error, the E values obtained from the DSN tests compare well with the literature ones.

Of further interest is the observation that, on the contrary to hardness, the scattering of the E values is larger in Ni than in Co. The scattering of E in Ni ranges from 110 to 250 GPa, while in Co, values between 160 and 210 GPa were measured. Figure 4.10.c shows the Young's modulus of Ni and the Ni (100) monocrystal. It can be observed that the E values measured in Ni (100) are located in the upper portion of the range of E values obtained for polycrystalline Ni and the scattering of the E values in the monocrystal is much smaller than in the polycrystal.

Figures 4.11.a and b show, respectively, the variation of H_i and E with chemical composition in the Ni-Co system (the tested samples are Ni, Ni-21%Co, Ni-60%Co, Ni-85%Co and Co, all mechanically polished). The samples were tested using three different loads: 2.5, 5 and 10 mN. The hardness increase with decreasing load (or indentation depth) previously observed in pure Ni and Co tested with DSN is also observed in the Ni-Co alloys, and the experimental scattering of H increases for the Co-rich samples. The hardness presents an increasing trend for higher Co content, reaching its maximum value for the Ni-85%Co alloy (Figure 4.11.a). The highest hardness value in this alloy, reached for the lowest testing load (2.5 mN), is 5.5 GPa. Within the experimental error, the alloy composition does not seem to greatly affect the average value of the Young's modulus of the samples (Figure 4.11.b). The experimental scattering of E tends to decrease for the Co-rich samples, in opposition to what occurs with the hardness of the Ni-Co samples. Figure 4.11.c shows the hardness to Young's modulus ratio (H_i/E) as function of composition, calculated from the results presented in Figures 4.11.a and b. It is interesting to note that, within the experimental error, H_i/E is not overly sensitive to load. The value of this parameter is constant up to a Co content of 60%, with an approximate average value of 0.02. For Co concentrations of 85% a clear increase from 0.02 to 0.03 is observed, followed by a slight decrease for pure Co.

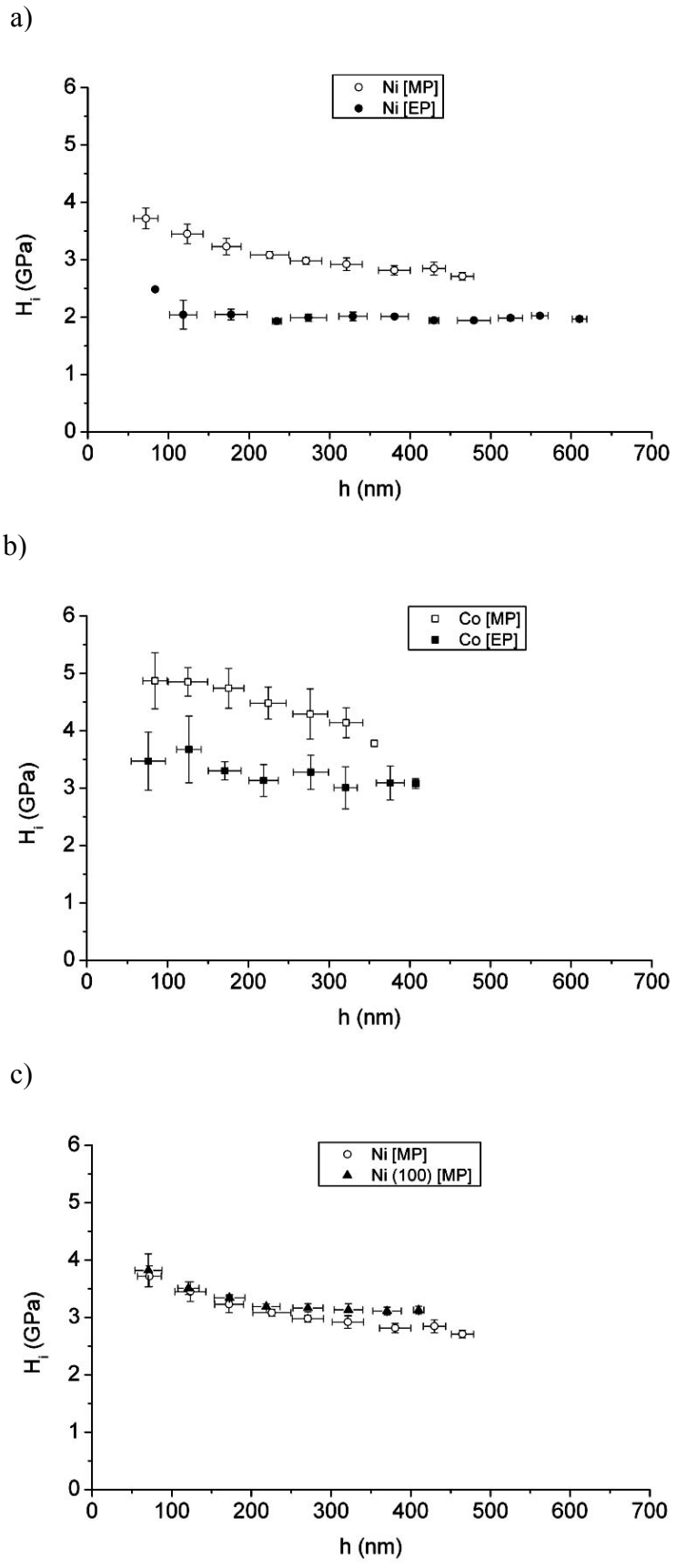

Figure 4.9. Variation of H_i with h and surface finishing method in Ni (a) and Co (b). (c) Variation of H_i with h in Ni and the Ni (100) monocrystal. MP and EP stand for mechanically and electrolitically polished samples.

a)

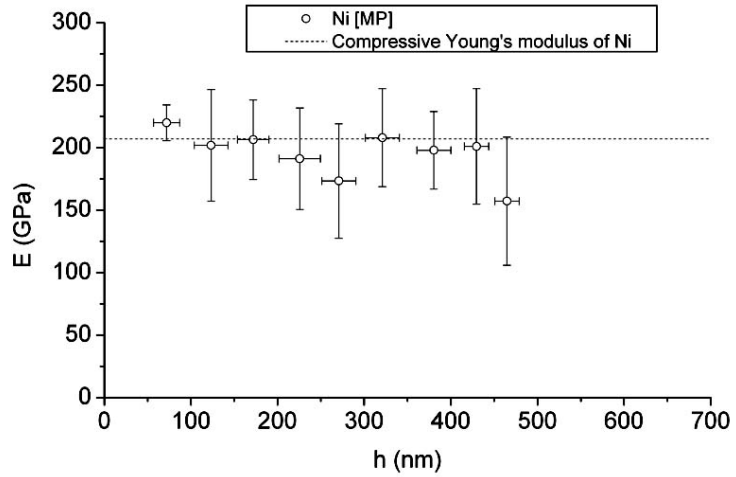

b)

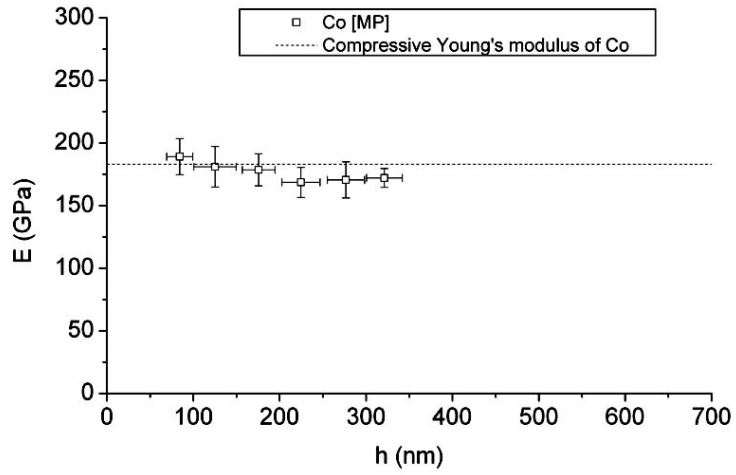

c)

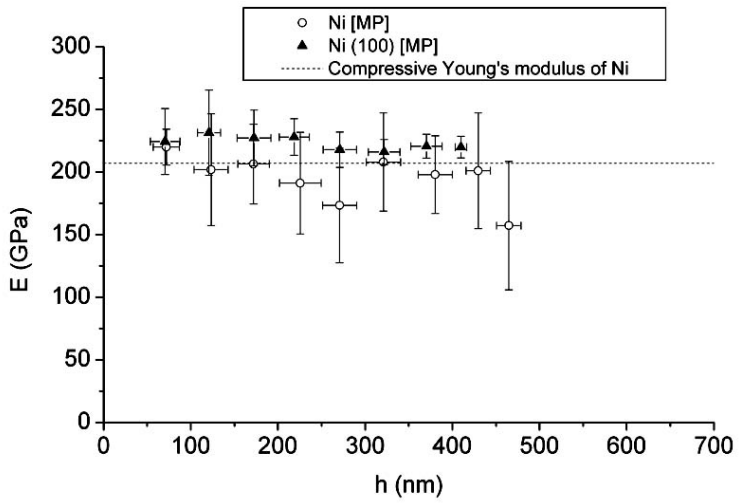

Figure 4.10. Variation of *E* with *h* in Ni (a) and Co (b). (c) Variation of *E* with *h* in Ni and the Ni (100) monocrystal. Values of *E* obtained under compressive conditions [139] are also shown for comparison.

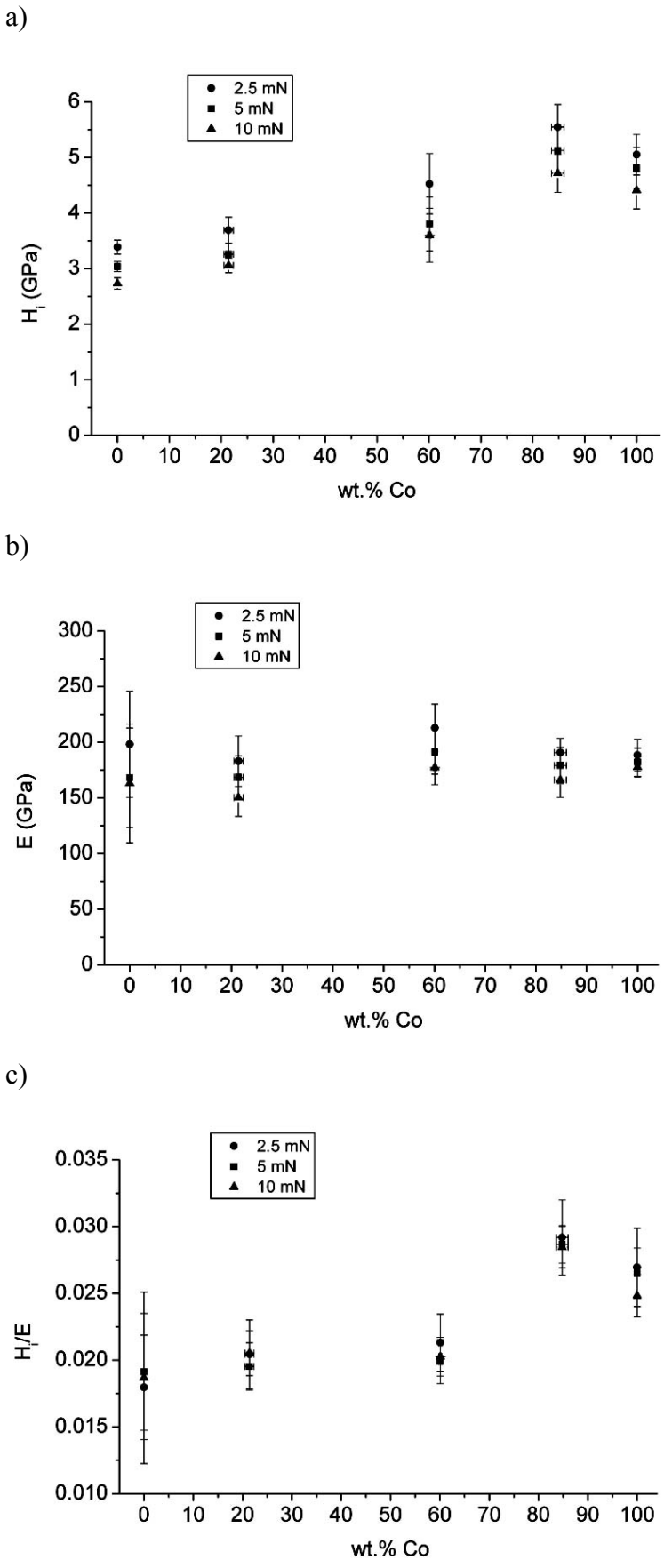

Figure 4.11. a) Variation of H_i (a), E (b) and H_i/E (c) with composition in the Ni-Co system.

4.2.2. Discussion

The comparison of the results obtained in the mechanically polished and electropolished samples (Figures 4.9.a and b) shows that, although indentation size effect can be observed in both conditions, the strain hardened layer, which results from mechanical polishing, can increase the material's hardness up to 1.5 GPa, both in Ni and Co. An estimation of the increase of dislocation density due to mechanical polishing can be made by using the Taylor hardening model (Eq. 4.3), the von Mises yield criterion ($\sigma_Y = \sqrt{3}\tau$) and the Tabor relation ($H_i = 3\sigma_Y$). By introducing the hardness values presented in Figure 4.9 into the previous equations, one can conclude that the mechanical polishing procedure, although carefully carried out with a 0.1 μm diamond particles suspension, can lead to a two to three times increase of the dislocation density in the near-surface region of the material.

The contact between the samples and the conospherical indenter is first established with the spherical portion of the indenter. Swadener *et al*. [96] have shown that hardness measurements with spherical indenters should not present any depth dependence, contrary to what occurs with conical and pyramidal indenters. The reason is that the extension of the Nix-Gao model to a spherical geometry does not result in an increase of the density of GNDs for decreasing penetration depth but for decreasing curvature radius of the spherical indentation (Eq. 1.37). Therefore, for a perfectly spherical indenter, indentation size effects due to depth dependent strain gradients do not occur. However, ISE was observed in all the samples, independently of the surface polishing method. The apparent contradiction between the DSN results of this work and the Swadener *et al*. approach can be understood by looking to the information retrieved from the indenter shape calibration procedure carried out using fused silica (Figure 2.27.a). This procedure showed that the geometry of the conospherical indenter deviates from the ideal spherical geometry, even for the smallest contact depths, where only the spherical part of the conospherical indenter contacts the sample. One can expect that this deviation becomes increasingly relevant as the penetration depth decreases. Therefore, deviations from the perfect spherical geometry become increasingly relevant as the penetration depth decreases and strain gradient related effects increasingly affect hardness as the contact scale decreases. The combination of these two factors explains the size effect observed in this work for the indentations performed with the conospherical indenter.

The results in Figures 4.9.a and b also showed that the hardness anisotropy is higher in polycrystalline Co than in polycrystalline Ni: the dispersion of the hardness values in Ni is about 10%, whereas in Co it can be higher than 20%. This difference results from the lower

number of slip systems in Co than in Ni (3 and 12, respectively [92]), which allows larger differences in orientation between the slip plane and the stress axis in Co. Moreover, the high number of slip systems in Ni and the absence of stress-induced transformations (e.g. martensitic transformation) and secondary deformation mechanisms such as twining make this material relatively isotropic in terms of plasticity, which can explain the similarity of hardness results in poly- and monocrystalline Ni (Figure 4.9.c).

Regarding the Young's modulus, no noteworthy size effect could be observed. The average value of E of Ni is similar to that of Co (180 and 185 GPa, respectively) but, more importantly, the scattering is larger in Ni-rich than in Co-rich polycrystalline samples (Figure 4.11.b). In fact, while the scattering of the experimental values of E in Ni can be higher than 100 GPa, in Co it does not exceed 50 GPa (see Figures 4.10.a and b, respectively). Moreover, the dispersion of E in monocrystalline Ni is much smaller than in polycrystalline Ni (Figure 4.10.c), suggesting that Ni is highly anisotropic from the elastic point of view.

The Young's modulus in any direction of a cubic crystal, described by its direction cosines o, p and q, is given by [92]:

$$E = \left[S_{11} - 2\left[\left(S_{11} - S_{12}\right) - \frac{1}{2} S_{44} \right] \left(o^2 p^2 + p^2 q^2 + o^2 q^2\right) \right]^{-1}, \tag{4.5}$$

where S_{11}, S_{12}, and S_{44} are the independent elastic compliance constants. In the case of hexagonal crystals, E, in a direction normal to the (hkl) plane is given by [199]:

$$E = \frac{\left[h^2 + \frac{(h+2k)^2}{3} + \left(\frac{a}{c} l\right)^2 \right]^2}{S_{11}\left(h^2 + \frac{(h+2k)^2}{3} \right)^2 + S_{33}\left(\frac{a}{c} l\right)^4 + \left(2S_{13} + S_{44}\right)\left(h^2 + \frac{(h+2k)^2}{3} \right)\left(\frac{a}{c} l\right)^2}, \tag{4.6}$$

where S_{11}, S_{33}, S_{13} and S_{44} are four of the five independent elastic compliance constants in a hexagonal crystal, and a and c are the lattice parameters. Values of E along the normal direction of some main crystallographic planes in Ni and Co are presented in Table 4.1 and were calculated using the following values for the compliance constants: S_{11} = 7.34 TPa^{-1}, S_{12} = -2.74 TPa^{-1} and S_{44} = 8.02 TPa^{-1} for Ni [200]; S_{11} = 10.87 TPa^{-1}, S_{12} = -4.52 TPa^{-1} and S_{44} =

10.87 TPa^{-1} for FCC Co [201]•; S_{11} = 4.72 TPa^{-1}, S_{33} = 3.19 TPa^{-1}, S_{13} = -0.69 TPa^{-1} and S_{44} = 13.24 TPa^{-1} for HCP Co [200] (the considered lattice parameters of HCP Co were a = 2.507 Å and c = 4.069 Å).

The agreement between the theoretical values, shown in Table 4.1, and the experimental ones, shown in Figure 4.10, is exceptionally good. The theoretical E in Ni is between 136 GPa (along <100>) and 304 GPa (along <111>), which comprises the experimental values shown in Figure 4.10.a. Concerning Co, the experimental values (Figure 4.10.b) are comparable to those calculated for HCP Co, in agreement with the α(FCC) → ε'(HCP) martensitic transformation observed in the Co-rich samples (see §3.4). This result confirms that the scattering of the experimental values of the Young's modulus, obtained from DSN tests, is essentially due to the crystallographic anisotropy of the surface in polycrystalline materials.

The combined parametric ratio H_i/E reflects the elastic and plastic behaviour of the material. The first aspect to note is that this parameter is not overly sensitive to size effects, at least within the load range used in the DSN tests, due to the anchoring effect of the Young's modulus values, which are typically two orders of magnitude higher than those of hardness. Figure 4.11.c shows that, from pure Ni to the Ni-60%Co alloy, the average H_i/E is approximately constant with a value of 0.02. However, pure Ni, due to its higher elastic anisotropy, presents an extremely large spectrum of H_i/E values, ranging from 0.012 to 0.025. The H_i/E ratio of Co-rich samples is considerably higher, reaching its maximum (0.026-0.032) for the Ni-85%Co alloy.

These observations suggest that, if the H_i/E ratio is used as a design parameter for wear resistance in the Ni-Co system, the alloys with compositions around Ni-80%Co present clear advantages over the Ni-richer alloys. As mentioned previously, the α → ε' martensitic transformation in alloys with Co > 68% results in an increase of the hardness without significantly affecting the Young's modulus (Figures 4.11.a and b). This leads to an increase of H_i/E, i.e. in a higher yield strain limit for the rupture of the surface asperities that results in wear. Most certainly, this is the main cause for the previously reported excellent tribological behaviour of Co-based stellite-type hardfacing alloys [202]. Nevertheless, it is worth mentioning that the large spectrum of E values in Ni, which results in the large spectrum of H_i/E values obtained in this sample, opens the possibility of optimizing the tribological behaviour of Ni-rich alloys by promoting the formation of surface textures, i.e. tuning tribological behaviour by crystallographic control of the surface.

• Values converted from the correspondent stiffness constants C_{ij}

Table 4.1. Young's modulus along the normal direction of some main crystallographic planes in Ni and Co (FCC and HCP) calculated with Eqs. (4.5) and (4.6). *E* values are given in GPa units.

Plane	***E* (Ni)**	***E* (FCC Co)**	***E* (HCP Co)**
{100}	136	92	–
{110}	232	170	–
{111}	304	236	–
{0001}	–	–	313
$\{10\bar{1}0\}$	–	–	212
$\{10\bar{1}2\}$	–	–	204

4.3. Conclusions

The indentation hardness of the Ni-Co system increases with decreasing contact scale (indentation size effect). The main factors responsible for this effect are the increase of the dislocation density with decreasing indentation depth, which results from the mechanical preparation of the surface and the larger magnitude of plastic strain gradients at smaller depths, and the surface free energy of the material when the depths are nanometric, especially in the case of sharp indenter geometries. An equation (Eq. 4.4) that accounts for both these factors and describes the depth dependence of indentation hardness in the materials used in this work was developed. The reliability of Eq. 4.4 is confirmed by the excellent agreement between the ρ values obtained from this equation and the experimental values measured from TEM observations. Moreover, this equation has been recently validated by other authors in different materials.

Hardness results obtained from displacement sensing nanoindentation tests in mechanically polished and electropolished samples showed that, even though the mechanical polishing procedure was carefully carried out with a 0.1 μm diamond particles suspension, a two to three times increase of the dislocation density in the near-surface region of the material resulted from this procedure.

Due to the small indentation size to grain size ratio involved in the DSN tests, it was possible to study the influence of crystallographic anisotropy on the hardness and Young's modulus of the samples. It was observed that Ni-rich samples are more elastically anisotropic, whereas Co-rich ones are more plastically anisotropic. The high elastic anisotropy of Ni leads to a large spectrum of H_i/E values and, therefore, can be used to optimize the tribological

behaviour of Ni-rich alloys by promoting the formation of surface textures. On the other hand, the highest H_i/E values occur in alloys with Co percentages around 80%. This result suggests that, if this ratio is used as a design parameter for wear resistance in the Ni-Co system, the alloys with compositions around Ni-80%Co present clear advantages over the Ni-richer alloys.

Finally, it is worth to mention that the effect of chemical composition and microstructure on hardness is less defined when the contact is established at the nanometric scale. This is due to the larger influence of scale related factors that do not depend so extensively on composition and microstructure.

5. INCIPIENT PLASTICITY AT THE NANOSCALE

One of the consequences of reducing contact scale is to increase the probability of finding dislocation-free regions in the material. If dislocations are absent in the loaded regions, new dislocations must be nucleated in order for plastic deformation to occur. In the extreme case where dislocation sources (e.g. Frank-Read sources, grain boundaries and second phase particles) are absent, nucleation of dislocations must occur homogeneously, which greatly increases the resistance of the material to plastic deformation and can be responsible, to a certain extent, for the observed indentation size effect. The Nix-Gao model (§1.4.2) accounts for the effect of the increase of dislocation density on the hardness of small indented volumes. However, it is a simplified geometrical model.

In this chapter, a study of the nucleation and arrangement of dislocations in the early stages of plastic deformation of an indented crystalline material is performed. The onset of plasticity was studied in the two pure samples of the Ni-Co system by using two different techniques. Indirect observation of this phenomenon was possible through the usage of displacement sensing nanoindentation, due to the high depth sensitivity of this technique. Transmission electron microscopy was also used to directly observe indentations performed with AFM cantilever-based nanoindentation in the electron transparent regions of TEM samples.

5.1. Indirect observation by displacement sensing nanoindentation

Besides the determination of hardness and Young's modulus, the load-displacement curves that result from DSN tests also enable retrieving information on the onset of plasticity, as it will be shown in the following two sections.

5.1.1. Results

Figures 5.1 to 5.3 show load-displacement curves resulting from DSN tests in Ni-Co samples. In mechanically polished samples no large discontinuities are present at the beginning of the loading curves (Figures 5.1 and 5.2) and even very small discontinuities are rarely present (an example is pointed with an arrow at the beginning of the loading curve of Figure 5.1.c). On the contrary, a large discontinuity is usually found at the beginning of the loading curves of electropolished samples (Figures 5.3.a to e). The large discontinuity in the loading curves of electropolished Ni was found to occur at loads in the range 0.06 to 0.36 mN, whereas in electropolished Co it occurred at loads between 0.08 and 0.38 mN. The jump in indenter displacement corresponding to this discontinuity is in the range 5 to 42 nm and 3 to 21 nm in the case of electropolished Ni and Co, respectively. Some tests were performed in both electropolished samples using a load of 0.05 mN, but the resulting loading and unloading curves were always overlapped, which means that only elastic deformation of the material occurred, i.e. the onset of plasticity was not overcome. In a few tested regions of electropolished Ni and Co smaller discontinuities occurred in other portions of the loading curve (Figures 5.3.c and e), whereas in a few other regions no discontinuities were found in the loading curve (Figure 5.3.f).

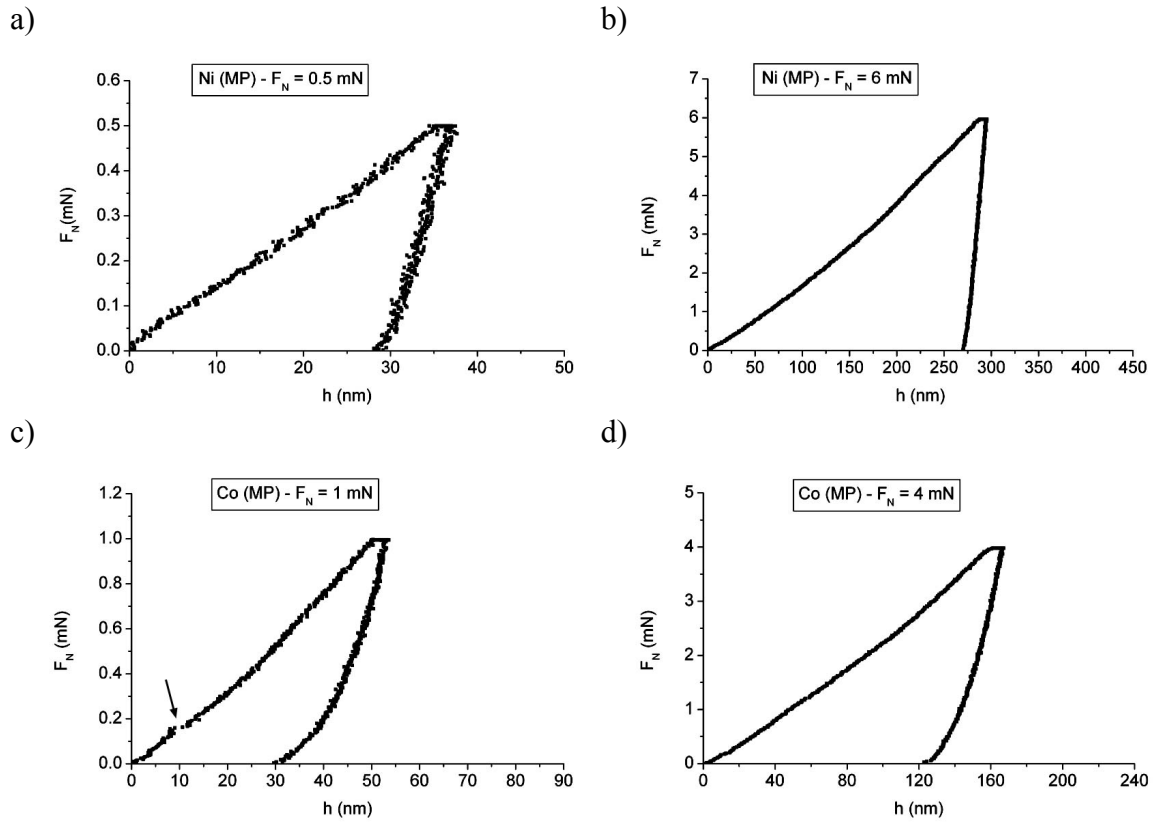

Figure 5.1. Load-displacement curves resulting from DSN tests in mechanically polished Ni (a and b) and Co (c and d).

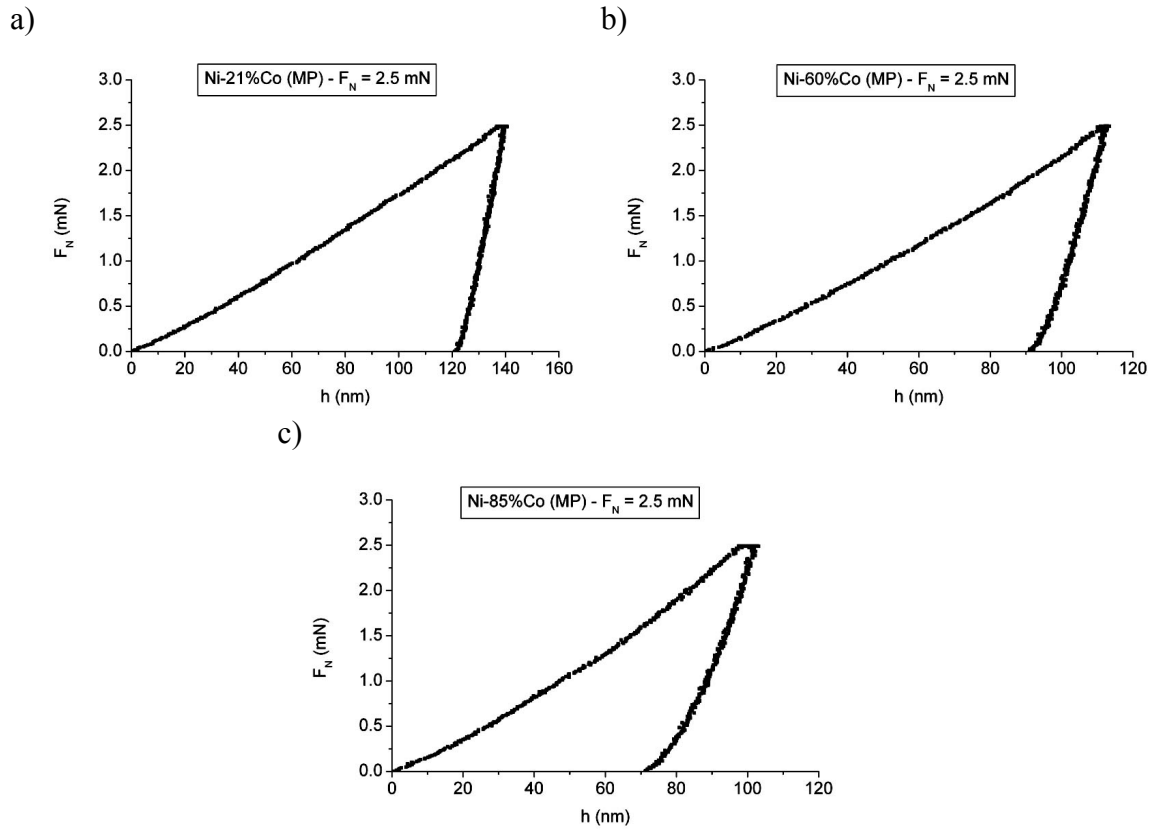

Figure 5.2. Load-displacement curves resulting from DSN tests in mechanically polished Ni-Co alloys: a) Ni-21%Co; b) Ni-60%Co; c) Ni-85%Co.

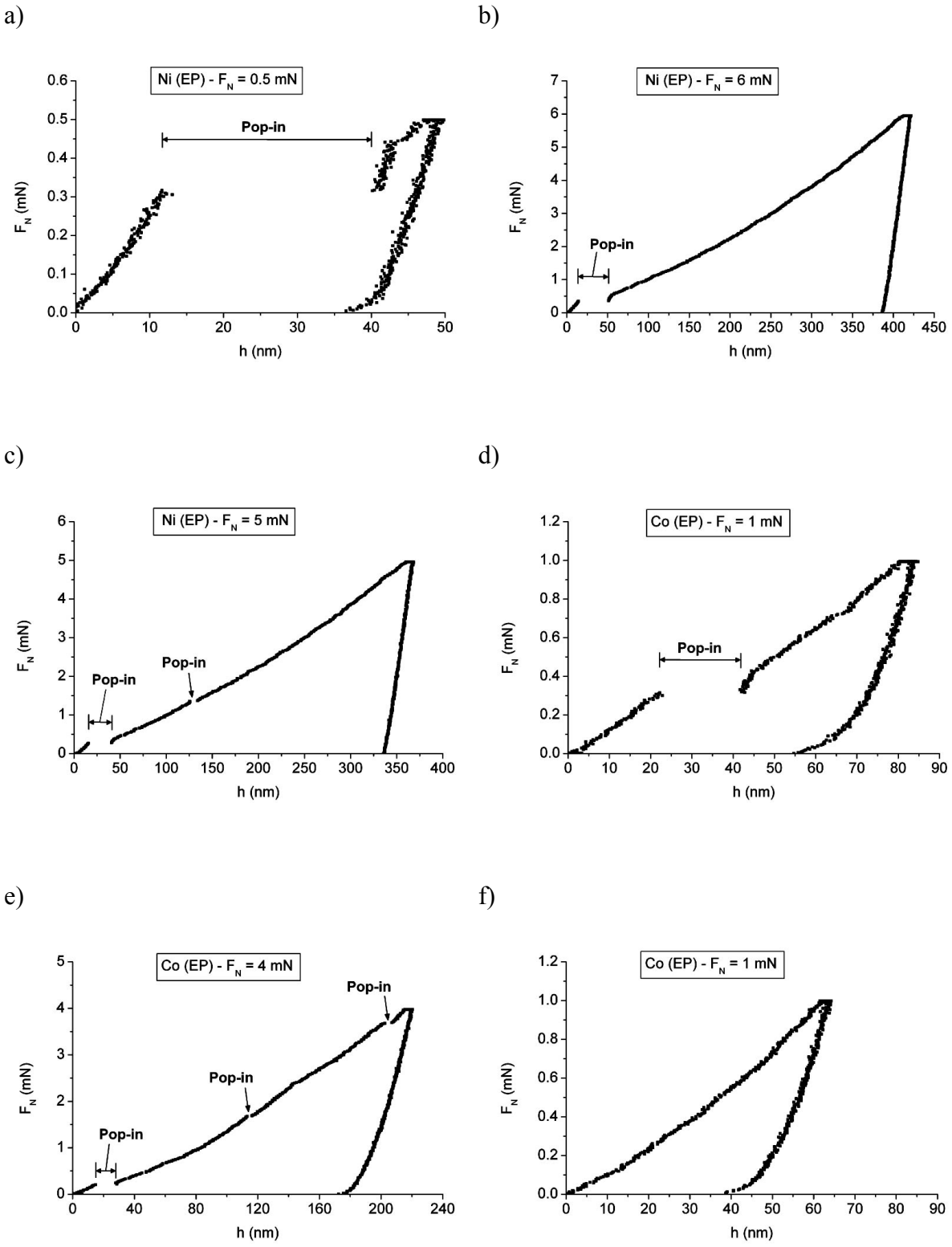

Figure 5.3. Load-displacement curves resulting from DSN tests in electropolished Ni (a to c) and Co (d to f). The discontinuities in the loading curves are designated as pop-ins.

5.1.2. Discussion

The presence of a sudden jump in indenter displacement without a load increase has been previously observed in load-displacement curves of other materials (see, for instance, [73, 79, 82]) and is commonly designated in the literature as *pop-in*. This phenomenon is usually attributed to the nucleation of dislocation loops followed by rapid multiplication, and is preceded by a situation of purely elastic contact between sample and indenter.

The onset of plasticity will occur at the point of maximum shear stress in the indented material (see §1.2.1). Therefore, if the critical load for pop-in, the reduced Young's modulus of the contact and the indenter radius are known, the critical shear stress for the onset of plasticity (τ_{max}) can be estimated by using Eq. 1.6. The indenter radius (R) can be estimated from the purely elastic part of the loading curve (which corresponds to the portion before the pop-in) by fitting the data points with Eq. 1.4.

Figure 5.4 shows the fitting of the data points of the purely elastic portion of a loading curve of electropolished Ni (curve presented in Figure 5.3.a) with Eq. 1.4. By using the value of the parameter resulting from the fitting ($4/3E_rR^{1/2}$ = 0.00764 mN.nm$^{-3/2}$) and the reduced Young's modulus of the contact (E_r = 170 GPa), calculated by introducing the elastic constants of the sample (E = 180 GPa•; ν = 0.31 [139]) and of the indenter (E_i = 1141 GPa and ν_i = 0.07 [74]) in Eq. 1.2, a value of R = 1140 nm is estimated for the indenter radius••.

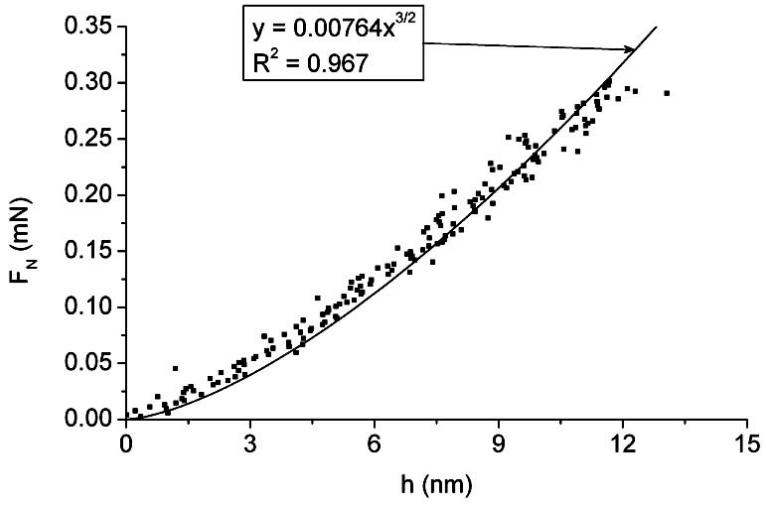

Figure 5.4. Purely elastic portion of the loading curve of electropolished Ni shown in Figure 5.3.a, fitted by Eq. 1.4.

• Average Young's modulus obtained from the DSN tests in laser clad Ni (see §4.2).
•• Note that the nominal value of R supplied by the indenter manufacturer is 1 μm.

The maximum shear stress just prior to the pop-in event can then be estimated by introducing the values of E_r and R in Eq. 1.6, along with the value of the critical load at which the pop-in occurs. The critical load measured from the curve in Figure 5.4 is approximately 0.3 mN, which results in $\tau_{max} \approx 3.4$ GPa.

The theoretical shear stress to homogeneously nucleate a dislocation by rupturing atomic bounds is on the order of $G/30$ to $G/15$, where G is the shear modulus of the material [92]. Since the shear modulus of Ni is 76 GPa [139], the shear stress for the homogeneous nucleation of dislocations in Ni is in the range 2.5 to 5.1 GPa, which includes the value of τ_{max} measured experimentally for electropolished Ni. Moreover, for the range of critical loads (F_N = 0.06 − 0.36 mN) obtained in the tests of electropolished Ni, τ_{max} is in the range 2 to 3.6 GPa, which is in excellent agreement with the theoretical shear stress values for the homogeneous nucleation of dislocations in Ni. A value of 175 GPa is obtained for the E_r of Co when introducing the elastic constants of the sample (E = 185 GPa[•]; ν = 0.32 [139]) and of the indenter in Eq. 1.2. The shear modulus of Co is 82.6 GPa [139], which results in a range of theoretical shear stresses for the homogeneously nucleation of dislocations between 2.8 and 5.5 GPa. For the range of critical loads (F_N = 0.08 − 0.38 mN) obtained in the tests of electropolished Co, the value of τ_{max} calculated from Eq. 1.6 is in the range 2.2 to 3.8 GPa, which is also in excellent agreement with the theoretical shear stress values for the homogeneous nucleation of dislocations in Co.

This agreement between the experimental and theoretical shear stress values confirms that the pop-in events occurring in the electropolished samples are associated to the homogeneous nucleation of dislocations. Therefore, the analysis of pop-in events enables retrieving information on the initial yield mechanisms of the material when submitted to indentation.

A pop-in event can be characterised by two features, which are the critical load at which it occurs and the amount of indenter displacement that results from it, henceforth designated as *pop-in length*. The tests in electropolished Ni and Co showed that pop-ins do not occur always at the same critical load value nor is the pop-in length always the same. The variation of the critical load for pop-in is, certainly, related to the polycrystallinity of the samples, since some crystallographic orientations will favour the homogeneous nucleation of dislocations in relation to others, leading to smaller critical loads for pop-in. On the other hand, the presence

[•] Average Young's modulus obtained from the DSN tests in laser clad Co (see §4.2).

of a finite surface roughness may also contribute to the scattering of the critical load values, since asperities may act as stress concentration points.

Regarding the pop-in length, it has been previously suggested [71, 79] that this parameter is related to the number of dislocation loops generated during the pop-in event. If the stress field created by the indenter can reach a few residual dislocations away from the core of the indentation, than a smaller number of dislocations need to be nucleated. This can explain the usually larger pop-in lengths in Ni than in Co, since the dislocation density in Co is larger than in Ni, as a result of the martensitic transformation of Co.

The occurrence of multiple pop-in events in a single indentation test has been previously observed in other materials and is known as *staircase yielding* [203-205]. It consists on successive pop-in events, separated by short purely elastic stages of deformation. The explanation of Corcoran *et al*. [203] for such phenomenon in Au monocrystals was that a pop-in event is initiated by the nucleation of a single dislocation, whose ends are pinned at the free surface and which acts as a Frank-Read source. This source creates a pile-up of dislocations under the indenter until the back forces from the pile-up are sufficient to stop the source from operating, marking the end of the pop-in event. The sample is then further loaded elastically until another source is created on a parallel slip plane, marking the beginning of the next pop-in event. After a few pop-in events, the number of dislocations is enough to allow deformation to proceed in the usual elastoplastic way. The displacement intervals between pop-ins in some of the curves of electropolished Ni and Co (Figures 5.3.c and e) are relatively large, with several tens of nanometres. Therefore, it is unlikely that these portions of the loading curve are solely elastic.

A complementary explanation for the occurrence of more than one pop-in event has been proposed by Gerberich *et al*. [82] and consists on the breaking of the native oxide layer present at the surface of most metals by some of the dislocations nucleated under the indenter, which cross slip to planes leading back to the free surface. The pile-up of these dislocations at the oxide-metal interface produces a forward force on the oxide and a back force on the indenter. When the strength of the oxide layer is exceeded at the point of maximum tensile stress, which is located at the contact periphery (see Figure 1.5.a), the oxide will fracture and the dislocations escape to the free surface. As consequence, the back force against the indenter suddenly disappears and a jump in indenter displacement occurs, until a new equilibrium of forces is reached. Local variations of the oxide layer thickness [204] and the

presence of stress concentrators in the oxide (e.g. flaws) [206] can lead to fluctuations in the critical load for oxide rupture.

Although the oxide layer may have some influence on the multiple pop-in events that occur in a few regions of electropolished Ni and Co, it cannot be the main cause for the observed behaviour because multiple pop-ins are not observed in the loading curves of mechanically polished samples, which are covered by an oxide layer as well. Furthermore, *in situ* TEM observations of nanoindentation tests in an Al film carried out by Minor *et al*. [207], showed that the pop-in events in Al are associated to the formation of dislocations and not to the rupture of the native oxide layer.

Even though multiple pop-in events were much less frequently observed than single ones, they were more commonly found in electropolished Co than in electropolished Ni. This suggests that the presence of multiple pop-ins may have some relation to the crystallography of the samples. The FCC structure of Ni enables the occurrence of cross slip, which allows the movement of dislocations produced by Frank-Read sources to other slip systems. On the other hand, because slip in Co occurs only along the (0001) plane of the HCP structure [92], dislocations cannot cross slip between parallel (0001) planes in a martensite plate. This fact leads to a faster saturation of the Frank-Read sources by the pile-up of dislocations generated by these sources. Therefore, it is more probable that new dislocations have to be nucleated in Co than in Ni in order for plastic deformation to proceed. This can explain the larger number of multiple pop-in events in electropolished Co than in electropolished Ni.

Soer *et al*. [208, 209] have also proposed that the transmission of piled-up dislocations across grain boundaries can contribute to multiple pop-in events. If a nanoindentation is made close to a grain boundary and the slip system is oriented in its direction, the dislocations nucleated in the first pop-in event may glide in the direction of the grain boundary and pile up at the boundary. With increasing load, this pile-up generates a stress high enough to nucleate dislocations in the adjacent grain, thus producing another pop-in event. In the nanoindentation experiments of Soer *et al*. in a Fe-14%Si bicrystal, the next pop-in events were separated by almost 100 nm from the first one, which is exactly what is observed when multiple pop-in events occur in electropolished Ni and Co (Figures 5.3.c and e). Moreover, due to the possibility of dislocations to cross-slip in Ni, the dislocations may move to other slip systems before piling up at a grain boundary, thus preventing the occurrence of a second pop-in event. On the other hand, because dislocations cannot cross-slip in Co, the probability of dislocation pile-up at grain boundaries increases and, accordingly, the probability of dislocation

transmission across grain boundaries, which results in further pop-in events. Finally, the fact that multiple pop-in events are much less frequently observed than single ones can be explained by the small indentation size to grain size ratio, i.e. there is a higher probability of performing nanoindentations far from grain boundaries than close to them. Therefore, the mechanism proposed by Soer *et al*. gives the best explanation for the multiple pop-in events observed in electropolished Ni and Co.

Pop-in events were rarely observed in the mechanically polished Ni-Co samples (and the ones occurring were single and extremely small), in agreement with previous observations in other mechanically polished materials [72, 73, 204], because contrary to electropolished surfaces, mechanically polished surfaces contain several pre-existing dislocations, which not only can be moved under the influence of the applied shear stresses, but also can act as Frank-Read sources. Furthermore, the absence of a large pop-in event in a few loading curves of the electropolished samples (Figure 5.3.f) may be due to a higher concentration of remaining dislocations (those resulting from the solidification process) in some of the tested regions, since the TEM observations of this work showed that the distribution of dislocations in the samples is relatively heterogeneous.

Besides the scale related factors previously discussed in §4.1.2 and §4.2.2, the occurrence of pop-in events in low dislocation density materials can also lead to significant changes in the tribological response of materials when the contact scale is reduced from micro to nanoscale. Moreover, in materials presenting large heterogeneity in dislocation distribution, a large variation in the tribological response from one contact region to the other may result. This is especially important in the case of MEMS and NEMS, where the contact areas are often submicrometric. An important consequence of the presence of pop-ins to the wear of ductile materials is that, if the critical load for pop-in is not reached in dislocation-free regions, plastic deformation will not start and, consequently, observable wear[•] will not occur. A further discussion on this topic will be made in §6.2.2.

5.2. Direct observation by transmission electron microscopy

Transmission electron microscopy was used to analyse the dislocation structure produced from AFM cantilever-based nanoindentation of Ni with a DNISP probe (probe 1 in Table 2.2). Arrays of nanoindentations were performed in the electron transparent regions of Ni TEM

[•] As discussed in §1.4.1, even when dislocation-based wear mechanisms are inactive, due to the extremely thin size of the interaction layers involved in the contact, atomic scale wear mechanisms, which are preceded by the formation of point defects in the first atomic layers of the surface, may still occur.

samples by using the Multimode atomic force microscope. Afterwards, the samples were observed in the transmission electron microscope, and the nanoindentation arrays were visualized.

From the experimental point of view, performing nanoindentations in the electron transparent regions of TEM samples is extremely complex and time consuming. Firstly, electron transparent regions cannot be distinguished from thicker ones by using the optical microscope that enables to position the AFM cantilever on the sample (Figure 5.5.a). Moreover, AFM imaging also does not allow knowing if the regions under observation are electron transparent or not. In this way, visualization of the samples by TEM prior to the indentation tests was necessary to acquire successive TEM images along the periphery of the hole produced by ion milling. By putting together the TEM images, as in a puzzle, the small areas visible by OM could be reconstructed, which helped locating the electron transparent regions for the indentation tests. The second difficulty of this experiment was to indent the electron transparent regions using an indenter mounted on a cantilever which is several times longer and wider than the largest of these regions (Figure 5.5.b).

Therefore, it was only possible to carry out the experiment by "blindly" performing a large number of nanoindentations (more than 200) in the areas containing electron transparent regions. Grids of nanoindentations with a spacing of about 1 μm were performed in these areas using a load of 57 μN.

a) b)

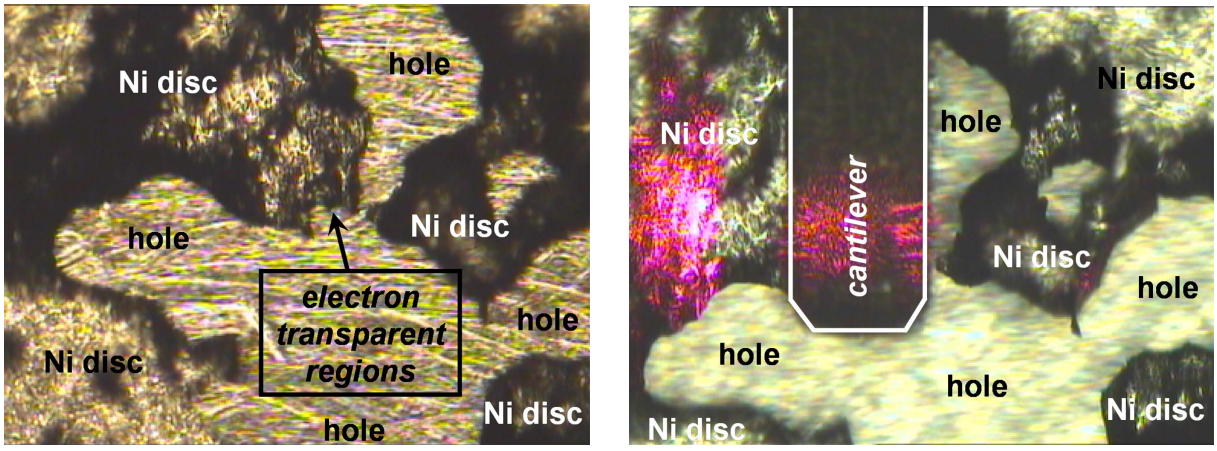

Figure 5.5. a) OM image of the central portion of a Ni TEM disc perforated by ion milling. Electron transparent regions are found in the periphery of the irregular shaped hole, but can only be identified by TEM. b) OM image of the same disc portion with a DNISP nanoindentation probe (tip facing down) located over the electron transparent regions pointed with an arrow in a). The white line shows the approximate contour of the cantilever, which has a width of about 111 μm. The two red areas in the image result from the reflection of the HeNe laser used to detect the position of the cantilever.

5.2.1. Results

Figures 5.6.a and b show BF TEM images of a dendrite in Ni, respectively, before and after nanoindentation testing with the DNISP probe. The white arrows in Figure 5.6.b point in the direction of rows of nanoindentations. A high magnification image of an indented region can be seen in Figure 5.6.c, which shows that the dislocation structure generated is formed by agglomerates of dislocations at the centre, from where helical prismatic dislocations (HPD), prismatic dislocation loops (PDL) and (almost) straight dislocation lines are emitted. The diameter of the helices and loops is of a few tens of nanometres, as well as the spacing between successive loops.

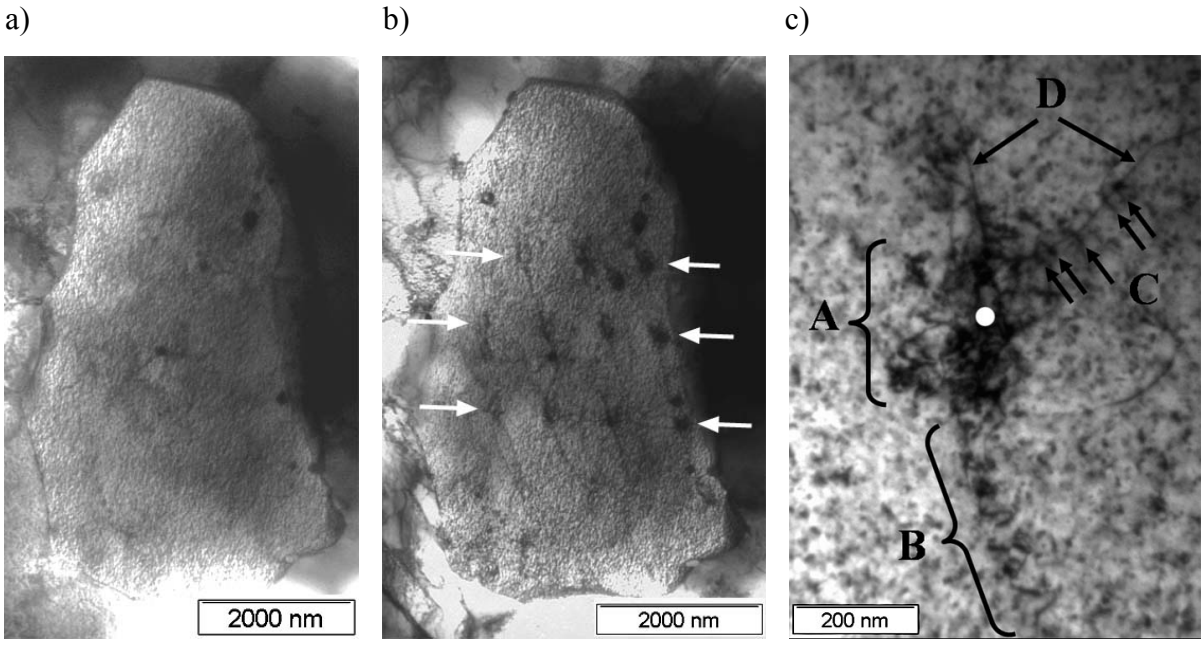

Figure 5.6. BF TEM images showing a dendrite in Ni before (a) and after (b) indentation testing with the DNISP probe. The white arrows in b) point in the direction of rows of nanoindentations. c) BF TEM image of an indented region containing agglomerates of dislocations (A), helical prismatic dislocations (B), prismatic dislocation loops (C) and straight dislocations (D). The white spot in c) marks the approximate centre of the indentation.

SAD [010] and [011] zone-axis diffraction patterns were taken at the dendrite containing nanoindentations (Figure 5.6.b) and are shown in Figure 5.7. These patterns were the starting points for obtaining the two-beam conditions used in the visualization of the dislocation structures created in the dendrite. Figure 5.8 shows BF TEM images of indented regions in this dendrite, taken under three different two-beam conditions: (000)/(200) – a and b; (000)/(00$\bar{2}$) – c and d; (000)/($\bar{1}$ $\bar{1}$ 1) – e and f. It can be observed from Figures 5.8.a, c and e that agglomerates of dislocations (pointed with white arrows in these figures) are formed in the indented regions. In Figures 5.8.b and f, HPD that are emitted from the centre of one of

the indented regions can be seen, but not in d), where these dislocations are invisible. On the other hand, PDL that are emitted from the centre of another indented region can be observed in Figures 5.8.b and d, but not in f.

Table 5.1 presents the values of $g \cdot b$ for perfect dislocations in FCC crystals [210], for the three reflections used, where g is the reciprocal lattice vector for the *hkl* reflection. Combining the information retrieved from this table with that from the TEM images of Figure 5.8, and applying the criterion for dislocation invisibility in elastically isotropic materials, $g \cdot b = 0$ [210], the Burgers vectors of the dislocations emitted from the centre of the indented regions can be determined. In this way, the HPD in the top half of Figure 5.8.b have a b of $\pm\frac{1}{2}[110]$, whereas the PDL in the bottom half of the same figure have a b of $\pm\frac{1}{2}[101]$.

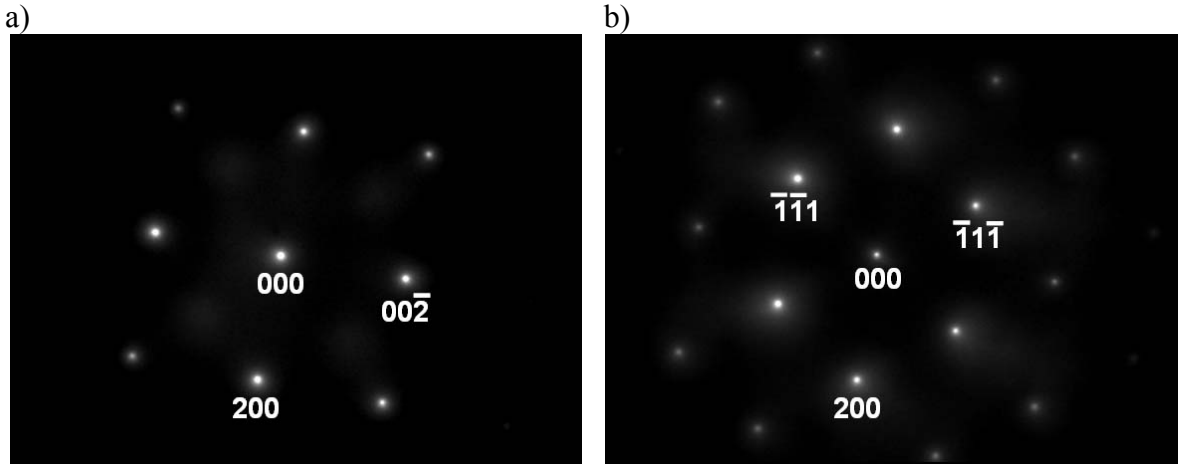

Figure 5.7. SAD [010] (a) and [011] (b) zone-axis diffraction patterns taken at the dendrite in Figure 5.6 where nanoindentations were performed.

Table 5.1. Values of $g.b$ for perfect dislocations in FCC crystals, for the three reflections used to obtain the images in Figure 5.8. Dislocations become invisible when $g \cdot b = 0$ [210].

g / **b**	2 0 0	0 0 $\bar{2}$	$\bar{1}$ $\bar{1}$ 1
± ½ [1 1 0]	± 1	0	± 1
± ½ [1 0 1]	± 1	± 1	0
± ½ [0 1 1]	0	± 1	0
± ½ [1 $\bar{1}$ 0]	± 1	0	0
± ½ [1 0 $\bar{1}$]	± 1	± 1	± 1
± ½ [0 1 $\bar{1}$]	0	± 1	± 1

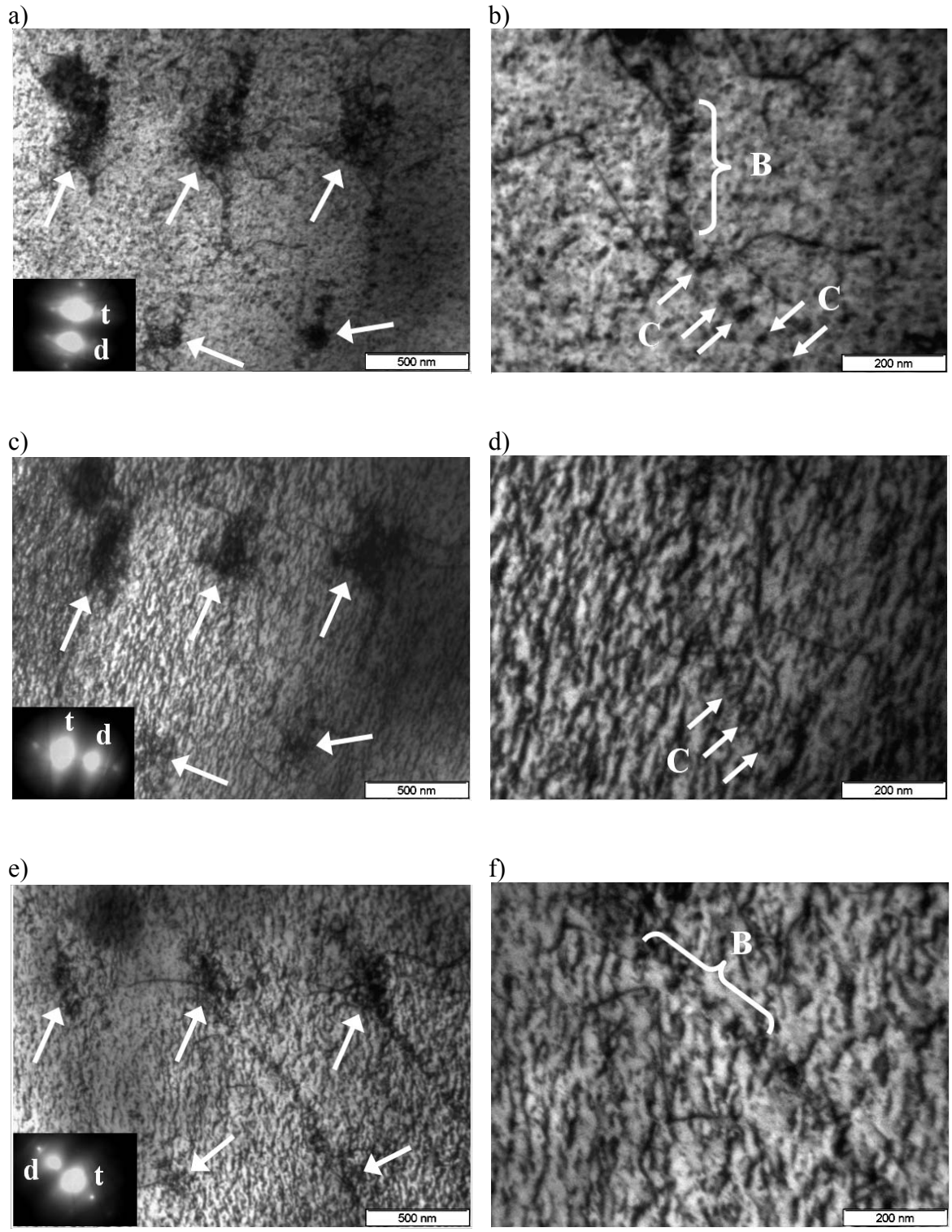

Figure 5.8. BF TEM images of indented regions, taken under three different two-beam conditions: (000)/(200) – (a) and (b); (000)/(00 $\bar{2}$) – (c) and (d); (000)/($\bar{1}$ $\bar{1}$ 1) – (e) and (f). In the bottom left corner of a), c) and e), SAD patterns corresponding to the different two-beam conditions can be seen, where "t" and "d" correspond, respectively, to the transmitted and diffracted spots. In b), d) and f), helical prismatic dislocations and/or prismatic dislocation loops are denoted, respectively, by letters "B" and "C".

In the identification of the Burgers vectors of the dislocations emitted from the centre of the indented regions it was assumed that the only possible values of *b* were those of perfect

dislocations in FCC crystals (Table 5.1). This assumption enabled identifying *b* without finding two reflections for which *g.b = 0*. In order to assure that the dislocations emitted from the indented regions move along <110> directions, TEM observations of these regions with the electron beam approximately parallel to the [011] direction of the dendrite (deviated from the [011] direction by ~ 1º) were carried out (see Figure 5.9.a)•. The software Carine Crystallography 3.1 (distributed by Divergent S. A.) was then used to obtain the stereographic projection for a cubic crystal, with the line of sight along the [011] direction and rotated in order to match the orientation of the SAD [011] pattern in Figure 5.7.b (Figure 5.9.b). By comparing this projection (black dashed arrows in Figure 5.9.b) with the direction of propagation of the dislocations (white arrows in Figure 5.9.a) it is confirmed that the HPD and PDL are emitted along the <110> directions of the crystal.

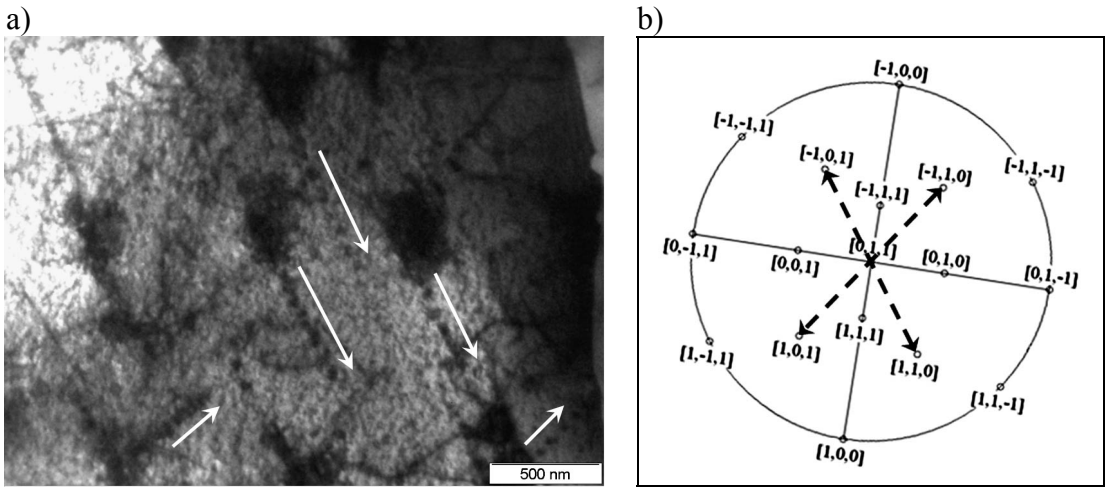

Figure 5.9. BF TEM image of indented regions in the dendrite of Figure 5.6.b, taken with the electron beam approximately parallel to the [011] direction of the dendrite. White arrows represent the directions of propagation of the dislocations from the centre of the indented regions. b) Stereographic projection for a cubic crystal, where the line of sight is along the [011] direction. The projection is slightly rotated in order to mach the orientation of the SAD [011] pattern in Figure 5.7.b. Directions of the <100>, <110> and <111> forms are represented in the projection.

The direction of load application was assumed to be that of the electron beam when the *tilt* and *azimuth* angles of the sample holder are both zero (see Figure 2.16). When the electron beam is parallel to the [011] direction of the dendrite in Figure 5.6.b, *tilt* = 7.9º and *azimuth* = -7.3º. Therefore, the direction of load application in the nanoindentation tests performed in this dendrite could be determined as ~ $[\bar{1}\,54]$ by reconstructing the [011] SAD pattern of Figure 5.7.b (Figure 5.10.a) and then rotating it by *tilt* = -7.9º and *azimuth* = 7.3º (Figure 5.10.b).

• The observations could not be performed with the electron beam exactly parallel to the [011] direction because in this orientation the dendrite became totally dark and dislocations could no longer be distinguished from the background. However, deviations from this orientation of about 1º already enable visualizing the dislocations.

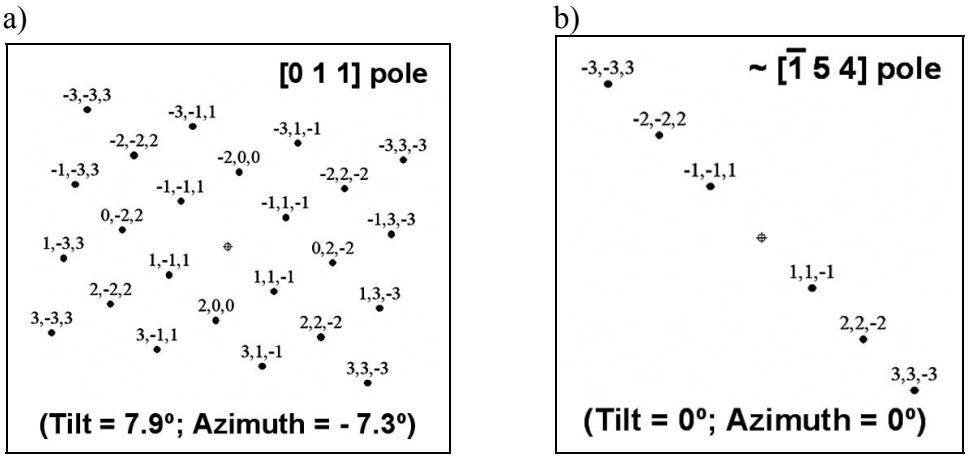

Figure 5.10. a) [011] pattern obtained with the software Carine Crystallography 3.1, with the same orientation of the SAD [011] pattern in Figure 5.7.b. b) Pattern obtained by rotating the pattern in a) by *tilt* = -7.9º and *azimuth* = 7.3º, where the zone-axis is ~ [$\bar{1}$ 54].

5.2.2. Discussion

The TEM observations of regions in Ni submitted to nanoindentation showed that, at the nanometric contact scale, the plastic deformation is accommodated through three mechanisms: 1) nucleation of dislocations in the neighbourhood of the indentation, forming agglomerates; 2) emission of prismatic dislocation loops and helical prismatic dislocations from the centre of the indented region; 3) in a few cases, emission of straight dislocations from the centre of the indented region.

In this way, two distinct regions are formed: a) a high dislocation density region in the inner vicinity of the indentation, resulting from mechanism 1; b) a low dislocation density region surrounding the previous one, resulting from mechanisms 2 and 3.

The high dislocation density at the inner region suggests that some of the nucleated dislocations become sessile, which can occur through the formation of non-conservative jogs due to the intersection of screw dislocations, or other trapping mechanisms, such as Lomer-Cottrell locks, which are common in FCC materials [93]. Since immobilized dislocations cannot glide as the indenter is further pressed against the sample, plastic deformation proceeds through the formation and gliding of PDL and HPD (mechanism 2) and, less frequently, with the formation of straight dislocations (mechanism 3).

Recent TEM observations of nanoindentations in a Ni_3Al(Cr,B) monocrystal [211], Ni_3Al [212], and Ti-6Al-4V [213] also showed that there is an accumulation of dislocations in the neighbourhood of the indentation and emission of dislocations from this high dislocation density region. However, the presence of HPD has not been observed in these materials. The formation of PDL and HPD has also been observed during cooling of annealed silver chloride

crystals containing spherical glass spheres with diameters between 0.5 and 5 μm [214]. In this case, the dislocations were generated by the compressive stress field in the silver chloride matrix, which results from the differential contraction between the matrix and the glass spheres on cooling.

In the present case, the PDL formed in Ni are interstitial, i.e. the extra half-plane of atoms is inside the loop, since they result from punching [215] and not from the aggregation of vacancies into disks [93]. Molecular dynamics atomistic simulations of nanoindentation experiments with a spherical indenter in an Al (111) monocrystal [216, 217] showed that plasticity begins with the homogenous nucleation of a few dislocation loops, which then expand and intersect each other, producing sessile dislocation segments. As the indenter is further displaced, PDL with the shape of a rhombus are emitted from this region and glide along <110> directions, as shown in the schematic of Figure 5.11.a. Nevertheless, due to the high strain energy associated to the corners of the rhombus, some bending of the dislocation line should occur, especially at the sharpest corners of 70.53º. Therefore, the shape of the dislocation loops observed in TEM images must correspond to a round-edged rhombus, i.e. to an elliptical-like shape.

The observed geometry of the PDL emitted from the indented regions (Figure 5.11.b) agrees remarkably well with the predictions from MD simulations. The typical dislocation core diameter is smaller than 2 nm [93], whereas the thickness of the dislocation loop line pointed with a black arrow in Figure 5.11.b, measured from the image, is in the range 5 to 10 nm, which shows the effect of the highly deformed core region in the dislocation line contrast.

Another important feature of the loops is their diameter, which will be a function of the amount of material displaced by the indenter and of the strain energy generated per unit length of dislocation line. Therefore, there will be a compromise between the loop diameter and the number of emitted loops for the displacement of a certain volume of material, which minimizes the energy of the crystal. The diameter of the PDL in Ni is of a few tens of nanometres, which is of the same order of magnitude as the contact diameter.

The mechanism by which HPD are formed should be far more complex than that responsible for the generation of PDL, since it must involve the rotation and displacement of one of the ends of the dislocation in relation to the other, which should remain fixed. This is probably the reason why HPD were less frequently found in Ni in comparison to PDL. Nevertheless, the crystallographic restrictions represented in Figure 5.11.a for the case of PDL should also be applied to HPD.

a)

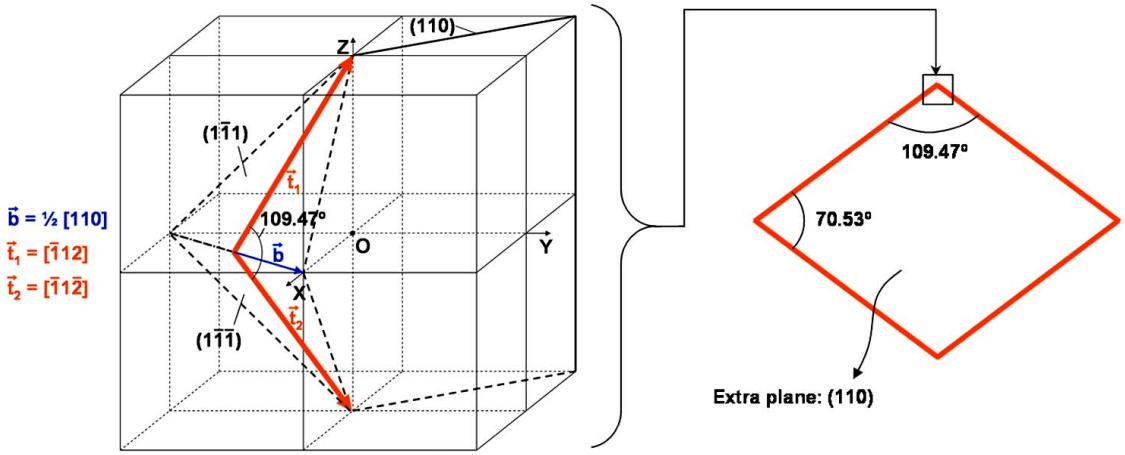

b)

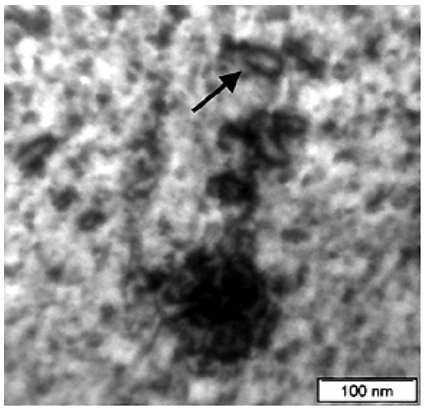

Figure 5.11. a) Schematic of: two dislocation line segments of a dislocation loop, where vectors t_1 and t_2 give the crystallographic direction of the segments (left); prismatic dislocation loop with the shape of a rhombus, formed by several dislocation line segments (right). b) BF TEM image of an indented region in Ni, with the sample tilted in a way that enables distinguishing clearly the elliptical-like shape of one of the dislocation loops (pointed with a black arrow) emitted from the centre of this region.

The results obtained from the TEM observations of nanoindentations in Ni can now be confronted with the basic assumptions of the Nix-Gao model (see §1.4.2 for a detailed description). For simplicity, in the Nix-Gao model it is assumed that geometrically necessary dislocations, which accommodate the shape of the indentation, are generated in the indented material in the form of prismatic loops with Burgers vector normal to the plane of surface and remain within a hemispherical volume. Consequently, the loops glide in the direction of the applied load. Of course, in real crystals, this represents an extreme situation since both the slip planes and directions would have to be oriented perpendicularly to the surface. The large accumulation of dislocations in the neighbourhood of the nanoindentations performed in Ni shows that the fundamental idea underlying the Nix-Gao model, which is that the increase of the density of GNDs with decreasing indentation depth leads to an indentation size effect, is

correct. However, the emission of PDL and HPD from the centre of the indented region, gliding in the slip planes and directions of the crystal lattice, is not considered in the model.

Some authors have observed that the Nix-Gao model overestimates the hardness for small indentation depths (e.g. below 1 μm in iridium [96] and below 200 nm in MgO [84]). According to the model and, therefore, Eq. 4.4, the hardness increases indefinitely when $h \rightarrow 0$, as a result of the increase of the density of GNDs. Swadener *et al*. [96] suggested that, for very small depths, the strong repulsive forces between GNDs would cause them to spread beyond the hemispherical volume defined by the contact radius r_c, resulting in a density of GNDs smaller than that assumed in the Nix-Gao model.

This is exactly what is observed in the nanoindentations in Ni, where a high concentration of dislocations is found in the indented region and PDL and/or HPD are emitted from this region, gliding in the compact directions of the FCC lattice (Figures 5.6.c, 5.8 and 5.9). Nevertheless, as was previously shown [84, 97, 98], the overestimation of the density of GNDs in the Nix-Gao model can be compensated by assuming an effective radius of the plastic zone $f.r_c$ larger than r_c, where $1 < f < 2.4$ for several metallic materials, which results in an increase of the storage volume for GNDs. Because the parameter f is already incorporated in the characteristic length h^* determined from the fitting of the Nix-Gao equation (Eq. 4.2) to the indentation hardness data [84, 97], the h^* value determined experimentally is already corrected for the size of the plastic region. Consequently, as long as f stays independent of indentation depth, h^* can be used in Eq. 4.4. Disagreement on the depth dependence of f is found in the literature. According to the results of Feng and Nix for MgO [84], f presents an approximately exponential decay from 1.66 (when $h \rightarrow 0$) to 1 (when $h \rightarrow \infty$), resulting in an overestimation of the hardness for indentation depths less than 200 nm. On the other hand, recent work by Durst *et al*. in several metallic materials [99] showed that a single f value can be used to model quantitatively the depth dependence of hardness from about 50 nm to macroscopic depths, where f depends only on the material used.

Moreover, as could be observed from Figure 4.7, the agreement between the indentation hardness data of this work and Eq. 4.4 is excellent, even for the hardness values retrieved from nanoindentations with a depth of only a few tens of nanometers, which supports the conclusions of Durst *et al*.

Therefore, even though the Nix-Gao model is based on assumptions that are simple from the crystallographic point of view, its application to materials of relatively complex structure, such as mechanically polished polycrystalline Ni and Co produced by laser cladding, still enables predicting the contact scale dependence of hardness with good confidence.

5.3. Conclusions

In the absence of dislocations and dislocation sources, the plastic deformation of an indented crystalline material is initiated by the homogeneous nucleation of dislocations when the maximum shear stress in the material reaches the theoretical shear stress of the perfect crystal, as could be observed in electropolished Ni and Co. This phenomenon is responsible for a jump in indenter displacement at the beginning of the loading curve (pop-in) and is followed by the rapid multiplication of dislocations.

The TEM observations of nanoindented regions in Ni showed that the dislocation structure produced consists of an agglomerate of dislocations in the neighbourhood of the indentation, forming a high dislocation density region, from where prismatic dislocation loops, helical prismatic dislocations and, less often, straight dislocations are emitted, forming a lower dislocation density region. It is tempting to relate the large pop-in event at the beginning of indentation loading curves to the generation of the high dislocation density region, in which the dislocations become sessile, thus forcing other dislocations to be emitted outside this region so that plastic deformation can continue. However, this hypothesis can only be validated by performing TEM observation of the indented region during the indentation test while monitoring the path of the loading curve.

For one side, the presence of a high dislocation density region at the core of the indentation supports the fundamental idea of the Nix-Gao model, in which the indentation size effect is caused by an increase of the density of GNDs with decreasing indentation depth, and, for the other side, the presence of a low dislocation density region surrounding the previous one justifies the correction proposed by Feng and Nix and Durst *et al*. to the volume containing the GNDs in the Nix-Gao model. As the indenter penetrates more deeply into the material, the deformed volume increases and the effect of the high dislocation density region becomes less pronounced, thereby reducing the magnitude of the ISE.

The presence of dislocation-free regions in materials, due to low dislocation densities and/or heterogeneous distributions of dislocations, can lead to irregularities in their plastic behaviour and hence in their tribological response, when the contact is established at small scales[•]. This is particularly important in the case of MEMS and NEMS, where the contact areas are often submicrometric. If the critical load for dislocation nucleation is not reached in dislocation-free regions and wear mechanisms other than plastic deformation (e.g. fracture) are absent, detectable wear will be prevented because plastic deformation will not occur.

[•] See Figure 4.1, in which the scatter of hardness increases significantly from micro- to nanoscale indentations.

6. CONTACT SCALE DEPENDENCE OF ABRASION RESISTANCE

Up to this point, the influence of contact scale on the hardness of the Ni-Co system has only been analysed for the case of static (indentation) contact, where the material is vertically pressed by a hard indenter under the influence of an applied normal load. In this chapter, the analysis of the influence of contact scale on hardness is extended to non-static contact conditions by submitting the Ni-Co samples to scratch tests with diamond indenters and loads in the μN to the N range. The consequences of the scale dependence of hardness in terms of abrasive wear resistance are then analysed by submitting the samples to AFM nanoabrasive wear tests and through the combination of hardness and wear models.

6.1. Scratch hardness

The contact scale dependence of scratch hardness was analysed by submitting the samples to conventional microscratch tests with a Rockwell C indenter and AFM cantilever-based nanoscratch tests using a DNISP tip. In the following two sections, a comparison between scratch hardness and indentation hardness results will be made.

6.1.1. Results

Figures 6.1.a and b show the variation of hardness with chemical composition in the Ni-Co system, measured from microscratch and nanoscratch tests, respectively. The microscratch tests were performed with a load of 20 ± 10 N, while the nanoscratch tests were performed with a load of 69 ± 12 μN.

Similarly to the case of indentation hardness (see Figure 4.1), an increase of the scratch hardness with decreasing load is also observed for the entire range of compositions. Although the tendency of H_s with Co proportion is not as clearly defined as that of H_i in both micro- and nanoscale results, a minimum of H_s in the range 21 to 26% Co, as well as the hardness increase for Co proportions over 68%, can be observed both in Figures 6.1.a and b. The influence of image convolution on the nanoscratch results is almost inexistent, as can be observed by comparing the H_s values retrieved from nanoscratches in Ni and Co visualized with the DNISP tip (cross markers in Figure 6.1.b) and with a sharper Si tip (square markers in Figure 6.1.b).

In terms of absolute values, H_s is larger than H_i when both are retrieved from tests performed with loads in the N range (Figures 6.1.a and 4.1.a, respectively). On the contrary, when hardness is retrieved from the nanoscale tests, in general, H_s is smaller than H_i (Figures 6.1.b and 4.1.b, respectively). This means that, while in microhardness tests the ratio H_s/H_i is larger than 1 ($1.16 < H_s/H_i < 2.32$), at the nanoscale this ratio is smaller ($0.58 < H_s/H_i < 1.06$). Consequently, the increase of hardness with decreasing contact scale is more pronounced in indentation than in scratching.

a)

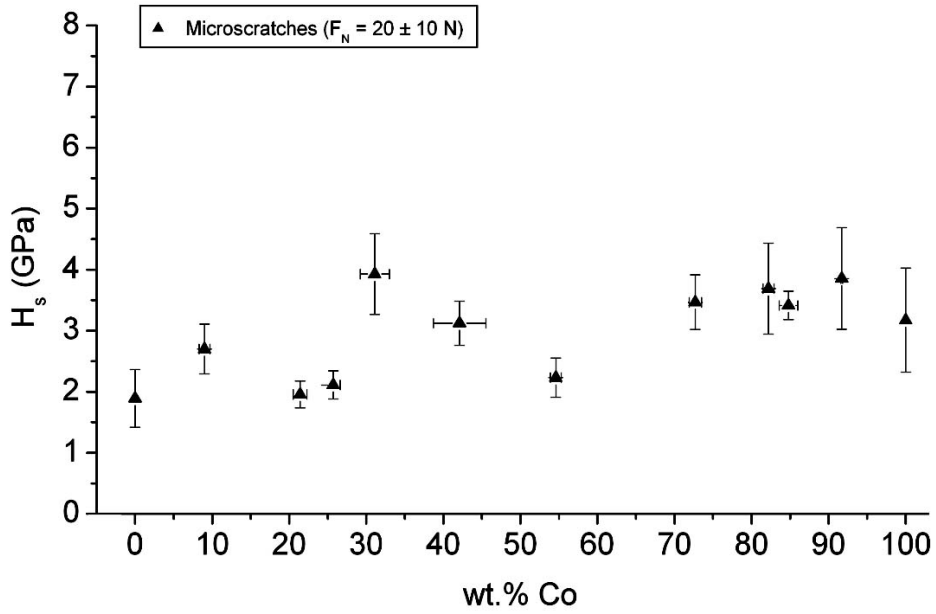

b)

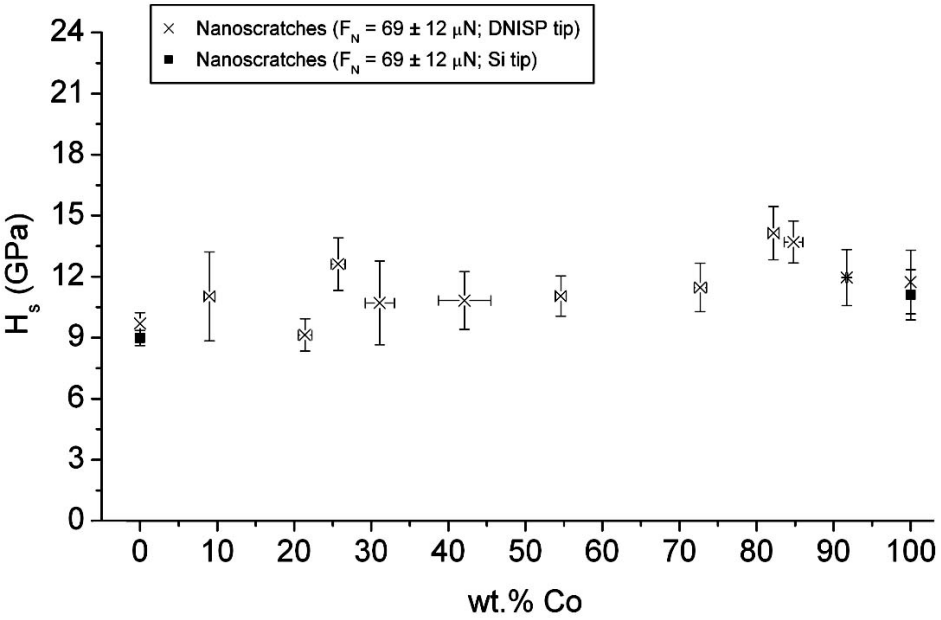

Figure 6.1. Variation of microscratch (a) and nanoscratch (b) hardness with chemical composition in the Ni-Co system. A Rockwell C indenter was used in the microscratch tests, whereas the nanoscratch tests were performed with a Veeco DNISP nanoindentation probe. Visualization of the nanoscratches was carried out with the DNISP tip in all samples and also with a Si tip in Ni and Co.

Figures 6.2 to 6.4 show SEM images of microscratches in Ni, Co and some Ni-Co alloys. The wavy morphology of the surface reliefs in the lateral regions of microscratches in Ni and Ni-42%Co (Figures 6.2.b and d, respectively), shows that plastic deformation in these materials occurs by slip, which can be expected due to the large number of slip systems in the FCC α-phase, as was previously discussed in §4.1.2.1. The lateral regions of the microscratches in Ni-85%Co and Co are formed mostly by mechanical twins (Figures 6.3.b and d, respectively), which, in this case, is probably a result of the low number of slip systems in the HCP ε' phase. This factor may difficult slip because it increases the probability of unfavourable orientations of the slip systems in relation to the stress axis. Although twinning itself does not allow accommodating a large amount of plastic deformation, the crystal re-orientation that results from it may place the slip systems in a more favourable orientation with respect to the stress axis, allowing slip to take place.

Of further interest are the SEM images of the microscratch in Ni-73%Co, where plastic deformation occurs by slip in some portions of the scratch (Figure 6.4.b), while in others the preferred mechanism is mechanical twinning (Figure 6.4.d). This clearly reveals the biphasic nature of this alloy, as was shown in the XRD results of Figure 3.9.f. The difference between the traces of plastic deformation by slip and those of mechanical twinning is also clearly visible in the end portions of the microscratches in Ni-42%Co and Ni-73%Co (Figures 6.2.e and 6.4.e, respectively).

AFM images of the nanoscratches performed in Ni and Co are shown in Figures 6.5.a and b, respectively. The nanoscratches performed in all Ni-Co samples are similar in shape to those of Figure 6.5 and no traces of mechanical twinning are found in the deformed regions.

As was previously observed (§4.1.1), the formation of mechanical twins also occurs during the microindentation tests in Co-rich samples (Figure 4.2.b), but not in ultramicro- and nanoindentation ones (Figures 4.2.d and 4.3.b, respectively). Of course that the formation of mechanical twins in Co-rich samples subjected to microscale tests results from the much larger deformed volumes involved in these tests, which cannot be accommodated just by slip when only three slip systems are active. This also explains the larger number of twins near the microscratches than near the microindentations, since the deformed volumes are larger in the first case than in the second one. Therefore, both the indentation and scratch results strongly suggest that, at submicrometric penetration depths, plastic deformation in the Ni-Co system occurs only by slip.

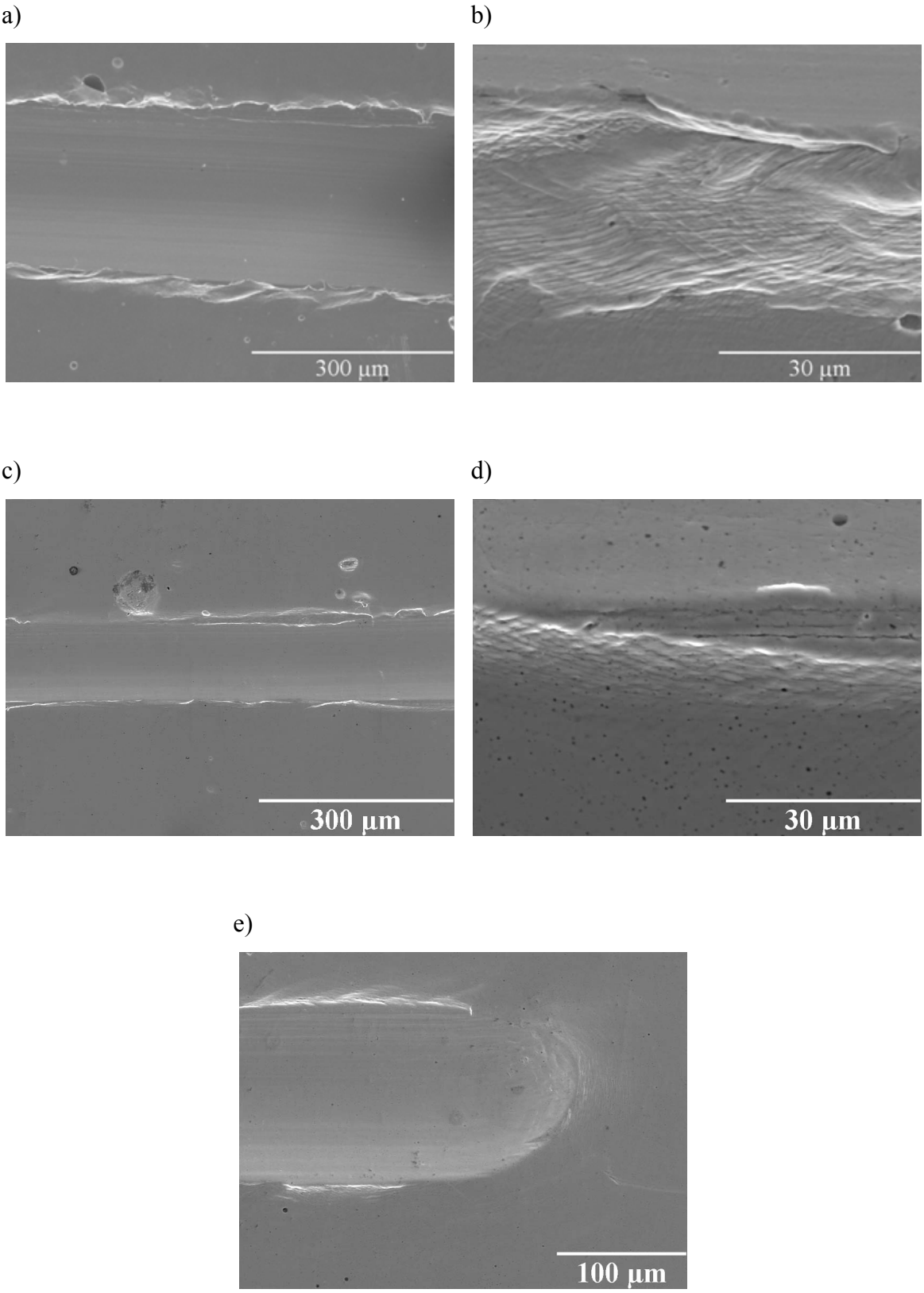

Figure 6.2. SE SEM images of Rockwell C microscratches in Ni (a and b) and Ni-42%Co (c to e), performed with a load of 20 ± 10 N.

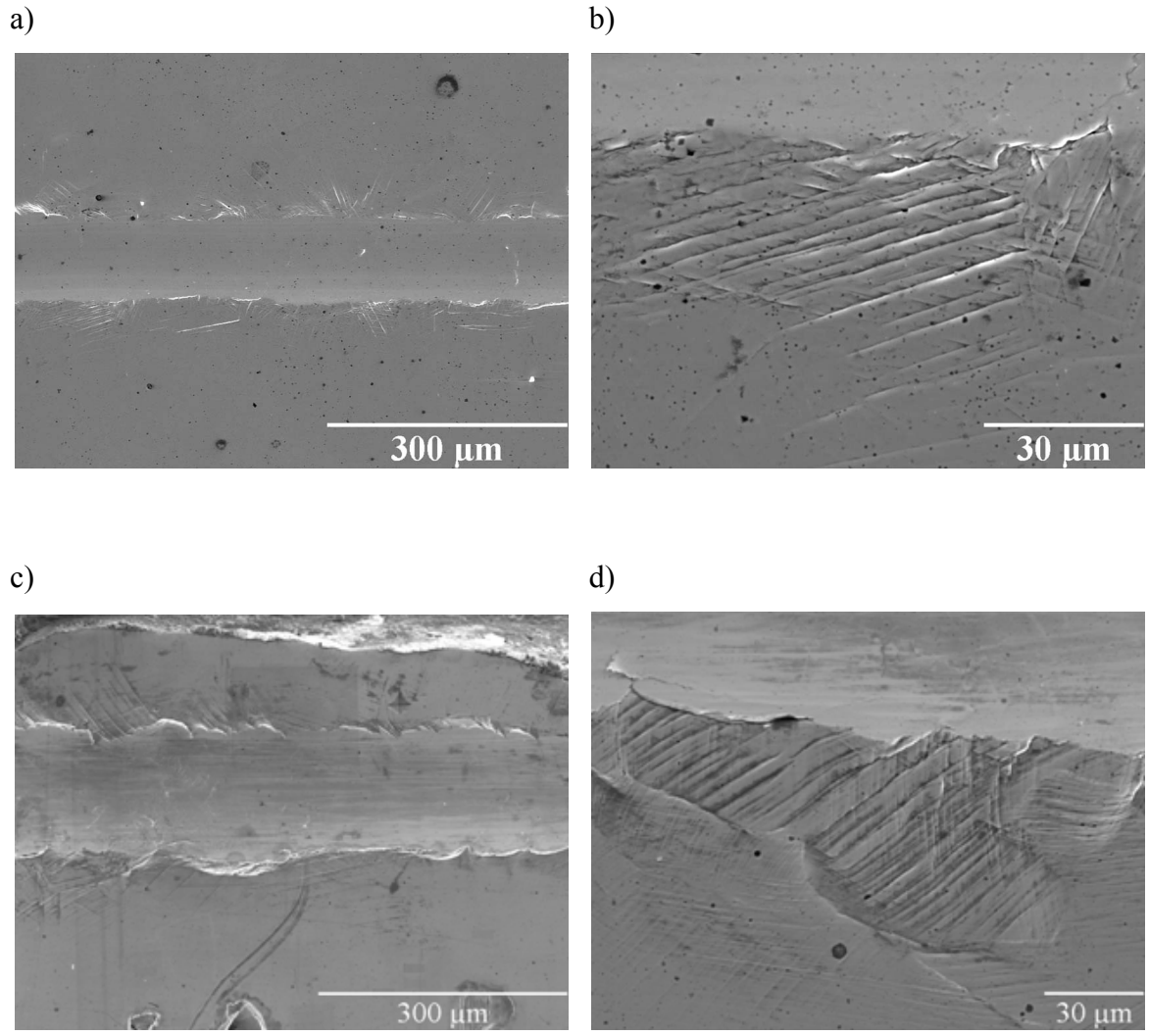

Figure 6.3. SE SEM images of Rockwell C microscratches in Ni-85%Co (a and b) and Co (c and d), performed with a load of 20 ± 10 N.

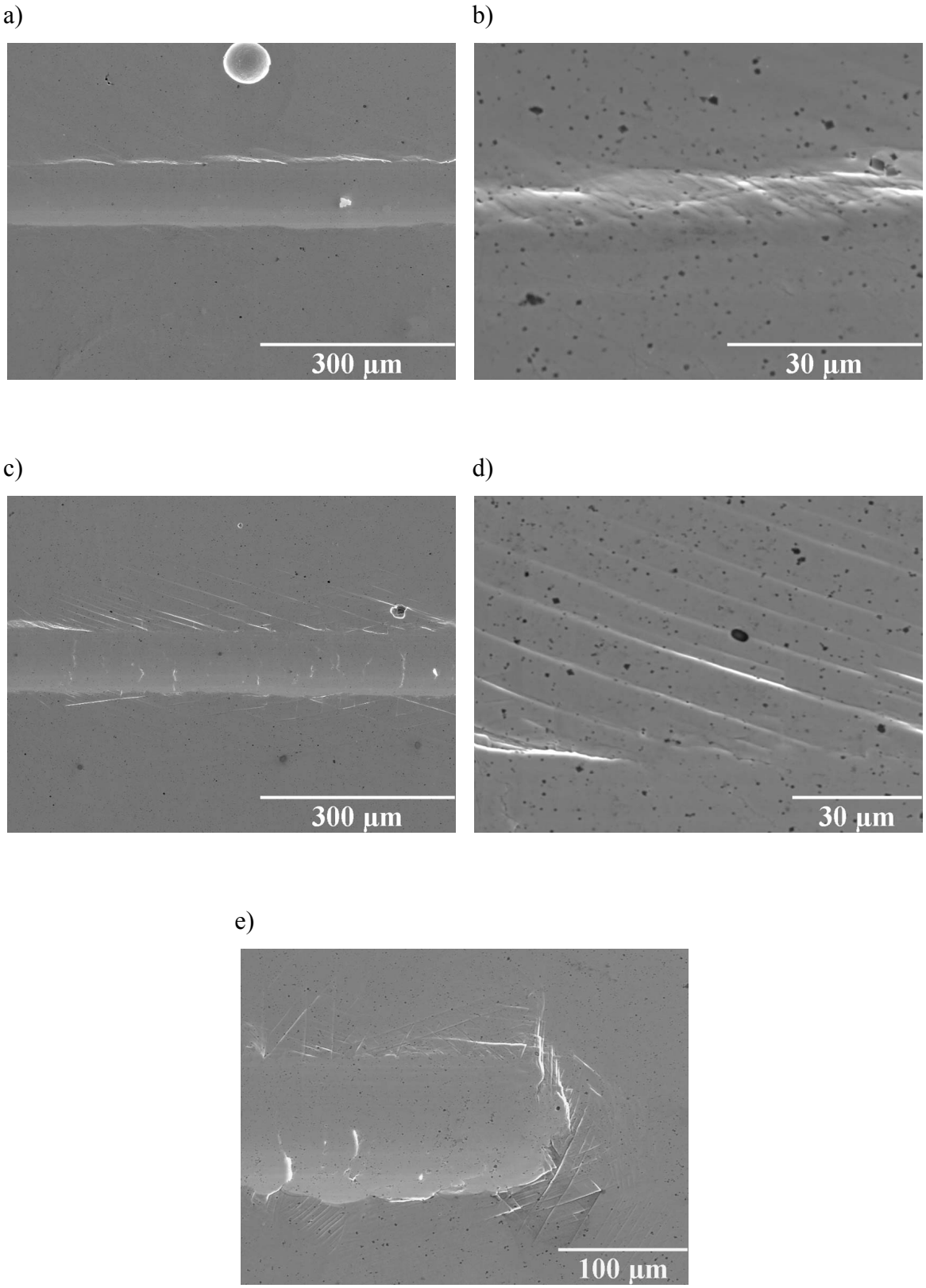

Figure 6.4. SE SEM images of a Rockwell C microscratch in Ni-73%Co, performed with a load of 20 ± 10 N.

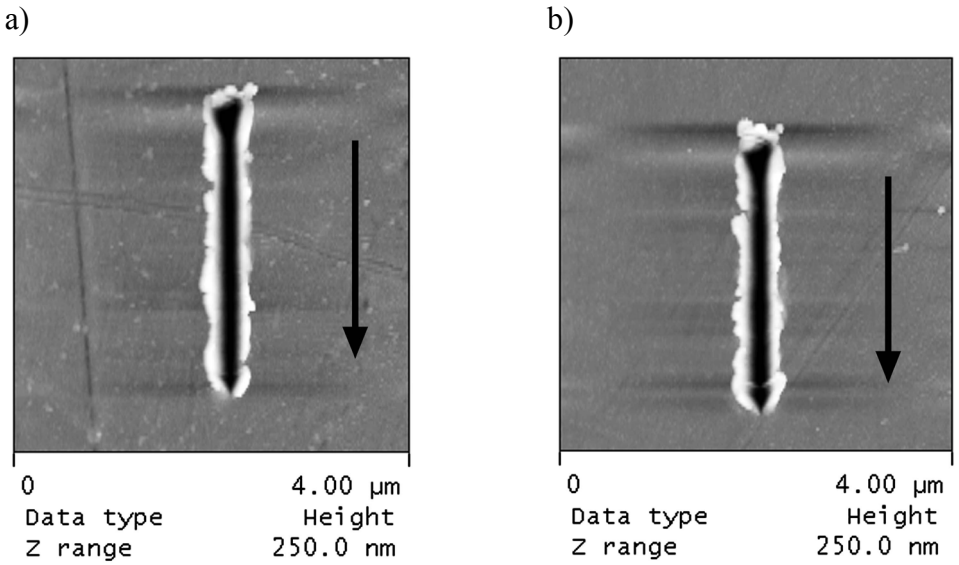

Figure 6.5. AFM topographic images of nanoscratches in Ni (a) and Co (b) performed with a DNISP tip and a load of 69 ± 12 µN. The nanoscratches were visualized with a Si tip. The black arrows in the figures indicate the scratching direction. A few residual scratches from polishing can also be observed in the images.

6.1.2. Discussion

In contrast to the considerable attention that has been dedicated to size effects in indentation, few works exist about size effects in scratch hardness. The present results, together with the early unique observations of Gane and Skinner of scratch size effects in Au and Cu [59], confirm that size effects occur not only in the static hardness response of metallic materials, but also in their response to non-static tests. More recently, Wo and Ngan [218] found experimental evidence of incipient plasticity effects under scratching conditions. These authors observed the occurrence of pop-in events during nanoscratching of Ni_3Al with a Berkovich tip mounted in a Hysitron nanomechanical test instrument. In addition, the recent TEM observations by Wo *et al*. [219] of nanoscratches in Ni_3Al showed the existence of a high dislocation density region within the scratch core, and a lower dislocation density region surrounding the former one, which is similar to what happens in nanoindentations, as was previously shown in §5.2. In spite of the similarities observed under static (indentation) contact conditions and non-static (scratch) ones, regarding the influence of contact scale on the plastic behaviour of the material, the differences between indentation and scratch hardness measurements prevent a direct comparison of the results and conclusions should be taken cautiously.

First of all, the differences between the measurement protocols for indentation and scratch hardness must be considered when comparing the results shown in Figure 4.1 with

those shown in Figure 6.1. In scratch tests, the width of the scratches (w) is measured at the surface mean line and not at the top of the ridges[•] (Figure 6.6), whereas in the case of microindentation hardness, the length of the diagonals of the Vickers indentations is measured from optical observation from the top. Therefore, the measurement protocol in indentation corresponds approximately to the situation of measuring w at the top of the scratch ridges. Consequently, this aspect leads to a trend of higher scratch hardness values as compared to indentation hardness ones. For example, the microscratch hardness of Ni and Co is 1.9 and 3.2 GPa, respectively, when w is measured at the surface mean line, and 1.4 and 2.4 GPa, respectively, when w is measured at the top of the ridges. These last values compare much better with the microindentation hardness of Ni and Co: 1.3 and 2.6 GPa, respectively. Secondly, scratch tests present an extra difficulty as compared to indentation ones, which consists of the fact that small inclinations of the surface of the sample relatively to the indenter sliding plane cause changes in the applied load during the tests. The influence of sample inclination can be observed by comparing the longitudinal cross-section profiles of nanoscratches performed in Ni and Co (Figures 6.7.a and b, respectively). In both cases the load chosen was 57 μN and the scratches were performed from the lower to the higher region of the inclined surface. Due to sample inclination, in this example, the load increased from 57 to 61 μN in the nanoscratch test in Ni, while in the nanoscratch test in Co the load increased from 57 to 95 μN, which means that the Co sample has larger local inclination of the surface than the Ni one. Since the local inclinations of samples surfaces are impossible to eliminate and no load control loop (keeps the load constant) is active during the scratch tests, the scratch hardness measurements are certainly affected by these variations of the normal applied load during the test. Even so, this latter error source leads, in general, to errors smaller than 10%, thus not affecting the trustworthiness of the scratch results if a statistically significant number of tests are performed. Nevertheless, it can lead to the smoothing of local steep variations of the hardness, which are more clearly detected in indentation hardness measurements.

[•] This procedure was adopted in this work due to the irregular shape of the ridges of many scratches and the uncertainty if the perimeter of the contact between indenter and sample is really located at the top of the ridges.

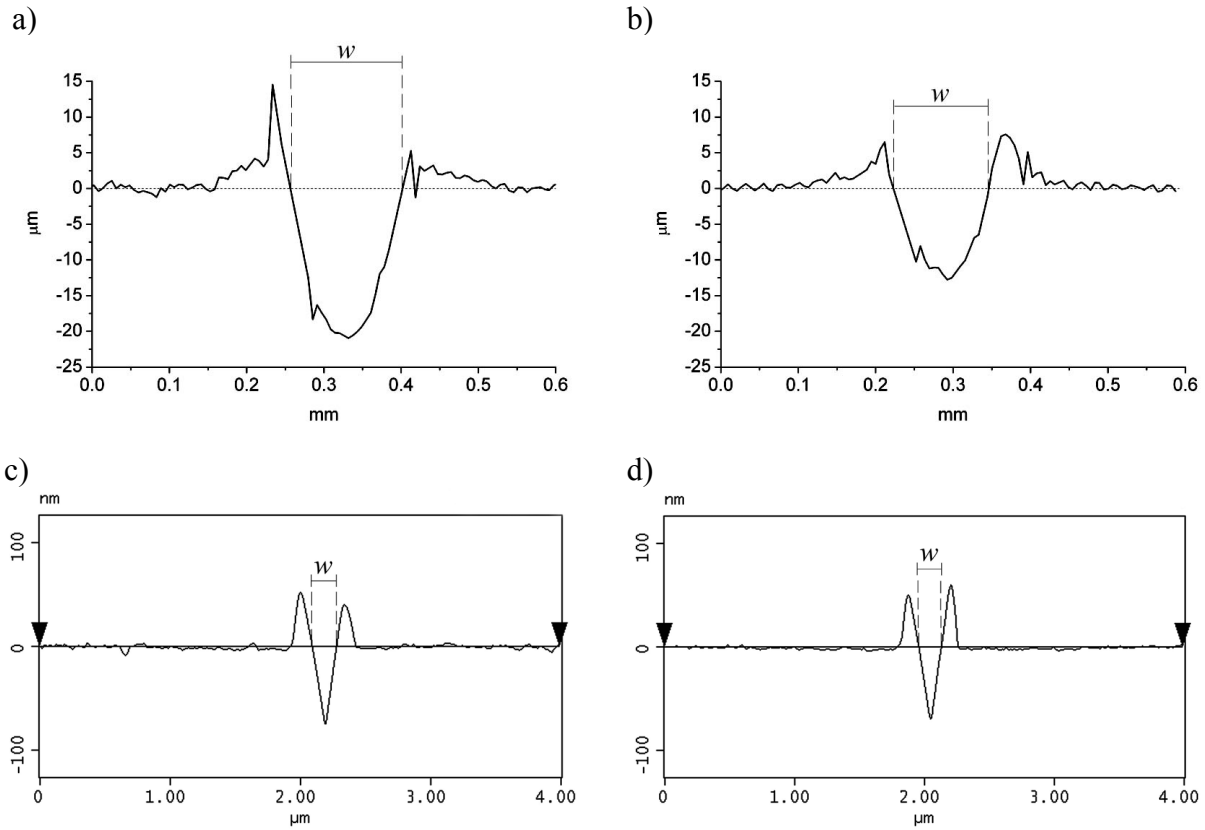

Figure 6.6. Topographic profiles of the transversal cross-section of scratches in Ni and Co: microscratches (a and b, respectively) and nanoscratches (c and d, respectively). Microscratch and nanoscratch profiles were obtained with optical profilometry and AFM, respectively. By looking to these profiles it is not clear if the perimeter of the contact between indenter and sample is located at the top of the scratch ridges or not. Therefore, the scratch width (w) is measured at the surface mean line.

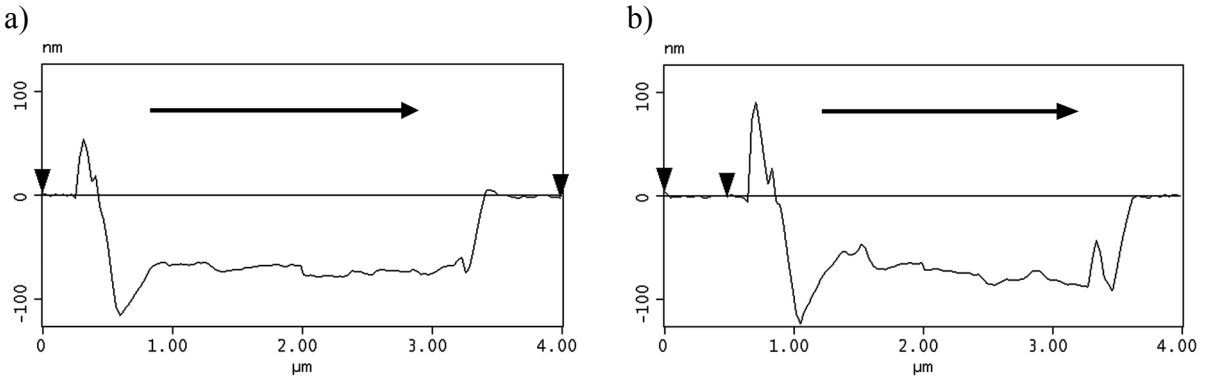

Figure 6.7. AFM topographic longitudinal profiles of the nanoscratches in Ni (a) and Co (b) shown in Figure 6.5. The scratches were performed from the lower to the higher region of the inclined surface. Black arrows in the profiles indicate the scratching direction.

Similarly to what occurs with indentation hardness, the scratch hardness appears to be more sensitive to the composition of the alloys as the penetration depth increases up to the micrometer range. The discussion on the hardness trend with composition made in §4.1.2.1 for the case of indentation hardness is equally applicable to the case of scratch hardness. In

addition to the less clear composition-related trend of hardness for penetration depths smaller than 100 nm (loads in the μN range), the increase in the absolute values of hardness (up to nine times in H_i and five times in H_s) shows that, at the nanometric contact scale, other factors besides composition and microstructure become increasingly relevant in the indentation and scratch response of the material. These factors (e.g. native oxide layers, surface free energy and strain hardening effects) have been extensively discussed in §4.1.2.2.

In particular, the native oxide layer may have some contribution to the difference between the nanoindentation and nanoscratch hardness values (Figures 4.1.b and 6.1.b, respectively). In spite of the differences of the measurement protocols, which tend to lead to higher scratch hardness values, as mentioned earlier, the nanoindentation hardness values are higher than nanoscratch ones. The depth of the nanoindentations and nanoscratches performed in Ni, Ni-55%Co and Co is shown in Table 6.1. The experimentally measured depth of the nanoindentations is about 30 nm while that of nanoscratches is about 70 nm. On the other hand, the thickness of the native oxide layers in metals under environmental conditions is on the order of a few nanometers [148, 165, 166]. In this way, a possible explanation for the lower nanoscratch hardness as compared to nanoindentation hardness is the presence of nanometric native oxide layers, which have a stronger influence in static nanohardness tests than in non-static ones, due to the spalling of the thin oxide film ahead of the indenter during scratching [220]. The compressive forces exerted by the indenter in the plane of the oxide film may lead to the formation of cracks in the oxide layer, which can propagate and lead to the detachment of the oxide layer region in front of the indenter, thereby decreasing the resistance to indenter penetration.

Table 6.1. Depth of nanoindentations and nanoscratches performed in Ni, Ni-55%Co and Co, retrieved directly from the AFM images of nanoindentations and nanoscratches obtained with sharp Si tips.

Sample	**Nanoindentations**		**Nanoscratches**	
	F_N (μN)	h (nm)	F_N (μN)*	h (nm)*
Ni	57	34 ± 3	59	64−78
Ni-55%Co	57	31 ± 3	64	61−76
Co	57	29 ± 3	76	64−87

* Average load.

Both the indention and scratch hardness results of the present work show that the strength of small regions can be much higher than the bulk strength, i.e. the contact hardness

under individual touching surface asperities can be considerably higher than that predicted from bulk measurements. Such effects might be of critical importance in the wear response of a material, either leading to a decrease of the wear rate as the penetration depth decreases or, as suggested by Gane and Skinner [59], to an increase of the size of the wear debris due to the breaking of cold welded junctions at regions distant from the original interface, which are weaker than the near interface regions. Therefore, the results presented up to now for the Ni-Co laser clad samples show that, if the contact scale during a tribological process is in the nanometre range (such as in finely polished surfaces submitted to average or low loads in dry or boundary lubrication conditions), macro and microhardness measurements, either indentation or scratch ones, can be of limited help for wear calculations or as criteria for materials selection. Consequently, the tribo-mechanical characterization of materials at the nanoscale, either by nanoindentation, nanoscratch or, as it will be shown in the next section, by nanowear tests, should be considered in the evaluation of their wear resistance.

6.2. Influence of contact scale on abrasive wear

The contact scale dependence of hardness in the Ni-Co system has been analysed in detail in previous sections. In this section, the analysis of the influence of contact scale is extended to the case of two-body abrasive wear. Since it was demonstrated that no great differences exist between the load dependence of hardness of the different materials used in this work, the influence of contact scale on abrasive wear was analysed only for the two terminal materials of the Ni-Co system, i.e. Ni and Co, and for the Ni-85%Co alloy, which presents one of the largest hardness values of this system. First, an evaluation of the abrasive wear behaviour of these materials at the nanometric contact scale is carried out by performing AFM cantilever-based nanoabrasive wear tests with a DNISP tip (the tip was previously submitted to a running-in period, as explained in §2.3.3). Then, the results from the nanoabrasive wear tests are combined with the information gathered from the previous sections to determine the consequences of reducing contact scale on the global abrasive wear response of ductile materials, such as those of the Ni-Co system.

6.2.1. Results

Figure 6.8 shows AFM images of regions in Ni, Ni-85%Co and Co where nanoabrasive wear tests were performed with a load of 2.5 μN. The topographic images (Figures 6.8.a, b and c) do not show signs of wear occurring in any of the samples. However, the friction images

(Figures 6.8.d, e and f) show a slight change of contrast at the regions where the tests were carried out (2 μm × 2 μm inner square), especially in Ni-85%Co and Co, which indicates the occurrence of small modifications of the surface in these regions.

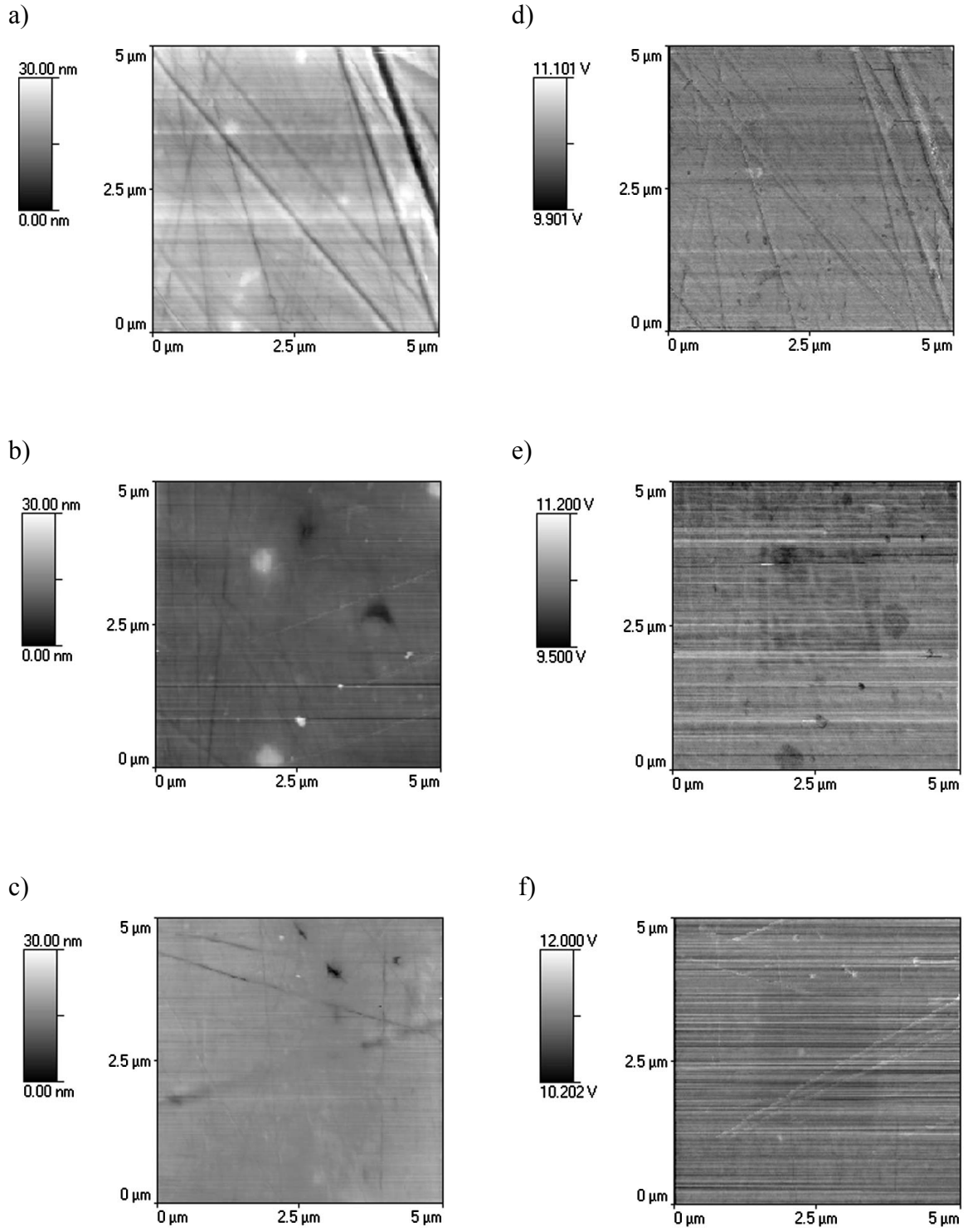

Figure 6.8. AFM topographic images and correspondent friction images of regions in Ni (a and d, respectively), Ni-85%Co (b and e, respectively) and Co (c and f, respectively), subjected to wear tests with a DNISP tip and F_N = 2.5 μN.

AFM topographic images of worn regions in the three samples, resulting from wear tests performed with a load of 15 μN, can be observed in Figure 6.9. In general, the accumulation of debris is larger at the right side of the worn area in comparison to the left side, and at the bottom side in comparison to the top side, which is a consequence of the application of the raster pattern scanning movement of the AFM scanner shown in Figure 2.39.b to single scan tests.

The worn volumes (V_{worn}) resulting from the wear tests performed on the three samples with F_N = 15 μN are presented in Figure 6.10. Each volume value in the plot is the average of 10 measurements performed in different regions of the sample, in order to take into consideration the influence of crystallographic orientation in the wear measurements.

It can be observed that Ni is the sample with the lowest wear resistance while Ni-85%Co is the most resistant sample. Moreover, Ni-85%Co is the sample that presents the largest scattering of V_{worn} values, which may be due to local variations of the Ni to Co proportion. The maximum depths of the worn regions, determined from the average horizontal cross-section profiles, were in the range 78 to 138 nm, 24 to 95 nm and 51 to 91 nm in Ni, Ni-85%Co and Co, respectively.

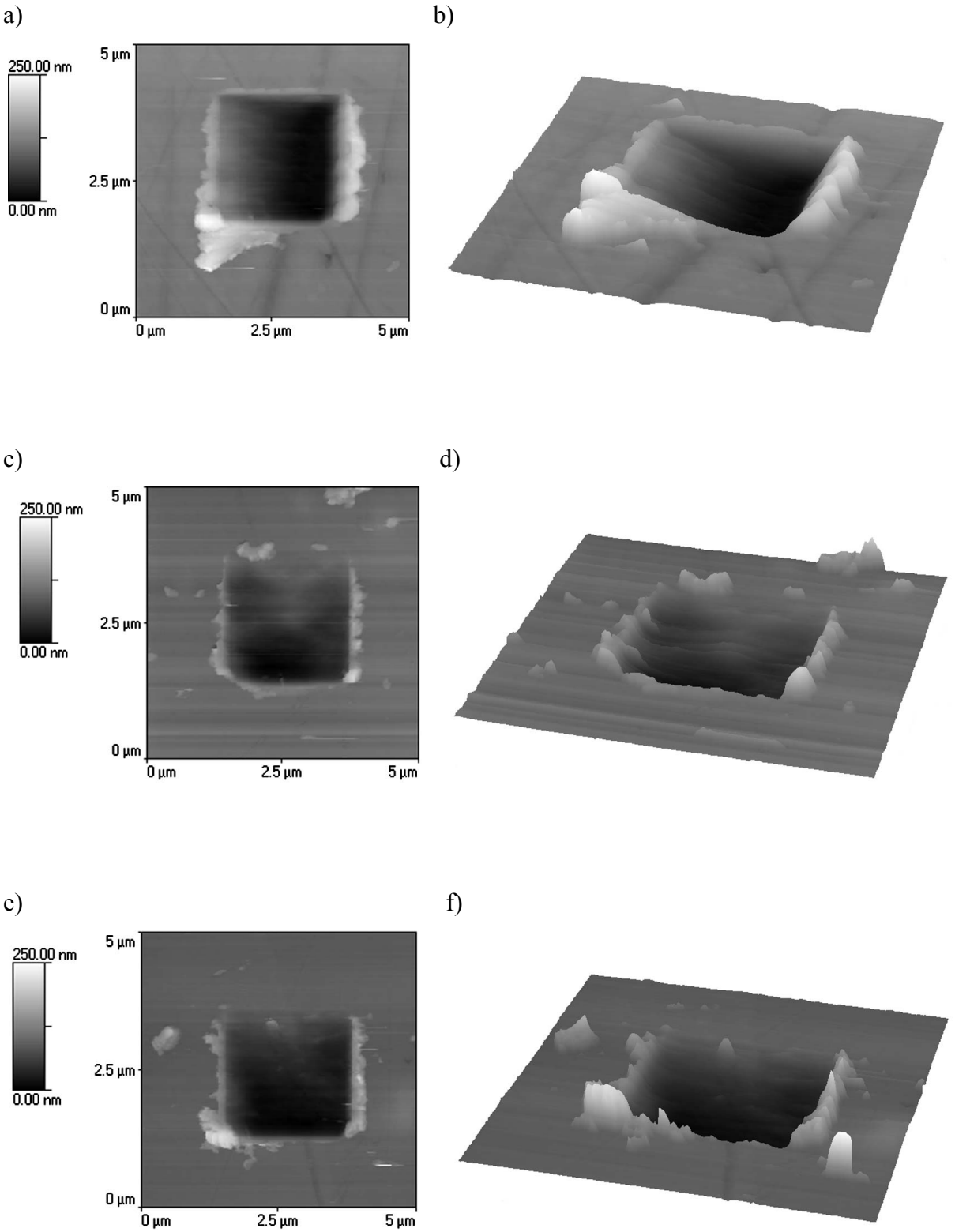

Figure 6.9. AFM topographic 2D and 3D images of regions in Ni (a and b, respectively), Ni-85%Co (c and d, respectively) and Co (e and f, respectively), subjected to wear tests with a DNISP tip and F_N = 15 µN. The *X*, *Y* and *Z* scales in the 2D and 3D images are the same.

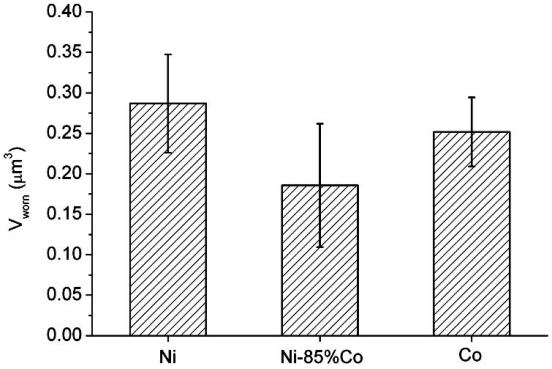

Figure 6.10. Volume worn during the wear tests in Ni, Ni-85%Co and Co with F_N = 15 μN.

6.2.2. Discussion

According to the Rabinowicz wear model (Eq. 1.19), the abrasive wear response of ductile materials (e.g. metals) both in single and multiple asperity contact conditions is closely related to their indentation hardness, which is assumed to be independent of contact scale. However, as could be observed from Figure 4.1, although the hardness ranking of Ni, Ni-85%Co and Co is not altered when contact scale decreases, the absolute values of H_i are much larger when contact occurs at the nanometric scale. Therefore, the following question can be raised: which of the H_i values (micro or nano) is related to the abrasive wear behaviour of materials that present ISE? The answer to this question is neither simple nor direct and the several aspects related to it will be presented next.

By assuming that the diamond tip has a spherical end that contacts a flat surface sample, and that both tip and sample are frictionless elastic half-spaces, Hertz theory can be applied [25]. In these circumstances, the variation of the mean contact pressure (σ_m) as function of the applied normal load is given by Eq. 1.5, whereas the radius of the contact circle (a_c) can be calculated by using Eq. 1.1. The reduced Young's modulus has been previously determined in §5.1.2 (E_r = 170 and 175 GPa for Ni and Co, respectively). The maximum shear stress in the sample (τ_{max}) occurs at a depth of about $0.47a_c$ below the centre of the contact area and is about $0.47\sigma_m$ (Eq. 1.6). If it is assumed that the diamond tip radius is equal to the centroid of the interval determined in §2.3.3 (R = 366−490 nm), i.e. R = 428 nm, the radius of the contact circle estimated with Eq. 1.1 is about 17 and 30 nm when the normal load is 2.5 and 15 μN, respectively. Consequently, the point of τ_{max} in the Ni-Co samples is located about 8 and 14 nm below the surface when the normal load is 2.5 and 15 μN, respectively.

The plots of Figure 6.11 show the variation of σ_m with F_N for Ni, Ni-85%Co and Co (thick solid line), according to Eq. 1.5. Note that this behaviour ($\sigma_m \propto F_N^{1/3}$) will only be

observed as long as the indented region remains in the elastic regime and assuming single contact conditions between tip and sample. However, in the real case the samples are not infinitely hard and plastic deformation occurs once the mean contact pressure reaches a certain threshold value.

The onset of plastic deformation in a plastic half-space indented by a rigid sphere occurs below the centre of the contact area, at the point of τ_{max}, when $\sigma_m \approx 1.1\sigma_Y$, while full plasticity of the contact occurs when $\sigma_m \approx 3\sigma_Y$ (see §1.2.1). According to Eq. 1.9, two ranges of σ_Y values can be estimated for each of the samples, one from the microindentation hardness values and the other from the nanoindentation hardness values (Figures 4.1.a and b, respectively). From now on, these values will be referred to as σ_Y (micro) and σ_Y (nano), respectively, and the intervals $1.1\sigma_Y$ (micro)–$3\sigma_Y$ (micro) and $1.1\sigma_Y$ (nano)–$3\sigma_Y$ (nano) are represented by the shaded areas (plus the respective error bars) in the plots of Figure 6.11[•]. These intervals represent the elastoplastic regime of the contact, i.e. the stress from the onset of plasticity to full plasticity.

The plots of Figure 6.11 can be used together with the AFM images of Figures 6.8 and 6.9 to determine if the plasticity of the contact is controlled by the microscale yield stress value or by the nanoscale one. In the first case, plastic deformation should only occur if the mean contact pressure for a given applied load is located within or above the interval $1.1\sigma_Y$ (micro)–$3\sigma_Y$ (micro), whereas in the second case, σ_m must be located within or above the interval $1.1\sigma_Y$ (nano)–$3\sigma_Y$ (nano). According to the plots of Figure 6.11, for $F_N = 15$ μN, $\sigma_m > 1.1\sigma_Y$ (micro)–$3\sigma_Y$ (micro) and $\sigma_m \subset 1.1\sigma_Y$ (nano)–$3\sigma_Y$ (nano)[••], which means that the contact should undergo plastic deformation whether its plasticity is controlled by σ_Y (micro) or σ_Y (nano). The AFM images of Figure 6.9 showed that wear of the samples occurs when $F_N = 15$ μN, which is in agreement with the observations in the plots of Figure 6.11. For $F_N = 2.5$ μN, $1.1\sigma_Y$ (micro)–$3\sigma_Y$ (micro) < σ_m < $1.1\sigma_Y$ (nano)–$3\sigma_Y$ (nano), which means that the contact should undergo plastic deformation only if σ_Y (micro) is the property controlling its plasticity. However, the AFM images of Figure 6.8 showed that no noticeable wear occurs when F_N = 2.5 μN, which corresponds to the condition $\sigma_m < 1.1\sigma_Y$ (nano)–$3\sigma_Y$ (nano). Therefore, we conclude that the plasticity of the contact is controlled by σ_Y (nano) and not by σ_Y (micro).

[•] In these plots it is assumed that the radius of the contact circle is solely determined by elastic deformation up to $\sigma_m = 3\sigma_Y$, which enables applying Eq. 1.5 until full plasticity is reached [221].

[••] In the case of Ni-85%Co and Co, the condition $\sigma_m \subset 1.1\sigma_Y$ (nano)–$3\sigma_Y$ (nano) is in the limit of being satisfied when $F_N = 15$ μN.

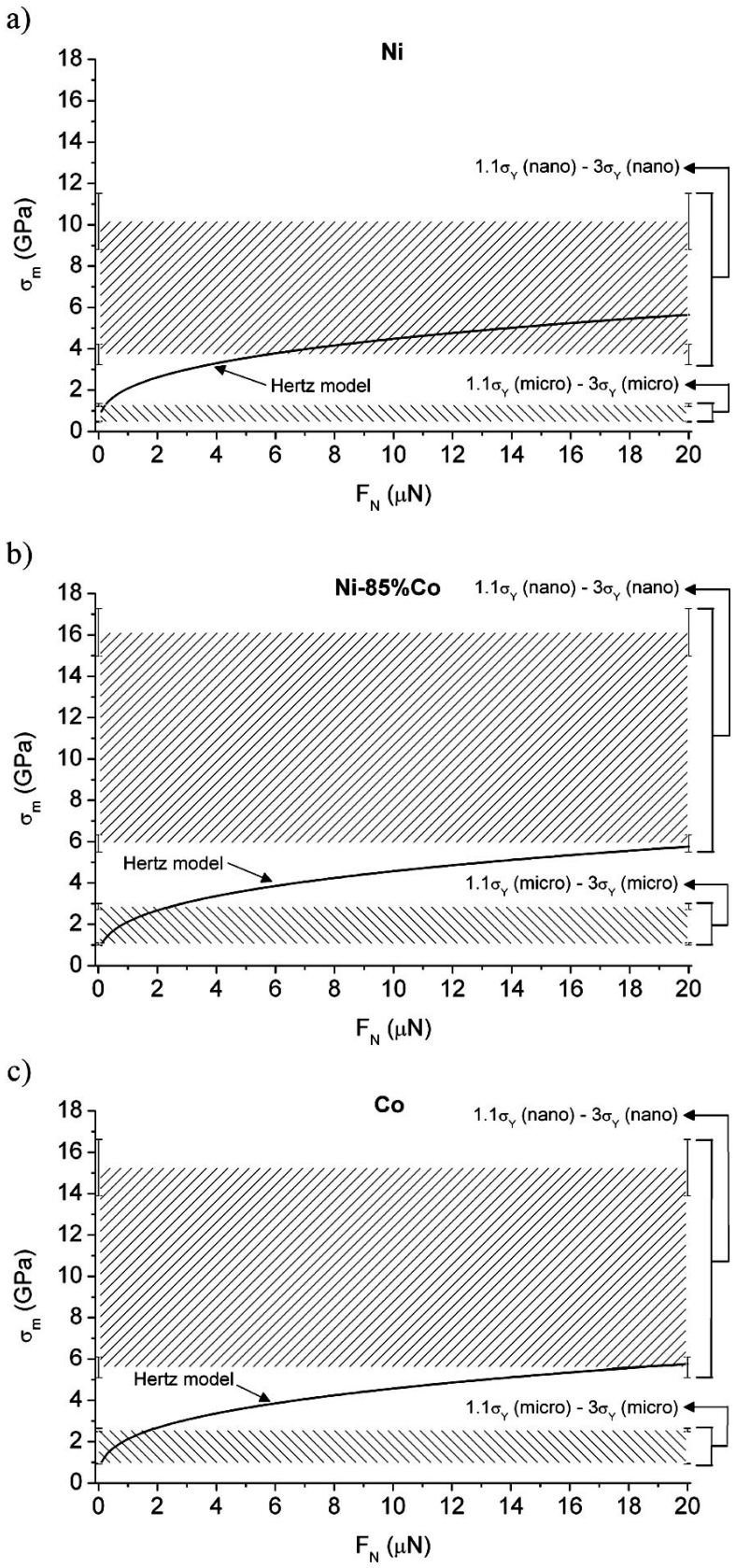

Figure 6.11. Variation of σ_m with F_N (thick solid line) for the elastic contact between a spherical diamond tip of R = 428 nm and Ni (a), Ni-85%Co (b) and Co (c). The shaded areas in the plots represent the intervals between $1.1\sigma_Y$ and $3\sigma_Y$ calculated from the micro- and nanoindentation hardness values presented in Figures 4.1.a and b, respectively. The error bars at the sides of the shaded areas result from the scattering of the hardness values.

It should be noted that in this analysis it is being assumed that the contacting surfaces are flat. In fact, a small but finite surface roughness exists both in the samples and the tip and, consequently, contact between the two surfaces first occurs between the closest asperities, as shown in Figure 6.12. Since the real contact area may be substantially smaller than the nominal contact area (see Figure 1.3), the pressure at contacting asperities can be much higher than the mean contact pressure at the indented region. Consequently, even if the indented region does not reach the fully plastic state under a given applied load ($\sigma_m < 3\sigma_Y$ (nano)), some of the contacting asperities of the sample will undergo fully plastic deformation ($\sigma_m \approx 3\sigma_Y$ (nano)).

On the other hand, by increasing the applied load more asperities will come into contact and some of those which were previously in the elastic regime may become plasticized (see Figure 1.7). By estimating the plasticity index, ψ (Eq. 1.14), an idea whether the sample asperities undergo preferentially elastic or plastic deformation can be given. Taking E_r determined in §5.1.2, H_i as the hardness measured from the AFM nanoindentation tests, $\sigma \approx 1.25R_a$ (for a Gaussian distribution of asperity heights [153]) and $r_a \approx 1-5$ nm (see Figure 3.2.c), a plasticity index in the range 5 to 22 is obtained for the Ni-Co samples. As mentioned in §1.2.2, if $\psi > 1$ the asperities will deform plastically under even the lightest of loads and, therefore, one can expect that most of the contacting asperities in the Ni-Co samples will undergo plastic deformation during the nanoabrasive wear tests. The addition of lateral movement between tip and sample will produce shearing of the plasticized asperities, resulting in sample wear.

Furthermore, the large contact radius to step size ratio used in the nanoabrasive wear tests causes scan overlap. When the normal load is 2.5 and 15 μN, the tip passes 10 and 14 times, respectively, over each scan line (see Figure 6.13). Scan overlap produces a cumulative effect in the contact region corresponding to each scan line [222], which can introduce some fatigue damage.

When the load increases from 2.5 to 15 μN, both the number of plastic contacting asperities and the number of tip passages over each scan line increase, which can explain the observation of large worn craters when F_N = 15 μN. Nevertheless, as could be seen from the AFM friction images of Figures 6.8.d, e and f, some signs of wear start to be observed even for F_N = 2.5 μN, which can be due to a slight plastic deformation of the contacting asperities.

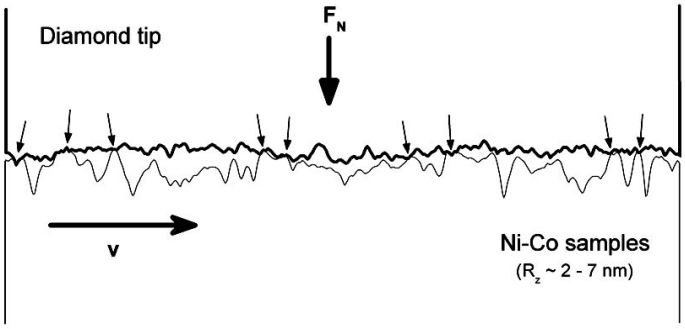

Figure 6.12. Schematic representation of the contact region during sliding contact between the Ni-Co samples and the diamond tip with a speed v, taking into consideration the existence of roughness in both surfaces. The average peak-to-valley height (R_z) of the Ni-Co samples, determined from AFM measurements, is also shown in the figure for a better perception of the roughness of the samples. The tip is assumed to be slightly smoother than the Ni-Co samples. The small arrows point towards the asperities which support the applied normal load.

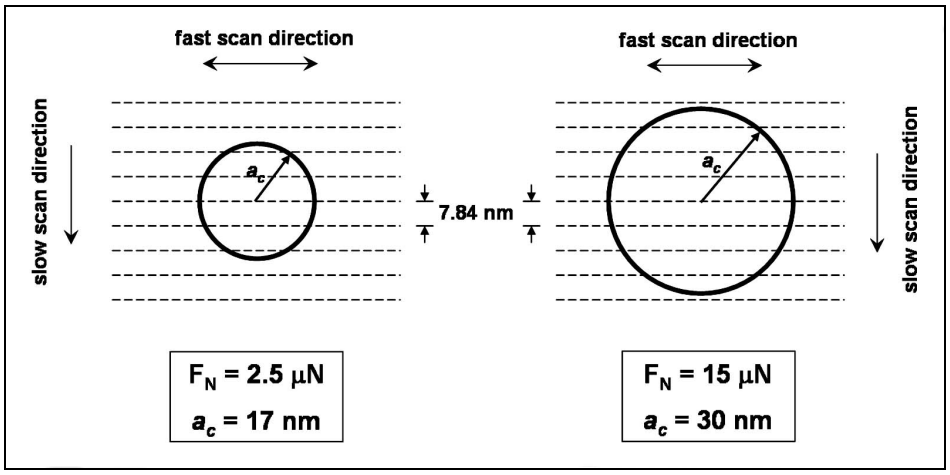

Figure 6.13. Comparison of the contact radius, a_c, with the step size (7.84 nm) in the nanoabrasive wear tests with normal loads of 2.5 and 15 μN (left and right schematics, respectively). The perimeter of the contact and the scan lines are represented by circumferences and dashed lines, respectively. Only a small portion of the scanned area is represented in the schematics, since the areas are composed of 256 lines with a length of 2 μm. During scanning, the tip passes 10 times (5 × 2 fast scan directions) over each scan line when F_N = 2.5 μN, and 14 times (7 × 2 fast scan directions) when F_N = 15 μN.

The tangential force (F_T) may also affect the plastic deformation of the contact region. When a spherical body slides against a plane body and the contact remains in the elastic regime, the magnitude of τ_{max} increases (in comparison to the static case) and the point of τ_{max} is located nearer to the surface or even in the surface, depending on the value of the coefficient of friction (μ) [223, 224]. For $\mu > 0.3$ the point of τ_{max} is located in the surface and at the trailing edge of the contact. However, for the experimental conditions of the nanoabrasive wear tests a coefficient of friction of less than 0.3 is expected• [225]. For a value

• Preliminary results on the tribological characterisation of the Ni-Co samples [225] showed that the coefficient of friction retrieved from AFM friction tests with a contact mode Si tip, under environmental conditions, is smaller than 0.2. Although Si is different from diamond, this result shows that at the nanoscale a small μ is expected for the materials of the Ni-Co system sliding against dissimilar materials.

of μ of 0.3, yielding first occurs at a depth of about $0.42a_c$ when $\sigma_m \approx \sigma_Y$ [224], which is very similar to what happens in static contact conditions (yielding at a depth of $0.47a_c$ when $\sigma_m \approx 1.1\sigma_Y$). Therefore, the influence of F_T on the point of τ_{max} should be negligible and cannot be responsible for the generation of large worn regions when F_N = 15 μN. Nevertheless, an important difference exists between static and sliding contact conditions in the elastic regime: in the first case the point of τ_{max} is fixed, occurring at a distance of $0.47a_c$ below the surface, while in the second case the point of τ_{max} moves with the sliding tip along the scan line. Consequently, during sliding, the material is subjected to contact conditions which are much more severe than in the static case.

The combination of sliding contact conditions with the influence of scan overlap and the fact that the point of τ_{max} is located just below the surface roughness, will most probably lead to the total plastification of the contact region during the scan of the abrasive tip over the surface, resulting in a sudden increase of the amount of material removed. It is also interesting to note that the worn volume ranking of the three tested materials (Figure 6.10) is opposite to the ranking of the H_i/E values obtained from the DSN tests (Figure 4.11.c), which confirms that higher yield strain limits for the rupture of surface asperities result in less wear.

The results obtained in §5.1 on the onset of plasticity of the samples can be used to further improve the discussion of the information in Figure 6.11. It was previously found (see page 153) that the values of τ_{max} for the homogenous nucleation of dislocations in Ni and Co are in the range 2 to 3.8 GPa, which corresponds to σ_m values in the range 4.2 to 8.1 GPa ($\tau_{max} \approx 0.47\sigma_m$). These σ_m values are closer to those obtained for $1.1\sigma_Y$ (nano) than to those obtained for $1.1\sigma_Y$ (micro), as can be concluded from Figure 6.11.

The analysis made above strongly suggests that, at the contact scale of asperities, the abrasive wear behaviour of the material depends on the nanoscale yield stress (and hence on the nanoscale hardness) and not on the microscale yield stress, at least when the surfaces are smooth. In fact, since the factors that affect the indentation and scratch behaviour of the material at the nanoscale (e.g. plastic strain gradients, strain hardening due to mechanical polishing, surface free energy, oxide and other contamination layers, dislocation-free regions and crystallographic anisotropy) are also present in tribological solicitations involving similar contact scales, this finding seems straightforward. Nevertheless, only very recently some works started giving attention to this possibility (see §1.4). It should be noted that an increase of load during sliding between smooth engineering surfaces should result in an increase of the number of contacting asperities but not on the average area of contact for each touching

asperity [28]. Therefore, if the surface roughness does not increase during macroscopic sliding, the abrasive wear behaviour of the samples will still be related to the nanoscale hardness and not to the bulk hardness. In the case of surfaces with a broader distribution of asperity heights, contact between the several asperities will occur at different depths, resulting in local variations of the hardness and hence in a more complex tribological response of the material. Even if the wear mechanism is independent of contact scale, the local wear rate caused by asperities contacting at different depths will be different due to the depth dependence of hardness, which in the case of the Ni-Co samples becomes relevant for depths of less than 2 μm.

The results presented up to now in the present work strongly suggest that the abrasive wear response of all the materials that exhibit indentation size effect is affected by contact scale, and that this effect should be considered in tribological evaluation. Therefore, a general analysis of the influence of contact scale on the abrasive wear response of ductile materials will be made in the following section by combining the classical Rabinowicz wear equation (Eq. 1.19) with the equation obtained in §4.1.2.2 (Eq. 4.4), which enables predicting the hardness for different penetration depths.

6.3. A model for the influence of contact scale on the abrasive wear response of ductile materials

According to the Rabinowicz model for the abrasive wear of ductile materials (Eq. 1.19), the wear rate (Q) depends on the indentation hardness of the softer material, which is assumed to be independent of contact scale. However, as has been extensively reported along this work, many ductile materials (including those studied here) present an increase of the hardness with decreasing indentation depth, when the depth of penetration is smaller than just a few micrometers.

As demonstrated in §4.1.2.2, the depth dependence of hardness can be accurately predicted by Eq. 4.4. Therefore, by replacing the depth independent hardness of Eq. 1.19 by the expression on the right side of Eq. 4.4, the contact scale dependence of hardness can be incorporated into the Rabinowicz model:

$$Q_h = K_{ab} \frac{F_N}{H_0 \sqrt{1 + \frac{h^*}{h}} + \kappa \frac{E_s}{h}}, \tag{6.1}$$

where Q_h is the wear rate resulting when the asperities of the hard material penetrate the surface of the soft material to a depth h. By dividing Eq. 6.1 by Eq. 1.19, taking the hardness value in Eq. 1.19 as the bulk hardness of the material (H_0), and assuming that the wear coefficient (K_{ab}) is invariant with scale, the influence of contact scale on the abrasive wear rate can be quantified by:

$$\frac{Q_h}{Q} = \frac{1}{\sqrt{1+\frac{h^*}{h}+\kappa\frac{E_s}{H_0 h}}}. \tag{6.2}$$

Before proceeding to the application of Eq. 6.2 to a particular material case, let us consider three general situations where an isotropic rigid-plastic material with flat surface slides against a rigid material (abrasive) with different surface topographies: single conical asperity (Figure 6.14.a); multiple conical asperities of constant height (Figure 6.14.b); multiple conical asperities of different heights (Figure 6.14.c). In single contact conditions the load is totally applied through one asperity, while for multiple contacts with asperities of same height, the load is distributed in equal fractions (f_N) through all contact points. Both cases involve a single indentation depth value, which results in the contribution of a single hardness value to the wear response of the material. Therefore, the influence of indentation size effect on the wear rate can be immediately determined from Eq. 6.2 if the several constants in the equation (h^*, κ, E_s and H_0) are known. The third and most complex situation corresponds to the case of real surfaces, where the distribution of asperity heights is different from a Dirac delta distribution (Figure 6.14.c). As a result, different indentation depths occur along the nominal contact area, leading to local variations of the hardness and hence to a wear response of the material much more complex than in the first two cases. In this case, the influence of ISE on the wear rate will depend on the distribution of asperity heights and this analysis it out of the scope of the present work. Nevertheless, Eq. 6.2 can be used to make a preliminary qualitative evaluation of the influence of ISE on the wear rate, by considering the models represented in Figures 6.14.a and b.

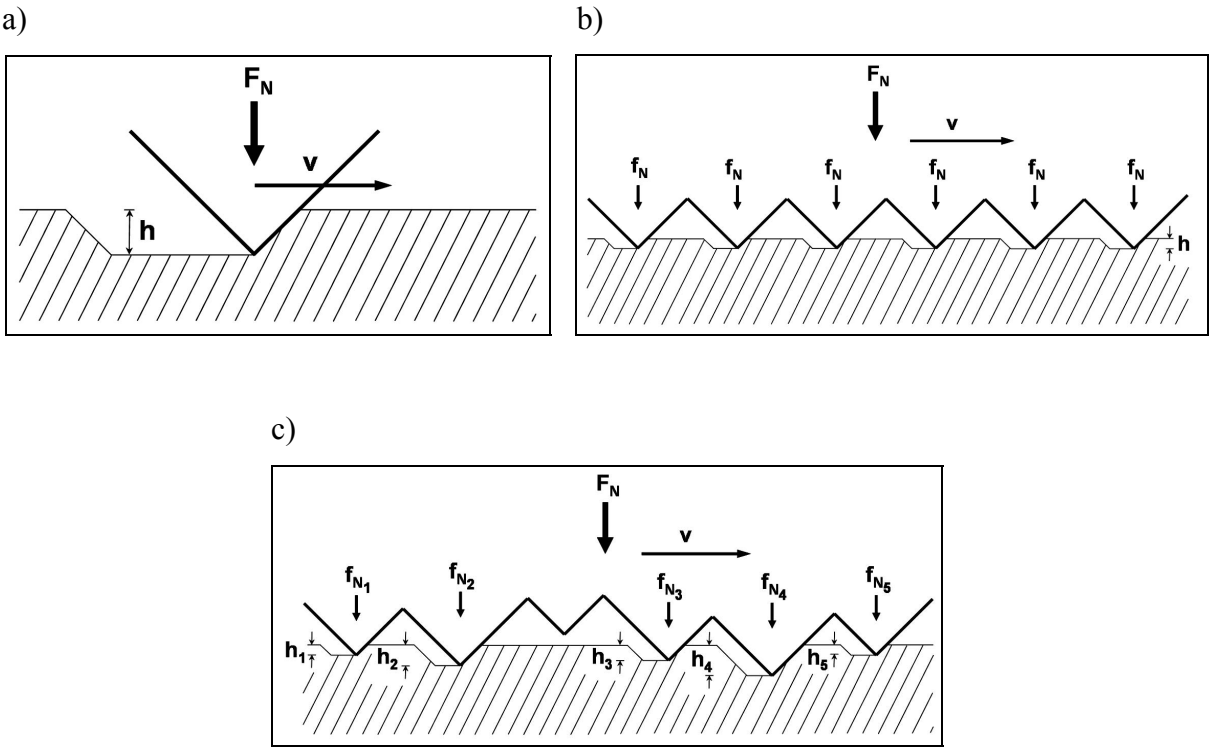

Figure 6.14. Schematic representation of sliding contact situations between a soft material with flat surface (bottom) and a hard material with different surface topographies composed of conical asperities (top): a) single asperity; b) multiple asperities of same height; c) multiple asperities of different heights. The sliding speed is represented by the letter v. Both the decrease of the load bearing area when sliding begins, which should result in an increase of h, and the accumulation of material in front of the abrasive asperities, are not considered in the schematics.

An evaluation of Eq. 6.2 is performed next for the particular cases of laser clad Ni and Co, using the values obtained in §4.1 for the several constants in the equation: for Ni, $H_0 = 1.3$ GPa and $h^* = 2.451$ μm, while for Co, $H_0 = 2.2$ GPa and $h^* = 2.023$ μm; $E_s = 2.2$ J/m^2 for both samples and $\kappa = 0.157$ for a Vickers indenter.

According to Eq. 4.4, the influence of SFE on hardness increases with decreasing depth. However, even for the extreme case of $h = 1$ nm, $Q_h/Q \approx 0.0200$ and 0.0221 for Ni and Co, respectively, while, if the SFE term in Eq. 6.2 is neglected, $Q_h/Q \approx 0.0202$ and 0.0222 for Ni and Co, respectively. Therefore, the influence of SFE on Q_h/Q is negligible in the case of Ni and Co and assuming the asperities with Vickers geometry. Nevertheless, in materials with higher SFE values and/or for shaper asperity geometries (corresponding to higher κ values), the influence of SFE may become significant.

Figure 6.15 shows the variation of Q_h/Q with h in Ni and Co, which is very similar for the two metals. When the penetration depth decreases from a macroscopic value to 10 μm, Q_h is only about 10% smaller than Q. However, as h further decreases, the decrease in Q_h/Q is more pronounced and, for $h = 1$ μm, Q_h is between 40 to 50% smaller than Q. This means that

the presence of ISE in both Ni and Co should result in a great reduction of the wear rate when the abrasive asperities penetrate the soft material to a depth of less than just a few micrometers. For larger penetration depths, the hardness at the contact region approximates the bulk hardness value and the influence of ISE on the wear rate vanishes. As was observed in the Vickers microindentation tests (Figure 4.4), the loads necessary to produce indentations several micrometers deep in Ni and Co are on the order of N. However, because in real surfaces the contact is established between multiple asperities (contact situation of Figure 6.14.c), the application of these "macroscale" loads will result in an average indentation depth much smaller than several micrometers. Therefore, even when such large loads are applied, a decrease of the wear rate due to ISE can still be expected (Figure 6.15).

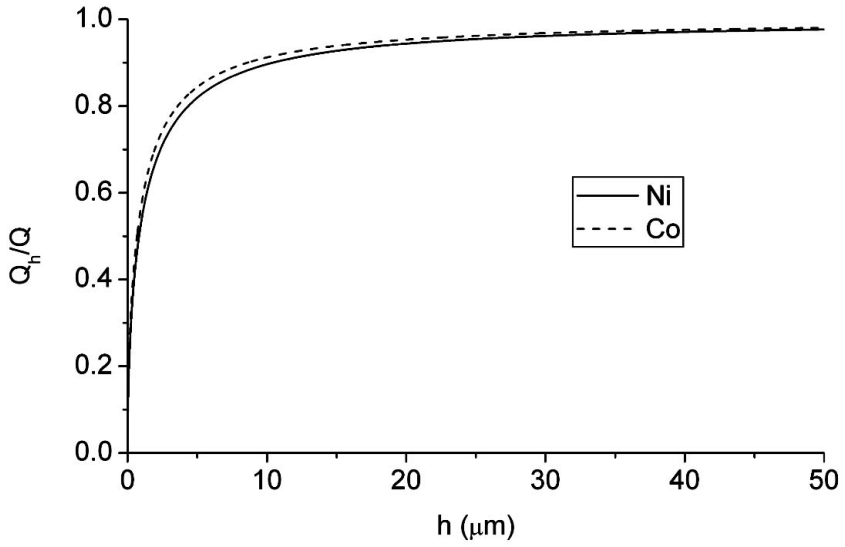

Figure 6.15. Variation of Q_h/Q with h (Eq. 6.2) in Ni and Co, assuming a Vickers geometry for the abrasive asperities ($\kappa = 0.157$).

At this moment, a relation can be established between the predictions of Eq. 6.2 and the frequently observed particle size effect, which consists on the reduction of the wear rate as the size of the abrasive particles continuously decreases below a critical size (usually ~ 100 μm in the case of ductile metals, as could be observed in Figure 1.10). In the particular case of two-body abrasive wear, the depth of cut is typically about 12% of the abrasive particle size, which results in a critical penetration depth of 12 μm when the critical particle size is 100 μm [63]. This depth value is comparable to the penetration depths below which the influence of ISE on the abrasive wear rate of Ni and Co becomes relevant (a few micrometers, according to Eq. 6.2), which provides some experimental support for the proposed combination of the Rabinowicz wear equation with Eq. 4.4. From all the explanations given previously for the

particle size effect (see §1.4.1), the explanation of Misra and Finnie [63], in which a strain hardened surface layer with a thickness around 10 μm is created during abrasion, thereby affecting the resistance to abrasive wear only in the case of small particles (those smaller than the critical size), is the most consistent with the influence of ISE on the abrasive wear rate. Still, the hard surface layer proposed by Misra and Finnie results from the wear process itself, whereas ISE is not only due to the presence of strain hardened surface layers (e.g. generated by the mechanical preparation of the surface), but also to other factors, such as plastic strain gradients, surface free energy and oxide layers.

Some deviations from the Q_h/Q trend with h given by Eq. 6.2 can occur at depths ranging from a few nanometres to several tens of nanometres, due to the purely elastic deformation of the asperities, the presence of oxide layers and the occurrence of pop-in events in low dislocation density materials. Nevertheless, it can be expected that the abrasive wear resistance of the material will continuously increase as the scale of the deformation is further reduced, due to the increasing resistance to plastic deformation.

Although this work has been exclusively concerned with the relation between the scale dependence of hardness and the abrasive wear of ductile materials, the influence of contact scale can also be extended to the case of sliding between materials of similar hardness. According to the Archard equation for adhesive wear [30] (see last footnote in page 14), the wear rate in this type of wear also depends on the hardness of the softer surface. Moreover, the asperity height of most engineering surfaces used in sliding contact applications is usually smaller than 10 μm [3, 4], which means that the contact between asperities generally involves normal displacements in the range where the hardness is scale dependent. The hardness increase with decreasing contact scale should contribute to the end of a running-in period characterised by the smoothing of the surface topography. Initially, contact between the two surfaces is established between the higher asperities, which support the entire applied load. Consequently, the plastically deformed volumes are larger than those occurring when contact is established between a larger number of asperities (e.g. after running-in), which results in a smaller hardness of the asperities due to ISE. As sliding proceeds and the higher asperities are worn, more asperities come into contact, leading to a reduction of the load applied at each asperity and, consequently, to an increase of the hardness of the asperities due to the decrease of the deformation volume. In terms of wear rate, two possible effects may result from ISE. On the one hand, the larger resistance to plastic deformation may result in a reduction of the size of the adhesion junctions, thus leading to a decrease of the wear rate. On the other hand, as mentioned previously in §6.1.2, the junctions may break at locations more distant from the

original interface, where the strength is smaller, thereby generating larger wear debris and hence increasing the wear rate.

The discussion made above shows the importance of characterising materials, in respect to their tribo-mechanical behaviour, with techniques that reproduce the true contact scale, i.e. the scale at which surface asperities interact. In the case of many engineering surfaces, such as those prepared for this work, contact is established at the submicrometric scale and, therefore, the usage of macro- or microhardness measurements for a preliminary evaluation of their wear resistance can lead to incorrect conclusions.

6.4. Conclusions

Similarly to the case of indentation hardness, the scratch hardness of the Ni-Co system also increases with decreasing contact scale and is less sensitive to the composition and microstructure of the samples when the penetration depth is within the nanometre range. These observations result from the influence of the scale related factors (e.g. strain hardening effects, surface free energy, oxide layers) analysed previously for the case of indentation hardness. In particular, the oxide layer may be responsible for the smaller hardness values obtained from nanoscratch tests in comparison to those obtained from nanoindentation tests, due to the spalling of the thin oxide film ahead of the indenter during scratching, which decreases the resistance to indenter penetration.

The results from the nanoabrasive wear tests strongly suggest that the abrasive wear behaviour of ductile materials with relatively smooth surfaces and that present ISE is related to the hardness measured at nanoscale and not to that measured at larger scales. They also show the important influence of surface roughness, even if minimum, on the onset of wear, due to the local plastification of the contacting asperities before the nominal contact region becomes fully plasticized. The plasticity index estimated for the Ni-Co samples is significantly larger than 1, which indicates that the surface asperities undergo plastic deformation under even the lightest of loads.

The ranking of the samples in terms of abrasive wear resistance, obtained from the measurements of the volume of material removed in the nanoabrasive wear tests, is in good agreement with that expected from the H_i/E values retrieved from displacement sensing nanoindentation tests, which confirms that higher yield strain limits for the rupture of asperities result in less wear.

The combination of the Rabinowicz wear model with Eq. 4.4 results in an equation (Eq. 6.2) that enables to make a preliminary qualitative evaluation of the influence of ISE on the

wear rate. The application of this equation to the Ni-Co samples shows that, when the abrasive asperities penetrate the soft material to a depth smaller than just a few micrometers, a great reduction of the wear rate is expected due to the influence of ISE (e.g. for h = 1 μm, a decrease of Q by 40 to 50% is expected in relation to the case where ISE is absent). Such small penetration depth values occur in rubbing engineering surfaces because the "macroscale" loads applied are distributed by a large number of asperities and, therefore, the influence of ISE on the wear rate must be present in real operation conditions. Furthermore, the predictions of Eq. 6.2 are in good agreement with the particle size effect experimentally observed in ductile materials, in which the wear rate decreases significantly when the size of the abrasive particles is reduced to a few tens of micrometers.

Therefore, the results presented in this work show that the tribo-mechanical behaviour of materials should be characterized with techniques that reproduce the true contact scale, i.e. the scale at which surface asperities interact, with the penalty of obtaining incorrect conclusions when not following this requirement.

7. FINAL CONCLUSIONS AND FUTURE WORK

In this final chapter a summary of the results obtained in this work is made. In addition, ideas for future work are suggested.

7.1. Summary of results

The main objective of the present work was to contribute to the "bridging of the gap" between macrotribology and nanotribology, a goal that is still far from being accomplished, as mentioned recently by Szlufarska *et al*. [16]. Within the field of tribology, the topic chosen for the proposed study was the abrasive wear of ductile materials, which is responsible for great economical losses and is much less studied in terms of influence of contact scale than the wearless regime of friction.

The Ni-Co system was chosen as case study due to its tribological importance and because it presents several interesting metallurgical characteristics that are common to other metallic systems (e.g. martensitic transformation), thus offering the possibility of generalization of results to such systems. Contrary to the samples frequently used in tribo-mechanical studies involving small scales, the samples prepared for this work present a structural complexity (e.g. polycrystallinity, strain hardened surface layers and native oxide layers) which is common in rubbing engineering metallic components, thereby representing an approach to real sliding contact applications.

The strategy adopted to fulfil the proposed objective was to analyse the influence of contact scale on hardness, since this property is intimately related to the abrasive wear behaviour of ductile materials. The first step was to characterise the topography and structure of the samples, after which the variation of the hardness, both under static (indentation) and non-static (scratch) contact conditions, was analysed as function of the applied load and of the chemical composition of the samples. The information retrieved from the hardness tests was then used in combination with the results from nanoabrasive wear tests to evaluate the impact of contact scale on the abrasive wear response of ductile materials. Finally, a simple model that enables to evaluate qualitatively the effect of the scale dependence of hardness on the abrasive wear rate of ductile materials was developed. A summary of the main results of this work is presented next.

Chapter 1 of the present work started with the motivation for this work. Afterwards, some concepts on the mechanics of the contact between two solid surfaces and on the abrasive wear of ductile materials were presented, with special emphasis on the Rabinowicz model. Finally, a review of the state of the art in the scale dependence of abrasive wear and hardness was made, with particular focus on the Nix-Gao and Jäger models for the contribution of geometrically necessary dislocations and surface free energy, respectively, to

the hardness of materials. The information presented in the first chapter was fundamental for the analysis and discussion of the results of the present work.

The sample preparation and characterisation methods were presented in Chapter 2. Special attention was given to the measurement protocols and calibration procedures adopted in the experimental work, which enabled minimizing the influence of experimental errors on the results.

In Chapter 3 the topographical and structural characterisation of the samples was made. The surfaces prepared by mechanical polishing are extremely smooth, with an average roughness of only a few nanometres, whereas those prepared by electropolishing are slightly rougher. The Auger depth profile chemical analysis showed that the native oxide layers of the Ni-Co alloys are thicker than those of pure Ni and Co, which can be a result of the presence of complex Ni-Co oxides in the alloys. The oxide layer thickness values estimated from the profiles are slightly overestimated in comparison to those found in the literature for metals under environmental conditions, which are on the order of a few nanometres. The most probable cause for this overestimation is the uncertainty on the sputtering rate value. The EDS analysis revealed that the distribution of Ni and Co in the samples is homogeneous and that the contamination by Fe and Cr coming from the substrate is relatively small (< 4.5%). These features show that the laser cladding process is reliable for quickly obtaining small amounts of high quality sample materials in given compositional ranges for research and development studies as the one presented in this work.

The grains that form the samples are relatively large, with dimensions of several tens of micrometers. The microstructural analysis using different techniques (OM, SEM, XRD and TEM) showed that the Ni-Co samples with less than 68% Co are formed only by the FCC α phase, those with more than 80% Co are formed mostly by the HCP ε' martensitic phase, and those with Co percentages in between are formed by a mixture of α and ε'. A residual quantity of submicrometric precipitates containing Fe and Cr were also found in the samples. A value on the order of 10^9 cm^{-2} was estimated by TEM for the dislocation density of laser clad Ni, using a procedure described in §3.5. This value is physically consistent for a material produced by laser cladding, since it is larger than those usually found in annealed metals (10^6–10^8 cm^{-2}) and smaller than those found in plastically deformed metals (10^{11}–10^{12} cm^{-2}). In a few sample regions no dislocations were found, which is a consequence of the heterogeneous distribution of dislocations.

The influence of contact scale on the indentation hardness of the Ni-Co system was analysed in Chapter 4. It was observed that the hardness trend with chemical composition is maintained in all the range of loads used (57 μN–1 N), though it is less defined in nanohardness values (Figure 4.1, page 122). Three particular features can be distinguished in the hardness trend: a local maximum at about 35%Co, which seems to be caused by solid solution strengthening; a jump in hardness for compositions with more than 68%Co, due to the presence of ε' martensite in these Co-rich samples; a local minimum at around 25%Co, which apparently can be related to a short-range order transformation, though definitely not in a direct manner.

It was observed that, independently of the composition, the indentation hardness increases with decreasing load (indentation size effect), reaching values up to nine times the bulk hardness in the case of nanohardness (Figure 4.1, page 122). A detailed investigation of the ISE in pure Ni and Co showed that this effect is only noticeable for indentation depths smaller than 2 μm.

Both the less defined hardness trend with composition in the case of nanohardness and the ISE are caused by factors which become increasingly relevant as the contact scale decreases. The analysis of several factors (§4.1.2.2) showed that the main responsible for the scale dependence of hardness are the increase of the dislocation density, which is caused by the mechanical preparation of the surface and the larger magnitude of plastic strain gradients at smaller depths, and the surface free energy of the material when the depths are nanometric and sharp indenter geometries are used. In addition, the native oxide layer present at the surface of the samples may have some contribution to the nanohardness values, though it is not the main cause for ISE. An equation that accounts for the influence of both dislocation density and SFE on hardness (Eq. 4.4, page 132) has been obtained by combining the Nix-Gao and Jäger models. This equation accurately describes the depth dependence of indentation hardness in the materials of this work (Figure 4.7, page 134) and has been recently validated by Ma *et al*. [198] in other materials. These authors proposed the designation GCV model (Graça, Colaço, Vilar) for Eq. 4.4.

By using the characteristic length h^*, which is included in Eq. 4.4 and related to the initial dislocation density of the material (Eq. 1.39, page 29), dislocation density values on the order of 10^9 cm^{-2} were estimated for Ni and Co. These values are in excellent agreement with those determined by TEM, thus supporting the reliability of Eq. 4.4 and showing that indentation hardness measurements using different loads can be used to estimate the

dislocation density of metals that exhibit ISE. Moreover, this method of determination of the dislocation density presents clear advantages over TEM-based methods: it is statistically more representative, since the sampled volumes are much larger than those involved in TEM observations, and is simpler and faster, since the laborious TEM sample preparation and observation steps are avoided.

The influence of the surface preparation method on hardness was deeply analysed by using displacement sensing nanoindentation (§4.2). It was found that the fine polishing procedure used to prepare the surfaces in this work can increase the material's hardness up to 1.5 GPa, which corresponds to a two to three times increase of the dislocation density in the near-surface region of the material.

DSN was also used to analyse the influence of crystallographic anisotropy on the hardness and Young's modulus of the samples. It was observed that Co-rich samples are more plastically anisotropic than Ni-rich ones (Figure 4.11.a, page 140) due to the lower number of slip systems in the ε' phase in comparison to the α phase, which allows larger differences in orientation between the slip plane and the stress axis in Co-rich samples. On the contrary, Ni-rich samples present a larger elastic anisotropy (Figure 4.11.b, page 140) due to the particular combination of the stiffness constants in these samples, as was demonstrated by the theoretical calculations of E for FCC Ni and HCP Co (Table 4.1, page 144). It was also observed that, contrary to the case of hardness, the Young's modulus in the Ni-Co system is not greatly affect by the alloys composition and the applied load.

From the H_i and E values retrieved from the DSN tests, it was possible to determine the H_i/E ratio of the samples (Figure 4.11.c, page 140), which is related to the plasticity index (Eq. 1.14, page 12) and hence to the tribological response of the material. It was found that the alloys with Co percentages around 80% present the highest H_i/E values of the Ni-Co system, which indicates that these samples present the highest yield strain limits for the rupture of surface asperities. Therefore, if this ratio is used as a design parameter for wear resistance in the Ni-Co system, the alloys with compositions around Ni-80%Co present clear advantages over the Ni-richer alloys. Nevertheless, the high elastic anisotropy of Ni leads to a large spectrum of H_i/E values, thus opening the possibility of optimizing the tribological behaviour of Ni-rich alloys by promoting the formation of surface textures, i.e. tuning tribological behaviour by crystallographic control of the surface.

Another factor that can be responsible, to a certain extent, for the observed ISE, is the homogenous nucleation of dislocations when the indented regions are dislocation free and

dislocation sources are absent. However, the Nix-Gao model is a simplified geometrical model and hence does not take into consideration this phenomenon, as well as the influence of crystallographic orientation. In Chapter 5, the nucleation and arrangement of dislocations in the early stages of plastic deformation of an indented crystalline material were studied by using two different techniques: analysis of the loading curves resulting from DSN tests in the samples (indirect method) and TEM observation of nanoindentations performed with an AFM tip in the electron transparent regions of TEM samples (direct method).

A large discontinuity (pop-in) was generally present at the beginning of the loading curves of electropolished samples (Figure 5.3, page 151) but not in the curves of mechanically polished samples (Figures 5.1 and 5.2, page 150). It was found that, when this discontinuity occurs, the maximum shear stress in the material under indentation is on the order of the theoretical shear stress of the perfect crystal, which confirms that the homogenous nucleation of dislocations occurs in the electropolished samples. The absence of such discontinuity in mechanically polished samples is caused by the presence of several pre-existing dislocations, which result from the polishing process and can be moved under the influence of the applied shear stresses and act as Frank-Read sources.

Other discontinuities after that at the beginning of the loading curve were observed in a few curves of the electropolished samples (Figures 5.3.c and e, page 151), and are most probably caused by the pile-up of the dislocations produced in the first pop-in event against grain boundaries, which generates a stress high enough to nucleate dislocations in the adjacent grain. This mechanism explains the smaller frequency of these multiple pop-in events in Ni than in Co, since in Ni the dislocations can cross-slip, thus avoiding pilling up at grain boundaries. Furthermore, it can also explain why multiple pop-in events occur less often than a single large one at the beginning of the loading curve, because there is a higher probability of performing nanoindentations inside a grain than close to a grain boundary, due to the small indentation size to grain size ratio associated to the DSN tests of this work.

The TEM observations of nanoindented regions in Ni (Figure 5.6.c, page 158) showed that, at the nanometric contact scale, the plastic deformation is accommodated through three mechanisms: 1) nucleation of dislocations in the neighbourhood of the indentation, forming agglomerates; 2) emission of prismatic dislocation loops and helical prismatic dislocations from the centre of the indented region; 3) in a few cases, emission of straight dislocations from the centre of the indented region. As a result of mechanism 1, a high dislocation density region is formed near the indentation, and is surrounded by a low dislocation density region

which results from mechanisms 2 and 3. The TEM observations are in good agreement with the predictions from molecular dynamics atomistic simulations of nanoindentation in dislocation-free crystals. Both the experimental results and the theoretical predictions indicate that plastic deformation begins with the homogeneous nucleation of dislocations, which intersect each other and become sessile (mechanism 1). As the indenter is further displaced, other dislocations are emitted from this region, allowing plastic deformation to proceed (mechanisms 2 and 3). Though it is tempting to associate mechanism 1 to the large pop-in event at the beginning of the loading curves, the only way to confirm this hypothesis is to perform TEM observation of the indented region during the indentation test while monitoring the path of the loading curve.

The formation of a high dislocation density region at the core of the indentation supports the fundamental idea of the Nix-Gao model, in which the ISE is caused by an increase of the density of GNDs with decreasing indentation depth. Furthermore, the formation of a low dislocation density region surrounding the previous one justifies the correction proposed by Feng and Nix [84] and Durst *et al*. [97] to the volume containing the GNDs in the Nix-Gao model. This correction is already included in the parameter h^* which is used to estimate the dislocation density from indentation hardness measurements (Eq. 1.39, page 29). As the indenter is further displaced into the material, the contribution of the high dislocation density region to the hardness decreases in relation to contribution of the low dislocation density region and, consequently, the magnitude of the ISE is reduced.

Both the pop-in events in the loading curves from DSN tests and the TEM observations of nanoindented regions show that the presence of dislocation-free regions in materials, due to low dislocation densities and/or heterogeneous distributions of dislocations, can cause irregularities in their plastic behaviour and hence affect their tribological response, when the contact is established at small scales. This effect is particularly important in the case of MEMS and NEMS, where the contact areas are often submicrometric. Therefore, in materials whose wear behaviour is exclusively governed by plastic deformation, wear can be minimized by reducing their dislocation density and applying loads below the critical load for the onset of plasticity.

In the first part of Chapter 6, the study of the contact scale dependence of hardness was extended to the case of non-static (scratch) contact conditions, where there is an additional influence of a tangential load in comparison to static (indentation) contact conditions. Similarly to the case of indentation hardness, the scratch hardness of the Ni-Co system also

increases with decreasing load, reaching values up to five times the bulk hardness in the case of nanohardness, and is less sensitive to the composition and microstructure of the alloys when the penetration depth is within the nanometre range (Figure 6.1, page 170). These observations are caused by the same scale related factors that affect indentation hardness measurements.

SEM and AFM observations of indentations (§4.1.1) and scratches (§6.1.1) performed in the samples containing the ε' phase showed that mechanical twins are formed when these samples are submitted to microscale tests but not in smaller scale tests. This can be explained by the larger deformed volumes involved in microscale tests, which cannot be accommodated just by slip when only three slip systems are active, as in the case of the ε' phase. At submicrometric penetration depths, plastic deformation seems to occur only by slip in all the samples of the Ni-Co system.

The H_s/H_i ratio in microscale tests is larger than 1, whereas in nanoscale tests it is generally smaller than 1, which indicates that the influence of contact scale on hardness is more pronounced in indentation than in scratching. However, the difference between H_i and H_s in the case of microscale tests can also be due to the difference between the measurement protocols for H_i and H_s. In the case of nanoscale tests, the larger H_i values in comparison to the H_s ones can be due to the spalling of the thin native oxide film ahead of the indenter during scratching, which reduces the resistance to indenter penetration.

In the second part of Chapter 6, the influence of ISE on the abrasive wear of ductile materials was analysed by combining the information obtained previously on the scale dependence of hardness with the results from AFM cantilever-based nanoabrasive wear tests in Ni, Ni-85%Co and Co. This analysis strongly suggests that the abrasive wear behaviour of ductile materials that present ISE, at least those with relatively smooth surfaces (the most common case in rubbing engineering components), is related to the hardness measured at nanoscale and not to that measured at larger scales. Surface roughness also seems to play an important role on the onset of wear, because it allows the local plastification of the touching asperities prior to the total plastification of the nominal contact region. This effect is particularly significant in materials that present a plasticity index larger than 1 (such as those used in the present work), since their asperities undergo plastic deformation under even the lightest of loads.

The abrasive wear resistance ranking of the samples, obtained from the measurements of the volume worn in the nanoabrasive wear tests (Figure 6.10, page 183), is in good

agreement with that expected from the H_i/E values retrieved from DSN tests (Figure 4.11.c, page 140), thus confirming that asperities with higher yield strain limits are more difficult to remove.

In the final part of Chapter 6, a model that enables to make a preliminary qualitative evaluation of the influence of ISE on the abrasive wear rate of ductile materials (Eq. 6.2, page 190) was developed by combining the Rabinowicz model with Eq. 4.4. For simplicity, it is assumed in the model that all abrasive asperities have the same height and that the abrasive wear coefficient is invariant with contact scale. The application of Eq. 6.2 to the materials of this work (Figure 6.15, page 192) shows that, when the abrasive asperities penetrate the soft material to a depth smaller than just a few micrometers, a great reduction of the wear rate is expected due to the influence of ISE (e.g. for h = 1 μm, a decrease of Q by 40 to 50% is expected in relation to the case where ISE is absent). For larger penetration depths the influence of ISE vanishes and Q is described by the Rabinowicz equation. Penetration depths of less than a few micrometers occur in rubbing engineering surfaces because the typical "macroscale" loads applied at such surfaces are distributed by a large number of asperities, which strongly suggests that the influence of ISE on the wear rate is present in real operation conditions. Experimental support for Eq. 6.2 is given by the particle size effect observed in ductile materials (Figure 1.10, page 21), in which the wear rate decreases significantly when the size of the abrasive particles is reduced to a few tens of micrometers.

Because the indentation size effect is intrinsic to the tested material, it should be present in all types of wear solicitations involving scales of deformation typically of less than a few micrometers. In the particular case of adhesive wear, the presence of ISE may either lead to a decrease of the wear rate, due to the reduction of the size of the adhesion junctions in the stronger small contact regions, or to an increase, due to the breaking of junctions at weaker locations far from the original interface.

The results of the present work strongly indicate that the tribo-mechanical behaviour of materials should be characterized with techniques that reproduce the true contact scale, i.e. the scale at which surface asperities interact. In the case of many engineering surfaces, such as those prepared for this work, contact is established at the submicrometric scale and, therefore, the usage of macro- or microhardness measurements for a preliminary evaluation of their wear resistance can lead to incorrect conclusions.

We believe that the experimental results presented and the models developed in the present work enabled improving the understanding of the impact of contact scale on the abrasive wear response of ductile materials, thus helping to bridge the gap between macrotribology and nanotribology. Hopefully, this work will motivate others to proceed with the challenging task of unravelling the fundamentals of the wear process, so that it can be better controlled, which will certainly bring significant improvements to the technology of sliding components. In this way, some suggestions for future work are given in the following section.

7.2. Suggestions for future work

Uncertainty on a few aspects concerning the structural characterisation of the samples still remains. As mentioned in §3.6, XRD does not allow detecting the presence of an ordered phase Ni_3Co in the alloys with Co percentages around 25% Co. The results from the literature show that, if existent, only a small amount of short-range order will be present. Therefore, it would be useful to perform high resolution transmission electron microscopy (HRTEM) observations of alloys with these compositions to clarify on the presence or absence of order, which may enlighten on the irregular local minimum of hardness that occurs at these compositions (Figure 4.1, page 122). On the other hand, the ferromagnetic behaviour of the samples can be characterised by using magnetic force microscopy (MFM), to determine if there is a magnetic anomaly for compositions around Ni-25%Co that can be responsible for the local minimum of hardness.

Another point that was not totally clarified was the exact value of the thickness of the native oxide layer in the samples. Two possible ways to confirm if the oxide layer thickness is of a few nanometres, as is generally found in the literature, are: 1) by performing Auger depth profile chemical analysis of thin films of known thickness of NiO, CoO and Co_3O_4, using the same operation parameters of the Auger experiments of this work, the correct values for the sputtering rates of the native oxides of the samples can be determined, which would allow to correctly convert the sputtering time to depth in the profiles; 2) by performing cross-sectional HRTEM observation of the samples, the thickness of the native oxide layer can be directly measured.

From all the depth ranges analysed in respect to hardness, the nanometre range is the most complex due to the larger relevance of scale related factors. One of the factors whose contribution to the hardness is more difficult to determine is the native oxide layer. A possible

way to estimate this contribution would be to perform AFM cantilever-based nanoindentation under UHV conditions, after removing the oxide layer by applying successive cycles of sputtering and annealing inside the UHV chamber, and compare the measured hardness values with those of the present work. A detailed study of the influence of the oxide layer on hardness may allow incorporating its contribution in the GCV model (Eq. 4.4, page 132).

A topic that is still in its infancy and hence definitely deserves to be further explored is the onset of plastic deformation in nanoscale contacts. More studies involving TEM observation of regions submitted to tribo-mechanical tests (e.g. nanoindentation, nanoscratching and nanowear), such as that presented in §5.2, have to be performed so that the onset of wear in ductile materials can be deeply understood. In particular, real-time observations of tribo-mechanical tests in a transmission electron microscope, which have started a decade ago, seem to be promising to fulfil this goal.

A point that has not been explored in the present work is the influence of contact scale on the coefficient of friction, along with its consequences to the hardness determined from a scratch test. Perhaps this study could help clarifying on the larger scale dependence of hardness in indentation than in scratching. A particularly interesting experiment would be to conduct indentation and scratch tests under lubrication conditions, to check if this difference is maintained.

In addition to the nanoabrasive wear tests of this work, it would be interesting to perform a group of abrasive wear experiments involving the same equipment, the same abrasive body, and a large range of loads, so that the influence of contact scale on the abrasive wear rate of the samples could be measured experimentally and compared to the predictions of the model developed in the final part of Chapter 6 (Eq. 6.2, page 190). A possible way to accomplish this is by using the Nano-tribometer from CSM instruments [226], which has been recently acquired by our group. This equipment allows performing linear reciprocating or rotating sliding tests with indenters of varying geometry (e.g. spherical, flat) and loads in the range 50 μN to 1 N, under different environments.

The model developed in the final part of Chapter 6 is very simplified and can be extended by taking into account the influence of contact scale on the abrasive wear coefficient, i.e. considering possible variations of the wear mechanism with scale, and the distribution of asperity heights of the tested surface.

It would also be interesting to extend the present study to adhesive wear, which, together with abrasive wear, are the most frequent forms of wear.

APPENDIX: Contribution of surface free energy to the indentation hardness

The extension of the Jäger model to the Veeco DNISP tip geometry is based on the same assumptions of the original model, which was presented in §1.4.2. For simplicity, some of the equations presented in §2.3.2.2 are repeated in this appendix. Schematic drawings of an indentation made with the DNISP tip are shown in Figure A.1.

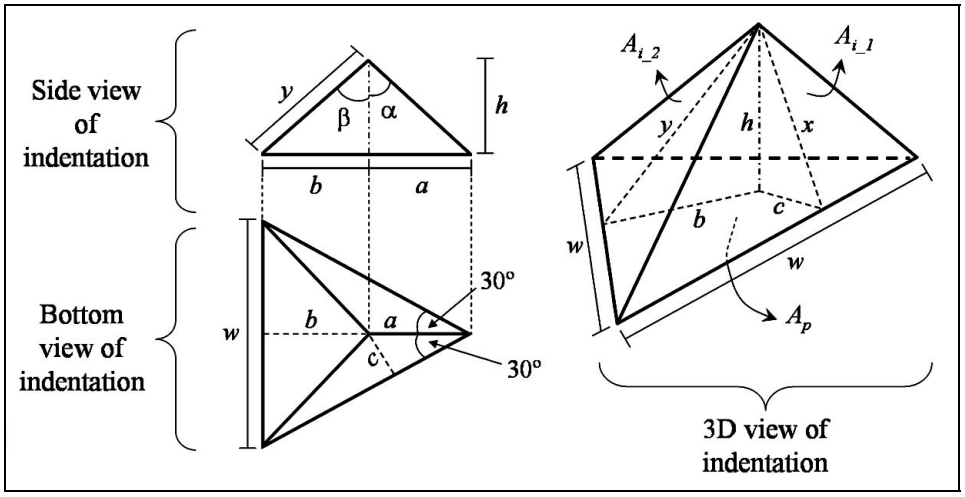

Figure A.1. Schematic drawings of an indentation made with the DNISP tip, viewed from different perspectives. The indentation is oriented upside-down. It is assumed that the indentation keeps the original shape after removing the tip, without any influence of elastic recovery or the generation of sink-in or pile-up.

By using simple trigonometric relations, the following equations can be obtained:

$$a = h\tan\alpha\,, \tag{A1}$$

$$b = h\tan\beta\,, \tag{A2}$$

$$w = \frac{a+b}{\cos 30}\,. \tag{A3}$$

Combining Eqs. A1, A2 and A3, the projected area of the indentation, A_p, can be obtained as function of indentation depth, h:

$$A_p = \frac{w(a+b)}{2} = \frac{1}{\sqrt{3}}\left(\tan\alpha + \tan\beta\right)^2 h^2\,. \tag{A4}$$

Replacing the apex semi-angles α and β by the values retrieved from the SEM image of the DNISP tip 2 (Figure 2.38.b), an approximated value of A_p can be obtained:

$$A_p \approx 2.568h^2 . \tag{A5}$$

From Figure A.1 follows:

$$c = a\sin 30 \tag{A6}$$

and

$$x^2 = c^2 + h^2 . \tag{A7}$$

From the combination of Eqs. A1, A6 and A7 results:

$$x = \sqrt{\frac{\tan^2\alpha}{4} + 1} \cdot h , \tag{A8}$$

which combined with Eq. A3, enables determining the area of one of the front faces of the indentation, A_{i_1} (note that the two front faces of the indentation have the same area):

$$A_{i\_1} = \frac{wx}{2} = \sqrt{\frac{\tan^2\alpha}{4} + 1} \cdot \frac{1}{\sqrt{3}}(\tan\alpha + \tan\beta)h^2 . \tag{A9}$$

From Figure A.1 results also:

$$y = \frac{h}{\cos\beta}, \tag{A10}$$

which combined with Eq. A3, enables determining the area of the back face of the indentation, A_{i_2}:

$$A_{i\_2} = \frac{wy}{2} = \frac{1}{\cos\beta}\frac{1}{\sqrt{3}}(\tan\alpha + \tan\beta)h^2 . \tag{A11}$$

By using Eqs. A9 and A11, the surface area of the indentation, A_i, can be determined:

$$A_i = 2A_{i\_1} + A_{i\_2} = \left(2\sqrt{\frac{\tan^2\alpha}{4}+1} + \frac{1}{\cos\beta}\right)\frac{1}{\sqrt{3}}(\tan\alpha + \tan\beta)h^2 . \quad \text{(A12)}$$

Knowing A_p and A_i, the excess surface area created by the indentation process, A', is given by:

$$A' = A_i - A_p = \left[\left(2\sqrt{\frac{\tan^2\alpha}{4}+1} + \frac{1}{\cos\beta}\right)\frac{1}{\tan\alpha + \tan\beta} - 1\right]A_p \quad \text{(A13)}$$

and the force necessary to create this surface is:

$$F_s = \frac{d}{dh}(A' \cdot E_s) = \frac{2}{h}A_p\left[\left(2\sqrt{\frac{\tan^2\alpha}{4}+1} + \frac{1}{\cos\beta}\right)\frac{1}{\tan\alpha + \tan\beta} - 1\right]E_s , \quad \text{(A14)}$$

where E_s is the surface free energy of the material.

Finally, the contribution of surface free energy to hardness is given by:

$$\Delta H_{SFE} = \frac{F_s}{A_p} = \frac{2E_s}{h}\left[\left(2\sqrt{\frac{\tan^2\alpha}{4}+1} + \frac{1}{\cos\beta}\right)\frac{1}{\tan\alpha + \tan\beta} - 1\right]. \quad \text{(A15)}$$

This equation can be written in the form:

$$\Delta H_{SFE} = \kappa\frac{E_s}{h}, \quad \text{(A16)}$$

with

$$\kappa = 2\left[\left(2\sqrt{\frac{\tan^2\alpha}{4}+1} + \frac{1}{\cos\beta}\right)\frac{1}{\tan\alpha + \tan\beta} - 1\right]. \quad \text{(A17)}$$

Replacing the apex semi-angles α and β in Eq. A17 by the values retrieved from the SEM image of the DNISP tip 2 leads to $\kappa = 1.532$. If the same procedure presented in this appendix is applied for the Vickers geometry, a κ of 0.157 is obtained.

The angles α and β of the DNISP tip are similar (α = 45.5º and β = 47.5º). Therefore, if it is assumed that $\alpha = \beta = \phi / 2$, where ϕ is the apex angle, Eq. A17 becomes:

$$k = \sqrt{4\tan^{-2}\left(\frac{\phi}{2}\right)+1} + \sin^{-1}\left(\frac{\phi}{2}\right) - 2\,. \tag{A18}$$

Equation A18 enables analysing the variation of κ with ϕ, as depicted in Figure A.2. By decreasing the indenter apex angle, κ may increase significantly, thus resulting in a larger value of ΔH_{SFE} (Eq. A16).

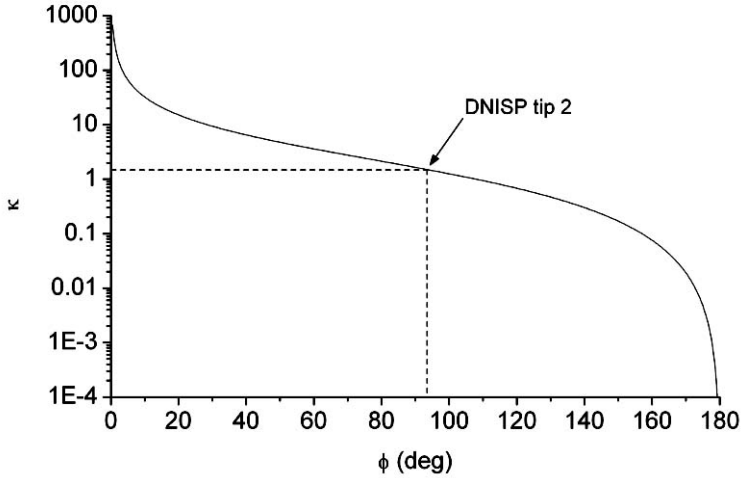

Figure A.2. Variation of the geometrical constant κ with the apex angle ϕ of a DNISP tip, according to Eq. A18 (thick line). The location in the curve corresponding to the DNISP tip used in the nanoindentation tests of this work is pointed with an arrow.

REFERENCES

[1] E. Rabinowicz. *Friction and Wear of Materials*, 2nd Ed., John Wiley and Sons, New York, (1995).

[2] M. Madou. *Fundamentals of Microfabrication*, CRC Press, Boca Raton, (1997).

[3] K.-H. Z. Gahr. *Microstructure and Wear of Materials*, Elsevier, Amsterdam, (1987).

[4] I. M. Hutchings. *Tribology, Friction and Wear of Engineering Materials*, Edward Arnold, London, (1992).

[5] H. Li and R. C. Bradt, Journal of Materials Science **28**, 917 (1993).

[6] N. A. Stelmashenko, M. G. Walls, L. M. Brown and Y. V. Milman, Acta Metallurgica Et Materialia **41**, 2855 (1993).

[7] Q. Ma and D. R. Clarke, Journal of Materials Research **10**, 853 (1995).

[8] K. W. McElhaney, J. J. Vlassak and W. D. Nix, Journal of Materials Research **13**, 1300 (1998).

[9] Y. Liu and A. H. W. Ngan, Scripta Materialia **44**, 237 (2001).

[10] A. A. Elmustafa and D. S. Stone, Acta Materialia **50**, 3641 (2002).

[11] J. G. Swadener, A. Misra, R. G. Hoagland and M. Nastasi, Scripta Materialia **47**, 343 (2002).

[12] S. J. Bull, Zeitschrift für Metallkunde **94**, 787 (2003).

[13] R. Colaço, "Surface-Damage Mechanisms: from Nano- and Microcontacts to Wear of Materials". In: *Fundamentals of Friction and Wear on the Nanoscale*, Springer-Verlag, Berlin, (2007).

[14] B. Bhushan, Microelectronic Engineering **84**, 387 (2007).

[15] G. Binnig, C. F. Quate and C. Gerber, Physical Review Letters **56**, 930 (1986).

[16] I. Szlufarska, M. Chandross and R. W. Carpick, Journal of Physics D **41**, (2008).

[17] P. Crook and H. N. Farmer, "Friction and Wear of Hardfacing Alloys". In: *ASM Handbook: Friction, Lubrication and Wear Technology*, Vol. 18, ASM International, Metals Park (OH), (1992).

[18] T. Lyman (ed). *Metals Handbook*, Vol. 8, 8th Ed., ASM, Metals Park (OH), (1973).

[19] T. B. Massalski. *Binary Alloy Phase Diagrams*, Vol. 2, 2nd Ed., ASM International, Materials Park (OH), (1990).

[20] J. W. Edington. *Electron Diffraction in the Electron Microscope (Monographs in Practical Electron Microscopy in Materials Science)*, Vol. 2, Macmillan, London, (1975).

[21] Z. Nishiyama. *Martensitic Transformation*, Academic Press, New York, (1978).

[22] D. Chaudhuri, D. Xie and A. N. Lakshmanan, Wear **209**, 140 (1997).

[23] A. Korner and H. P. Karnthaler, Philosophical Magazine A **48**, 469 (1983).

[24] H. Hertz, Journal für die reine und angewandte Mathematik **92**, 156 (1882).

[25] K. L. Johnson. *Contact Mechanics*, Cambridge University Press, Cambridge, (1985).

[26] B. Bhushan. *Principles and Applications of Tribology*, John Wiley and Sons, New York, (1999).

[27] D. Tabor. *The Hardness of Metals*, Oxford University Press, Oxford, (2000).

[28] J. A. Greenwood and J. B. Williamson, Proceedings of the Royal Society of London A, **295**, 1966, p. 300.

[29] E. Rabinowicz. *Friction and Wear of Materials*, 1st Ed., John Wiley and Sons, New York, (1965).

[30] J. F. Archard, Journal of Applied Physics **24**, 981 (1953).

[31] N. K. Mukhopadhyay and P. Paufler, International Materials Reviews **51**, 209 (2006).

[32] H. P. Jost, "Lubrication (tribology) - A Report on the Present Position and Industry's Needs", Dept. of Education and Science, Her Majesty's Stationary Office, (1966).

[33] J. Hu, X. D. Xiao, D. F. Ogletree and M. Salmeron, Surface Science **327**, 358 (1995).

[34] B. Bhushan, Wear **250**, 1105 (2001).

[35] M. Surtchev, N. R. de Souza and B. Jerome, Nanotechnology **16**, 1213 (2005).

[36] K. Degiampietro and R. Colaco, Wear **263**, 1579 (2007).

[37] R. W. Carpick and M. Salmeron, Chemical Reviews **97**, 1163 (1997).

[38] S. Miyake, Applied Physics Letters **67**, 2925 (1995).

[39] P. E. Sheehan, Chemical Physics Letters **410**, 151 (2005).

[40] E. Gnecco, R. Bennewitz and E. Meyer, Physical Review Letters **88**, 215501 (2002).

[41] B. Bhushan and A. V. Kulkarni, Thin Solid Films **278**, 49 (1996).

[42] Z. G. Jiang, C. J. Lu, D. B. Bogy and T. Miyamoto, Journal of Tribology **117**, 328 (1995).

[43] K. H. Chung and D. E. Kim, Tribology Letters **15**, 135 (2003).

[44] B. Such, F. Krok and M. Szymonski, Applied Surface Science **254**, 5431 (2008).

[45] X. C. Lu, B. Shi, L. K. Y. Li, J. B. Luo, J. H. Wang and H. D. Li, Surface and Coatings Technology **128**, 341 (2000).

[46] S. P. Ho, R. W. Carpick, T. Boland and M. LaBerge, Wear **253**, 1145 (2002).

[47] D. D. Woodland and W. N. Unertl, Wear **203**, 685 (1997).

[48] F. Iwata, T. Matsumoto and A. Sasaki, Nanotechnology **11**, 10 (2000).

[49] J. M. Helt and J. D. Batteas, Langmuir **21**, 633 (2005).

[50] A. Socoliuc, E. Gnecco, R. Bennewitz and E. Meyer, Physical Review B **68**, (2003).

[51] R. Ribeiro, Z. Shan, A. M. Minor and H. Liang, Wear **263**, 1556 (2007).

[52] M. A. Wall and U. Dahmen, Microscopy Research and Technique **42**, 248 (1998).

[53] U. Landman, W. D. Luedtke and E. M. Ringer, Wear **153**, 3 (1992).

[54] J. A. Harrison, R. J. Colton, C. T. White and D. W. Brenner, Wear **168**, 127 (1993).

[55] M. D'Acunto, Nanotechnology **15**, 795 (2004).

[56] M. Chandross, C. D. Lorenz, M. J. Stevens and G. S. Grest, Langmuir **24**, 1240 (2008).

[57] B. Bhushan, Wear **259**, 1507 (2005).

[58] N. A. Fleck, G. M. Muller, M. F. Ashby and J. W. Hutchinson, Acta Metallurgica Et Materialia **42**, 475 (1994).

[59] N. Gane and J. Skinner, Wear **24**, 207 (1973).

[60] H. Cimenoglu, Wear **210**, 204 (1997).

[61] G. Pintaude, D. K. Tanaka and A. Sinatora, Scripta Materialia **44**, 659 (2001).

[62] W. R. Backer, E. R. Marshall and M. C. Shaw, Transactions of the American Society of Mechanical Engineers **74**, 61 (1952).

[63] A. Misra and I. Finnie, Wear **65**, 359 (1981).

[64] R. Gahlin and S. Jacobson, Wear **224**, 118 (1999).

[65] H. M. Clark and R. B. Hartwich, Wear **248**, 147 (2001).

[66] D. V. De Pellegrin and G. W. Stachowiak, Tribology International **37**, 255 (2004).

[67] H. Sin, N. Saka and N. P. Suh, Wear **55**, 163 (1979).

[68] B. W. E. Avient, J. Goddard and H. Wilman, Proceedings of the Royal Society of London A, **258**, 1960, p. 159.

[69] N. Gane and F. P. Bowden, Journal of Applied Physics **39**, 1432 (1968).

[70] J. B. Pethica and D. Taylor, Surface Science **89**, 182 (1979).

[71] W. W. Gerberich, S. K. Venkataraman, H. Huang, S. E. Harvey and D. L. Kohlstedt, Acta Metallurgica Et Materialia **43**, 1569 (1995).

[72] D. Lorenz, A. Zeckzer, U. Hilpert, P. Grau, H. Johansen and H. S. Leipner, Physical Review B **67**, 172101 (2003).

[73] J. B. Pethica and W. C. Oliver, Materials Research Society Symposium Proceedings, **130**, 1989, p. 13.

[74] W. C. Oliver and G. M. Pharr, Journal of Materials Research **7**, 1564 (1992).

[75] S. K. Venkataraman, D. L. Kohlstedt and W. W. Gerberich, Journal of Materials Research **8**, 685 (1993).

[76] H. Bei, Y. F. Gao, S. Shim, E. P. George and G. M. Pharr, Physical Review B **77**, (2008).

[77] A. B. Mann and J. B. Pethica, Applied Physics Letters **69**, 907 (1996).

[78] H. S. Leipner, D. Lorenz, A. Zeckzer, H. Lei and P. Grau, Physica B-Condensed Matter **308**, 446 (2001).

[79] T. F. Page, W. C. Oliver and C. J. Mchargue, Journal of Materials Research **7**, 450 (1992).

[80] Y. Gaillard, C. Tromas and J. Woirgard, Acta Materialia **51**, 1059 (2003).

[81] Y. Gaillard, C. Tromas and J. Woirgard, Philosophical Magazine Letters **83**, 553 (2003).

[82] W. W. Gerberich, J. C. Nelson, E. T. Lilleodden, P. Anderson and J. T. Wyrobek, Acta Materialia **44**, 3585 (1996).

[83] W. J. Poole, M. F. Ashby and N. A. Fleck, Scripta Materialia **34**, 559 (1996).

[84] G. Feng and W. D. Nix, Scripta Materialia **51**, 599 (2004).

[85] T. Chudoba and F. Richter, Surface and Coatings Technology **148**, 191 (2001).

[86] H. Li, A. Ghosh, Y. H. Han and R. C. Bradt, Journal of Materials Research **8**, 1028 (1993).

[87] W. D. Nix and H. Gao, Journal of the Mechanics and Physics of Solids **46**, 411 (1998).

[88] M. F. Ashby, Philosophical Magazine **21**, 399 (1970).

[89] J. F. Nye, Acta Metallurgica **1**, 153 (1953).

[90] G. I. Taylor, Journal of the Institute of Metals **62**, 307 (1938).

[91] X. Qiu, Y. Huang, W. D. Nix, K. C. Hwang and H. Gao, Acta Materialia **49**, 3949 (2001).

[92] G. E. Dieter. *Mechanical Metallurgy*, SI Metric Edition, McGraw-Hill, London, (1988).

[93] D. Hull and D. J. Bacon. *Introduction to Dislocations*, 3rd Ed., Butterwoth-Heinemann, Oxford, (1984).

[94] A. A. Elmustafa and D. S. Stone, Journal of the Mechanics and Physics of Solids **51**, 357 (2003).

[95] Y. Y. Lim and M. M. Chaudhri, Philosophical Magazine A **79**, 2979 (1999).

[96] J. G. Swadener, E. P. George and G. M. Pharr, Journal of the Mechanics and Physics of Solids **50**, 681 (2002).

[97] K. Durst, B. Backes and M. Göken, Scripta Materialia **52**, 1093 (2005).

[98] K. Durst, B. Backes, O. Franke and M. Goken, Acta Materialia **54**, 2547 (2006).

[99] K. Durst, O. Franke, A. Böhner and M. Göken, Acta Materialia **55**, 6825 (2007).

[100] K. Durst, M. Goken and G. M. Pharr, Journal of Physics D **41**, (2008).

[101] Y. Huang, F. Zhang, K. C. Hwang, W. D. Nix, G. M. Pharr and G. Feng, Journal of the Mechanics and Physics of Solids **54**, 1668 (2006).

[102] Y. Huang, X. Feng, G. M. Pharr and K. C. Hwang, Modelling and Simulation in Materials Science and Engineering **15**, S255 (2007).

[103] W. W. Gerberich, N. I. Tymiak, J. C. Grunlan, M. F. Horstemeyer and M. I. Baskes, Journal of Applied Mechanics **69**, 433 (2002).

[104] T.-Y. Zhang and W.-H. Xu, Journal of Materials Research **17**, 1715 (2002).

[105] T. Y. Zhang, W. H. Xu and M. H. Zhao, Acta Materialia **52**, 57 (2004).

[106] I. L. Jäger, Surface Science **565**, 173 (2004).

[107] L. Hong and R. C. Bradt, Journal of Materials Science **31**, 1065 (1996).

[108] K. Sangwal, Materials Chemistry and Physics **63**, 145 (2000).

[109] R. Vilar, Journal of Laser Applications **11**, 64 (1999).

[110] B. J. Kestel, "Polishing Methods for Metallic and Ceramic Transmission Electron Microscopy Specimens" (Technical Report), South Bay Technology, (1986).

[111] K. C. Thompson-Russel and J. W. Edington, "Monograph 5 - Electron Microscope Specimen Preparation Techniques in Materials Science". In: *Monographs in Practical Electron Microscopy in Materials Science*, Macmillan, Philips Technical Library, London, (1977).

[112] L. Bretherick. *Handbook of Reactive Chemical Hazards*, 3rd Ed., Butterworths, London-Boston, (1985).

[113] P. J. Goodhew (ed). *Specimen preparation for transmission electron microscopy of materials*, Vol. 3, Oxford University Press, London, (1984).

[114] E. Meyer, R. M. Overney, K. Dransfeld and T. Gyalog. *Nanoscience: Friction and Rheology on the Nanometer Scale*, World Scientific Publishing Company, Singapore, (1998).

[115] https://www.veecoprobes.com/probes.asp, April 30, 2008.

[116] A. L. Weisenhorn, P. K. Hansma, T. R. Albrecht and C. F. Quate, Applied Physics Letters **54**, 2651 (1989).

[117] L. Howald, E. Meyer, R. Luthi, H. Haefke, R. Overney, H. Rudin and H. J. Guntherodt, Applied Physics Letters **63**, 117 (1993).

[118] R. Wiesendanger. *Scanning Probe Microscopy and Spectroscopy: Methods and Applications*, Cambridge University Press, Cambridge, (1994).

[119] G. Meyer and N. M. Amer, Applied Physics Letters **57**, 2089 (1990).

[120] O. Marti, J. Colchero and J. Mlynek, Nanotechnology **1**, 141 (1990).

[121] "DI CP-II User's Guide - Part II: Advanced Techniques", Digital Instruments - Veeco Metrology Group, (2004).

[122] "Scanning Probe Microscopy Training Notebook", Digital Instruments - Veeco Metrology Group, (1997).

[123] J. Goldstein, D. Newbury, D. Joy, C. Lyman, P. Echlin, E. Lifshin, L. Sawyer and J. Michael. *Scanning Electron Microscopy and X-Ray Microanalysis*, 3rd Ed., Springer, New York, (2003).

[124] R. W. Cahn and P. Haasen. *Physical Metallurgy*, Vol. 2, 4th Ed., North-Holland, Amsterdam, (1996).

[125] L. Reimer. *Transmission Electron Microscopy: Physics of Image Formation and Microanalysis*, Vol. 36, 2nd Ed., Springer-Verlag, Berlin, (1989).

[126] D. B. Williams and C. B. Carter. *Transmission Electron Microscopy: A Textbook for Materials Science*, Plenum Press, New York, (1996).

[127] I. Ferguson. *Auger Microprobe Analysis*, Adam Hilger, Bristol, (1989).

[128] F. Montemor, personal communication, October 21, 2004.

[129] B. D. Cullity and S. R. Stock. *Elements of X-Ray Diffraction*, 3rd Ed., Prentice Hall, New Jersey, (2001).

[130] L. S. Zevin and G. Kimmel. *Quantitative X-Ray Diffractometry*, Springer-Verlag, New York, (1995).

[131] J. M. Antunes, A. Cavaleiro, L. F. Menezes, M. I. Simões and J. V. Fernandes, Surface and Coatings Technology **149**, 27 (2002).

[132] E. Meyer, Zeitschrift des Vereines Deutscher Ingenieure **52**, 645 (1908).

[133] ISO/FDIS 14577-1, (2002).

[134] N. A. Stilwell and D. Tabor, Proceedings of the Physical Society of London **78**, 169 (1961).

[135] "TriboIndenter Users Manual", Hysitron, (2001).

[136] S. I. Bulychev, V. P. Alekhin, M. K. Shorshorov, A. P. Ternovskii and G. D. Shnyrev, Zavodskaya Laboratoriya **41**, 1137 (1975).

[137] G. M. Pharr, W. C. Oliver and F. R. Brotzen, Journal of Materials Research **7**, 613 (1992).

[138] R. B. King, International Journal of Solids and Structures **23**, 1657 (1987).

[139] ASM. *Metals Handbook - Properties and Selection: Nonferrous Alloys and Special-Purpose Materials*, Vol. 2, 10th Ed., ASM International, Metals Park (OH), (1990).

[140] M. F. Doerner and W. D. Nix, Journal of Materials Research **1**, 601 (1986).

[141] "Overview of Mechanical Testing Standards - Indentation Test Standards" (Technical Report), CSM Instruments, (2002).

[142] A. C. Trindade, A. Cavaleiro and J. V. Fernandes, Journal of Testing and Evaluation **22**, 365 (1994).

[143] "Procedure #6-010 : Tip Shape Calibration Procedure", Hysitron, (1996).

[144] G. Constantinides, E. C. C. M. Silva, G. S. Blackman and K. J. Van Vliet, Nanotechnology **18**, 1 (2007).

[145] B. Cappella and G. Dietler, Surface Science Reports **34**, 1 (1999).

[146] "Nanoindentation and Nanoscratching with SPMs For NanoScope™ Version 4.32 Software", Digital Instruments - Veeco Metrology Group, (1998).

[147] M. VanLandingham, Microscopy Today **97-10**, 12 (1997).

[148] S. M. Hues, C. F. Draper and R. J. Colton, Journal of Vacuum Science and Technology B **12**, 2211 (1994).

[149] J. S. Villarrubia, Surface Science **321**, 287 (1994).

[150] J. S. Villarrubia, Journal of Vacuum Science and Technology B **14**, 1518 (1996).

[151] P. M. Williams, K. M. Shakesheff, M. C. Davies, D. E. Jackson, C. J. Roberts and S. J. B. Tendler, Journal of Vacuum Science and Technology B **14**, 1557 (1996).

[152] J. S. Villarrubia, Journal of Research of the National Institute of Standards and Technology **102**, 425 (1997).

[153] T. R. Thomas (ed). *Rough Surfaces*, Longman Group Limited, New York, (1982).

[154] S. Jacobsson, M. Olsson, P. Hedenqvist and O. Vingsbo, "Scratch Testing". In: *ASM Handbook: Friction, Lubrication and Wear Technology*, Vol. 18, ASM International, Metals Park (OH), (1992).

[155] A. G. Khurshudov, K. Kato and H. Koide, Wear **203**, 22 (1997).

[156] G. F. V. Voort. *Metallography: Principles and Practice*, ASM International, Metals Park (OH), (1999).

[157] E. E. Underwood. *Quantitative Stereology*, Addison-Wesley Publishing Company, Massachusetts, (1970).

[158] A. Pelzmann, M. Mayer, C. Kirchner, D. Sowada, T. Rotter, M. Kamp, K. J. Ebeling, S. Christiansen, M. Albrecht, H. P. Strunk, B. Hollander and S. Mantl, Mrs Internet Journal of Nitride Semiconductor Research **1**, art. no. 40 (1996).

[159] S. C. Wang, Z. Zhu and M. J. Starink, Journal of Microscopy - Oxford **217**, 174 (2005).

[160] J. E. Bailey and P. B. Hirsch, Philosophical Magazine **5**, 485 (1960).

[161] P. M. Kelly, A. Jostsons, R. G. Blake and J. G. Napier, Physica Status Solidi A **31**, 771 (1975).

[162] S. M. Allen, Philosophical Magazine A **43**, 325 (1981).

[163] D. B. Williams and C. B. Carter. *Transmission Electron Microscopy: II Diffraction*, II, Plenum Press, New York, (1996).

[164] P. B. Hirsch. *Electron Microscopy of Thin Crystals*, 2nd Ed., Robert E. Krieger Publishing Company, New York, (1977).

[165] H. J. Mathieu, M. Datta and D. Landolt, Journal of Vacuum Science and Technology A **3**, 331 (1985).

[166] G. Bhargava, I. Gouzman, C. M. Chun, T. A. Ramanarayanan and S. L. Bernasek, Applied Surface Science **253**, 4322 (2007).

[167] H. A. E. Hagelin-Weaver, G. B. Hoflund, D. A. Minahan and G. N. Salaita, Applied Surface Science **235**, 420 (2004).

[168] W. M. Steen. *Laser Material Processing*, Springer-Verlag, London, (1991).

[169] D. A. Mirzaev, V. M. Schastlivtsev, V. G. Ul'yanov, S. E. Karzunov, I. L. Yakovleva, K. Y. Okishev and Y. V. Khlebnikova, Physics of Metals and Metallography **93**, 552 (2002).

[170] A. Taylor, Journal of the Institute of Metals **77**, 585 (1950).

[171] Y. L. Yao, Journal of Chemical Physics **33**, 741 (1960).

[172] K. P. Gupta, Scripta Metallurgica **5**, 329 (1971).

[173] S. K. Si and K. P. Gupta, Scripta Metallurgica **7**, 963 (1973).

[174] A. Wolfenden, W. H. Robinson and A. W. Thompson, Scripta Metallurgica **11**, 71 (1977).

[175] A. W. Thompson, Metallurgical Transactions A **10**, 126 (1979).

[176] W. Garlipp, M. Cilense and C. R. S. Beatrice, Scripta Metallurgica et Materialia **29**, 1035 (1993).

[177] J. W. Cable, W. C. Koehler, M. K. Wilkinson and E. O. Wollan, Journal of Applied Physics **33**, 1340 (1962).

[178] M. F. Collins and D. A. Wheeler, Proceedings of the Physical Society of London **82**, 633 (1963).

[179] J. W. Cable, E. O. Wollan and W. C. Koehler, Physical Review **138**, A755 (1965).

[180] I. M. Puzey and V. I. Gomankov, Physics of Metals and Metallography **23**, 61 (1967).

[181] T. J. Burch, J. I. Budnick and S. Skalski, Journal of the Physical Society of Japan **28**, 1180 (1970).

[182] A. W. Thompson, Scripta Metallurgica **8**, 1167 (1974).

[183] R. E. Smallman. *Modern Physical Metallurgy*, 4th Ed., Butterworths, London, (1985).

[184] R. Vilar, O. Conde and D. Colin, Surface Modification Technologies **III**, 343 (1990).

[185] E. A. Brandes. *Smithells Metals Reference Book*, 6th Ed., Butterworths, London, (1983).

[186] W. D. Callister. *Materials Science and Engineering: An Introduction*, 5th Ed., John Wiley and Sons, New York, (2000).

[187] D. A. Porter and K. E. Easterling. *Phase Transformations in Metals and Alloys*, 2nd Ed., Chapman and Hall, London, (1992).

[188] A. A. Elmustafa and D. S. Stone, Materials Science and Engineering A **358**, 1 (2003).

[189] M. Rester, C. Motz and R. Pippan, Scripta Materialia **58**, 187 (2008).

[190] R. E. Reed-Hill and R. Abbaschian. *Physical Metallurgy Principles*, 3rd Ed., PWS-KENT, Boston, (1992).

[191] X. Chen, Y. Xiang and J. J. Vlassak, Journal of Materials Research **21**, 715 (2006).

[192] A. L. Gurson, Journal of Engineering Materials and Technology **99**, 2 (1977).

[193] Y. H. Qi, P. Bruckel and P. Lours, Journal of Materials Science Letters **22**, 371 (2003).

[194] D. M. Turley and L. E. Samuels, Metallography **14**, 275 (1981).

[195] L. E. Samuels. *Metallographic Polishing by Mechanical Methods*, ASM, Metals Park (OH), (1982).

[196] M. Mendik, S. Sathish, A. Kulik, G. Gremaud and P. Wachter, Journal of Applied Physics **71**, 2830 (1992).

[197] J. M. Howe. *Interfaces in Materials: Atomic Structure, Thermodynamics and Kinetics of Solid-Vapor, Solid-Liquid and Solid-Solid Interfaces*, John Wiley and Sons, New York, (1997).

[198] Z. Ma, S. Long, Y. Pan and Y. Zhou, Journal of Applied Physics **103**, 043512 (2008).

[199] H. M. Zhang, Y. Zhang, K. W. Xu and V. Ji, Solid State Communications **139**, 87 (2006).

[200] D. E. Gray. *American Institute of Physics Handbook*, 2nd Ed., McGraw-Hill, New York, (1963).

[201] J. Gump, H. Xia, M. Chirita, R. Sooryakumar, M. A. Tomaz and G. R. Harp, Journal of Applied Physics **86**, 6005 (1999).

[202] K. C. Antony, Journal of Metals **35**, 52 (1983).

[203] S. G. Corcoran, R. J. Colton, E. T. Lilleodden and W. W. Gerberich, Physical Review B **55**, 16057 (1997).

[204] D. F. Bahr, D. E. Kramer and W. W. Gerberich, Acta Materialia **46**, 3605 (1998).

[205] Y. Gaillard, C. Tromas and J. Woirgard, Acta Materialia **54**, 1409 (2006).

[206] D. E. Kramer, K. B. Yoder and W. W. Gerberich, Philosophical Magazine A **81**, 2033 (2001).

[207] A. M. Minor, J. W. Morris and E. A. Stach, Applied Physics Letters **79**, 1625 (2001).

[208] W. A. Soer and J. T. M. De Hosson, Materials Letters **59**, 3192 (2005).

[209] W. A. Soer, K. E. Aifantis and J. T. M. De Hosson, Acta Materialia **53**, 4665 (2005).

[210] J. W. Edington. *Interpretation of Transmission Electron Micrographs (Monographs in Practical Electron Microscopy in Materials Science)*, Vol. 3, Macmillan, London, (1975).

[211] Y. L. Chiu and A. H. W. Ngan, Acta Materialia **50**, 2677 (2002).

[212] P. C. Wo, A. H. W. Ngan and Y. L. Chiu, Scripta Materialia **55**, 557 (2006).

[213] G. B. Viswanathan, E. Lee, D. M. Maher, S. Banerjee and H. L. Fraser, Materials Science and Engineering A **400**, 463 (2005).

[214] D. A. Jones and J. W. Mitchell, Philosophical Magazine **3**, 1 (1958).

[215] F. Seitz, Physical Review **79**, 723 (1950).

[216] J. Li, K. J. Van Vliet, T. Zhu, S. Yip and S. Suresh, Nature **418**, 307 (2002).

[217] Y. Lee, J. Y. Park, S. Y. Kim, S. Jun and S. Im, Mechanics of Materials **37**, 1035 (2005).

[218] P. C. Wo and A. H. W. Ngan, Philosophical Magazine **84**, 3145 (2004).

[219] P. C. Wo, I. P. Jones and A. H. W. Ngan, Philosophical Magazine **88**, 1369 (2008).

[220] M. D. Thouless, Engineering Fracture Mechanics **61**, 75 (1998).

[221] J. S. Field and M. V. Swain, Journal of Materials Research **8**, 297 (1993).

[222] J. M. Helt and J. D. Batteas, Langmuir **22**, 6130 (2006).

[223] G. M. Hamilton and L. E. Goodman, Journal of Applied Mechanics **33**, 371 (1966).

[224] A. Sackfield and D. A. Hills, Journal of Strain Analysis for Engineering Design **18**, 107 (1983).

[225] S. Graça, "Tribology of Ni-Co alloys: from micro to nanoscale" (Materials Engineering graduation Thesis), (2004).

[226] http://www.csm-instruments.com/en/Nano-Tribometer, November 7, 2008.